2020-07-17

3D Geologic Mapping and Characterization Using Digital Outcrop Models Generated from Uninhabited Aerial Vehicles and Structure-from-Motion Photogrammetry

Nesbit, Paul Ryan

UNIVERSITY OF CALGARY

3D Geologic Mapping and Characterization Using Digital Outcrop Models Generated from Uninhabited Aerial Vehicles and Structure-from-Motion Photogrammetry

by

Paul Ryan Nesbit

A THESIS

SUBMITTED TO THE FACULTY OF GRADUATE STUDIES

IN PARTIAL FULFILMENT OF THE REQUIREMENTS FOR THE

DEGREE OF DOCTOR OF PHILOSOPHY

GRADUATE PROGRAM IN GEOGRAPHY

CALGARY, ALBERTA

JULY, 2020

Abstract

Outcrops are a primary source of geologic information and key in developing knowledge for teaching, training, and research. Observations from outcrop exposures provide opportunities to directly characterize detailed sedimentological composition, architectural characteristics, and link observations across various scales. Conventional field mapping techniques have remained largely unchanged for the past two centuries and are commonly limited in their ability to quantitatively constrain measurements, extend observations laterally, and document features at multiple scales. Recently, technological advances in uninhabited/unmanned aerial vehicles (UAVs) have prompted wide use in various geoscience disciplines to supplement field data with quantifiable digital information. However, application of UAVs to geologic mapping has been limited, due to unique challenges in data collection, processing, analysis, and visualization predominantly associated with intricate 3D exposures in complex topographic settings. This dissertation is focused on detailed investigation of 3D mapping, analysis, and dissemination from UAV-derived digital outcrop models (DOMs) that can potentially provide multi-scale perspectives and quantitative measurements that were previously difficult, or impossible to achieve with conventional field methods alone.

Preface

This thesis is the original work of the author, Paul Ryan Nesbit, with the exception of contributions from co-authors as explicitly described below. Where appropriate, the terms 'we' and 'our' are used throughout chapters (published manuscripts) comprising this thesis.

Chapter 2 has been reproduced with minor modifications from Nesbit et al. (2018) titled '3-D stratigraphic mapping using a digital outcrop model derived from UAV images and structure-from-motion photogrammetry', published in the Geological Society of America peer-reviewed journal *Geosphere* [doi:10.1130/GES01688.1], with permission from the Geological Society of America and written consent of each co-author (Appendix B).

Research design, methodology, analysis, and writing of this manuscript were performed by the author under the supervision of Christopher H. Hugenholtz. Paul R. Durkin and Stephen M. Hubbard provided expert assistance in understanding facies and stratigraphic architecture within the Dinosaur Provincial Park field area. Digital datasets were collected (with assistance from Paul R. Durkin and Maja Kucharczyk), processed, and analyzed by the author. Original field datasets used for comparison were collected by Paul R. Durkin and Stephen M. Hubbard with field assistance from Zennon Weleschuk, Daniel Niquet, and Reid van Drecht. The manuscript was greatly improved through several revisions from Christopher H. Hugenholtz, Paul R. Durkin, Stephen M. Hubbard, and Maja Kucharczyk.

Chapter 3 has been reproduced in this thesis with minor modifications from Nesbit and Hugenholtz (2019) titled 'Enhancing UAV-SfM 3D model accuracy in high-relief landscapes by incorporating oblique images', published in the peer-reviewed journal *Remote Sensing*

[doi:10.3390/rs11030239], with permission from Multidisciplinary Digital Publishing Institute (MDPI) and written consent of co-authors (Appendix B).

This research was conceptualized, designed, and written by the author under the supervision of Christopher H. Hugenholtz. Datasets were collected by the author with field assistance from Paul R. Durkin and Maja Kucharczyk. Processing and analysis of all datasets were performed by the author. This original manuscript was written and prepared by the author with input on analysis, content review, and editing by Christopher H. Hugenholtz.

Chapter 4 is in preparation for submission to a peer-reviewed internationally reputable journal as Nesbit, P.R., Hubbard, S.M., Daniels, B.G., Englert, R.G., Bell, D., and Hugenholtz, C.H., 'Digital re-evaluation of down-dip channel fill architecture in deep-water slope deposits: multi-scale perspectives from UAV-SfM.'

Research design, methodology, analysis, and writing of this manuscript were performed by the author under the supervision of Christopher H. Hugenholtz. The author collaborated with Stephen M. Hubbard for research design and framing. Datasets were collected, processed, and analyzed by the author. Stephen M. Hubbard, Benjamin G. Daniels, Rebecca Englert, and Daniel Bell provided expertise in understanding digital observations of facies and stratigraphic architecture within the deep-water channel deposits of the Tres Pasos Formation. Conventional field-based datasets were collected and prepared by Benjamin G. Daniels. This manuscript has undergone review from several co-authors, including Stephen M. Hubbard, Benjamin G. Daniels, Rebecca G. Englert, and Daniel Bell whose suggestions and comments have improved the manuscript.

Chapter 5 has been reproduced with minor modifications from Nesbit et al. (2020) titled 'Visualization and sharing of 3D Digital Outcrop Models to promote open science' published in the Geological Society of America peer-reviewed journal *GSA Today* [doi:10.1130/GSATG425A.1], with permission from the Geological Society of America and written consent of all co-authors (Appendix B).

Contents of this chapter were designed and written by the author under the supervision of Christopher H. Hugenholtz. The author generated the content and user interfaces within the Unity platform with assistance from Adam D. Boulding. Data collection was performed by the author with field assistance from Paul R. Durkin and Mozhou Gao. Data processing was completed by the author. Interpretations and content included in final user visualization platforms was guided by experts in the Dinosaur Provincial Park field area, Paul R. Durkin and Stephen M. Hubbard. Christopher H. Hugenholtz, Stephen M. Hubbard, Paul R. Durkin, and Adam D. Boulding provided thoughtful revisions to written and graphical content that improved the manuscript and accompanying materials.

Acknowledgements

I owe a great deal of gratitude to a number of people in my life who have made this personal achievement possible through funding opportunities, intellectual input, and moral support.

First, I want to express my appreciation to the University of Calgary and my supervisor, Dr. Chris Hugenholtz, for making this research and relocation of my family possible through an Eyes High Doctoral Scholarship. I want to thank Chris for inspiring me to grow as a researcher, writer, and educator – I would not be here without your guidance, support, and encouragement. I am grateful to my supervisory committee, Dr. Steve Hubbard and Dr. Darren Sjogren, who provided counsel, insight, and care in my academic and professional development. I must thank a number of co-authors: Dr. Paul Durkin, Dr. Ben Daniels, Dr. Daniel Bell, Maja Kucharczyk, Rebecca Englert, and Adam Boulding, who provided expertise and were critical in completing this work.

I am extremely fortunate to have amazing family and friends who have been there for me through my upbringing and during this endeavor. Many that have passed through Earth Sciences at U of C have made this journey truly enjoyable and have developed into lasting relationships. Lifelong friends and extended family in California have continued to provide the encouragement and love I needed to reach my goals and keep our family connected to home. I must send love to my family, who are my role models and have made this all possible. To my parents – thank you for being my biggest advocates, even for the tough decision to move to Calgary. To my sister – I continue to look up to you and your family, who bring me so much joy, though we are far away.

Finally, to my partner, Elsa – I am forever indebted to you for your readiness to move abroad (though serendipitous) and for your optimism, selflessness, and love that have carried me through the toughest times. Truly, none of this would have been possible without you.

~ I sincerely thank you all

Table of Contents

Abstract ii
Preface iii
Acknowledgements vi
List of Figures xi
List of Tables xvii
List of Abbreviations xviii
Chapter 1 Introduction 1
1.1 Project Motivation 1
1.2 Research Objectives 7
1.3 Thesis Format 8
1.4 References 13
Chapter 2 3-D Stratigraphic Mapping Using a Digital Outcrop Model Derived from UAV Images and Structure-from-Motion Photogrammetry 24
2.1 Abstract 24
2.2 Introduction 25
2.3 Geologic Setting and Study Area 29
2.4 Methods 31
2.4.1 Field data acquisition 31
2.4.2 UAV data acquisition 32
2.4.3 UAV data processing 34
2.4.4 Processing outputs 38
2.4.5 Digital interpretation and measurement 41
2.5 Results 43
2.5.1 Channel-belt contact 43
2.5.2 Sedimentary logs 44
2.6 Discussion 52
2.6.1 DOMs 53
2.6.2 3-D interpretation 54
2.6.3 3-D measurements 55
2.7 Conclusions 58

2.8 References 59
Chapter 3 Enhancing UAV-SfM 3D Model Accuracy in High-Relief Landscapes by Incorporating Oblique Images 72
3.1 Abstract 72
3.2 Introduction 73
3.3 Materials and Methods 79
3.3.1 Study site 79
3.3.2 UAV data collection 80
3.3.3 UAV processing and scenarios 82
3.3.4 Reference data acquisition and processing 85
3.3.5 Point cloud accuracy 87
3.4 Results 88
3.4.1 Single camera angle and single flight direction 88
3.4.2 Single camera angle and cross-hatch flight lines 89
3.4.3 Nadir image block (NSEW) supplemented with oblique images 95
3.4.4 Nadir image blocks (single flight line) supplemented with oblique images 99
3.4.5 Combination datasets — flight pattern 99
3.5 Discussion 100
3.5.1 Nadir-only image blocks 101
3.5.2 Single oblique camera angle image blocks 102
3.5.3 Combination datasets 103
3.5.4 Cameras and calibration 105
3.5.5 GCPs 107
3.5.6 Software and settings 108
3.6 Conclusions 109
3.7 References 110
Chapter 4 Digital Re-Evaluation of Down-Dip Channel Fill Architecture in Deep-Water Slope Deposits: Multi-Scale Perspectives from UAV-SfM 124
4.1 Abstract 124
4.2 Introduction 125
4.3 Geologic Setting and Study Area 129

4.4 Methods 131
4.4.1 Digital data collection and processing 133
4.4.2 Digital outcrop characterization, projection, and interpretation 134
4.5 Results 136
4.5.1 Sedimentary Facies 136
4.5.2 Traditional Field-Based Approach 136
4.5.2.1 Description 136
4.5.2.2 Interpretation 140
4.5.3 Digital DOM Approach 142
4.5.3.1 Description 142
4.5.3.2 Interpretation 145
4.6 Discussion 146
4.6.1 Comparison of Results from Field and Digital Approaches 146
4.6.2 Implications of New Fine-Scale Digital Observations 148
4.6.3 Future Considerations for UAV-SfM DOM Mapping 150
4.7 Conclusions 151
4.8 References 152
Chapter 5 Visualization and Sharing of 3D Digital Outcrop Models to Promote Open Science 167
5.1 Abstract 167
5.2 Introduction 168
5.3 Related Work 171
5.4 Case Study: Fluvial Stratigraphy, Dinosaur Provincial Park 173
5.4.1 Geological overview 173
5.4.2 Data collection and DOM processing 174
5.4.3 Visualization approaches 174
5.4.3.1 Web-based 3D mesh (Sketchfab) 175
5.4.3.2 Web-based 3D point cloud (potree) 175
5.4.3.3 Videogame engine (Unity) 176
5.5 Discussion 177
5.6 Conclusions and Recommended Use 181

5.7 References 182
Chapter 6 Thesis Summary and Concluding Remarks 189
6.1 Detailed Summary of Research Findings and Contributions 189
6.2 Limitations and Implications for Future Work 193
6.3 Final Remarks 197
6.4 References 198
Appendix A Additional Peer-Reviewed Contributions 203
Appendix B Copyright Permissions 204
Appendix C Supplemental Files and Resources 212

List of Figures

Figure 2.1. Locations of conventional ground survey field area (3.5 km^2, red dashed polygon) and unmanned aerial vehicle (UAV) survey area (0.52 km^2, black dashed polygon) within the badlands of Dinosaur Provincial Park (southeastern Alberta, Canada). UAV ground control point (GCP) locations (black Xs) were used for georeference during UAV structure-from-motion (UAV-SfM) processing, and sedimentary logs were collected in the field and used to locate the same numbered sections in the DOM (light-blue diamonds). 28

Figure 2.2. Lithostratigraphy of the Belly River Group, including the Dinosaur Park Formation, modified from Eberth (2005)..... 30

Figure 2.3. Simplified unmanned aerial vehicle data collection parameters programmed into the eBee autopilot: 90% overlap between successive images (blue rectangles to the left), 75% sidelap between flight lines (blue rectangles at the top), and a second flight (gray lines) programmed to fly perpendicular to flight 1 (black lines)..... 34

Figure 2.4. Typical outputs from the full unmanned aerial vehicle structure-from-motion multiview stereo process: (A) two-dimensional orthomosaic image; and (B) two-and a-half dimensional digital surface model. The resolution of these outputs is 0.02 m/pixel, but details along steep slopes are distorted or omitted. 37

Figure 2.5. Profile view of channel-belt basal contact (yellow arrows), with shallow-dipping counter-point-bar deposits (sandstone and siltstone) overlying flat-lying floodplain mudstone: (A) field photograph; (B) unmanned aerial vehicle–structure-from-motion (UAV-SfM) dense point cloud (see Supplemental Files 2.1–2.2 [Appendix C]); and (C) UAV-SfM triangulated mesh. Light-blue arrows in B and C represent the interpreted contact from the digital outcrop model (DOM); pink bars represent ~3 m on the ground..... 39

Figure 2.6. Profile view of thin-bedded, shallow-dipping, counter-point-bar deposits: (A) field photograph; (B) unmanned aerial vehicle–structure-from-motion (UAV-SfM) dense point cloud; and (C) UAV-SfM triangulated mesh. Note the “gaps” in the dense point cloud (B, yellow arrows) and the loss of fine detail due to interpolation in the triangulated mesh (C). Pink bar represents ~3 m. 40

Figure 2.7. Identification of channel-belt basal contact from the unmanned aerial vehicle–structure-from-motion (UAV-SfM) dense point cloud (light blue) and field differential

global positioning system (dGPS; red): (A) contact locations throughout field site, where yellow boxes denote locations of images in B and C; (B) profile view of digitized points (light blue) and imported field dGPS points (red) with vertical disagreements up to 1.44 m; and (C) profile view of digitized points and imported field dGPS points showing agreement. Pink bars in B and C represent ~3 m. DOM—digital outcrop model. 41
Figure 2.8. Digital sedimentary log interpretation (log 08; Fig. 2.9H). (A) Bedding contacts (light blue) on the dense point cloud were determined by spectral changes on the dense point cloud digital outcrop model, digitized within Pix4Dmapper. The bottom and top of sedimentary logs were determined from differential global positioning system locations (red arrows) collected in the field. (B) Digital sedimentary log (log 08) resulting from digital identification of changing lithology (symbology is consistent with Fig. 2.9). Pink bars in A represent ~3 m. Grain-size abbreviations: si—silt; vfs—very fine sand; fs—fine sand; ms—medium sand; cs—coarse sand. 43
Figure 2.9. Sedimentary logs and facies logs collected independently in the field and digitally from the unmanned aerial vehicle–structure-from-motion (UAV-SfM) dense point cloud digital outcrop model (DOM). Each subfigure (A–J) contains a side-by-side comparison of the field and digital logs: (A) log 01; (B) log 02; (C) log 03; (D) log 04; (E) log 05; (F) log 06; (G) log 07; (H) log 08; (I) log 09; (J) log 10. 47
Figure 2.10. Profile view of sedimentary log 01 (Fig. 2.9A): (A) within the digital outcrop model, where light-blue points separate digitally identified units within a one-dimensional sedimentary log; (B) lateral interpretation of bedding surfaces (purple polygons), which allows three-dimensional quantification and interpretation of geologic deposits; and (C) overview showing the same surfaces in the context of the surrounding geology indicative of a point bar migrating 90° east (left in the image). Pink bars in A–C represent ~3 m. For interactive model, see Supplemental Files 2.3–2.4 (Appendix C). 50
Figure 2.11. Profile view of sedimentary log 09 (Fig. 2.9I): (A) within the digital outcrop model, where light-blue points separate digitally identified units within a one-dimensional sedimentary log; (B) lateral interpretation of bedding surfaces (purple polygons), which allows three-dimensional quantification and interpretation of geologic deposits; and (C) overview showing the same surfaces in the context of the surrounding geology indicative of

a counter point bar migrating 190° south-southwest (right in the image). Pink bars in A–C represent ~3 m. For interactive model, see Supplemental Files 5–6 (Appendix C). 51
Figure 3.1. (A) Field location with UAV and terrestrial laser scanner (TLS) data extents, ground control points (GCPs), and TLS scan locations; (B) digital surface model (DSM) of the field area used for data assessment. 80
Figure 3.2. Oblique combination scenarios (A) outside box, BoxO; (B) inside box, BoxI; (C) inside and outside box, BoxIO; (D) single convergent arcs; (E) double convergent arcs. Note light-grey lines represent north–south (NS) nadir image flight lines. 83
Figure 3.3. Average M3C2-calculated difference between TLS reference dataset and various UAV–SfM image configurations; (A) standard deviation (precision); (B) mean difference (accuracy). M3C2: Multiscale Model to Model Cloud Comparison; NSEW: NS and EW flight lines combined. 89
Figure 3.4. M3C2-calculated difference between TLS reference dataset and UAV–SfM image configurations collected with a single camera angle and various image overlap settings (70/70, 90/70, and 90/90) with cross-hatch flight lines (NSEW); (A) standard deviation (precision); (B) mean difference (accuracy). 91
Figure 3.5. M3C2-calculated distance between TLS reference dataset and UAV–SfM data sets collected with nadir camera angles and cross-hatch flight lines (NSEW) with various image overlap settings: (A) 70/70, (B) 90/70, and (C) 90/90. Positive values indicate UAV–SfM surface above TLS reference surface; negative values suggest UAV–SfM surface below. Note the systematic distribution of error with low points (near the center of the field area) higher than the reference dataset and high points (near the perimeter of the field area) lower than the reference dataset. This systematic error is similar to that noted by James and Robson (2014) and is present regardless of overlap. 92
Figure 3.6. M3C2-calculated distance between TLS reference dataset and UAV–SfM image sets collected with 90/70 overlap, cross-hatch flight lines (NSEW), and a single camera angle; (A) 00° (nadir); (B) 05°; (C) 10°; (D) 15°; (E) 20°; (F) 25°; (G) 30°; (H) 35°. Positive values indicate UAV–SfM surface above TLS reference surface; negative values suggest UAV–SfM surface below. 94
Figure 3.7. M3C2-calculated distance between TLS reference dataset and UAV–SfM combination image sets: (A) 70/70—05° BoxIO; (B) 70/70—20° BoxIO; (C) 70/70—35 °

BoxIO; (D) 90/70—05° BoxIO; (E) 90/70—20° BoxIO; (F) 90/70—35° BoxIO. See Figure 3.2 for description of flight patterns. Positive values indicate UAV–SfM surface above TLS reference surface; negative values suggest UAV–SfM surface below. 97
Figure 3.8. M3C2-calculated difference between TLS reference dataset and various UAV–SfM combination datasets with different image configurations: (A) standard deviation, 70/70 overlap combinations; (B) standard deviation, 90/70 overlap combinations; (C) mean difference, 70/70 overlap combinations; (D) mean difference, 90/70 overlap combinations. See Figure 3.2 for description of flight patterns. 98
Figure 4.1. Overview of regional lithostratigraphy and field area. A) summary of Late Cretaceous formations associated with the Magallanes-Austral basin.; B) regional dip-oriented stratigraphic cross-section of the Tres Pasos and Dorotea formations showing coarse-scale clinoforms, modified from (Bauer et al., 2020); C) field location relative to A and B. Note: red box in (B-C) indicates area displayed in Figure 4.2..... 130
Figure 4.2. A) Oblique perspective of field area from satellite imagery in Google Earth including the locations of measured stratigraphic sections (yellow lines). B) Regional cross-section produced from GPS mapping and measured section field data documented with traditional field methods (Daniels, 2015). C) Stratigraphic hierarchical framework of deep-water channel systems in strike-oriented cross-section, modified from (Covault et al., 2016). Note: blue box in (A-B) specifies location for UAV-SfM analysis in this study (Figure 4.5). 132
Figure 4.3. Methodology for documenting stratigraphic architecture. A) 3D DOM processed and visualized in Pix4Dmapper; B) Interpret potential surfaces using manual tie points directly within Pix4Dmapper; C) Export points, project from 3D to 2D plane following Englert et al. (2018) and interpret related sedimentary bodies on 2D plane while cross-referencing data in the 3D model resulting in Figure 4.5B. 135
Figure 4.4. Lithofacies associations within the Tres Pasos Formation in the study area described in Table 4.1 adapted from Daniels (2019). A) F1: thick-bedded sandstone and/or conglomerate; B) F2: thick- to thin-bedded sandstone and mudstone; C) F3: thin-bedded mudstone with sandstone; D) F4: chaotically bedded, poorly sorted mudstone and sandstone associated with Mass Transport Deposits (MTD). 137
Figure 4.5. Down-dip cross-sectional profile of interpreted stratigraphic architecture. A) Traditional field methods (Daniels, 2015); B) Digital UAV-SfM DOM methods. 139

Figure 4.6. Examples of surface characteristics as seen in the field (A-C) and in the digital outcrop model (D-F). Channel complex boundary (A and D, red); channel element boundary (B and E, blue); internal element surfaces (C and F, black). Note: arrows indicate paleoflow direction. 141
Figure 4.7. Example of discontinuous internal surfaces that become undetectable in amalgamated sandstone. A) Contextual overview (see Figure 4.5B for broader context), yellow box specifies location in (B-C); B) UAV image of inaccessible amalgamated sandstone; C) line drawing of overlying channel element surface (blue) and discontinuous internal element surfaces (black) superimposed on image from part B. 143
Figure 4.8. Example of internal surfaces revealing nuanced detail of a sequence of low-angle inclined surfaces. A) Oblique view of UAV-SfM DOM; B) line drawing of underlying channel complex boundary (red), overlying channel element boundary (blue), and internal element surfaces (black) superimposed on image in part A. Internal surfaces bound lenticular wedge-shaped bodies with low-angle inclined surfaces that dip in the upslope direction forming a backsetting stacking pattern. These features are similar in scale and geometry to upslope migrating bedforms that were not recognized with conventional field-based approaches. C) Field logs collected following digital DOM analysis to lithologically calibrate digital interpretations of architecture. 144
Figure 5.1. Geologic interpretations (line drawing on 2D field photograph), a common conventional method to highlight stratigraphic architecture and distribution of related units. Mudstones are grey to light brown, sandstones are light grey to white. This process is often performed on photos or a photomosaic acquired in the field. 169
Figure 5.2. Traditional geologic map used to share field measurements, observations, and interpretations in 2D plan-view. This geologic map was constructed from the integration of traditional field work methods (measured sections as well as paleoflow and bedding measurements) with DOM mapping to characterize heterolithic channel-belt deposits exposed at Dinosaur Provincial Park, southeastern Alberta, Canada. Field-based Facies Associations (FA)1: sandy point bar; FA2: heterolithic point bar; FA3 Counter-point bar; FA4: abandoned channel; FA5: mudstone. Bedding surfaces, noted in Figure 5.1 (red), were digitally mapped on the 3D model and yield a more refined and detailed interpretation of

accretion surface orientation and stratigraphic architecture. These methods are being widely applied, yet the results are difficult to disseminate and share in 3D. 170
Figure 5.3. Digital outcrop models (DOMs) of the heterolithic channel-belt deposits in Figure 5.1, presented in two different viewers. A) Sketchfab viewer contains 3D textured mesh DOM, but is limited by resolution and only supports text annotations to provide supplemental information; note the limited field area loaded to preserve detail in texture and topography – additional interactive models of the field area can be found on the web at https://sketchfab.com/paulnesbit or by following the QR code. Additional proprietary web viewers include Euclidean Vault (https://www.euclideon.com/vaultinfo/), and voxxlr (https://www.voxxlr.com/). B) Visualization of the 3D dense point cloud DOM of the entire 1 km^2 field area (>805 million points) in a standard web browser using potree code applied in customized web viewer from Pix4D. QR code provides digital access to the fully interactive viewer also available at http://tiny.cc/Pix4DpotreeViewer. 178
Figure 5.4. Videogame viewer (executable application) of the entire 1 km^2 field area rendered as a textured mesh and created with Unity. Note the dynamic orientation arrow in the upper left corner of the game, the options menu to the right of the screen and interpretations of geologic surfaces turned ‘on’. Drop-down menu in the side panel provides end-users with options to navigate to pre-defined 'points of interest' throughout the field area, simulating virtual field trip stops. Note the resolution difference between the foreground UAV model and the peripheral topography and landscape, created with a DEM draped with a 10 m satellite image. End-users can also select 'Free Fly' mode in order to navigate throughout the field site on their own. Full interactive viewer available in Supplementary File 5.1 and 5.2 (Appendix C; also accessible from the QR code)..... 179

List of Tables

Table 2.1. Field facies and digital facies..... 32
Table 2.2. Channel-belt basal contact interpretation. 44
Table 2.3. Results of facies comparison – field and digital. 49
Table 3.1. Recommended oblique image angles for supplementing structure-from-motion (SfM) nadir image blocks from the literature..... 78
Table 3.2. UAV–SfM processing scenarios..... 83
Table 3.3. Processing settings in Pix4Dmapper selected for all UAV–SfM scenarios. 84
Table 4.1. Characteristic facies for the Tres Pasos Formation at Alvarez Ridge. 138

List of Abbreviations

Abbreviation	
2D	Two-Dimensional
2.5D	Two and a Half-Dimensional
3D	Three-Dimensional
AAT	Automatic Aerial Triangulation
AGL	Above Ground Level
AGU	American Geophysical Union
API	Application Programming Interface
BBA	Bundle Block Adjustment
CMOS	Complementary Metal Oxide Semiconductor
CPU	Central Processing Unit
CSPG	Canadian Society of Petroleum Geologists
DEM	Digital Elevation Model
dF_{1-4}	Digital Facies (1-4)
dGPS	Differential Global Positioning System
DOM	Digital Outcrop Model
DSM	Digital Surface Model
DTM	Digital Terrain Model
EOP	External Orientation Parameters (of a camera)
EW	East-West (flightlines)
F_{1-6}	Facies (1-6)
FA_{1-5}	Facies Associations (1-5)
Fm	Formation
GAC	Geological Association of Canada
GB	Gigabytes
GCP	Ground Control Point
GIS	Geographic Information System
GNSS	Global Navigation Satellite System
GPS	Global Positioning System

GPU	Graphics Processing Unit
GSA	Geological Society of America
GSD	Ground Sampling Distance
IMU	Inertial Measurement Unit
IOP	Internal Orientation Parameters (of a camera)
LiDAR	Light Detection and Ranging
LoD	Level of Detail
M3C2	Multiscale Model to Model Cloud Comparison algorithm
MAE	Mean Absolute Error
MB	Megabytes
MP	Megapixels
MTD	Mass Transport Deposit
MVS	Multi-View Stereo
NS	North-South (flightlines)
NSEW	North-South and East-West (flightlines)
RAM	Random Access Memory
RGB	Red, Green, Blue (color channels of an image)
RMSE	Root Mean Squared Error
RTK	Real Time Kinematic
SfM	Structure-from-Motion
SfM-MVS	Structure-from-Motion-Multi-View Stereo
SIFT	Scale Invariant Feature Transform
TIN	Triangulated Irregular Network
TLS	Terrestrial Laser Scanner
UAV	Uninhabited (or unmanned) Aerial Vehicle
UAV-SfM	Uninhabited Aerial Vehicle-based Structure-from-Motion
UI	User Interface
USGS	United States Geological Survey
VRGS	Virtual Reality Geological Studio

Chapter 1

Introduction

1.1 Project Motivation

Ancient geologic deposits are key in guiding our knowledge of past environments, understanding earth surface processes, and interpreting subsurface development and movement of resources (e.g., groundwater and natural gas). Recording observations of ancient deposits, however, can be challenging and typically only provide a limited perspective. For example, subsurface deposits offer opportunities to understand regional and basin-scale characteristics, but datasets (e.g., seismic reflection data, boreholes, and wireline logs) are typically coarse resolution (10s of meters, vertically) that exclude the ability to deduce internal heterogeneity (e.g., Deptuck et al., 2007; Labourdette and Jones, 2007). Outcrop exposures at the surface present the ability to directly characterize detailed sedimentological composition, architectural characteristics, and contextualize fine-scale observations within a regional context (Bryant et al., 2000; Hodgetts, 2013; Howell et al., 2014). However, conventional outcrop mapping techniques are restricted by inaccessibility, discontinuity, orientation of exposure, and typically require interpolation between field observations, which often result in increased uncertainty, oversimplification, and lack of quantitative constraints (Jones et al., 2004; Bond et al., 2007). Despite these limitations, conventional field mapping techniques have remained largely unchanged for the past two centuries (Jones et al., 2004, 2008; McCaffrey et al., 2005; Pavlis et al., 2010; Whitmeyer et al., 2010).

In the past two decades, a host of geospatial technologies have integrated into outcrop mapping workflows, transforming the way in which field data can be collected

(House et al., 2013; Pavlis and Mason, 2017). For example, it is now common for field geologists to carry a handheld GPS and digital camera to accompany field observations (McCaffrey et al., 2005; Bond et al., 2007). These familiar technologies can provide geolocation of observations, enable integration within Geographic Information Systems (GIS), and provide supplemental information during interpretation. However, the limited precision of handheld GPS units (~5-10 m) and absence of geographic scaling constraints in photographs, inhibits use for quantitative characterization.

Georeferenced imagery and digital elevation models (DEMs) from airborne or satellite platforms are often used to complement field-based geoscience investigations. Although these datasets can enhance mapping of large areas ($> 10^6$ m^2), they are not always suitable for outcrop studies, due to limited spatial resolution (typically m/pixel) and exposure orientation. Airborne and satellite datasets are typically collected with a nadir-, or downward-, viewing sensor that is susceptible to distortion, or complete loss of detail, along planes non-normal to data acquisition; for example, steep slopes (> 45°) commonly associated with outcrop exposures (Bellian et al., 2005; James and Quinton, 2014; Rittersbacher et al., 2014; Pavlis and Mason, 2017).

More advanced remote sensing techniques using laser scanning and/or photogrammetry have been used to supplement field studies with photorealistic, three-dimensional (3D) digital outcrop models (DOMs), or virtual outcrops (Hodgetts et al., 2004; Bellian et al., 2005; McCaffrey et al., 2005; Trinks et al., 2005; Enge et al., 2007; Labourdette and Jones, 2007; Pranter et al., 2007; Buckley et al., 2008; Vollgger and Cruden, 2016; Cawood et al., 2017; Pavlis and Mason, 2017). DOMs have demonstrated several advantages in outcrop studies including (i) dynamic and interactive 3D views, (ii)

accurately scaled and oriented data that can be used to make observations, (iii) ability to record measurements of inaccessible or dangerous sections of outcrop, and (iv) digital archiving for iterative interpretation and analysis (McCaffrey et al., 2005; Hodgetts, 2013). Ground-based terrestrial laser scanning (TLS) has been the most common method for obtaining DOMs (Hodgetts, 2013), but is often hindered by line-of-sight constraints, requiring multiple viewpoints to eliminate data occlusions. Although there are exceptions (e.g., Rarity et al., 2014), this generally limits the lateral extent that can be practically captured to relatively small areas (e.g., $< 10^4$ m^2); this is particularly true for highly incised landscapes with high drainage density or areas without suitable scanning locations (Pringle et al., 2004; Hodgetts, 2013; James and Quinton, 2014). Additionally, laser scanning systems are often prohibitively expensive, practically immobile, and require dedicated computing hardware and software to process, visualize, and analyze datasets (Rittersbacher et al., 2014; Chesley et al., 2017).

In recent years, small uninhabited/unmanned aerial vehicles (UAV) have emerged as an alternative, low-cost remote sensing technique capable of generating high spatial resolution data over a broader extent than ground-based methods (James and Robson, 2012; Niethammer et al., 2012; Colomina and Molina, 2014; Whitehead and Hugenholtz, 2014; Toth and Jóźków, 2016). Image sets collected from UAV are commonly processed using structure-from-motion multi-view stereo (SfM-MVS) photogrammetry to generate high-resolution (cm/pixel) orthomosaic images and digital elevation models (DEM). SfM-MVS, or more commonly SfM photogrammetry, is a recently popularized image-based modeling technique developed in the computer vision community that estimates 3D structure of a scene from a series of overlapping 2D images (Snavely et al., 2006;

Furukawa and Ponce, 2007; Szeliski, 2010; Fonstad et al., 2013; Colomina and Molina, 2014). SfM workflows have similarities to conventional photogrammetry, however one of the main differences is that SfM is highly automated and does not require any a priori knowledge about the scene, camera location/orientation, camera settings, or any manual identification of tie points. Instead of manual inputs, SfM uses automated feature detection and matching algorithms (e.g., Scale Invariant Feature Transform, SIFT) to estimate the location of images relative to one another while concurrently calculating the object geometry of a scene (Lowe, 2004; Brown and Lowe, 2005; Snavely et al., 2008; Westoby et al., 2012; Fonstad et al., 2013).

UAV-SfM techniques have been widely used in the earth sciences, primarily within sub-disciplines of geomorphology (e.g., Niethammer et al., 2012; Harwin and Lucieer, 2012; James and Robson, 2012, 2014; Whitehead et al., 2013; Hugenholtz et al., 2013; Javernick et al., 2014; Smith and Vericat, 2015; Smith et al., 2015; Tamminga et al., 2015; Westoby et al., 2015; Clapuyt et al., 2015; Woodget et al., 2015; Hackney and Clayton, 2015; Harwin et al., 2015; Carrivick et al., 2016; Eltner et al., 2016; Carbonneau and Dietrich, 2017; James et al., 2017a, 2017b; Woodget and Austrums, 2017), but have seen limited uptake in geologic mapping applications (e.g., Bemis et al., 2014; Johnson et al., 2014; Chen et al., 2015; Vollgger and Cruden, 2016; Zahm et al., 2016; Cawood et al., 2017; Chesley et al., 2017; Nieminski and Graham, 2017). This may be related to a number of practical challenges, such as limited battery life, constantly changing regulations, and difficult or unsuitable flying conditions (Colomina and Molina, 2014; Cawood et al., 2017; Nesbit et al., 2017); however, this could also be explained by innate barriers and unique challenges in geologic mapping scenarios that require exclusive

consideration. Specifically, geologic features are inherently 3D and often exposed in outcrop along vertical or steeply sloping gradients (i.e., cliffs), creating difficulties for data collection, analysis, and visualization, even when using modern UAV-SfM workflows.

In light of the inherent complexities associated with 3D outcrops, the motivation for this thesis is driven by the paucity of practical 3D geological mapping techniques to obtain, analyze, and visualize accurate and detailed geologic data from outcrop. Though UAV-SfM has demonstrated potential in geoscience applications to bridge the area-resolution divide between airborne and ground-based datasets, there are various challenges that must be addressed. The most common UAV-SfM products used in the geosciences are 2D or 2.5D representations of 3D information (e.g., orthomosaic images, DEMs; Carrivick et al., 2016). Although measurements and interpretations from 2D remotely sensed datasets may be suitable for relatively flat, featureless outcrops exposed in plan-view (e.g., Chesley et al., 2017), they may not achieve their suggested potential for more complex 3D exposures and landscapes, such as vertical or overhanging cliffs.

An alternative approach is to take advantage of the 3D data created during intermediate steps of the SfM-MVS processing workflow, such as the dense point cloud or textured triangulated mesh. These datasets retain 3D information and can be used as digital outcrop models (DOM) for recording measurements, interpretations, and characterization of complex scenes. UAV-SfM DOMs have demonstrated similar benefits to TLS-derived DOMs (e.g., high-resolution, scaled) and can be practically applied to inaccessible and intricate outcrop exposures over large spatial extents. The geologic mapping literature has yet to detail UAV-SfM data collection and processing strategies in

high-relief scenarios. For example, although it has been suggested that UAV images collected at oblique angles can increase coverage along slopes (Bemis et al., 2014; Vollgger and Cruden, 2016; Cawood et al., 2017), investigation into the effects of off-nadir images on resulting 3D DOM accuracy has not been sufficiently addressed prior to this thesis. Recent research from the geomorphological and photogrammetric literature has suggested that including off-nadir images may be beneficial for eliminating systematic errors in SfM models (James and Robson, 2014; Harwin et al., 2015; Carbonneau and Dietrich, 2017; James et al., 2017). However, there has been no consensus on ideal imaging angles or implementation of practical UAV flight plans to strengthen imaging geometry and final model accuracy.

Strategies for recording geologic observations from these 3D datasets are also underdeveloped and seldom assessed for accuracy. Identification and measurement of geologic features has been made from 2D UAV-SfM datasets (e.g., Johnson et al., 2014; Zahm et al., 2016; Chesley et al., 2017; Chesley and Leier, 2018), but workflows to derive observations from UAV-SfM 3D DOMs have rarely been documented. Moreover, measurements made from UAV-SfM datasets (2D or 3D) have seldom been assessed for accuracy or compared for commensurability with field-based observations (e.g. Cawood et al., 2017). Although quality and accuracy of 3D DOMs are inherently dependent on input datasets (i.e., images, GCPs) for an individual study, it is important to establish baseline understanding of the potential and limitations of digitally derived observations and interpretations.

Another consideration that is generally overlooked in all UAV-SfM applications, is the inability to share 3D models and communicate interpretations and results.

Visualization of 3D datasets remains taxing on computational hardware and requires specialty software (e.g., Virtual Reality Geology Studio - Hodgetts et al., 2007; LIME - Buckley et al., 2019), often hindered by licensing restrictions and considerable learning curves. Researchers rely on specialist software for analysis and visualization, but must often revert to traditional formats for sharing data (e.g., 2D screen captures or fly-through videos with pre-defined viewpoints), limiting the open exchange of datasets and results. Although several studies have suggested the potential of UAV-SfM for geologic mapping applications (e.g., Chesley et al., 2017; Nieminski and Graham, 2017; Pavlis and Mason, 2017), no previous studies have fully addressed the inherent challenges associated with implementation of UAV-SfM for mapping complex 3D outcrop exposures.

1.2 Research Objectives

The overarching objective of this doctoral research is to better constrain, document, and advance digital workflows for 3D geologic mapping applications using small UAVs and SfM photogrammetry. Although UAV-SfM has been widely applied in the geosciences, use in geologic mapping applications has remained challenging, due to the 3D nature of geologic outcrops and tendency to be exposed in complex (e.g., high-relief) topographic settings. These inherent challenges require deliberate consideration and investigation of data collection, visualization, analysis, and dissemination strategies. The following research objectives address each of these discrete challenges and contribute in achieving the overall goal of this doctoral research:

i. To compare digital observations, measurements, and facies estimation from UAV-SfM derived DOMs with traditional (field-based) methods in order to assess commensurability of digital and conventional techniques.

ii. To evaluate the effects of imaging strategy, particularly image overlap, flight pattern, and inclusion of oblique images, on accuracy, precision, and resolvable detail along steep slopes within UAV-SfM derived 3D models.

iii. To demonstrate the additional multi-scale perspectives and quantitative potential provided by a UAV-SfM workflow in recognizing and recording subtle features in outcrop that may be easily overlooked or impossible to identify in the field.

iv. To examine and review modern platforms for visualizing and disseminating 3D datasets without the need for specialized software and/or hardware to share datasets, interpretations, and results with a broad audience.

1.3 Thesis Format

This manuscript-based doctoral thesis consists of six chapters, composed of four research papers (Chapters 2-5) that have been published, or prepared for publication, in international peer-reviewed journals. Chapters 2, 3, and 5 are adopted with minimal modifications from published research articles, while Chapter 4 is currently in final preparation for submission. As this thesis is manuscript-based with an overall objective in constraining and advancing UAV-SfM workflows for geologic mapping applications, some of the introductory materials within individual chapters may contain comparable information. A summary of primary findings, contributions, and publication information for each chapter is presented below.

Chapter 2 evaluates digital observations from UAV-derived datasets and their commensurability with conventional, field-based observations at multiple scales (e.g., bed- and channel belt-scales) for outrop exposures along steep slopes in high-relief

landscapes. This chapter describes the UAV-SfM workflow for data collection, generation, and interpretation of 3D digital outcrop models (DOMs) and details the challenges in using common 2D datasets (e.g., orthomosaic images and DEMs) for analysis. Results demonstrate that observations from UAV-SfM 3D data products (e.g., dense point cloud and textured mesh) are comparable to field-based observations (± 4.9%) for bed-level (decimeter) detail and for characterizing macro-scale features. Additionally, this study suggests that digital observations can provide quantitative measures at multiple scales of laterally extensive features that are difficult, if not impossible, to identify using traditional field methods.

This work primarily addresses Research Objective (i), introduces Research Objective (iii), and sets the foundational workflow for Chapters 3-5. Results are peer-reviewed and published in The Geological Society of America journal, *Geosphere*. Some results from this chapter were also presented at the *American Geophysical Union (AGU) Annual Fall Meeting*, December 2016 in San Francisco, California. Additionally, this chapter contributed to supplemental analysis for a co-authored manuscript recently published in the peer-reviewed journal *Sedimentology* (Appendix A, Durkin et al., 2020).

Nesbit, P.R., Durkin, P.R., Hugenholtz, C.H., Hubbard, S.M., and Kucharczyk, M. 2018. 3-D stratigraphic mapping using a digital outcrop model derived from UAV images and structure-from-motion photogrammetry. *Geosphere*, 14 (6), p. 2469-2486. doi:10.1130/GES01688.1.

Nesbit, P.R., Hugenholtz, C.H., Durkin, P.R., Hubbard, S.M., Kucharczyk, M., and Barchyn, T. 2016. High resolution stratigraphic mapping in complex terrain: a

comparison of traditional remote sensing techniques with unmanned aerial vehicle - structure from motion photogrammetry. *American Geophysical Union. 12-16 Dec 2016. San Francisco, CA.* 2016AGUFMNH13B..08N.

Chapter 3 features a detailed investigation of the influence of image collection strategy on accuracy, precision, and detail of UAV-SfM derived 3D datasets. In particular, this chapter considers integration of images collected at various oblique angles along with different image overlap and flight patterns for a high-relief landscape. This paper confirms the presence of systematic errors associated with the most common UAV surveying strategies (i.e., grid pattern with a nadir-facing camera), reveals errors associated with different oblique camera angles, and provides practical imaging strategies to reduce errors in final 3D datasets.

This work directly addresses Research Objective (ii), which strives to improve accuracy, precision, and resolvable detail of digital measurement and observations in order to provide more reliable quantitative measures in Research Objectives (i) and (iii). Results are peer-reviewed and published in *Remote Sensing*.

Nesbit, P.R. and Hugenholtz, C.H. 2019. Enhancing UAV-SfM 3D model accuracy in high-relief landscapes by incorporating oblique images. *Remote Sensing*, 11 (239), p. 2469-2486. doi:10.3390/rs11030239.

Chapter 4 builds on previous chapters to demonstrate the potential of UAV-SfM workflows in adding multi-scale perspectives and quantitative observations to recognize and record subtle features in sedimentary deposits that may be easily overlooked or

impossible to identify using field-based approaches alone. Specifically, this paper uses the UAV-SfM methods documented in Chapters 2-3 to revisit an extensive cliff-side outcrop previously mapped and documented with conventional field methods (sedimentary logs, field observations, and differential GPS surface mapping; Daniels, 2015, 2019). Results are reasonably aligned with previous interpretations of meso- and macro-scale architecture, while also revealing nuanced internal detail that was not evident from field-based perspectives alone.

This chapter addresses Research Objective (iii) and co-addresses Research Objective (i) in comparison of field-based and digital methodologies. This work is currently in preparation for submission to the *Journal of Sedimentary Research*. Some results from this chapter were also presented at the *American Geophysical Union (AGU) Annual Fall Meeting*, December 2019 in San Francisco, California.

Chapter 5 examines and reviews modern visualization platforms to disseminate and visualize 3D datasets without the need for specialty software and/or hardware or transfer of large files. This chapter specifically provides a practical introduction to modern 3D visualization platforms, demonstrates a range of features and functionality of three representative viewers, and describes potential use cases for each platform that expand the ability to share datasets, interpretations, and results with a broad audience.

This chapter utilizes results derived from Research Objectives (i-iii) in presenting a case study that addresses Research Objective (iv). Results are peer-reviewed and published in The Geological Society of America journal, *GSA Today*. Some results from this chapter were also presented at the *American Geophysical Union (AGU) Annual Fall*

Meeting, December 2019 in San Francisco, California and have been accepted for presentation at the 2020 *GeoConvention* hosted by the *Geological Association of Canada (GAC)* and *Canadian Society of Petroleum Geologists (CSPG)* in Calgary, Alberta, (11-13 May 2020, postponed TBD).

Nesbit, P.R., Boulding, A.D., Hugenholtz, C.H., Durkin, P.R., and Hubbard, S.M. 2020. Visualization and sharing of 3D Digital Outcrop Models to promote open science. *GSA Today*, 30 (5), p. 4-10. doi:10.1130/GSATG425A.1.

Nesbit, P.R., Hugenholtz, C.H., Boulding, A.D., Durkin, P.R., and Hubbard, S.M. 2019. Interactive 3D visualization and dissemination of UAV-SfM models for virtual outcrop geology. *American Geophysical Union. 9-13 Dec 2019. San Francisco, CA.* 2019AGUFMEP11C..2131

Nesbit, P.R., Boulding, A.D., Hugenholtz, C.H., Durkin, P.R., and Hubbard, S.M. 2019. Visualization and sharing of 3D Digital Outcrop Models. *GeoConvention. 11-13 May 2020 (postponed TBD). Calgary, AB.*

Chapter 6 summarizes the results and primary contributions from Chapters 2-5, followed by a discussion of limitations and implications for future work and concluding remarks. **Appendix A** includes a list of co-authored publications directly associated with the research projects described above. **Appendix C** includes a list of supplemental files associated with publications in Chapters 2 and 5.

1.4 References

Bellian, J.A., Kerans, C., Jennette, D.C., and Jennete, D.C., 2005, Digital outcrop models: applications of terrestrial scanning lidar technology in stratigraphic modeling: Journal of Sedimentary Research, v. 75, p. 166–176, doi:10.2110/jsr.2005.013.

Bemis, S.P., Micklethwaite, S., Turner, D., James, M.R., Akciz, S., Thiele, S.T., Bangash, H.A., T. Thiele, S., and Bangash, H.A., 2014, Ground-based and UAV-Based photogrammetry: A multi-scale, high-resolution mapping tool for structural geology and paleoseismology: Journal of Structural Geology, v. 69, p. 163–178, doi:10.1016/j.jsg.2014.10.007.

Bond, C.E., Shipton, Z.K., Jones, R.R.R., Butler, R.W.H., and Gibbs, A.D., 2007, Knowledge transfer in a digital world: Field data acquisition, uncertainty, visualization, and data management: Geosphere, v. 3, p. 568, doi:10.1130/GES00094.1.

Brown, M., and Lowe, D.G., 2005, Unsupervised 3D object recognition and reconstruction in unordered datasets: Proceedings of International Conference on 3-D Digital Imaging and Modeling, 3DIM, p. 56–63, doi:10.1109/3DIM.2005.81.

Bryant, I., Carr, D., Cirilli, P., Drinkwater, N.J., McCormick, D.S., Tilke, P., and Thurmond, J., 2000, Use of 3D digital analogues as templates in reservoir modelling: Petroleum Geoscience, v. 6, p. 195–201, doi:10.1144/petgeo.6.3.195.

Buckley, S.J., Howell, J.A., Enge, H.D., and Kurz, T.H., 2008, Terrestrial laser scanning in geology: Data acquisition, processing and accuracy considerations: Journal of the Geological Society, v. 165, p. 625–638, doi:10.1144/0016-76492007-100.

Buckley, S.J., Ringdal, K., Naumann, N., Dolva, B., Kurz, T.H., Howell, J.A., and

Dewez, T.J.B., 2019, LIME : Software for 3-D visualization , interpretation , and communication of virtual geoscience models: Geosphere, v. 15, p. 1–14, doi:10.1130/GES02002.1/4610849/ges02002.pdf.

Carbonneau, P.E., and Dietrich, J.T., 2017, Cost-effective non-metric photogrammetry from consumer-grade sUAS: Implications for direct georeferencing of structure from motion photogrammetry: Earth Surface Processes and Landforms, v. 42, p. 473–486, doi:10.1002/esp.4012.

Carrivick, J.L., Smith, M.W., and Quincey, D.J., 2016, Structure from Motion in the Geosciences: Oxford, UK, Wiley-Blackwell.

Cawood, A.J., Bond, C.E., Howell, J.A., Butler, R.W.H., and Totake, Y., 2017, LiDAR, UAV or compass-clinometer? Accuracy, coverage and the effects on structural models: Journal of Structural Geology, v. 98, p. 67–82, doi:10.1016/j.jsg.2017.04.004.

Chen, N., Ni, N., Kapp, P., Chen, J., Xiao, A., and Li, H., 2015, Structural Analysis of the Hero Range in the Qaidam Basin, Northwestern China, Using Integrated UAV, Terrestrial LiDAR, Landsat 8, and 3-D Seismic Data: IEEE Journal of Selected Topics in Applied Earth Observations and Remote Sensing, v. 8, p. 4581–4591, doi:10.1109/JSTARS.2015.2440171.

Chesley, J.T., and Leier, A.L., 2018, Sandstone-body variability in the medial-distal part of an ancient distributive fluvial system, Salt Wash Member of the Morrison Formation, Utah, U.S.A.: Journal of Sedimentary Research, v. 88, p. 568–582.

Chesley, J.T., Leier, A.L., White, S., and Torres, R., 2017, Using unmanned aerial vehicles and structure-from-motion photogrammetry to characterize sedimentary

outcrops: An example from the Morrison Formation, Utah, USA: Sedimentary Geology, v. 354, p. 1–8, doi:10.1016/j.sedgeo.2017.03.013.

Clapuyt, F., Vanacker, V., and Van Oost, K., 2015, Reproducibility of UAV-based earth topography reconstructions based on Structure-from-Motion algorithms: Geomorphology, v. 260, p. 4–15, doi:10.1016/j.geomorph.2015.05.011.

Colomina, I., and Molina, P., 2014, Unmanned aerial systems for photogrammetry and remote sensing: A review: ISPRS Journal of Photogrammetry and Remote Sensing, v. 92, p. 79–97, doi:10.1016/j.isprsjprs.2014.02.013.

Deptuck, M.E., Sylvester, Z., Pirmez, C., and O'Byrne, C., 2007, Migration-aggradation history and 3-D seismic geomorphology of submarine channels in the Pleistocene Benin-major Canyon, western Niger Delta slope: Marine and Petroleum Geology, v. 24, p. 406–433, doi:10.1016/j.marpetgeo.2007.01.005.

Eltner, A., Kaiser, A., Castillo, C., Rock, G., Neugirg, F., and Abellán, A., 2016, Image-based surface reconstruction in geomorphometry – merits, limits and developments of a promising tool for geoscientists: Earth Surface Dynamics Discussions, p. 1445–1508, doi:10.5194/esurfd-3-1445-2015.

Enge, H.D., Buckley, S.J., Rotevatn, A., and Howell, J.A., 2007, From outcrop to reservoir simulation model: Workflow and procedures: Geosphere, v. 3, p. 469–490, doi:10.1130/GES00099.1.

Fonstad, M.A., Dietrich, J.T., Courville, B.C., Jensen, J.L.R., and Carbonneau, P.E., 2013, Topographic structure from motion: A new development in photogrammetric measurement: Earth Surface Processes and Landforms, v. 38, p. 421–430, doi:10.1002/esp.3366.

Furukawa, Y., and Ponce, J., 2007, Accurate , Dense , and Robust Multi-View Stereopsis: IEEE Conference on Computer Vision and Pattern Recognition, v. 32, p. 1362–1376, doi:10.1109/CVPR.2007.383246.

Hackney, C., and Clayton, A.I.I., 2015, Unmanned Aerial Vehicles (UAVs) and their application in geomorphic mapping: Geomorphological Techniques, v. 7, p. 1–12, http://www.geomorphology.org.uk/sites/default/files/geom_tech_chapters/2.1.7_UAV.pdf.

Harwin, S., and Lucieer, A., 2012, Assessing the accuracy of georeferenced point clouds produced via multi-view stereopsis from Unmanned Aerial Vehicle (UAV) imagery: Remote Sensing, v. 4, p. 1573–1599, doi:10.3390/rs4061573.

Harwin, S., Lucieer, A., and Osborn, J., 2015, The Impact of the Calibration Method on the Accuracy of Point Clouds Derived Using Unmanned Aerial Vehicle Multi-View Stereopsis: Remote Sensing, v. 7, p. 11933–11953, doi:10.3390/rs70911933.

Hodgetts, D., 2013, Laser scanning and digital outcrop geology in the petroleum industry: A review: Marine and Petroleum Geology, v. 46, p. 335–354, doi:10.1016/j.marpetgeo.2013.02.014.

Hodgetts, D., Drinkwater, N.J., Hodgson, J., Kavanagh, J., Flint, S.S., Keogh, K.J., and Howell, J.A., 2004, Three-dimensional geological models from outcrop data using digital data collection techniques: an example from the Tanqua Karoo depocentre, South Africa: Geological Prior Information: Informing Science and Engineering, v. 239, p. 57–75, doi:10.1144/GSL.SP.2004.239.01.05.

Hodgetts, D., L. Gawthorpe, R., Wilson, P., and Rarity, F., 2007, Integrating Digital and Traditional Field Techniques Using Virtual Reality Geological Studio (VRGS): 69th

EAGE Conference and Exhibition incorporating SPE EUROPEC 2007, p. 11–14, doi:10.3997/2214-4609.201401718.

House, P.K., Clark, R., and Kopera, J., 2013, Overcoming the momentum of anachronism : American geologic mapping in a twenty-first-century world: Geological Society of America Special Papers, v. 2502, p. 103–125, doi:10.1130/2013.2502(05).

Howell, J.A., Martinius, A.W., and Good, T.R., 2014, The application of outcrop analogues in geological modelling: a review, present status and future outlook: Geological Society, London, Special Publications, v. 387, p. 1–25, doi:10.1144/SP387.12.

Hugenholtz, C.H., Whitehead, K., Brown, O.W., Barchyn, T.E., Moorman, B.J., LeClair, A., Riddell, K., and Hamilton, T., 2013, Geomorphological mapping with a small unmanned aircraft system (sUAS): Feature detection and accuracy assessment of a photogrammetrically-derived digital terrain model: Geomorphology, v. 194, p. 16–24, doi:10.1016/j.geomorph.2013.03.023.

James, M.R., and Quinton, J.N., 2014, Ultra-rapid topographic surveying for complex environments: The hand-held mobile laser scanner (HMLS): Earth Surface Processes and Landforms, v. 39, p. 138–142, doi:10.1002/esp.3489.

James, M.R., and Robson, S., 2014, Mitigating systematic error in topographic models derived from UAV and ground-based image networks: Earth Surface Processes and Landforms, v. 39, p. 1413–1420, doi:10.1002/esp.3609.

James, M.R., and Robson, S., 2012, Straightforward reconstruction of 3D surfaces and topography with a camera: Accuracy and geoscience application: Journal of

Geophysical Research: Earth Surface, v. 117, p. 1–17, doi:10.1029/2011JF002289.

James, M.R., Robson, S., D'Oleire-Oltmanns, S., and Niethammer, U., 2017a, Optimising UAV topographic surveys processed with structure-from-motion: Ground control quality, quantity and bundle adjustment: Geomorphology, v. 280, p. 51–66, doi:10.1016/j.geomorph.2016.11.021.

James, M.R., Robson, S., and Smith, M.W., 2017b, 3-D uncertainty-based topographic change detection with structure-from-motion photogrammetry: precision maps for ground control and directly georeferenced surveys: Earth Surface Processes and Landforms, v. 42, p. 1769–1788, doi:10.1002/esp.4125.

Javernick, L., Brasington, J., and Caruso, B., 2014, Modeling the topography of shallow braided rivers using Structure-from-Motion photogrammetry: Geomorphology, v. 213, p. 166–182, doi:10.1016/j.geomorph.2014.01.006.

Johnson, K., Nissen, E., Saripalli, S., Arrowsmith, J.R., McGarey, P., Scharer, K., Williams, P., and Blisniuk, K., 2014, Rapid mapping of ultrafine fault zone topography with structure from motion: Geosphere, v. 10, p. 969–986, doi:10.1130/GES01017.1.

Jones, R.R., McCaffrey, K.J.W., Wilson, R.W., and Holdsworth, R.E., 2004, Digital field data acquisition: towards increased quantification of uncertainty during geological mapping: Geological Society, London, Special Publications, v. 239, p. 43–56, doi:10.1144/GSL.SP.2004.239.01.04.

Jones, R.R., Wawrzyniec, T.F., Holliman, N.S., McCaffrey, K.J.W.W., Imber, J., and Holdsworth, R.E., 2008, Describing the dimensionality of geospatial data in the earth sciences—Recommendations for nomenclature: Geosphere, v. 4, p. 354,

doi:10.1130/ges00158.1.

Labourdette, R., and Jones, R.R., 2007, Characterization of fl uvial architectural elements using a three-dimensional outcrop data set : Escanilla braided system, South-Central Pyrenees, Spain: Geosphere, p. 422–434, doi:10.1130/GES00087.1.

Lowe, D.G., 2004, Distinctive image features from scale-invariant keypoints: International Journal of Computer Vision, v. 60, p. 91–110, doi:10.1023/B:VISI.0000029664.99615.94.

McCaffrey, K.J.W., Jones, R.R., Holdsworth, R.E., Wilson, R.W., Clegg, P., Imber, J., Holliman, N.S., and Trinks, I., 2005, Unlocking the spatial dimension: digital technologies and the future of geoscience fieldwork: Journal of the Geological Society, v. 162, p. 927–938, doi:10.1144/0016-764905-017.

Nesbit, P.R., Barchyn, T.E., Hugenholtz, C.H., Cripps, S., and Kucharczyk, M., 2017, Reported UAV incidents in Canada : analysis and potential solutions: Journal of Unmanned Vehicle Systems, v. 5, p. 1–17, doi:10.1139/juvs-2016-0033.

Nieminski, N.M., and Graham, S.A., 2017, Modeling Stratigraphic Architecture Using Small Unmanned Aerial Vehicles and Photogrammetry: Examples From the Miocene East Coast Basin, New Zealand: Journal of Sedimentary Research, v. 87, p. 126–132, doi:10.2110/jsr.2017.5.

Niethammer, U., James, M.R., Rothmund, S., Travelletti, J., and Joswig, M., 2012, UAV-based remote sensing of the Super-Sauze landslide: Evaluation and results: Engineering Geology, v. 128, p. 2–11, doi:10.1016/j.enggeo.2011.03.012.

Pavlis, T.L., Langford, R.P., Hurtado, J.M., and Serpa, L., 2010, Computer-based data acquisition and visualization systems in field geology: Results from 12 years of

experimentation and future potential: Geosphere, v. 6, p. 275–294, doi:10.1130/GES00503.S2.

Pavlis, T.L., and Mason, K.A., 2017, The New World of 3D Geologic Mapping: GSA Today, v. 27, p. 4–10, doi:10.1130/GSATG313A.1.

Pranter, M.J., Ellison, A.I., Cole, R.D., and Patterson, P.E., 2007, Analysis and modeling of intermediate-scale reservoir heterogeneity based on a fluvial point-bar outcrop analog, Williams Fork Formation, Piceance Basin, Colorado: AAPG Bulletin, v. 91, p. 1025–1051, doi:10.1306/02010706102.

Pringle, J., Gardiner, A., and Westerman, R., 2004, Virtual geological outcrops - Fieldwork and analysis made less exhaustive? Geology Today, v. 20, p. 67–72, doi:10.1111/j.1365-2451.2004.00450.x.

Rarity, F., van Lanen, X.M.T., Hodgetts, D., Gawthorpe, R.L., Wilson, P., Fabuel-Perez, I., and Redfern, J., 2014, LiDAR-based digital outcrops for sedimentological analysis: workflows and techniques: Geological Society, London, Special Publications, v. 387, p. 1–31, doi:10.1144/SP387.5.

Rittersbacher, A., Buckley, S.J., Howell, J.A., Hampson, G.J., and Vallet, J., 2014, Helicopter-based laser scanning : a method for quantitative analysis of large-scale sedimentary architecture: Geological Society, London, Special Publications, v. 387, p. 185–202, doi:10.1144/SP387.3.

Smith, M.W., Carrivick, J.L., and Quincey, D.J., 2015, Structure from motion photogrammetry in physical geography: Progress in Physical Geography, v. 40, p. 247–275, doi:10.1177/0309133315615805.

Smith, M.W., and Vericat, D., 2015, From experimental plots to experimental

landscapes: Topography, erosion and deposition in sub-humid badlands from Structure-from-Motion photogrammetry: Earth Surface Processes and Landforms, v. 40, p. 1656–1671, doi:10.1002/esp.3747.

Snavely, N., Seitz, S.M., and Szeliski, R., 2008, Modeling the world from Internet photo collections: International Journal of Computer Vision, v. 80, p. 189–210, doi:10.1007/s11263-007-0107-3.

Snavely, N., Seitz, S.M., and Szeliski, R., 2006, Photo tourism: Exploring Photo Collections in 3D: ACM Transactions on Graphics, v. 25, p. 835–846, doi:10.1145/1141911.1141964.

Szeliski, R., 2010, Computer Vision : Algorithms and Applications: Springer Science & Business Media., v. 5, 832 p., doi:10.1007/978-1-84882-935-0.

Tamminga, A.D., Eaton, B.C., and Hugenholtz, C.H., 2015, UAS-based remote sensing of fluvial change following an extreme flood event: Earth Surface Processes and Landforms, v. 40, p. 1464–1476, doi:10.1002/esp.3728.

Toth, C., and Jóźków, G., 2016, Remote sensing platforms and sensors: A survey: ISPRS Journal of Photogrammetry and Remote Sensing, v. 115, p. 22–36, doi:10.1016/j.isprsjprs.2015.10.004.

Trinks, I., Clegg, P., McCaffrey, K.J.W., Jones, R.R., Hobbs, R., Holdsworth, B., Holliman, N.N.S., Imber, J.J., Waggott, S., and Wilson, R.W., 2005, Mapping and analysing virtual outcrops: Visual Geosciences, v. 10, p. 13–19, doi:10.1007/s10069-005-0026-9.

Vollgger, S.A., and Cruden, A.R., 2016, Mapping folds and fractures in basement and cover rocks using UAV photogrammetry, Cape Liptrap and Cape Paterson, Victoria,

Australia: Journal of Structural Geology, v. 85, p. 168–187, doi:10.1016/j.jsg.2016.02.012.

Westoby, M.J., Brasington, J., Glasser, N.F., Hambrey, M.J., and Reynolds, J.M., 2012, "Structure-from-Motion" photogrammetry: A low-cost, effective tool for geoscience applications: Geomorphology, v. 179, p. 300–314, doi:10.1016/j.geomorph.2012.08.021.

Westoby, M.J., Dunning, S.A., Woodward, J., Hein, A.S., Marrero, S.M., Winter, K., and Sugden, D.E., 2015, Instruments and methods: Sedimentological characterization of Antarctic moraines using uavs and Structure-from-Motion photogrammetry: Journal of Glaciology, v. 61, p. 1088–1102, doi:10.3189/2015JoG15J086.

Whitehead, K., and Hugenholtz, C.H., 2014, Remote sensing of the environment with small unmanned aircraft systems (UASs), part 1: a review of progress and challenges: Journal of Unmanned Vehicle Systems, v. 2, p. 1–17, doi:10.1139/juvs-2014-0007.

Whitehead, K., Moorman, B.J., and Hugenholtz, C.H., 2013, Brief Communication: Low-cost, on-demand aerial photogrammetry for glaciological measurement: The Cryosphere, v. 7, p. 1879–1884, doi:10.5194/tc-7-1879-2013.

Whitmeyer, S.J., Nicoletti, J., and De Paor, D.G., 2010, The digital revolution in geologic mapping: GSA Today, v. 20, p. 4–10, doi:10.1130/GSATG70A.1.

Woodget, A.S., and Austrums, R., 2017, Subaerial gravel size measurement using topographic data derived from a UAV-SfM approach: Earth Surface Processes and Landforms, v. 42, p. 1434–1443, doi:10.1002/esp.4139.

Woodget, A.S., Carbonneau, P.E., Visser, F., and Maddock, I.P., 2015, Quantifying

submerged fluvial topography using hyperspatial resolution UAS imagery and structure from motion photogrammetry: Earth Surface Processes and Landforms, v. 40, p. 47–64, doi:10.1002/esp.3613.

Zahm, C., Lambert, J., and Kerans, C., 2016, Use of unmanned aerial vehicles (UAVs) to create digital outcrop models: An example from the Cretaceous Cow Creek Formation, Central Texas.: GCAGS Journal, v. 5, p. 180–188.

Chapter 2

3-D Stratigraphic Mapping Using a Digital Outcrop Model Derived from UAV Images and Structure-from-Motion Photogrammetry

A version of this chapter was published as:

Nesbit, P.R., Durkin, P.R., Hugenholtz, C.H., Hubbard, S.M., and Kucharczyk, M. 2018. 3-D stratigraphic mapping using a digital outcrop model derived from UAV images and structure-from-motion photogrammetry. *Geosphere*, 14 (6), p. 2469-2486. doi:10.1130/GES01688.1

2.1 Abstract

Fluvial deposits are highly heterogeneous and inherently challenging to map in outcrop due to a combination of lateral and vertical variability along with a lack of continuous exposure. Heavily incised landscapes, such as badlands, reveal continuous three-dimensional (3D) outcrops that are ideal for constraining the geometry of fluvial deposits, enabling reconstruction of channel morphology through time and space. However, these complex 3D landscapes also create challenges for conventional field mapping techniques, which offer limited spatial resolution, coverage, and / or lateral contiguity of measurements. To address these limitations, we examined an emerging technique using images acquired from a small unmanned aerial vehicle (UAV) and structure from motion (SfM) photogrammetric processing to generate a 3D digital outcrop model (DOM). We applied the UAV-SfM technique to develop a DOM of an Upper Cretaceous channel-belt sequence exposed within a 0.52 km^2 area of Dinosaur Provincial Park (southeastern Alberta, Canada). Using the 3D DOM we delineated the

lower contact of the channel-belt sequence, created digital sedimentary logs, and estimated facies with similar conviction to field-based estimations (± 4.9%). Lateral accretion surfaces were also recognized and digitally traced within the DOM, enabling measurements of accretion direction (dip azimuth), that are nearly impossible to obtain accurately in the field. Overall, we found that measurements and observations derived from the UAV-SfM DOM were commensurate with conventional ground-based mapping techniques, but had the added advantage of lateral continuity, which aided interpretation of stratigraphic surfaces and facies. This study suggests that UAV-SfM DOMs can complement traditional field-based methods by providing detailed 3D views of topographically complex outcrop exposures spanning intermediate-large spatial extents.

2.2 Introduction

Stratigraphic surfaces resulting from ancient fluvial processes record spatial and temporal changes in river morphology at multiple hierarchical levels and inform our understanding of morphodynamics and paleoenvironments (Jordan and Pryor, 1992; Durkin et al., 2017). Fluvial deposits are highly heterogeneous and challenging to map in outcrop due to lateral and vertical variability, as well as inconsistent exposure (Miall, 1988; Labourdette and Jones, 2007; Pranter et al., 2007; Calvo and Ramos, 2015; Durkin et al., 2015a). Conventional mapping methods commonly include a posteriori correlation (or interpolation) between sedimentary field logs, which can result in subjective interpretations, unquantified uncertainty, and/or oversimplified information between data points (Jones et al., 2004; Bond et al., 2007). Supplemental datasets, such as panoramic photographs, have been used to improve interpretations between isolated sedimentary

logs (i.e., Sgavetti, 1992; Arnot et al., 1997); however, this method lacks the geometric and locational accuracy needed for detailed mapping of highly varied fluvial deposits.

Digital outcrop models (DOMs), or virtual outcrops (Trinks et al., 2005), provide a 3D scaled replica of outcrops and can supplement field observations with additional quantitative datasets (Xu et al., 2000; Bellian et al., 2005; Enge et al., 2007; Labourdette and Jones, 2007; Pranter et al., 2007; Buckley et al., 2008). Existing techniques used to generate DOMs generally incur a spatial coverage-resolution tradeoff. Ground-based photogrammetry and terrestrial laser scanning (TLS) are common techniques for creating DOMs, but are often hindered by restricted line-of-sight and require multiple viewpoints to eliminate data occlusions. Although there are exceptions (e.g., Rarity et al., 2014), ground-based methods are primarily used for sites smaller than 10^5 m^2 and are not practical for mapping extensive outcrop exposures (Hodgetts, 2013; James and Quinton, 2014). Airborne methods, such as aerial photogrammetry and light detection and ranging (LiDAR), are commonly considered for mapping larger areas (> 10^6 m^2); however, these methods typically have limited spatial resolution (i.e., > 0.3 m/pixel), high costs, and difficulty resolving geologic detail along sub-vertical slopes (Bellian et al., 2005; Hodgetts, 2013). Despite some unique solutions (e.g., Rittersbacher et al., 2014; James and Quinton, 2014), few techniques have emerged for detailed mapping of sedimentary rocks exposed within laterally extensive (> 10^5 m^2), topographically complex, 3D landscapes.

Small unmanned aerial vehicles (UAVs) paired with structure from motion multi-view stereo (SfM-MVS) photogrammetry has recently emerged as an alternative, low-cost remote sensing approach for generating high spatial resolution data spanning

intermediate extents (Hugenholtz et al., 2012; Colomina and Molina, 2014; Whitehead and Hugenholtz, 2014; Whitehead et al., 2014; Toth and Jóźków, 2016; Chesley et al., 2017; Nieminski and Graham, 2017). In the geosciences, UAV-based SfM-MVS (hereafter UAV-SfM) techniques have primarily been used for generating and analyzing 2D and 2.5D datasets, such as orthomosaic images and/or digital surface models (DSM; Carrivick et al., 2016). Although these 2D and 2.5D datasets may be suitable for measurement and interpretation of geologic features along planar surfaces, they are susceptible to compression, distortion, and over-generalization of details exposed along planes non-normal to image acquisition (Bellian et al., 2005; Pavlis and Mason, 2017; Thiele et al., 2017). Geologic features are commonly exposed along steep slopes and are particularly susceptible to these effects, therefore further consideration to data collection and visualization is necessary. An alternative approach is to use 3D datasets generated during intermediate stages of UAV-SfM processing, such as the dense point cloud or textured triangulated mesh, as DOMs for geologic analysis. These 'intermediate' datasets contain location (x, y, z) and color information (red/green/blue; RGB), maintain 3D topographic integrity, and resemble DOMs created with TLS.

To evaluate UAV-SfM generated DOMs as supplemental tools for providing reliable quantitative information, we compared DOM-derived measurements with independently collected field observations of fluvial surfaces and facies exposed within a complex and highly three-dimensional badlands landscape. This research is performed in a section of Dinosaur Provincial Park (southeastern Alberta, Canada; Figure 2.1) with extensive exposures of Upper Cretaceous fluvial channel-belt deposits. This paper describes the (i) UAV-SfM workflow; (ii) DOM visualization strategies, and (iii) a

method for digital interpretation of multi-scale stratigraphic surfaces and facies estimation. Results exhibit commensurability between geologic measurements and interpretations from field-based observations and the 3D UAV-SfM DOM, for which the limitations and potential are discussed.

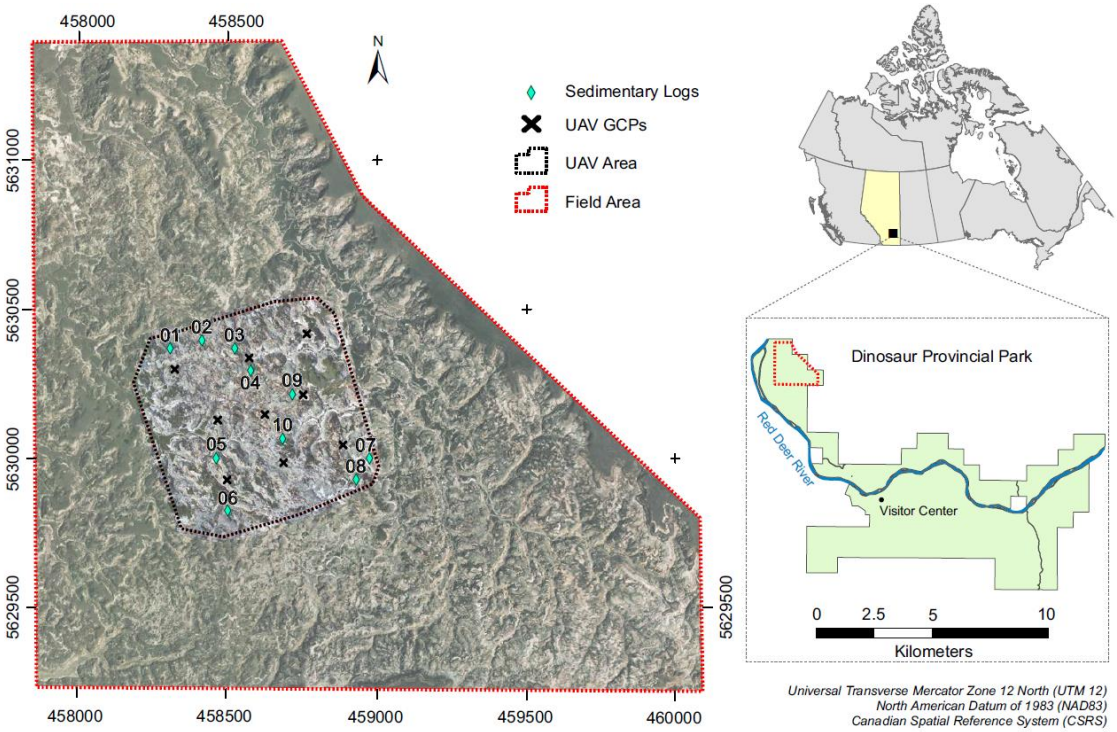

Figure 2.1. Locations of conventional ground survey field area (3.5 km^2, red dashed polygon) and unmanned aerial vehicle (UAV) survey area (0.52 km^2, black dashed polygon) within the badlands of Dinosaur Provincial Park (southeastern Alberta, Canada). UAV ground control point (GCP) locations (black Xs) were used for georeference during UAV structure-from-motion (UAV-SfM) processing, and sedimentary logs were collected in the field and used to locate the same numbered sections in the DOM (light-blue diamonds).

2.3 Geologic Setting and Study Area

Outcrop exposures within Dinosaur Provincial Park include lithologically contrasting layers of siltstone and fine- to medium-grained sandstone of the Dinosaur Park and Oldman formations (Eberth and Hamblin, 1993; Hamblin and Abrahamson, 1996; Eberth, 2005). Overall, the regional stratigraphy is nearly flat-lying, dipping ~ 0.05° to the southwest. The Dinosaur Park Formation is the uppermost unit within the Late Cretaceous non-marine clastic Judith River (Belly River) Group (Figure 2.2; Eberth and Hamblin, 1993; Hamblin and Abrahamson, 1996). The Dinosaur Park Formation was deposited at the onset of a regional transgression of the Bearpaw Sea into the subsiding foreland basin, and it interfingers with the overlying shallow marine deposits of the Bearpaw Formation (Eberth, 2005). Deposits of the Dinosaur Park Formation are consistent with meandering channel-belts originating from the north-central Canadian Cordillera highlands to the west, with an average paleo-current direction flowing east-southeast into the shallow Western Interior Seaway (Wood et al., 1988; Wood, 1989; Eberth and Hamblin, 1993; Ryan et al., 2001). There is agreement among investigators that deposition of sediment was from fluvial processes; however, the degree of tidal influence is disputed (Koster and Currie, 1987; Thomas et al., 1987; Wood, 1989; Eberth, 2005).

The study area is in the northeast section of the park, approximately 1 km east of the present day Red Deer River (Figure 2.1). This area contains exposures of the uppermost Dinosaur Park Formation and evidence of the overlying Bearpaw Formation. Previous work within the area identified an 8-10 m thick meandering channel-belt deposit with characteristic point bar and counter-point-bar elements (Smith et al., 2009b; Durkin

et al., 2015b; Weleschuk, 2015). The base of the channel-belt sequence is recognizable by the presence of coarser channel scour and bar deposits (fine-medium sandstone and siltstone) sharply overlying finer floodplain deposits (mudstone-siltstone). This contact represents laterally contemporaneous processes (i.e., deposition and erosion) and provides a common datum for identifying higher order stratigraphic surfaces.

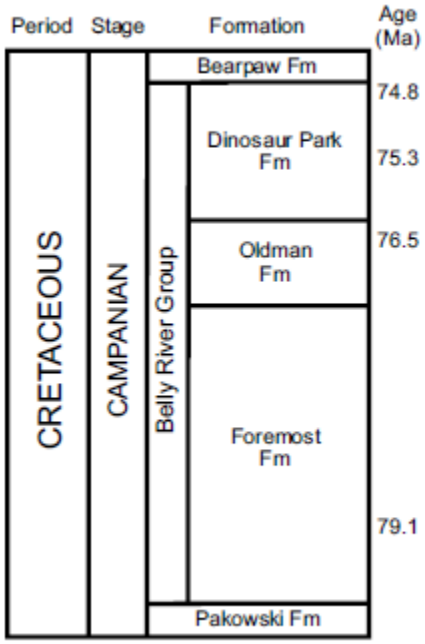

Figure 2.2. Lithostratigraphy of the Belly River Group, including the Dinosaur Park Formation, modified from Eberth (2005).

The heavily dissected badland landscape, typified by complex drainage networks, hoodoos, buttes, and mesas of various sizes, is characteristic throughout Dinosaur Provincial Park (Campbell, 1970). This landscape initiated during Wisconsinan deglaciation (~15,000 years ago) as the Laurentide Ice Sheet receded and exposed the landscape to contemporary, non-glacial, erosional processes (i.e., piping, overland flow,

mass flow) that continue to incise the highly erodible bedrock (Campbell, 1970; Bryan et al., 1987; Rains et al., 1993; Evans, 2000). The combination of naturally varying slope directions, minimal vegetation, and visually distinct lithologies presents excellent opportunities to examine the detailed fluvial stratigraphy in a 3D (cross-sectional) perspective.

2.4 Methods

2.4.1 Field data acquisition

Field observations and measurements were acquired by foot over a 3.5 km^2 area (Figure 2.1), prior to UAV data collection. Point locations along the basal contact of the channel-belt were recorded using a Trimble ProXRT2 differential Global Positioning System (dGPS) and integrated TruPulse 360B laser rangefinder to map features inaccessible by foot. This dGPS has a manufacturer-reported decimeter accuracy following post-processing (differential correction) with proprietary software; the attached rangefinder degrades precision to 0.30 – 1.00 m, depending on distance and scan angle (Xu et al., 2000).

Detailed sedimentological observations, including grain size, sedimentary structures, lithologic features, and bedding contacts were recorded in ten sedimentary logs within the field area (Figure 2.1). Bedding thickness was recorded by tape measure and Jacob staff. The Trimble dGPS system was used to measure the geolocation of the bottom and top of each sedimentary log. Six distinct facies were determined and associated with sedimentary observations in facies logs (Table 2.1). Sandstone facies were categorized as massive and cross-stratified (F1) or ripple laminated (F2). Dominantly sandstone (>50%) with siltstone interbeds (generally < 0.10 m thick) were

categorized as F3, while dominantly siltstone (>50%) interbedded with sandstone were separately classified as F4. Thicker siltstone without sandstone interbeds were assigned to F5. Organic rich mudstone layers, generally representing floodplain deposits, were classified as F6.

Table 2.1. Field facies and digital facies.

Field facies	Digital facies
Coarse-grained	
F1: massive and cross-stratified sandstone F2: ripple laminated sandstone	dF1: sandstone
Interbedded	
F3: sandstone with siltstone and organic interbeds	dF2: silty sandstone
F4: siltstone with sandstone and organic interbeds	dF3: sandy siltstone
Fine-grained	
F5: siltstone F6: organic-rich mudstone	dF4: siltstone and mudstone

Note: Coarse-grained field facies (F1 – F2) are considered equivalent to digital facies dF1 and fine-grained field facies (F5 – F6) are considered the same as dF4.

2.4.2 UAV data acquisition

UAVs have demonstrated the ability to capture very high resolution images in a broad range of geoscience case studies (e.g., Harwin and Lucieer, 2012; James and Robson, 2012; Niethammer et al., 2012; Whitehead et al., 2013; Hugenholtz et al., 2013; Bemis et al., 2014; Johnson et al., 2014; Vollgger and Cruden, 2016; Cawood et al., 2017; Chesley et al., 2017; Nieminski and Graham, 2017; Vasuki et al., 2017), but their application to geologic mapping requires careful consideration, especially where features are exposed in complex landscapes, such as cliff faces or steep slopes (Pavlis and Mason,

2017). For extensive outcrops, fixed-wing UAVs are more suitable because they generally have prolonged flight times compared with multi-rotor platforms (Colomina and Molina, 2014; Toth and Jóźków, 2016). Therefore, in this study a senseFly eBee fixed-wing UAV equipped with a Sony WX220 18.2 megapixel (MP) consumer-grade digital camera with focal length set constant at 4.6 mm (35 mm equivalent of approximately 26.2 mm) was selected to record images of the 0.52 km^2 field area (Figure 2.1: UAV area).

Flight parameters were programmed using accompanying flight planning software, eMotion 2. Flights were planned for 70 m above ground level with 90% image overlap and 75% sidelap (Figure 2.3). Although minimum overlap requirements for contemporary processing solutions specify that an object point (in the scene) should be clearly visible in three images (Snavely et al., 2008; Carrivick et al., 2016), we selected higher overlap settings to increase point visibility within the complex, highly dissected, three-dimensional topography. To further increase point visibility along sub-vertical surfaces, the camera was set to record images at an angle of 10° off-nadir. A second flight with the same parameters was flown over the same footprint with perpendicular flight lines to increase multi-viewpoint coverage (Figure 2.3). The two UAV flights were conducted on 07 July 2016 during diffuse lighting conditions (cloudy) to reduce shadows on steep outcrop exposures. Data collection resulted in an image block of 728 geotagged images. No additional post-processing corrections or enhancements were applied to the images.

Prior to UAV surveys, nine ground control points (GCPs) were distributed throughout the field site (Figure 2.1), following recommendations made by Harwin et al.

(2015). GCP locations were measured at sub-centimeter precision with a Trimble R4 real-time kinematic Global Navigation Satellite System (RTK-GNSS). Recorded GCP positions were imported and used for georeferencing during image processing.

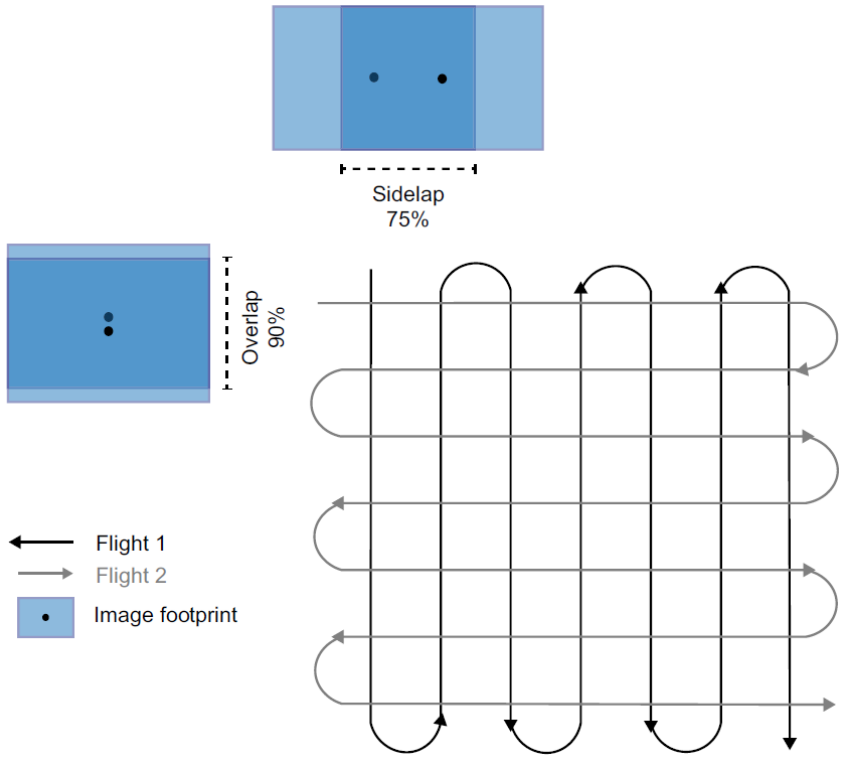

Figure 2.3. Simplified unmanned aerial vehicle data collection parameters programmed into the eBee autopilot: 90% overlap between successive images (blue rectangles to the left), 75% sidelap between flight lines (blue rectangles at the top), and a second flight (gray lines) programmed to fly perpendicular to flight 1 (black lines).

2.4.3 UAV data processing

To process the UAV images into 3D models, we used structure from motion (SfM) software, a recently popularized image-based modeling technique developed in the computer vision community that calculates the 3D structure of a scene from a series of overlapping 2D images (Snavely et al., 2006; Szeliski, 2010; James and Robson, 2012;

Westoby et al., 2012; Fonstad et al., 2013). SfM has some similarities with conventional photogrammetric workflows; however, one of the main differences is that SfM does not require any a priori knowledge about the scene, camera location/orientation/settings, or any manual identification of keypoints or tie points (i.e., homologous points occurring in multiple images). Instead, SfM uses automated feature detection and matching algorithms to estimate the location of images relative to one another (Lowe, 2004; Snavely et al., 2008; Westoby et al., 2012; Fonstad et al., 2013), making it more suitable for processing images collected with a non-metric camera and low-flying (close-range) UAV platform (Colomina and Molina, 2014).

SfM processing was completed using Pix4Dmapper commercial software and a high-performance computer (Intel® Core™ i9-7900X CPU @ 3.30 GHz with 64 GB RAM and an NVIDIA GeForce GTX 1080 graphics card). Pix4Dmapper is a commercial SfM program with a user-friendly interface and simple workflow that builds on previous web-based versions and follows similar steps (Kung et al., 2012):

i. Import photos (geotagged photos optional);
ii. Initial processing to calculate and match keypoints using feature matching algorithms similar to the Scale Invariant Feature Transform (SIFT; Lowe, 2004), followed by optimization through bundle block adjustment (Triggs et al., 2000);
iii. Import GCPs for georeferencing and optimization;
iv. Point densification using multi-view stereo algorithms, similar to Furukawa and Ponce (2010), and mesh interpolation;
v. Generate DSM and orthomosaic image.

The Scale Invariant Feature Transform (SIFT) algorithm, introduced by Lowe (1999, 2004), detects unique keypoints within each image determined by local pixel variances at a variety of scales. Keypoints are matched in adjacent photos and outliers / incorrect matches are removed. A bundle block adjustment (Triggs et al. 2000) is then iteratively performed to optimize 3D geometry of keypoint matches and camera parameters (Lourakis and Argyros, 2009). Outputs from this initial SfM process include a 'sparse' 3D point cloud composed of estimated locations (x, y, z) of keypoint matches, camera internal orientation parameters (IOPs: focal length and radial distortion), and camera external orientation parameters (EOPs: location, orientation, and scale) (Lowe, 2004; Brown and Lowe, 2005).

In a subsequent step, multi-view stereo (MVS) algorithms are used to calculate additional point observations, resulting in a ‘dense’ point cloud with point densities similar to typical TLS point clouds (Carrivick et al., 2016). MVS techniques use calculated EOPs and IOPs to limit search areas among overlapping photos and add reliable feature matches (Szeliski, 2010; Remondino et al., 2014). The resulting dense point cloud can have $> 10^3$ times more points than the initial sparse point cloud (James and Robson, 2012). Dense point clouds are typically interpolated into a continuous 3D mesh surface visualized as a triangulated irregular network (TIN). Surface interpolation algorithms often apply some adaptation of the Poisson Surface Reconstruction with texturing from segments of individual images (Furukawa and Ponce, 2010; Carrivick et al., 2016).

Final steps in UAV-SfM workflows include conversion of the 3D model into a 2D orthomosaic image and 2.5D digital surface model (DSM; Figure 2.4A-B). The latter is

calculated from the 3D dense point cloud using algorithms based on either inverse distance weighting or Delaunay triangulation. The 2D orthomosaic image is generated by removing perspective distortions from the original images using the 2.5D DSM to preserve correct geolocation of pixels (Pix4D [https://support.pix4d.com]).

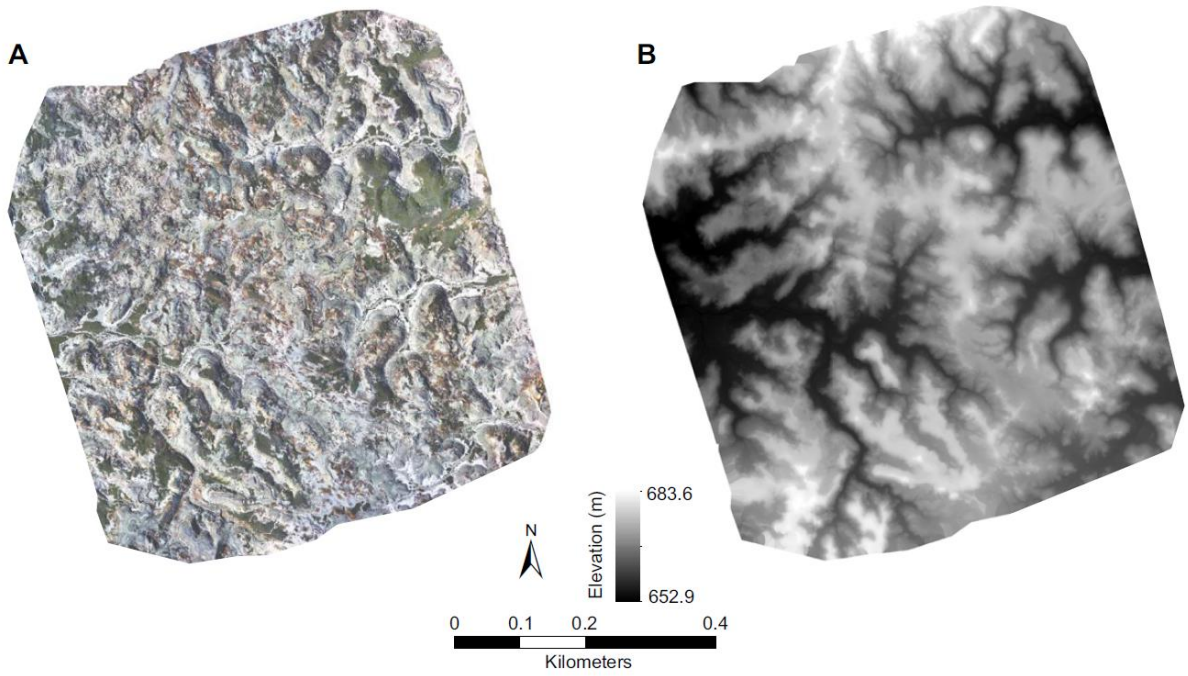

Figure 2.4. Typical outputs from the full unmanned aerial vehicle structure-from-motion multiview stereo process: (A) two-dimensional orthomosaic image; and (B) two-and a-half dimensional digital surface model. The resolution of these outputs is 0.02 m/pixel, but details along steep slopes are distorted or omitted.

2.4.4 Processing outputs

Stratigraphic features exposed along steep slope faces can be difficult to interpret and are subject to significant distortion within these 2D datasets. Therefore, we used the dense point cloud and textured mesh from the UAV-SfM workflow as 3D DOMs for geologic interpretation. The dense point cloud DOM and textured mesh DOM were visualized and navigated directly within Pix4Dmapper. The dense point cloud had 1.35 x 10^9 points, an average point spacing of 0.027 m, and was processed using the highest automated settings (original image size and 'high' point density). The 3D textured mesh had 9.99 x 10^5 triangles that resulted from the highest automated processing settings.

Figures 2.5 and 2.6 show examples from two field photographs of the outcrop (Figures 2.5A and 2.6A), the corresponding dense point cloud DOM (Figures 2.5B and 2.6B), and the textured mesh DOM (Figure 2.5C and 2.6C). The sharp channel-belt contact is clearly resolved in both the dense point cloud and textured mesh DOMs (Figure 2.5B-C, light blue arrows). Smaller features, such as the shallow dipping, thin-medium beds in Figure 2.6A are recognizable in the dense point cloud, but are noticeably distorted or undetectable in the textured mesh DOM (Figure 2.6B-C). Although the dense point cloud contained data gaps between points (Figure 2.6B yellow arrows), it can be used to identify fine stratigraphic detail that is noticeably distorted in the textured mesh DOM. Therefore, we used the dense point cloud to make digital measurements and interpretations for evaluation against field observations, see Supplemental Files 1-2 (Appendix C).

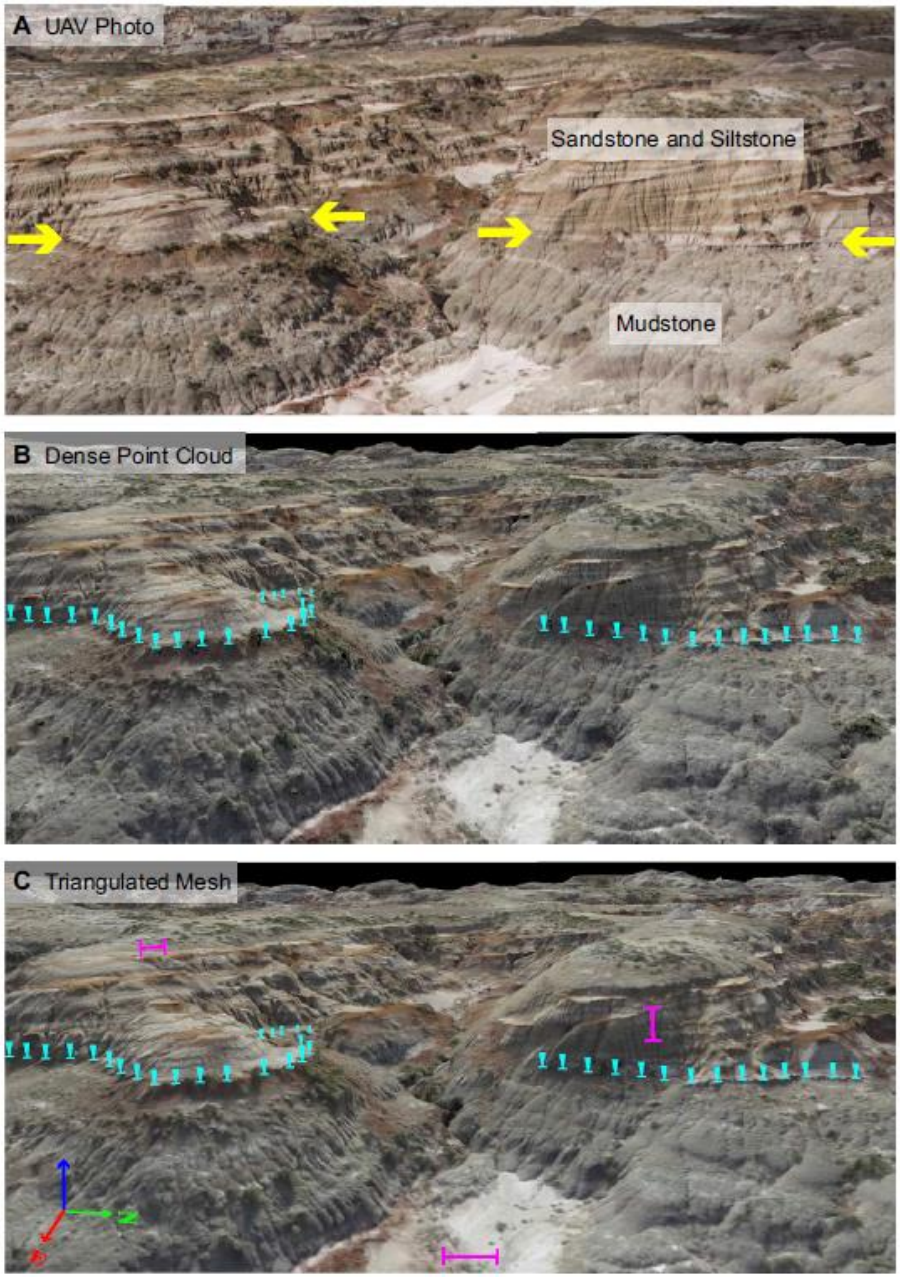

Figure 2.5. Profile view of channel-belt basal contact (yellow arrows), with shallow-dipping counter-point-bar deposits (sandstone and siltstone) overlying flat-lying floodplain mudstone: (A) field photograph; (B) unmanned aerial vehicle–structure-from-motion (UAV-SfM) dense point cloud (see Supplemental Files 2.1–2.2 [Appendix C]); and (C) UAV-SfM triangulated mesh. Light-blue arrows in B and C represent the interpreted contact from the digital outcrop model (DOM); pink bars represent ~3 m on the ground.

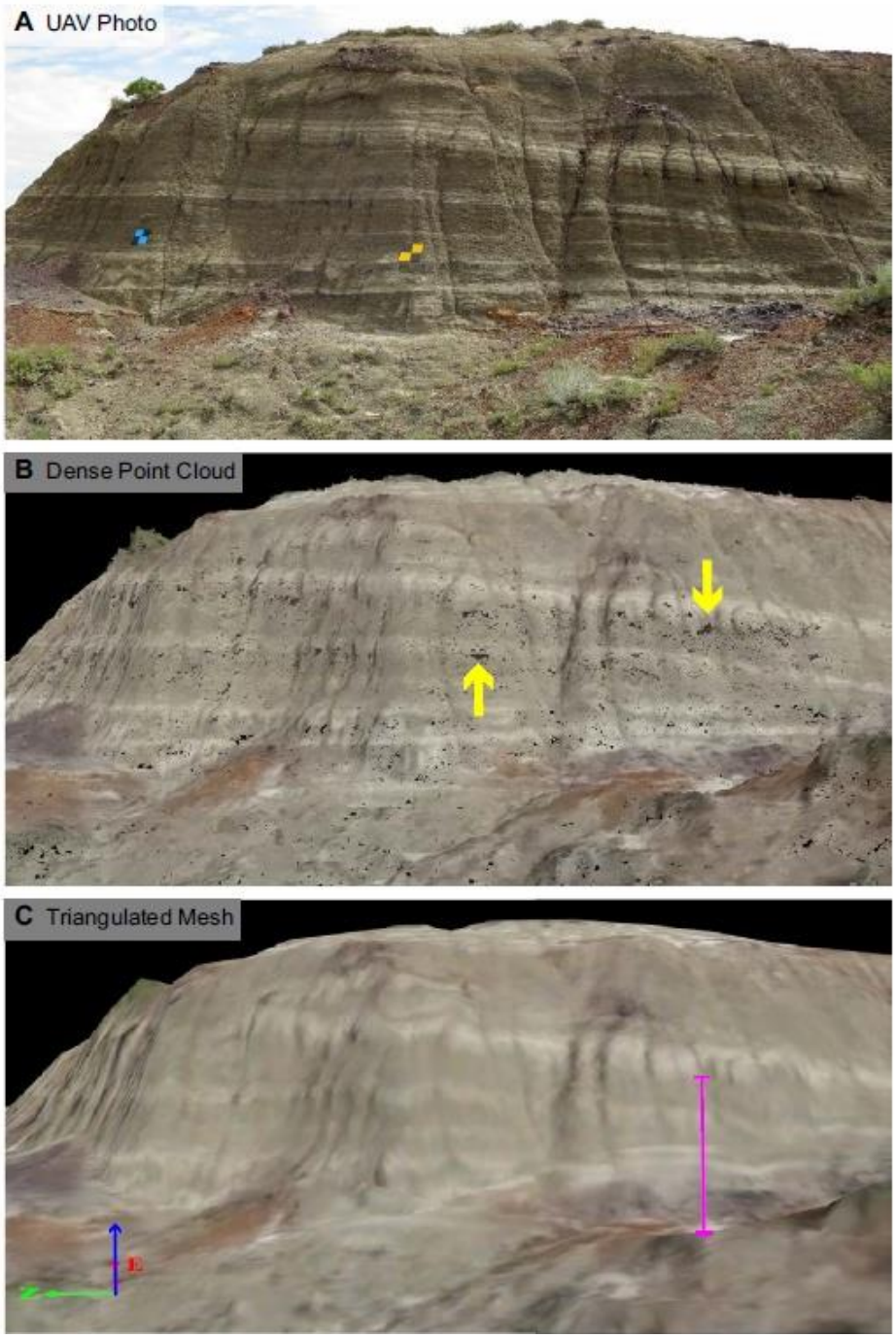

Figure 2.6. Profile view of thin-bedded, shallow-dipping, counter-point-bar deposits: (A) field photograph; (B) unmanned aerial vehicle–structure-from-motion (UAV-SfM) dense point cloud; and (C) UAV-SfM triangulated mesh. Note the "gaps" in the dense point cloud (B, yellow arrows) and the loss of fine detail due to interpolation in the triangulated mesh (C). Pink bar represents ~3 m.

2.4.5 Digital interpretation and measurement

Digital interpretations and measurements of geologic features at multiple scales were made directly on the dense point cloud DOM within Pix4Dmapper by digitizing 'manual tie points' in 3D space. This built-in function was used to trace the basal channel-belt contact (Figure 2.7), which is exposed on varying slope faces throughout the field area. Vertical offsets between digital and field measured points were measured by calculating the elevation value difference between the closest points. The length of the identified contact was quantified for comparison of the two methods.

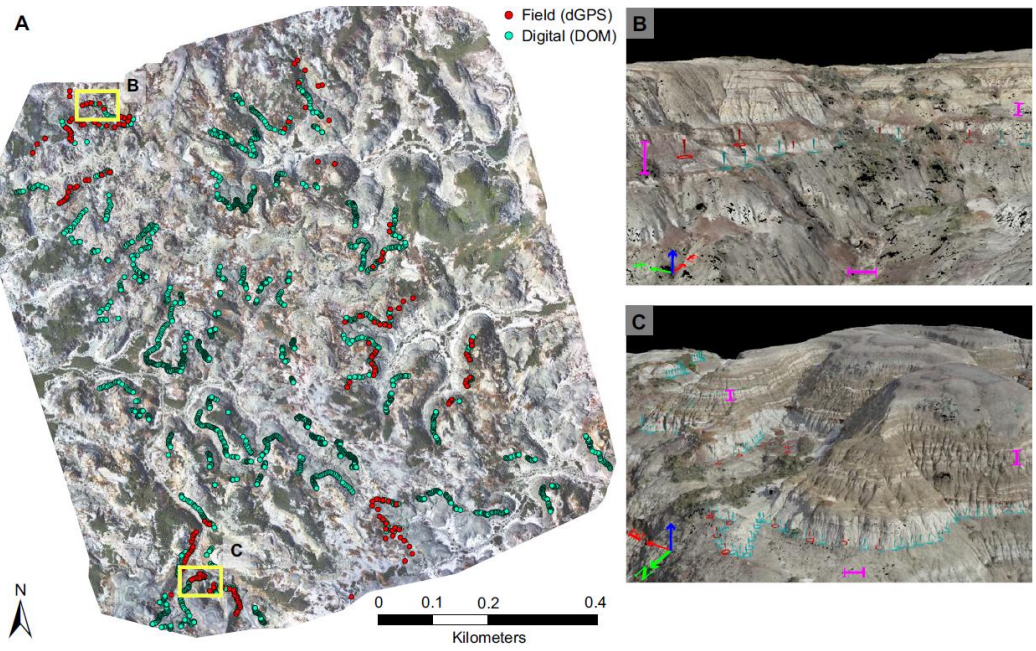

Figure 2.7. Identification of channel-belt basal contact from the unmanned aerial vehicle–structure-from-motion (UAV-SfM) dense point cloud (light blue) and field differential global positioning system (dGPS; red): (A) contact locations throughout field site, where yellow boxes denote locations of images in B and C; (B) profile view of digitized points (light blue) and imported field dGPS points (red) with vertical disagreements up to 1.44 m; and (C) profile view of digitized points and imported field dGPS points showing agreement. Pink bars in B and C represent ~3 m. DOM—digital outcrop model.

The digitization technique was also employed to identify higher order surfaces (i.e., individual unit contacts and lateral extent of accretionary surfaces) and define facies for individual units within digital sedimentary logs (Figure 2.8). The location of each sedimentary log was determined by GPS coordinates (red arrows) from the corresponding field logs. Unit contacts were digitally identified from spectral contrast (light blue points), recorded with manual tie points, and exported as x, y, z locations. Digital unit thickness was calculated by differencing the elevation (z) between the upper and lower contacts of each unit.

Units were given a simple lithofacies descriptor: sandstone, muddy sandstone, sandy mudstone, or mudstone. These facies were determined by distinct coloration discernible in the DOM and guided by field knowledge. Fine sedimentary structures (i.e., ripple laminated sandstone) could not be reliably distinguished in the DOM. Therefore, the two distinct sandstone facies identified in the field (F1 and F2) were considered matches for the digital sandstone facies (dF1; Table 2.1). Similarly, the field-identified fine-grained siltstone and mudstone facies (F5 and F6, respectively) were considered dF4 (Table 2.1).

Lateral accretion surfaces were identified using the same digitization method within Pix4Dmapper to delineate surfaces. Manual tie points were digitized laterally along bedding contacts, creating an interpolated surface fitted to all vertices. Bedding measurements, facies proportions, and observations from both digital- and field-based methods were summarized and sedimentary logs were qualitatively compared.

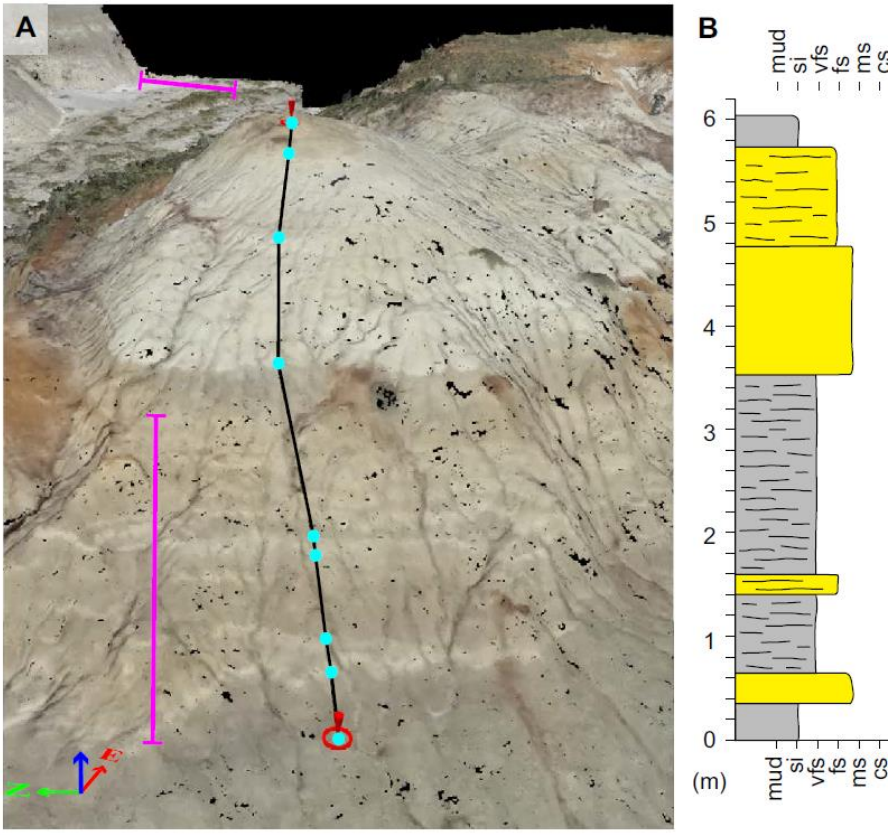

Figure 2.8. Digital sedimentary log interpretation (log 08; Fig. 2.9H). (A) Bedding contacts (light blue) on the dense point cloud were determined by spectral changes on the dense point cloud digital outcrop model, digitized within Pix4Dmapper. The bottom and top of sedimentary logs were determined from differential global positioning system locations (red arrows) collected in the field. (B) Digital sedimentary log (log 08) resulting from digital identification of changing lithology (symbology is consistent with Fig. 2.9). Pink bars in A represent ~3 m. Grain-size abbreviations: si—silt; vfs—very fine sand; fs—fine sand; ms—medium sand; cs—coarse sand.

2.5 Results

2.5.1 Channel-belt contact

DOM interpretation resulted in 3.50 km of channel-belt contact delineated throughout the 0.52 km^2 study area (Figure 2.7A; Table 2.2). Field observations identified and mapped 1.36 km of the contact within the focused UAV area (Figure

2.7A), although 4.26 km was identified and mapped throughout the larger 3.5 km^2 field area (Figure 2.1; Table 2.2). Digital points had an average point-to-point spacing of 1.69 m, whereas field-acquired points were much sparser, averaging one every 7.45 m (Table 2.2). Points were commonly analogous between the two methods with mean elevation offset of 0.32 m and a maximum offset of 1.44 m (Figure 2.7B-C).

Table 2.2. Channel-belt basal contact interpretation.

Method	Interpreted points	Length of contact identified (km)	Average point-to-point distance (m)	Field area (km^2)	Time (hours)
Field (dGPS)	654	4.26	7.45	3.5	~ 20
Digital (DOM)	2178	3.50	1.69	0.52	15.5*

* Digital UAV-SfM DOM interpretation required 1.5 hours to collect data, 13 hours to process at high resolution an accuracy, and 1.0 hours to interpret.

2.5.2 Sedimentary logs

Ten sedimentary logs measured in the field, totaling 78.0 m vertically, were co-located in the DOM dataset (Figure 2.9A-J). Field observations identified more than 250 unique beds, while 109 digital units were identified from the DOM. The average bed thickness from field measurements was 0.31 m with a median of 0.19 m, while digital units averaged 0.71 m with a median of 0.51 m. Individual beds < 0.11 m could not be distinguished in the DOM, yet constituted more than 30% of unique beds identified in the field. The total thickness of individual sedimentary logs varied by an average of 0.27 m with a maximum difference of 1.04 m (Figure 2.9F) and a minimum difference of 0.00 m (Figure 2.9H) between field and digital methods. Disparities could be attributed to

inconsistencies between individual units in field and DOM logs. For example, log 07 (Figure 2.9G) denotes a grouping of thick-bedded sandstone from 0.2 – 2.6 m, which appears to correspond to a similar DOM unit that measured 0.25 m thinner. If this 0.25 m difference is accounted for, the DOM and field logs would have similar overall measurement and comparable composition. Similarly, large disagreements were found between the mudstone layers (2.7 – 4.3 m) and groupings of mudstone / sandstone beds (4.6 – 7 m) in log 06 (Figure 2.9F), which measured 0.37 m and 0.53 m thicker than corresponding units measured from the DOM.

Thin beds distinguished as unique units in the field were commonly omitted in DOM logs. For example, the 0.2 m thick sandy mudstone bed (3.7 – 3.9 m) in log 01 was misclassified and / or not visible in its digital equivalent (Figure 2.9A). Similarly, the 0.1 m thick sandstone unit at the 3.8 m mark in log 04 was not observed in the digital counterpart (Figure 2.9D). More commonly, however, groupings of thin beds identified in the field corresponded to a larger generalized unit in the DOM, consistent with facies-level detail rather than bedding-level detail. For example, in log 05, the muddy sandstone unit at 5.0 – 6.0 m appears to correspond to the ten alternating sandstone and mudstone beds (< 0.1 m thick) within the same interval of the field log (Figure 2.9E). Disagreements between field and digital logs also included misclassification of units (i.e., log 03, 2.8 – 3.1 m; Figure 2.9C). However, these misclassifications were commonly minor in that the primary composition was maintained (i.e., muddy sandstone classified as a sandstone) or the proportion of sandstone: mudstone in a mixed composition unit was characterized differently (i.e., sandy mudstone classified as muddy sandstone in digital data).

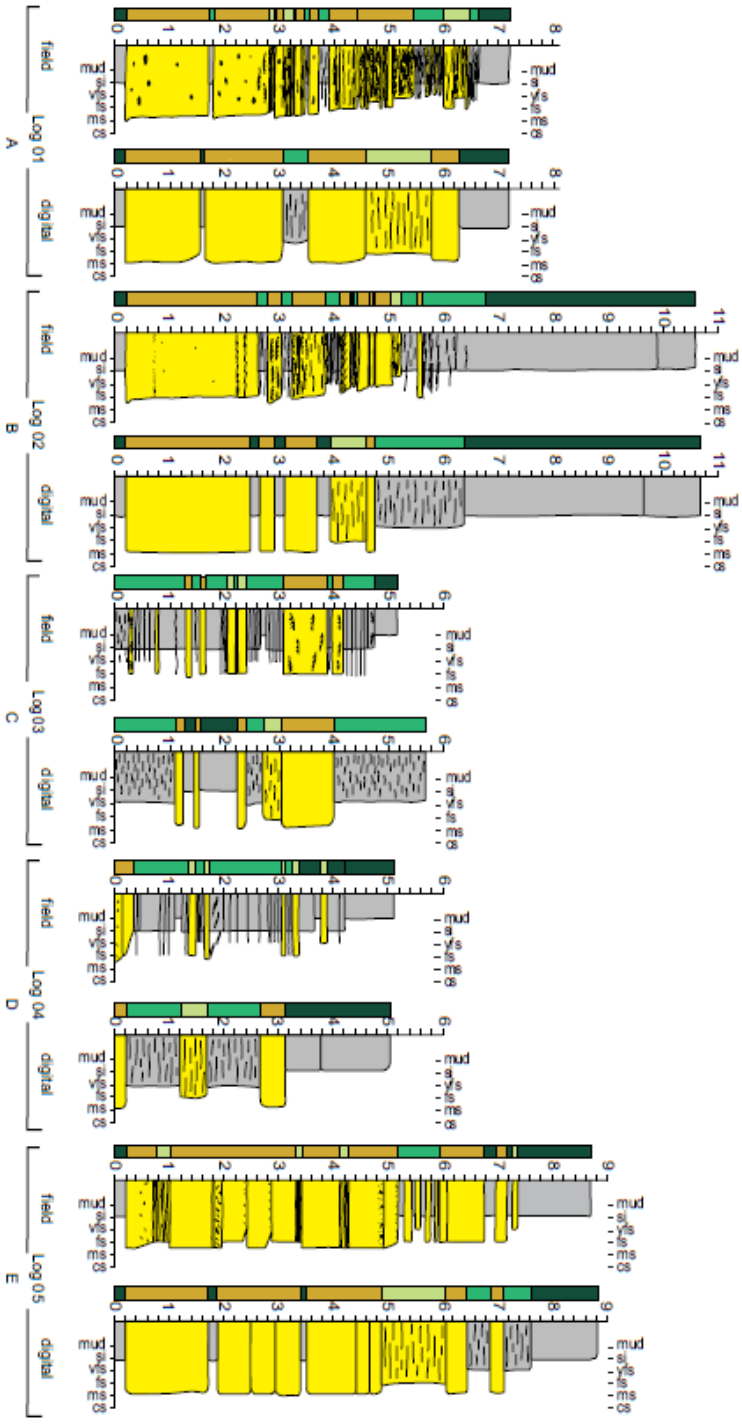
A
field
Log 01
digital
B
field
Log 02
digital
C
field
Log 03
digital
D
field
Log 04
digital
E
field
Log 05
digital
mud
si
vfs
fs
ms
cs

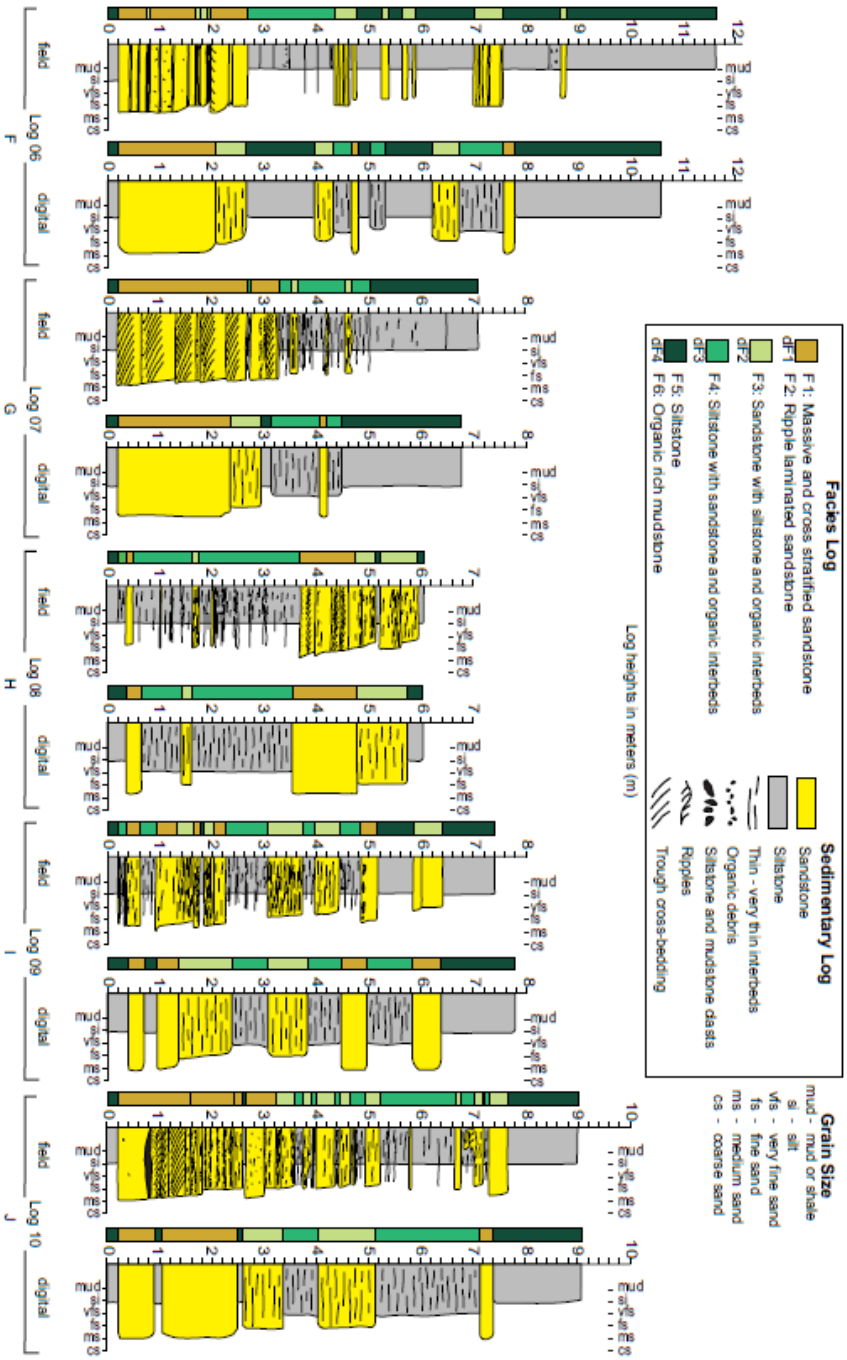

Figure 2.9. Sedimentary logs and facies logs collected independently in the field and digitally from the unmanned aerial vehicle–structure-from-motion (UAV-SfM) dense point cloud digital outcrop model (DOM). Each subfigure (A–J) contains a side-by-side comparison of the field and digital logs: (A) log 01; (B) log 02; (C) log 03; (D) log 04; (E) log 05; (F) log 06; (G) log 07; (H) log 08; (I) log 09; (J) log 10.

The 250 unique beds identified in the ten field logs were categorized into one of the six facies from Table 2.1, resulting in 160 unique facies units that could then be compared with the 109 digital stratigraphic units (facies) derived from the DOM. The mean thickness of the field-derived facies was 0.49 m with a median of 0.22 m. Table 2.3 summarizes the facies proportions determined for each field log and digital logs based on the four digital facies categories in Table 2.1. Digital units (dF1 – dF4) had an average absolute difference from field facies (F1 – F6) of ± 4.9% and a standard deviation of 0.06.The maximum discrepancy between field and digital facies proportions was 13.6% for the sandy mudstone (dF3) classification in log 03 (Figure 2.9C) and the smallest difference of 0.3% between muddy sandstone (dF2) in log 04 (Figure 2.9D).

Digitization of higher order surfaces resulted in the identification of several meander-belt elements throughout the DOM. Most notably were aligned sequences of shallow dipping planes characteristic of lateral accretion surfaces from a migrating point bar (e.g., Thomas et al., 1987; Figure 2.10, Supplemental Files 2.3-2.4 - Appendix C). Similar surfaces were also identified within relatively finer-grained facies, indicative of counter-point-bar surfaces (Smith et al., 2009a; Figure 2.11, Supplemental Files 2.5-2.6 - Appendix C). Shallow dipping (< 12°) surfaces of heterolithic strata correspond to the original depositional surface and are indicative of channel metrics (i.e., migration direction). Digital measurements of the point bar surfaces had a mean dip azimuth of 90° to the east, while counter-point-bar deposits had a mean dip azimuth of 190° towards the south-southwest.

Table 2.3. Results of facies comparison – field and digital.

Sedimentary log ID	Method	Sandstone dF1 (%)	Silty sandstone dF2 (%)	Sandy siltstone dF3 (%)	Siltstone and mudstone dF4 (%)
01	field	62	10	20	08
	digital	60	17	07	17
02	field	39	02	22	38
	digital	31	06	16	48
03	field	22	06	64	08
	digital	25	05	55	15
04	field	07	09	52	32
	digital	13	09	39	38
05	field	62	08	09	21
	digital	57	13	10	20
06	field	19	15	14	52
	digital	21	14	14	51
07	field	42	04	22	32
	digital	34	09	17	40
08	field	21	21	52	06
	digital	26	19	44	11
09	field	19	30	27	25
	digital	23	22	29	26
10	field	33	23	27	17
	digital	26	21	29	23

Note: dF1 is equivalent to coarse-grained field facies, F1 – F2, and dF4 is equivalent to fine-grained field facies, F5 – F6 (see Table 2.1).

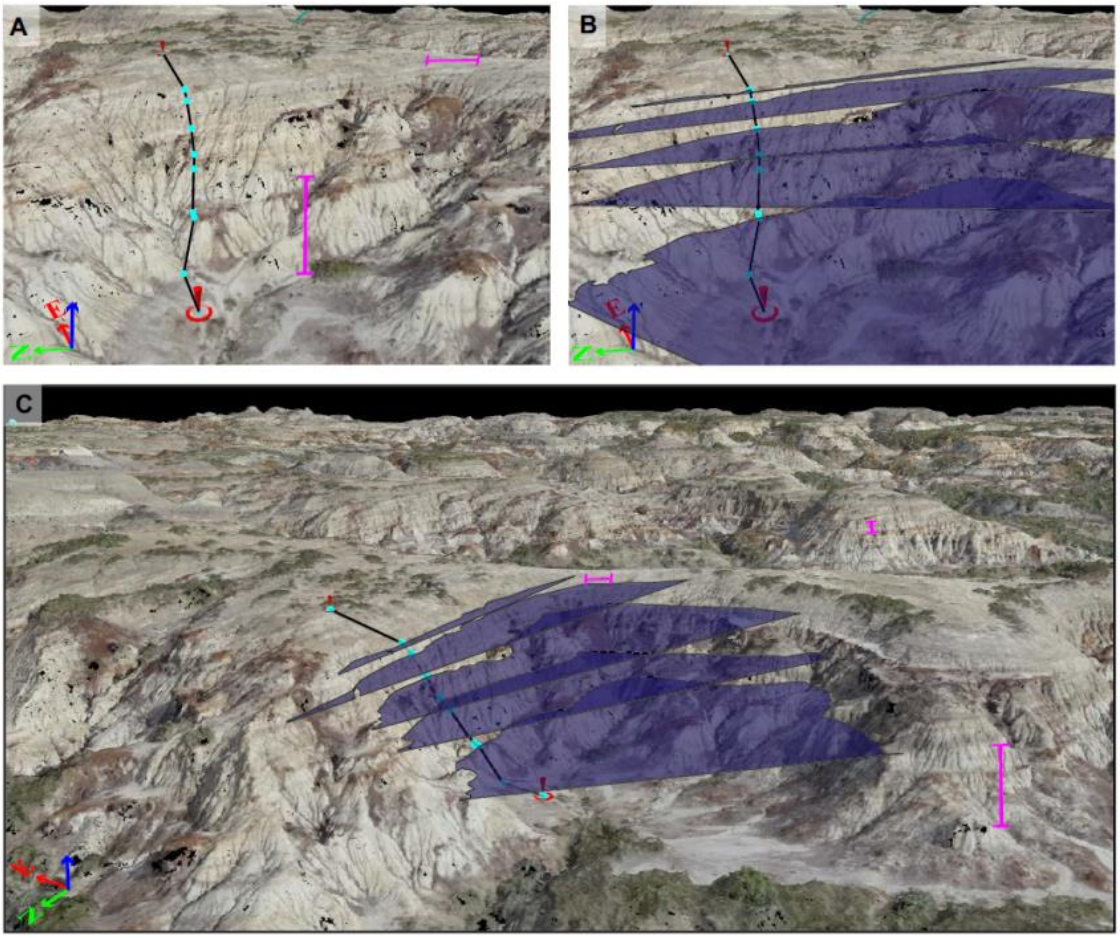

Figure 2.10. Profile view of sedimentary log 01 (Fig. 2.9A): (A) within the digital outcrop model, where light-blue points separate digitally identified units within a one-dimensional sedimentary log; (B) lateral interpretation of bedding surfaces (purple polygons), which allows three-dimensional quantification and interpretation of geologic deposits; and (C) overview showing the same surfaces in the context of the surrounding geology indicative of a point bar migrating 90° east (left in the image). Pink bars in A–C represent ~3 m. For interactive model, see Supplemental Files 2.3–2.4 (Appendix C).

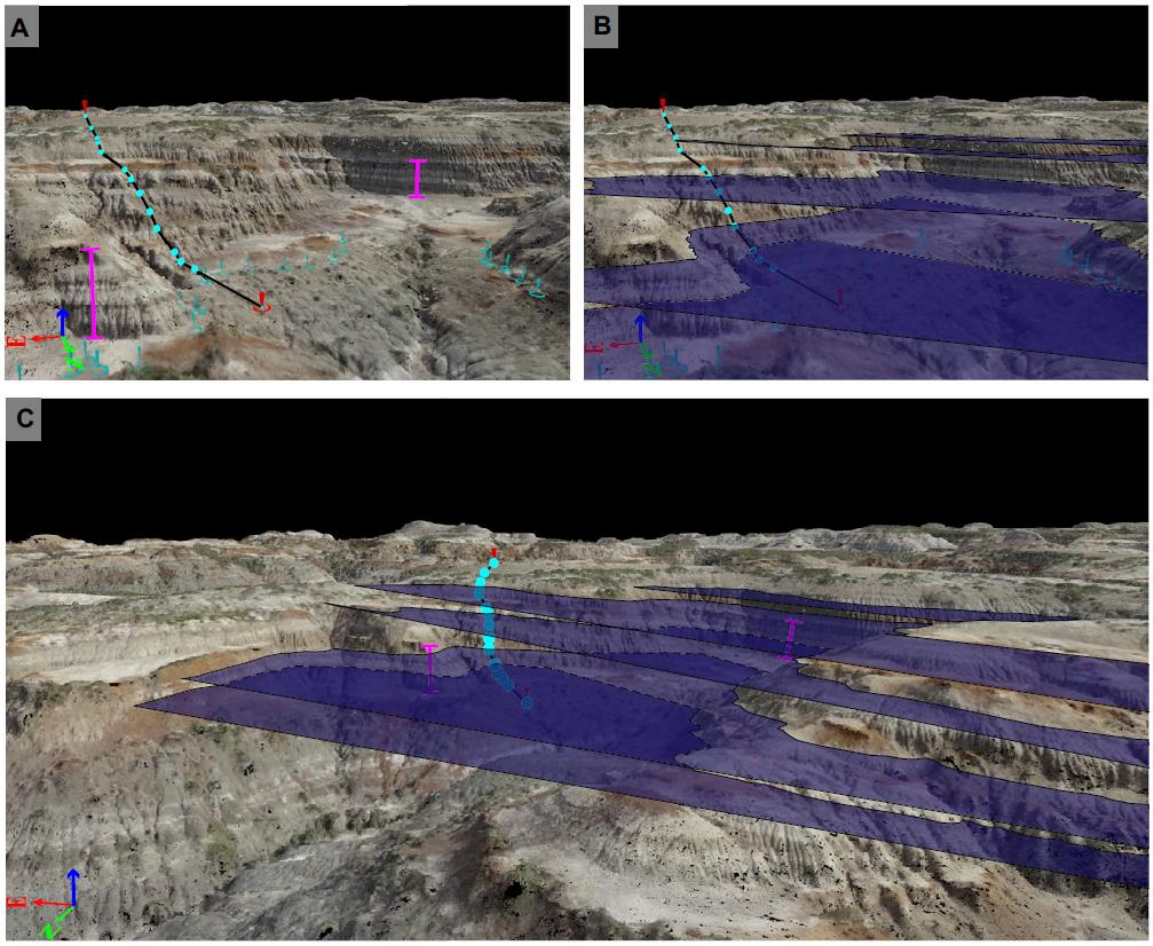

Figure 2.11. Profile view of sedimentary log 09 (Fig. 2.9I): (A) within the digital outcrop model, where light-blue points separate digitally identified units within a one-dimensional sedimentary log; (B) lateral interpretation of bedding surfaces (purple polygons), which allows three-dimensional quantification and interpretation of geologic deposits; and (C) overview showing the same surfaces in the context of the surrounding geology indicative of a counter point bar migrating 190° south-southwest (right in the image). Pink bars in A–C represent ~3 m. For interactive model, see Supplemental Files 5–6 (Appendix C).

2.6 Discussion

UAV-SfM applications in geology have primarily used 2D and 2.5D methods for analysis (e.g., Bemis et al., 2014; Johnson et al., 2014; Vasuki et al., 2014; Chen et al., 2015; Zahm et al., 2016; Chesley et al., 2017; Thiele et al., 2017). Although UAV-SfM derived orthomosaic images and DSMs have very high spatial resolution and have been used to identify fluvial stratigraphic surfaces in plan-view (i.e., Chesley et al., 2017), they are not always suitable for mapping laterally extensive exposures along steep slopes (cross-sectional view). Nieminski and Graham (2017) used UAV-SfM derived digital terrain models (DTMs), referred to here and elsewhere as DOMs, to map thin-bedded (0.1 - 0.7 m thick) turbidites and deformation features along an extensive vertical cliff. The authors suggested that more complex outcrop geometries would require additional photographs to limit distortion and obtain complete coverage in a DOM.

The Dinosaur Provincial Park badlands are an excellent example of a geometrically complex landscape with well-preserved, extensive exposures of fluvial channel-belt and floodplain deposits. To obtain complete coverage of the complex exposures, we acquired a highly redundant block of images, with high overlap, perpendicular flight lines, and oblique (off-nadir) image angles. It has been suggested that similar imaging networks would increase outcrop coverage (Bemis et al., 2014; Vollgger and Cruden, 2016; Cawood et al., 2017) and could also improve photogrammetric camera calibration and overall accuracy of model reconstruction (Wolf and Dewitt, 2000; Luhmann and Robson, 2006; James and Robson, 2014; Carbonneau and Dietrich, 2016; Luhmann et al., 2016; James et al., 2017). We found that the data collection strategy captured sufficient geologic detail along steep slopes; however, datasets required further

consideration of visualization strategies (i.e., use of the 3D dense point cloud) in order to retain geologic detail during analysis.

2.6.1 DOMs

We examined alternative UAV-SfM datasets as DOMs for mapping multi-scale fluvial channel-belt features and facies exposed within a topographically complex outcrop. Although the UAV-SfM dense point cloud functioned as a DOM for digital analysis and interpretation of fluvial features, other datasets can also be used to create a DOM. For example, both dense point cloud and textured mesh DOMs represent a scaled, georeferenced, and colorized representation of the field area. The main distinction between the two DOMs is use of interpolation and texturing. Point clouds resemble raw datasets collected with TLS and include a color (RGB) attribute calculated from corresponding image pixels. Textured meshes are interpolated into a continuous triangulated surface from the point cloud and are textured directly from corresponding images (Carrivick et al., 2016). Point clouds contain gaps between points (i.e., Figure 2.6B) that can lead to difficulties in analysis. Geologic applications, in particular, commonly process TLS point clouds into a triangulated mesh for interpretation and measurement (Enge et al., 2007; Buckley et al., 2008).

We found that, although the triangulated mesh provided a continuous view of the outcrop, a high resolution textured mesh could not be processed for the 0.52 km^2 study site due to computational limitations in processing a large dataset. Mesh triangulation for the entire study area required a limitation of triangles, resulting in more generalized topography, distortion of photo texture, and loss of bedding level detail. Although gaps

between points may complicate analysis, we found geologic features more clearly resolved in the dense point cloud than in the textured mesh.

2.6.2 3-D interpretation

Macro-scale features, such as the channel-belt basal contact, were clearly visible throughout the field site in both the textured mesh and dense point cloud (Figure 2.5). Recognition of this feature throughout the field site provides constraints on interpretation of finer scale fluvial features. Specifically, the channel-belt contact provides a common datum that serves as a reference surface for aligning detailed measurements (e.g., sedimentary logs; Calvo and Ramos, 2015). Mapping extensive surfaces in the field can be time consuming and problematic when traversing difficult terrain with exposures on slopes facing different azimuths and crossing drainages. Although field campaigns commonly employ GPS or dGPS units that can be used to record points along surface contacts, it remains difficult to keep track of the specific contact of interest, especially in fluvial environments with multiple channel-belts exposed.

Identification of the channel-belt basal contact using the DOM, however, is an efficient and straightforward exercise. Digitally tracing a contact around intricate topography, across drainages, and through vegetation is possible by way of flexible visualization and navigation throughout the 3D model. Identification of the lower channel-belt contact for the interval exposed within the field site was completed within 1.0 hour (15.5 hours if including image collection and processing) as compared to 20 hours required to map the contact in the field (Table 2.2). Digital (red points) and field locations (blue points) of the contact were not always in agreement, with vertical offsets up to 1.44 m (i.e., Figure 2.7B). These offsets could be explained by a combination of

factors, including reduced accuracy of field dGPS and laser rangefinder (i.e., satellite coverage obstruction, laser scan angle, or multipath error) or inaccurate reconstruction and georeferencing (location and orientation) of the UAV-SfM model. Based on the recent vetting of UAV-SfM models produced from a similar methodology (i.e., similar UAV platform, SfM software, and RTK-GNSS of GCPs: Whitehead and Hugenholtz, 2015; Hugenholtz et al., 2016), we strongly believe that the former are more likely the cause for discrepancies.

Furthermore, these inconsistencies signify errors in absolute location on Earth with respect to a geographic reference system (i.e., latitude, longitude, and/or elevation). Degraded absolute accuracy may complicate the ability to locate a particular feature or compare across datasets; however, UAV-SfM DOMs preserve relative spatial relationships (i.e., distance and direction) among points within the model. With appropriately defined scale and orientation from GCPs and/or ground measurements, UAV-SfM DOMs maintain high relative accuracies and can be used to record quantitative geologic measurements (i.e., bed thickness, lengths, and angular measurements of architectural features), although the DOM may not be accurately located in absolute space (Chesley et al., 2017).

2.6.3 3-D measurements

Attempts to identify individual beds from the UAV-SfM DOM had mixed results. In general, thicker units were more consistently plotted than thinner units, while beds < 0.11 m were not discernible in the DOM. This is similar to results found by Nieminski and Graham (2017) who were able to dependably identify beds ranging from 0.1 – 0.7 m thick. It is likely that increased resolution (from lower flight altitude, longer focal length,

or higher camera resolution), could result in identification of thinner beds. However, this would also reduce spatial coverage and provide excessive detail in some applications. Regardless, comparison of units identified from the DOM with field facies logs suggests that DOMs can reliably resolve facies-level detail. Digitally identified facies averaged ± 4.9% within proportions of facies identified in the field. Differences in unit thickness may be due to errors in UAV-SfM DOM, or errors in field measurements, which are not uncommon (Groshong Jr., 2006). Facies proportions reported from field logs are typically one-dimensional and, at best, can be estimated between sedimentary logs through interpolation. UAV-SfM DOMs present the opportunity to extend facies estimations laterally and contiguously throughout extensive outcrop exposures, with similar conviction as one-dimensional field interpretations.

Extending bedding measurements laterally from 1D sedimentary logs can provide additional geometric information about inherently 3D geologic features that is often difficult, if not impossible, to quantify using traditional field methods (McCaffrey et al., 2005). Using the digitization method in Pix4Dmapper, we were able to identify abundant inclined and aligned accretion surfaces characteristic of point bar (Figure 2.10) and counter-point-bar (Figure 2.11) elements (Thomas et al., 1987; Smith et al., 2009a). Figures 2.10A-11A show the (1D) digital sedimentary log (black line) with light blue points separating distinct lithologic units that were compared to field sedimentary and facies logs. Figures 2.10B-11B show the same views with bedding surfaces extended laterally from the sedimentary logs. Similar to the channel-belt basal contact, these interpretations can be easily followed to corresponding units around outcrop bends and across drainages to form 3D surfaces representing interpreted depositional surfaces

(purple polygons, see Supplemental Files 3-6 [Appendix C] for interactive models). An alternative approach could be to export manual tie points from Pix4Dmapper into an external software program that permits more complex surface interpolation options (i.e., Petrel, ArcGIS; e.g., Durkin et al., 2015a), however this was not considered necessary in this demonstration.

Lateral accretion surfaces have been recognized in plan-view using similar UAV-SfM methods to interpret a 2D orthomosaic image (Chesley et al., 2017). We extend these methods into 3D analysis through identification of accretionary bedding planes in multiple cross-section views, facilitating the detailed quantification and reconstruction of channel metrics. In particular, by measuring the attitude of a series of accretion surfaces, point bar migration directions can be reconstructed from the UAV-SfM datasets. These data are critical for detailed stratigraphic correlations and paleoenvironmental reconstructions (e.g., Durkin et al., 2015a; Chesley et al., 2017). Additionally, digital observations using DOMs can be shared, re-evaluated, and re-interpreted based on new information.

Digital identification of stratigraphic surfaces and lithologic units is reliant upon distinct surface coloration calibrated by extensive field knowledge of the facies within the local field area. Sandstone (dF1) and mudstone (dF4) were primarily identified by dominant surface coloration in the DOM (dF1: light tan - white; dF4: dark grey - brown). Muddy sandstone (dF2) and sandy mudstone (dF3) facies typically had colors ranging between the two end members. Correspondence between field and digital facies is attributed in large part to the marked contrast between fine- and coarse-grained members.

Without the contrasting weathered color of different lithofacies, digital interpretation may not be possible to the extent demonstrated here.

DOMs, whether derived from TLS, ground-based photogrammetry, or UAV-SfM, are not presented as a replacement for field observations. However, DOMs are well suited to provide supplemental quantitative measurements and interpretations that are difficult, or impossible, to acquire in the field. In this study, we demonstrated that multiple orders of fluvial stratigraphic surfaces and lithofacies could be independently interpreted from the DOM alone with similar results to field interpretations. Integration of detailed field measurements (i.e., sedimentary logs, paleocurrent measurements, and strike and dip measurements) with DOMs in a digital database yields potential for highly detailed vertical and lateral reconstruction of fluvial deposits and the processes that formed them through time.

2.7 Conclusions

We examined UAV-SfM datasets for mapping multi-scale stratigraphic surfaces and facies of a heterogeneous fluvial channel-belt deposit exposed within a topographically complex outcrop. We evaluated commensurability of digital measurements made from a 3D DOM derived from UAV-SfM and independently collected field observations. Building upon recent geologic mapping applications using UAV-SfM, the data acquisition, processing, and visualization methods proposed here preserve 3D topographic integrity and geologic detail, even in geometrically complex landscapes. Results indicate that UAV-SfM methods can produce visually representative DOMs that can be used to derive unaided interpretations and measurements comparable to field methods in myriad geologic applications. UAV-SfM DOMs are not a replacement

for field observations; however, they can efficiently provide supplemental measurements and enable guided interpretation between sparsely distributed 1D and 2D field data (i.e., sedimentary logs, cross-section sketches). Integration of multiple datasets can result in highly constrained geologic models that, for fluvial environments, can potentially result in more complete stratigraphic models. Future research will take on such challenges by using integrated datasets and UAV-SfM DOMs to better understand temporal evolution and preservation of channel-belt deposits.

2.8 References

Arnot, M.J., Good, T.R., and Lewis, J.J.M., 1997, Photogeological and image-analysis techniques for collection of large-scale outcrop data, *Journal of Sedimentary Research*, *67*(5), 984–987, doi:-.

Bellian, J.A., Kerans, C., and Jennete, D.C., 2005, Digital outcrop models: applications of terrestrial scanning lidar technology in stratigraphic modeling, *Journal of Sedimentary Research*, *75*(2), 166–176, doi:10.2110/jsr.2005.013.

Bemis, S.P., Micklethwaite, S., Turner, D., James, M.R., Akciz, S., Thiele, S.T., and Bangash, H.A., 2014, Ground-based and uav-based photogrammetry: a multi-scale, high-resolution mapping tool for structural geology and paleoseismology, *Journal of Structural Geology*, *69*, 163–178, doi:10.1016/j.jsg.2014.10.007.

Bond, C.E., Shipton, Z.K., Jones, R.R., Butler, R.W.H., and Gibbs, A.D., 2007, Knowledge transfer in a digital world: field data acquisition, uncertainty, visualization, and data management, *Geosphere*, *3*(6), 568, doi:10.1130/GES00094.1.

Brown, M., and Lowe, D.G., 2005, Unsupervised 3d object recognition and reconstruction in unordered datasets, *Proceedings of International Conference on 3-D Digital Imaging and Modeling, 3DIM*, 56–63, doi:10.1109/3DIM.2005.81.

Bryan, R.B., Campbell, I.A., and Yair, A., 1987, Postglacial geomorphic development of the Dinosaur Provincial Park badlands, Alberta, *Zeitschrift Fur Geomorphologie*, *24*(1), 135–146,

Buckley, S.J., Howell, J.A., Enge, H.D., and Kurz, T.H., 2008, Terrestrial laser scanning in geology: data acquisition, processing and accuracy considerations, *Journal of the Geological Society*, *165*(3), 625–638, doi:10.1144/0016-76492007-100.

Calvo, R., and Ramos, E., 2015, Unlocking the correlation in fluvial outcrops by using a dom-derived virtual datum: method description and field tests in the huesca fluvial fan, Ebro Basin (Spain), *Geosphere*, *11*(5), 1507–1529, doi:10.1130/GES01058.1.

Campbell, I.A., 1970, Erosion rates in the Steveville badlands, Alberta, *Canadian Geographer*, *XIV*(3)

Carbonneau, P.E., and Dietrich, J.T., 2016, Cost-effective non-metric photogrammetry from consumer-grade suas: implications for direct georeferencing of structure from motion photogrammetry, *Earth Surface Processes and Landforms* doi:10.1002/esp.4012.

Carrivick, J.L., Smith, M.W., and Quincey, D.J., 2016, *Structure from Motion in the Geosciences*: Oxford, UK, Wiley-Blackwell.

Cawood, A.J., Bond, C.E., Howell, J.A., Butler, R.W.H., and Totake, Y., 2017, Lidar, uav or compass-clinometer? Accuracy, coverage and the effects on structural models, *Journal of Structural Geology*, *98*, 67–82, doi:10.1016/j.jsg.2017.04.004.

Chen, N., Ni, N., Kapp, P., Chen, J., Xiao, A., and Li, H., 2015, Structural analysis of the Hero Range in the Qaidam Basin, northwestern China, using integrated uav, terrestrial lidar, landsat 8, and 3-d seismic data, *IEEE Journal of Selected Topics in Applied Earth Observations and Remote Sensing*, *8*(9), 4581–4591, doi:10.1109/JSTARS.2015.2440171.

Chesley, J.T., Leier, A.L., White, S., and Torres, R., 2017, Using unmanned aerial vehicles and structure-from-motion photogrammetry to characterize sedimentary outcrops: an example from the Morrison Formation, Utah, USA, *Sedimentary Geology*, *354*(June), 1–8, doi:10.1016/j.sedgeo.2017.03.013.

Colomina, I., and Molina, P., 2014, Unmanned aerial systems for photogrammetry and remote sensing: a review, *ISPRS Journal of Photogrammetry and Remote Sensing*, *92*, 79–97, doi:10.1016/j.isprsjprs.2014.02.013.

Durkin, P.R., Boyd, R.L., Hubbard, S.M., Shultz, A.W., and Blum, M.D., 2017, Three-dimensional reconstruction of meander-belt evolution, Cretaceous Mcmurray Formation, Alberta Foreland Basin, Canada, *Journal of Sedimentary Research*, *87*(October), 1075–1099, doi:10.2110/jsr.2017.59.

Durkin, P.R., Hubbard, S.M., Boyd, R.L., and Leckie, D.A., 2015a, Stratigraphic expression of intra-point-bar erosion and rotation, *Journal of Sedimentary Research*, *85*, 1238–1257, doi:10.2110/jsr.2015.78.

Durkin, P.R., Hubbard, S.M., Weleschuk, Z., Smith, D.G., Palmer, M., Torres, A., and Holbrook, J., 2015b, Spatial and temporal evolution of an ancient fluvial meanderbelt (upper Cretaceous Dinosaur Park Formation , southeastern Alberta, Canada) with emphasis on characterization of counter point bar deposits, In *AAPG*

Search and Discovery (p. Article 90216)

Eberth, D.A., 2005, The geology, In P. J. . Currie & E. B. Koppelhus (Eds.), *Dinosaur Provincial Park: a spectacular ancient ecosystem revealed* (1st ed., pp. 54–82). Indiana University Press.

Eberth, D. A., and Hamblin, A.P., 1993, Tectonic, stratigraphic, and sedimentologic significance of a regional discontinuity in the upper Judith River Group (Belly River wedge) of southern Alberta, Saskatchewan, and northern Montana, *Canadian Journal of Earth Sciences*, *30*, 174–200, doi:10.1139/e93-016.

Enge, H.D., Buckley, S.J., Rotevatn, A., and Howell, J.A., 2007, From outcrop to reservoir simulation model: workflow and procedures, *Geosphere*, *3*(6), 469–490, doi:10.1130/GES00099.1.

Evans, D.J.A., 2000, Quaternary geology and geomorphology of the Dinosaur Provincial Park area and surrounding plains, Alberta, Canada: the identification of former glacial lobes, drainage diversions and meltwater flood tracks, *Quaternary Science Reviews*, *19*(10), 931–958, doi:10.1016/S0277-3791(99)00029-3.

Fonstad, M.A., Dietrich, J.T., Courville, B.C., Jensen, J.L., and Carbonneau, P.E., 2013, Topographic structure from motion: a new development in photogrammetric measurement, *Earth Surface Processes and Landforms*, *38*(4), 421–430, doi:10.1002/esp.3366.

Furukawa, Y., and Ponce, J., 2010, Accurate , dense , and robust multi-view stereopsis, In *IEEE Computer Society Conference on Computer Vision and Pattern Recognition* (Vol. 32, pp. 1362–1376)

Groshong Jr., R.H., 2006, *3-d structural geology*. Berlin Heidelberg: Springer. doi:10.1017/CBO9780511777806.

Hamblin, A.P., and Abrahamson, B.W., 1996, Stratigraphic architecture of "basal belly river" cycles, Foremost Formation, Belly River Group, subsurface of southern Alberta and southwestern Saskatchewan, *Bulletin of Canadian Petroleum Geology*, *44*(4), 654–673,

Harwin, S., and Lucieer, A., 2012, Assessing the accuracy of georeferenced point clouds produced via multi-view stereopsis from unmanned aerial vehicle (uav) imagery, *Remote Sensing*, *4*(6), 1573–1599, doi:10.3390/rs4061573.

Harwin, S., Lucieer, A., and Osborn, J., 2015, The impact of the calibration method on the accuracy of point clouds derived using unmanned aerial vehicle multi-view stereopsis, *Remote Sensing*, *7*, 11933–11953, doi:10.3390/rs70911933.

Hodgetts, D., 2013, Laser scanning and digital outcrop geology in the petroleum industry: a review, *Marine and Petroleum Geology*, *46*, 335–354, doi:10.1016/j.marpetgeo.2013.02.014.

Hugenholtz, C.H., Brown, O.W., Walker, J., Barchyn, T.E., Nesbit, P.R., Kucharczyk, M., and Myshak, S., 2016, Spatial acccuracy of uav-derived orthoimagery and topography: comparing photogrammetric models processed with direct geo-referencing and ground control points, *Geomatica*, *70*(1), 21–30,

Hugenholtz, C.H., Moorman, B.J., Riddell, K., and Whitehead, K., 2012, Small unmanned aircraft systems for remote sensing and earth science research, *Eos, Transactions American Geophysical Union*, *93*(25), 236, doi:10.1117/1.3474649.

Hugenholtz, C.H., Whitehead, K., Brown, O.W., Barchyn, T.E., Moorman, B.J., LeClair, A., Riddell, K., and Hamilton, T., 2013, Geomorphological mapping with a small unmanned aircraft system (suas): feature detection and accuracy assessment of a photogrammetrically-derived digital terrain model, *Geomorphology*, *194*, 16–24, doi:10.1016/j.geomorph.2013.03.023.

James, M.R., and Quinton, J.N., 2014, Ultra-rapid topographic surveying for complex environments: the hand-held mobile laser scanner (hmls), *Earth Surface Processes and Landforms*, *39*(1), 138–142, doi:10.1002/esp.3489.

James, M.R., and Robson, S., 2012, Straightforward reconstruction of 3d surfaces and topography with a camera: accuracy and geoscience application, *Journal of Geophysical Research: Earth Surface*, *117*(3), 1–17, doi:10.1029/2011JF002289.

James, M.R., and Robson, S., 2014, Mitigating systematic error in topographic models derived from uav and ground-based image networks, *Earth Surface Processes and Landforms*, *39*(10), 1413–1420, doi:10.1002/esp.3609.

James, M.R., Robson, S., D'Oleire-Oltmanns, S., and Niethammer, U., 2017, Optimising uav topographic surveys processed with structure-from-motion: ground control quality, quantity and bundle adjustment, *Geomorphology*, *280*, 51–66, doi:10.1016/j.geomorph.2016.11.021.

Johnson, K., Nissen, E., Saripalli, S., Arrowsmith, J.R., McGarey, P., Scharer, K., Williams, P., and Blisniuk, K., 2014, Rapid mapping of ultrafine fault zone topography with structure from motion, *Geosphere*, *10*(5), 969–986, doi:10.1130/GES01017.1.

Jones, R.R., McCaffrey, K.J.W., Wilson, R.W., and Holdsworth, R.E., 2004, Digital field data acquisition: towards increased quantification of uncertainty during geological mapping, *Geological Society, London, Special Publications*, *239*(1), 43–56, doi:10.1144/GSL.SP.2004.239.01.04.

Jordan, D.W., and Pryor, W.A., 1992, Hierarchical levels of heterogeneity in a Mississippi River meander belt and application to reservoir systems, *American Association of Petroleum Geologists Bulletin* doi:10.1306/BDFF8A6A-1718-11D7-8645000102C1865D.

Koster, E.H., and Currie, P.J., 1987, Upper Cretaceous coastal plain sediments at Dinosaur Provincial Park, southeast Alberta, *Field guide/Geological Society of America*

Kung, O., Strecha, C., Beyeler, A., Zufferey, J.-C., Floreano, D., Fua, P., and Gervaix, F., 2012, The accuracy of automatic photogrammetric techniques on ultra-light uav imagery, *ISPRS - International Archives of the Photogrammetry, Remote Sensing and Spatial Information Sciences* (Vol. XXXVIII-1/) https://doi.org/10.5194/isprsarchives-XXXVIII-1-C22-125-2011

Labourdette, R., and Jones, R.R., 2007, Characterization of fluvial architectural elements using a three-dimensional outcrop data set : escanilla braided system, south-central Pyrenees, Spain, *Geosphere*, (6), 422–434, doi:10.1130/GES00087.1.

Lourakis, M.I.A., and Argyros, A.A., 2009, Sba: a software package for generic sparse bundle adjustment, *ACM Transactions on Mathematical Software*, *36*(1), 1–30, doi:10.1145/1486525.1486527.

Lowe, D.G., 1999, Object recognition fromlocal scale-invariant features, *IEEE International Conference on Computer Vision*, 1150–1157, doi:10.1109/ICCV.1999.790410.

Lowe, D.G., 2004, Distinctive image features from scale-invariant keypoints, *International Journal of Computer Vision*, *60*(2), 91–110, doi:10.1023/B:VISI.0000029664.99615.94.

Luhmann, T., Fraser, C., and Maas, H.G., 2016, Sensor modelling and camera calibration for close-range photogrammetry, *ISPRS Journal of Photogrammetry and Remote Sensing*, *115*, 37–46, doi:10.1016/j.isprsjprs.2015.10.006.

Luhmann, T., and Robson, S., 2006, Close range photogrammetry : principles, techniques and applications - 2 (pp. 159–316)

McCaffrey, K.J.W., Jones, R.R., Holdsworth, R.E., Wilson, R.W., Clegg, P., Imber, J., Holliman, N.S., and Trinks, I., 2005, Unlocking the spatial dimension: digital technologies and the future of geoscience fieldwork, *Journal of the Geological Society*, *162*(6), 927–938, doi:10.1144/0016-764905-017.

Miall, A.D., 1988, Reservoir heterogeneities in fluvial sandstones: lesson from outcrop studies., *American Association of Petroleum Geologists Bulletin*, *72*(6), 682–697, doi:10.1306/703C8F01-1707-11D7-8645000102C1865D.

Nieminski, N.M., and Graham, S.A., 2017, Modeling stratigraphic architecture using small unmanned aerial vehicles and photogrammetry: examples from the Miocene East Coast Basin, New Zealand, *Journal of Sedimentary Research*, *87*(2), 126–132, doi:10.2110/jsr.2017.5.

Niethammer, U., James, M.R., Rothmund, S., Travelletti, J., and Joswig, M., 2012, Uav-based remote sensing of the Super-Sauze landslide: evaluation and results, *Engineering Geology*, *128*, 2–11, doi:10.1016/j.enggeo.2011.03.012.

Pavlis, T.L., and Mason, K.A., 2017, The new world of 3d geologic mapping, *GSA Today*, 4–10, doi:10.1130/GSATG313A.1.

Pranter, M.J., Ellison, A.I., Cole, R.D., and Patterson, P.E., 2007, Analysis and modeling of intermediate-scale reservoir heterogeneity based on a fluvial point-bar outcrop analog, Williams Fork Formation, Piceance Basin, Colorado, *AAPG Bulletin*, *91*(7), 1025–1051, doi:10.1306/02010706102.

Rains, B., Shaw, J., Skoye, R., Sjogren, D., and Kvill, D., 1993, Late Wisconsin subglacial megaflood paths in Alberta, *Geology*, *21*(4), 323–326, doi:10.1130/0091-7613(1993)021<0323:LWSMPI>2.3.CO;2.

Rarity, F., van Lanen, X.M.T., Hodgetts, D., Gawthorpe, R.L., Wilson, P., Fabuel-Perez, I., and Redfern, J., 2014, Lidar-based digital outcrops for sedimentological analysis: workflows and techniques, *Geological Society, London, Special Publications*, *387*(1), 1–31, doi:10.1144/SP387.5.

Remondino, F., Spera, M.G., Nocerino, E., Menna, F., and Nex, F., 2014, State of the art in high density image matching, *The Photogrammetric Record*, *29*(146), 144–166, doi:10.1111/phor.12063.

Ryan, M.J., Russell, A.P., Eberth, D.A., and Currie, P.J., 2001, The taphonomy of a Centrosaurus (ornithischia: certopsidae) bone bed from the Dinosaur Park Formation (upper Campanian), Alberta, Canada, with comments on cranial ontogeny, *Palaios*, *16*(5), 482–506, doi:10.1669/0883-1351(2001)016<0482:TTOACO>2.0.CO;2.

Sgavetti, M., 1992, Criteria for stratigraphic correlation using aerial photographs: examples from the south-central Pyrenees, *American Association of Petroleum Geologists Bulletin*, *76*(5), 708–730,

Smith, D.G., Hubbard, S.M., Leckie, D.A., and Fustic, M., 2009a, Counter point bar deposits: lithofacies and reservoir significance in the meandering modern Peace River and ancient McMurray Formation, Alberta, Canada, *Sedimentology*, *56*(6), 1655–1669, doi:10.1111/j.1365-3091.2009.01050.x.

Smith, D.G., Hubbard, S.M., Putnam, P.E., Fustic, M., Leckie, D.A., Eberth, D.A., Lavigne, J.M., and Hugenholtz, C.H., 2009b, Earthquakes as probable causes of chaotic and deformed stratigraphy in an ancient river meander deposit, Dinosaur Provincial Park, Alberta, In *CSPG Convention* (pp. 767–770). Calgary

Snavely, N., Seitz, S.M., and Szeliski, R., 2006, Photo tourism: exploring photo collections in 3d, *ACM Transactions on Graphics*, *25*(3), 835–846, doi:10.1145/1141911.1141964.

Snavely, N., Seitz, S.M., and Szeliski, R., 2008, Modeling the world from internet photo collections, *International Journal of Computer Vision*, *80*(2), 189–210, doi:10.1007/s11263-007-0107-3.

Szeliski, R., 2010, *Computer vision : algorithms and applications* (Vol. 5). Springer Science & Business Media. doi:10.1007/978-1-84882-935-0.

Thiele, S.T., Grose, L., Samsu, A., Micklethwaite, S., Vollgger, S.A., and Cruden, A.R., 2017, Rapid, semi-automatic fracture and contact mapping for point clouds, images and geophysical data, *Solid Earth Discussions*, (August), 1–19, doi:10.5194/se-2017-83.

Thomas, R.G., Smith, D.G., Wood, J.M., Visser, M.J., Calverley-Range, E.A., and Koster, E.H., 1987, Inclined heterolithic stratification - terminology, description, interpretation and significance, *Sedimentary Geology*, *53*(September), 123–179, doi:10.1016/S0037-0738(87)80006-4.

Toth, C., and Jóźków, G., 2016, Remote sensing platforms and sensors: a survey, *ISPRS Journal of Photogrammetry and Remote Sensing*, *115*, 22–36, doi:10.1016/j.isprsjprs.2015.10.004.

Triggs, B., McLauchlan, P., Hartley, R., and Fitzgibbon, A., 2000, *Bundle adjustment - a modern synthesis*, *Vision Algorithms: Theory and Practice* (Vol. 1883) doi:10.1007/3-540-44480-7_21.

Trinks, I., Clegg, P., McCaffrey, K.J.W., Jones, R.R., Hobbs, R., Holdsworth, B., Holliman, N.S., Imber, J., Waggott, S., and Wilson, R.W., 2005, Mapping and analysing virtual outcrops, *Visual Geosciences*, *10*(1), 13–19, doi:10.1007/s10069-005-0026-9.

Vasuki, Y., Holden, E.-J., Kovesi, P., and Micklethwaite, S., 2014, Semi-automatic mapping of geological structures using uav-based photogrammetric data: an image analysis approach, *Computers and Geosciences*, *69*, 22–32, doi:10.1016/j.cageo.2014.04.012.

Vasuki, Y., Holden, E.-J., Kovesi, P., and Micklethwaite, S., 2017, An interactive image segmentation method for lithological boundary detection: a rapid mapping tool for geologists, *Computers & Geosciences*, *100*(May 2016), 27–40, doi:10.1016/j.cageo.2016.12.001.

Vollgger, S.A., and Cruden, A.R., 2016, Mapping folds and fractures in basement and cover rocks using uav photogrammetry, Cape Liptrap and Cape Paterson, Victoria, Australia, *Journal of Structural Geology*, *85*, 168–187, doi:10.1016/j.jsg.2016.02.012.

Weleschuk, Z., 2015, *Sedimentology and stratigraphic architecture of late Cretaceous meander belt deposits, Dinosaur Park Formation [B.Sc. Thesis]*. University of Calgary

Westoby, M.J., Brasington, J., Glasser, N.F., Hambrey, M.J., and Reynolds, J.M., 2012, "Structure-from-motion" photogrammetry: a low-cost, effective tool for geoscience applications, *Geomorphology*, *179*, 300–314, doi:10.1016/j.geomorph.2012.08.021.

Whitehead, K., and Hugenholtz, C.H., 2014, Remote sensing of the environment with small unmanned aircraft systems (uass), part 1: a review of progress and challenges, *Journal of Unmanned Vehicle Systems*, *2*, 1–17, doi:10.1139/juvs-2014-0007.

Whitehead, K., and Hugenholtz, C.H., 2015, Applying asprs accuracy standards to surveys from small unmanned aircraft systems (uas), *Photogrammetric Engineering & Remote Sensing*, *81*(10), 787–793, doi:10.14358/PERS.81.10.787.

Whitehead, K., Hugenholtz, C.H., Myshak, S., Brown, O.W., LeClair, A., Tamminga, A.D., Barchyn, T.E., Moorman, B.J., and Eaton, B.C., 2014, Remote sensing of the environment with small unmanned aircraft systems (uass), part 2: scientific and commercial applications 1, *Journal of Unmanned Vehicle Systems*, *2*(3), 86–102, doi:10.1139/juvs-2014-0007.

Whitehead, K., Moorman, B.J., and Hugenholtz, C.H., 2013, Brief communication: low-cost, on-demand aerial photogrammetry for glaciological measurement, *The*

Cryosphere, *7*(6), 1879–1884, doi:10.5194/tc-7-1879-2013.

Wolf, P.R., and Dewitt, B.A., 2000, *Elements of photogrammetry: with applications in gis*. New York: McGraw-Hill.

Wood, J.M., 1989, Alluvial architecture of the upper Cretaceous Judith River Formation, Dinosaur Provincial Park, Alberta, Canada, *Bulletin of Canadian Petroleum Geology*, *37*(2), 169–181,

Wood, J.M., Thomas, R.G., and Visser, J., 1988, Fluvial processes and vertebrate taphonomy: the upper Cretaceous Judith River Formation, south-central Dinosaur Provincial Park, Alberta, Canada, *Palaeogeography, Palaeoclimatology, Palaeoecology*, *66*(1–2), 127–143, doi:10.1016/0031-0182(88)90085-5.

Xu, X., Aiken, C.L. V., Bhattacharya, J.P., Corbeanu, M., Nielsen, K.C., McMechan, G.A., and Abdelsalam, M.G., 2000, Creating virtual 3-d outcrop, *The Leading Edge*, *9*(c), 197–202,

Zahm, C., Lambert, J., and Kerans, C., 2016, Use of unmanned aerial vehicles (uavs) to create digital outcrop models: an example from the Cretaceous Cow Creek Formation, central Texas., *GCAGS Journal*, *5*(December), 180–188,

Chapter 3

Enhancing UAV-SfM 3D Model Accuracy in High-Relief Landscapes by Incorporating Oblique Images

A version of this chapter was published as:

Nesbit, P.R. and Hugenholtz, C.H. 2019. Enhancing UAV-SfM 3D model accuracy in high-relief landscapes by incorporating oblique images. *Remote Sensing*, 11 (239), p. 2469-2486. doi:10.3390/rs11030239.

3.1 Abstract

Complex landscapes with high topographic relief and intricate geometry present challenges for complete and accurate mapping of both lateral (x, y) and vertical (z) detail without deformation. Although small uninhabited/unmanned aerial vehicles (UAVs) paired with structure-from-motion (SfM) image processing has recently emerged as a popular solution for a range of mapping applications, common image acquisition and processing strategies can result in surface deformation along steep slopes within complex terrain. Incorporation of oblique (off-nadir) images into the UAV–SfM workflow has been shown to reduce systematic errors within resulting models, but there has been no consensus or documentation substantiating use of particular imaging angles. To address these limitations, we examined UAV–SfM models produced from image sets collected with various imaging angles (0–35°) within a high-relief 'badland' landscape and compared resulting surfaces with a reference dataset from a terrestrial laser scanner (TLS). More than 150 UAV–SfM scenarios were quantitatively evaluated to assess the effects of camera tilt angle, overlap, and imaging configuration on the precision and accuracy of the reconstructed terrain. Results indicate that imaging angle has a profound

impact on accuracy and precision for data acquisition with a single camera angle in topographically complex scenes. Results also confirm previous findings that supplementing nadir image blocks with oblique images in the UAV–SfM workflow consistently improves spatial accuracy and precision and reduces data gaps and systematic errors in the final point cloud. Subtle differences among various oblique camera angles and imaging patterns suggest that higher overlap and higher oblique camera angles (20–35°) increased precision and accuracy by nearly 50% relative to nadir-only image blocks. We conclude by presenting four recommendations for incorporating oblique images and adapting flight parameters to enhance 3D mapping applications with UAV–SfM in high-relief terrain.

3.2 Introduction

Uninhabited/unmanned aerial vehicles (UAVs) paired with structure-from-motion and multiview stereopsis (SfM–MVS) photogrammetric workflows (henceforth UAV–SfM) have become widely accepted tools for mapping and modeling in the geosciences (Harwin and Lucieer, 2012; Hugenholtz et al., 2012; Niethammer et al., 2012; Westoby et al., 2012; Fonstad et al., 2013; Bemis et al., 2014; Whitehead et al., 2014; Smith et al., 2015; Carrivick et al., 2016; Chesley et al., 2017). UAV–SfM workflows are particularly attractive because they can produce higher-resolution datasets (centimeter–decimeter) than conventional airborne and satellite sensors and can cover a larger area (10^4–10^6 m^2) than can practically be collected from ground-based techniques (Colomina and Molina, 2014; Toth and Jóźków, 2016; James et al., 2017a). In the geosciences, UAV–SfM workflows have been used to map laterally extensive planform landscapes (Bemis et al., 2014; Zahm et al., 2016; Chesley et al., 2017) and demonstrated the ability to map

inaccessible or dangerous areas, such as vertical cliff sections (Carvajal-Ramírez et al., 2016; Thoeni et al., 2016; Nieminski and Graham, 2017; Agüera-Vega et al., 2018). Though effective, a majority of these applications have centered on mapping a single two-dimensional (2D) plane. Complex landscapes, characterized by high-relief topography and intricate geometric morphology, require a deeper consideration of image collection and processing techniques to reduce data gaps and maintain accuracy and detail in both horizontal (x, y) and vertical (z) dimensions.

UAV data acquisition strategies are commonly modeled after conventional airborne photogrammetry (i.e., Mikhail et al., 2001; Wolf et al., 2014), in which an 'image block' is formed from parallel flight lines, flown in a 'lawnmower' or 'snaking' pattern at a stable altitude, with consistent overlap (frontlap and sidelap), and a nadir (or straight down)-facing camera angle (James and Robson, 2014; Martin et al., 2016). This classic gridded flight plan is straightforward and can be generated automatically by specifying a few basic flight parameters in modern flight planning software (e.g., Pix4Dcapture, DroneDeploy). However, these flight patterns take little account of a scene's 3D geometry (Martin et al., 2016). In particular, they are not ideal for recording features exposed along vertical façades (e.g., stratigraphic surfaces along a vertical cliff face) as these features are prone to greater deformation and/or chance of omission from nadir-view sensors (Dueholm and Olsen, 1993; Rittersbacher et al., 2014; Rossi et al., 2017).

Pragmatic solutions for capturing vertical façades from a UAV include adjusting the camera angle to collect images with the image plane roughly parallel to the feature of interest (Carvajal-Ramírez et al., 2016; O'Connor et al., 2017) and rotating the typical

image block so flight lines mirror the vertical plane. However, these single look-direction, gridded image blocks typically do not capture enough detail or geometric information in more complex scenes with features of interest extending in all directions (Vollgger and Cruden, 2016; Pavlis and Mason, 2017).

An alternative approach is to acquire oblique images in which the camera axis is intentionally angled ≥5.0° from nadir (Shufelt, 1999). Two common subcategories of oblique images are high-oblique images, which include the horizon, and low-oblique images, which do not (Verykokou and Ioannidis, 2018). Oblique images are commonly used in classic close-range photogrammetry and have recently been incorporated in UAV–SfM modeling of isolated 3D objects, such as archaeological structures or buildings (Aicardi et al., 2016; Vacca et al., 2017), for assessing building damage (Vetrivel et al., 2015), and inspecting transmission line towers/pylons (Jiang et al., 2017). Common survey methods involve a series of orbital flight patterns collecting inward-looking, low-oblique images at various altitudes, occasionally in conjunction with nadir images (Verhoeven et al., 2012; Aicardi et al., 2016). These data collection strategies may be suitable for *modeling* spatially constrained objects or outcrops (e.g., Cawood et al., 2017) for which orbital patterns may be easily obtained, but may not provide complete coverage for *mapping* extensive scenes with high-relief (e.g., cities, badlands).

Integration of oblique images into the photogrammetric workflow for mapping complex scenes is not a new issue and has been an appealing solution for urban applications in order to obtain complete coverage of both planar and façade features (Gerke, 2009; Nex et al., 2015; Rau et al., 2015; Ostrowski, 2016; Verykokou and Ioannidis, 2018). Research in this field commonly employs multisensor systems

containing four oblique and one nadir-facing camera (e.g., Maltese cross configuration), typically onboard piloted aircraft (Toth and Jóźków, 2016). Initial photogrammetric processing of these multiview angle images through aerial triangulation approaches produced unsatisfactory results, due to the complexity of oblique images, which contain vastly different-perspective viewing angles, large-scale differences within individual images, and occlusion of objects within a scene (Rupnik et al., 2014; Gerke et al., 2016; Ostrowski, 2016; Ostrowski and Bakuła, 2016). Development of unique processing solutions that maintain the rigorous standards of aerial triangulation while capitalizing on the advantages presented by airborne oblique views continues to be a key topic in photogrammetric research (Xie et al., 2016; Jiang and Jiang, 2017; Wu et al., 2018).

Alternatively, SfM–MVS processing solutions were developed to match features in images with different scales and viewpoints (Snavely et al., 2008; James and Robson, 2012; Westoby et al., 2012; Fonstad et al., 2013) and are well-suited for challenging datasets collected with low-flying UAVs (Colomina and Molina, 2014) and/or oblique images (James and Robson, 2014; Gerke et al., 2016; Ostrowski and Bakuła, 2016). Incorporation of oblique images into UAV–SfM datasets has been suggested as an approach to improve geologic mapping applications by providing more complete coverage, especially along steep slopes (Bemis et al., 2014; Vollgger and Cruden, 2016; Cawood et al., 2017; Nieminski and Graham, 2017; Nesbit et al., 2018).

Additionally, integration of oblique images with nadir image blocks can reduce the systematic deformation that is well-known to result from inaccurate modeling of internal camera geometry during self-calibrating bundle adjustment, in both conventional close-range photogrammetry (Luhmann and Robson, 2006; Wackrow and Chandler,

2008) and modern SfM–MVS photogrammetry (James and Robson, 2014; Eltner and Schneider, 2015; Harwin et al., 2015; Carbonneau and Dietrich, 2017; James et al., 2017a). Camera calibration is the determination of the internal geometry of a camera and has the most significant influence on the accuracy and reliability of photogrammetric measurements (Luhmann et al., 2016). SfM calibration approaches use a large number of automatically identified tie points, which provide redundancy in the solution. However, the high number of tie points may also impart a false sense of calibration quality (i.e., small reported errors) due to high internal consistency (Luhmann et al., 2016; Mosbrucker et al., 2017). Errors may remain undetected and propagate into final point locations in 3D object space. Furthermore, consumer digital cameras are currently the most commonly employed sensors on UAVs (Carrivick et al., 2016) and generally have unstable internal geometry that may fluctuate over time, perhaps as often as between image exposures (Nex and Remondino, 2014).

There are no simple solutions to solve the problem of instability in low-cost sensors (Fraser, 1997), but an accurate self-calibration through bundle adjustment (Brown, 1971) can improve results. Following well-proven rules for self-calibration can minimize observation errors and provide more accurate estimates of calibration parameters, enabling accurate and reliable measurements from almost any camera (Fraser, 1997; Luhmann and Robson, 2006; Remondino and Fraser, 2006; Wackrow and Chandler, 2008; Luhmann et al., 2016). These 'rules', as summarized by Luhmann et al. (2016), include:

1. Incorporate convergent images (i.e., oblique images) in the imaging network
2. Include diverse camera roll angles (i.e., landscape and portrait orientation)
3. Obtain images with sufficient variation in scale (i.e., depth variation in object/scene or images acquired at various distances/altitudes)
4. Image sets should have a high amount of redundancy in image content
5. Cameras should be set to a fixed zoom/focus and aperture settings

Although use of oblique images in UAV–SfM workflows has been shown to improve resulting outputs, applications within high-relief terrain have been sparse and there is no consensus or documentation substantiating use of particular oblique camera angles (Table 3.1).

Table 3.1. Recommended oblique image angles for supplementing structure-from-motion (SfM) nadir image blocks from the literature.

Imaging Strategy	Author	Suggested Angle	Additional notes
Airborne UAV [1]	Bemis et al. (2014)	10–20°	
	James and Robson (2014)	20–30°	
	Markelin et al. (2014)	25–30°	
	Harwin et al. (2015)	45–65°	
	Carbonneau and Dietrich (2017)	20–45°	>10% of image sets
	Carvajal-Ramirez et al. (2016)	35°	Orthogonal to surface
	James et al. (2017b)	20°	
	Rossi et al. (2017)	60°	Orthogonal to surface
	Agüera-Vega et al. (2018)	45°	
Ground-based	Moreels and Perona (2007)	<25–30°	Angle of incidence >40°
	Gienko and Terry (2014)	<20°	
	James and Robson (2014)	10–20°	
	Stumpf et al. (2015)	<30°	
Multicam	Fritsch and Rothermel (2013)	45°	Higher angles of intersection are optimal
	Rupnik et al. (2015)	35 or 45°	Higher tilt angle was more robust but more susceptible to occlusions

[1] Uninhabited/unmanned Aerial Vehicle.

To evaluate how imaging angle influences accuracy and detail of UAV–SfM 3D outputs, we compared more than 150 scenarios with various combinations of oblique and nadir camera angles, image overlap settings, and flight line orientations to a reference dataset collected with a terrestrial laser scanner (TLS). Datasets were collected in a section of Dinosaur Provincial Park (southeastern Alberta, Canada) with a complex array of diverse slope gradients ranging from flat to nearly vertical and a maximum elevation gain of ~20 m. This paper builds on previous work (James and Robson, 2014; Nesbit et al., 2018) to quantitatively evaluate UAV–SfM datasets processed from (1) nadir-only image blocks, (2) image blocks collected with a single oblique camera angle (05–35°), and (3) combinations of nadir image blocks supplemented with various oblique image configurations and angles. Results empirically demonstrate the benefits of including oblique images as part of a UAV image network to reduce systematic errors and increase detailed coverage of steep slopes.

3.3 Materials and Methods

3.3.1 Study site

To develop the test dataset, we performed a series of UAV flights over 'badland' terrain associated with high drainage density. The site was located in Dinosaur Provincial Park (Figure 3.1A)—a UNESCO World Heritage site containing fossil-rich deposits from the Late Cretaceous Dinosaur Park and Oldman formations (Wood, 1989). The incised topography, which initiated during deglaciation of the Laurentide Ice Sheet, reveals laterally continuous layers of siltstone and fine-to-medium-grained sandstone deposited by meandering channel belts (Campbell, 1970; Rains et al., 1993; Durkin et al., 2015; Nesbit et al., 2018). To test UAV–SfM data collection and processing strategies, a

representative section of the park was selected that contains a wide range of slope azimuths and gradients (20° mean slope), multiple changes in relief (~20 m maximum), and limited vegetation cover (Figure 3.1).

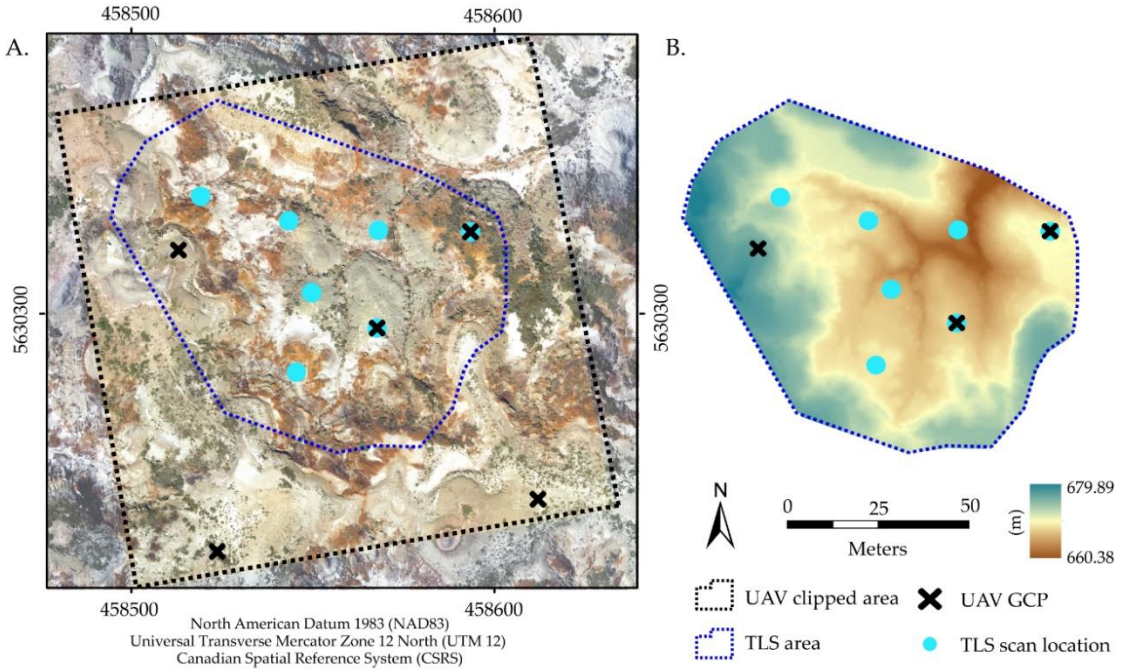

Figure 3.1. (A) Field location with UAV and terrestrial laser scanner (TLS) data extents, ground control points (GCPs), and TLS scan locations; (B) digital surface model (DSM) of the field area used for data assessment.

3.3.2 UAV data collection

UAV images were collected using a DJI Phantom 3 Professional quadcopter equipped standard with a 1/2.3" complementary metal oxide semiconductor (CMOS) sensor with 12 megapixels. The camera has a 20-mm focal length (35 mm equivalent), and a nadir image records an approximate ground footprint of 87 m × 65 m at a flying height of 50 m above ground level. This UAV records geolocation (x, y, z) to a

manufacturer-stated accuracy of ±1.5 m (horizontal) and ±0.5 m (vertical) (https://www.dji.com/phantom-3-pro/info; accessed 22 January 2019), though operational conditions may be less precise (Rosenberg, 2009). The Phantom 3 Professional was selected because the camera is mounted on a three-axis gimbal that can be programmed to capture images between 0–90° and record the roll, pitch, and yaw (stated accuracy ±0.02°) relative to the flight lines of the aircraft. UAV image sets were collected over the same 125 m × 125 m footprint. UAV image blocks were pre-programmed using the freely available Pix4Dcapture application for iOS, with consistent settings for flight area, altitude (40 m above take off), and overlap (90/90 frontlap/sidelap). Pix4Dcapture also allows the user to select the camera angle for data collection, which was adjusted at 05° increments for each flight ranging from 00° (nadir) to 35° off-nadir. Higher imaging angles (e.g., 45°) were not considered in this study because SfM image-matching algorithms can be unreliable and/or camera calibration can fail with large perspective differences (Bemis et al., 2014; Verykokou and Ioannidis, 2016; Wu et al., 2018).

Each camera angle was applied for an entire image block with flight lines oriented north–south (NS), followed by a separate flight with flight lines oriented east–west (EW), creating a ‘cross-hatch’, or double-grid, image block. This resulted in 16 total image sets consisting of 231 images each. Uncontrolled variables, notably lighting conditions, were accounted for by flying during optimal (diffuse) lighting conditions whenever possible; however, natural variations and changes in cloud cover and sun angle did occur and were noted. A set of five ground control points (GCPs) were distributed throughout the field site and measured at subcentimeter precision with a Trimble R4 real-time kinematic global navigation satellite system (RTK-GNSS) and used in image processing.

3.3.3 UAV processing and scenarios

Pix4Dmapper commercial software was used to process all scenarios following steps outlined by (Kung et al., 2012; Nesbit et al., 2018) on a high-performance computer (Intel® Core™ i9-7900X CPU @ 3.30 GHz with 64 GB RAM and an NVIDIA GeForce GTX 1080 graphics card). Scenarios were created with variations to camera angle, changes to image overlap, different flight line directions, and combinations of nadir and oblique image sets. Image blocks collected with oblique camera angles formed convergent imaging geometry with alternating flight lines containing camera angles posed in opposing directions. To emulate lower overlap settings, images in the original image block were selectively removed so every third image and/or flight line were retained, resulting in overlap settings of 90/70 and 70/70, respectively. Image blocks composed of both NS and EW flight lines combined (NSEW) were processed for each individual camera angle (0–35°) and overlap scenario (90/90, 90/70, and 70/70).

We also evaluated dataset combinations of the scenarios above based on suggestions from the literature for ideal imaging geometry and practical flight plans with common UAVs (e.g., James and Robson, 2014). Combinations included standard nadir-facing image blocks with various overlap and flight line settings supplemented with images selected from oblique image sets to match suggested flight patterns (Figure 3.2 and Table 3.2). Combination datasets included oblique images facing inward in (1) a box around the perimeter of nadir flight lines (Figure 3.2A; 'BoxO'); (2) a box around the center of the nadir flight lines (Figure 3.2B; 'BoxI'); (3) a combination of both boxes (Figure 3.2C; 'BoxIO'); single convergent arcs (Figure 3.2D); and double convergent arcs (Figure 3.2E).

Table 3.2. UAV–SfM processing scenarios.

	Overlap	Image Pattern [1]	Camera Angles
Single camera angle	90/90 or 90/70 or 70/70	Image block (parallel flight lines)	0–35°
Combination datasets	90/70 or 70/70	BoxO BoxI BoxIO Single arcs Double arcs	Image block at nadir + image pattern collected with an oblique camera angle (5–35°)

[1] See Figure 3.2 for description of combination patterns.

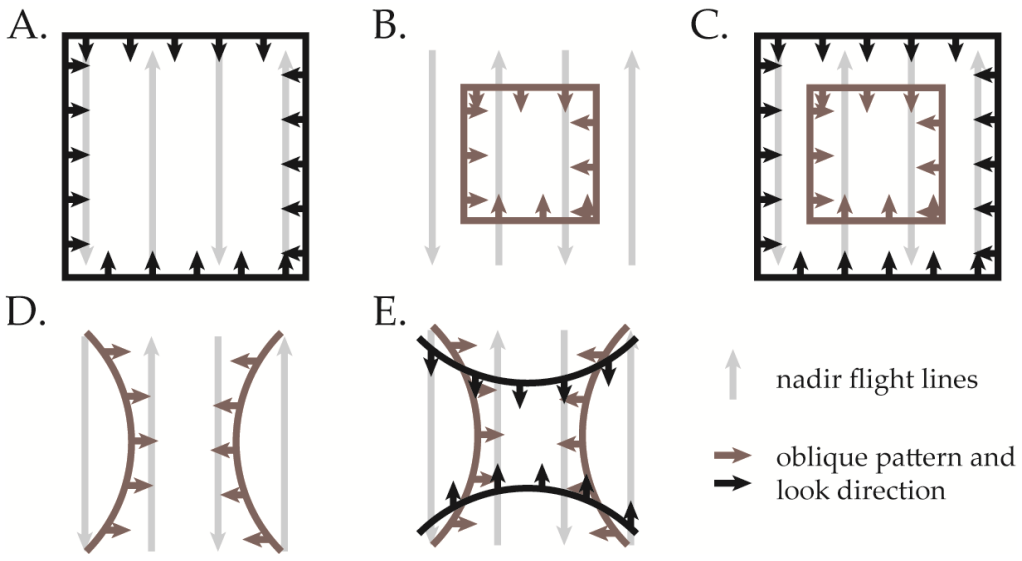

Figure 3.2. Oblique combination scenarios (A) outside box, BoxO; (B) inside box, BoxI; (C) inside and outside box, BoxIO; (D) single convergent arcs; (E) double convergent arcs. Note light-grey lines represent north–south (NS) nadir image flight lines.

To ensure comparability among imaging scenarios, a consistent processing area was defined, a common GCP marking strategy used, and consistent processing settings applied. Initial image sets (90/90 overlap and both NS and EW flight lines) were imported for each camera angle and georeferenced by manually marking GCPs in every

photo in which they clearly appeared. Images were then removed from the initial datasets to setup the scenarios described in the paragraphs above (Figure 3.2) and reprocessed using consistent processing settings for each scenario (Table 3.3). Processing included self-calibrating bundle block adjustment using camera internal orientation parameters: principal distance (focal length), principal point (x, y), and lens distortion terms (three radial [R1, R2, R3] and two tangential [T1, T2]) and camera external orientation parameters (location [x, y, z] and orientation [roll, pitch, yaw]). Appropriate weighting of image and GCP locations (precisions) within processing is crucial for obtaining accurate and repeatable SfM–MVS reconstructions, yet are seldom (if ever) reported in geoscience applications (James et al., 2017a). Precision of GCPs were defined according to instrument precisions: 0.005 and 0.010 m (horizontal and vertical) for GCPs surveyed with RTK-GNSS and a conservative 5 m and 10 m (horizontal and vertical) for UAV geotagged images.

Table 3.3. Processing settings in Pix4Dmapper selected for all UAV–SfM scenarios.

Step	Processing Option	Setting
1. Initial processing	Keypoint image scale	Full
	Matching image pairs	Aerial grid or corridor
	Calibration	Standard (AAT [1], BBA [2], camera self-calibration)
2. Point cloud densification	Image scale	1 (original image size, slow)
	Point density	Multiscale Optimal
	Minimum number of matches	4
	Matching window size	9 × 9 pixels

[1] Automatic aerial triangulation (AAT); [2] Bundle block adjustment.

Resulting UAV–SfM datasets had an expected ground sample distance (GSD) of 1.75–2.91 cm/pixel. Variation in GSD is caused by (1) variation of scale within individual oblique images and (2) flying height relative to underlying terrain. Pixels within an individual aerial oblique image will have a range of GSDs, such that pixels near the top of the tilted image have elongated (trapezoidal) footprints on the ground (Xie et al., 2016). Additionally, although UAV surveys maintained a fairly consistent altitude, 40 m above takeoff from the highest local point in the field area, UAV altitude above ground level (AGL) varied up to an additional 20 m due to undulating terrain, resulting in a variation to relative flying height ranging from 40–60 m AGL. Dense point clouds produced during intermediate UAV–SfM processing steps were used for comparison (see Section 2.5 below) and had an average point spacing of 0.035–0.051 m (70/70 overlap scenarios) and 0.019–0.032 m (90/70 overlap scenarios).

A recent survey of published geoscience literature reported the ratio of root mean squared error (RMSE):viewing distance for more than 40 investigations and found a median ratio of ~1:640 (Smith and Vericat, 2015). Within our datasets, this would produce expected precisions ranging from 0.063–0.094 m. However, UAV–SfM combination scenarios, which include oblique images, should produce higher-precision datasets as a result of stronger image network geometry. As a result, we expect precisions to exceed this ratio and range from 0.04–0.06 m (~1:1000, precision:viewing distance), as achieved by James and Robson (2012).

3.3.4 Reference data acquisition and processing

Reference data were recorded with a FARO Focus^{3D} S120 TLS, also referred to as ground-based light detection and ranging (LiDAR). This TLS can record up to 976,000

points per second using a phase-based laser (905-nm wavelength) and has a precision of 0.01 m at a scan distance of 50 m (https://doarch332.files.wordpress.com/2013/11/e866_faro_laser_scanner_focus3d_manual_en.pdf, accessed 22 January 2019). Laser scanners are capable of recording high-precision point measurements in 3D space, but are susceptible to data gaps in locations not in direct line-of-sight of the scanner. Therefore, to avoid occlusions and data gaps around the scene, a total of six scans were acquired from various perspectives within the 7240 m^2 field area. Each scan location, along with 25 checkerboard targets distributed throughout the field area, were recorded using the RTK-GNSS system described above and incorporated into scan coregistration and georeferencing processes.

Each TLS scan was individually imported, processed, and georeferenced within FARO Scene 7.1.1.81 software. Initial scan locations (applied from RTK-GNSS) and orientation information (from integrated sensors) were refined by manual identification of at least four checkerboard targets appearing in multiple TLS scans. Fine registration was then performed using cloud-to-cloud registration of all TLS datasets and then merged into a single point cloud. A final alignment and optimization was performed to fit the merged point cloud to RTK-GNSS control points, resulting in a final registration error of 0.013 m, approximately half the size of the expected GSD within UAV–SfM models. Points were filtered to remove any colocated points within 0.002 m of another point, resulting in a merged point cloud of 231 million points. This point cloud was filtered to remove vegetation using the CANUPO plugin (Brodu and Lague, 2012) in the open source CloudCompare software (CloudCompare, 2019). Vegetation was removed due to the added uncertainty in point cloud datasets and issues known in UAV–SfM reconstruction

(Dandois and Ellis, 2010, 2013), creating a final reference dataset of 186 million points with an average point spacing of 0.004 m.

3.3.5 Point cloud accuracy

Several methods have been used to validate SfM–MVS accuracy in the geosciences, with point-based metrics, such as RMSE and mean absolute error (MAE), being the most common. Though point measurements can be extremely precise, spatial variability of errors may remain imperceptible without sufficient number and distribution of validation points (Smith and Vericat, 2015). Surface-to-surface comparisons have been used to document the changes between two continuous surfaces, such as digital elevation models (DEMs). DEMs are 2.5D interpolations with a single elevation (z) attribute for each planar (x, y) location that may reveal spatial variability, but can also result in overgeneralization and degradation of highly three-dimensional landscapes (Lague et al., 2013; Carbonneau and Dietrich, 2017; James et al., 2017b; Nesbit et al., 2018).

To assess the accuracy of the various UAV–SfM processing scenarios in our topographically complex field area, we use the freely available Multiscale Model to Model Cloud Comparison (M3C2) plugin for open-source CloudCompare software (Lague et al., 2013). M3C2 calculates local differences between two point clouds relative to local surface normal orientation and point cloud roughness. Normal orientations are locally calculated by averaging points within a user-defined radius (D/2) in the reference point cloud (PC_1). A cylinder with user-defined radius (d/2) is then projected along the normal direction (N) to specify the search space on the target point cloud (PC_2). The algorithm then calculates the average position of points within the cylinder for both PC_1 and PC_2 and calculates the local difference between the two positions. To limit the

influence of point cloud roughness on difference calculations, D was defined as 0.1 m, following recommendations to define D as >20 to 25 times the average local roughness (Lague et al., 2013) and methods in (Bash et al., 2018). A subsample of the TLS reference cloud was created using 10% of the point cloud and used to compare all UAV–SfM point clouds with a consistent reference dataset. M3C2 distances between point clouds were calculated between the TLS reference point cloud (0.004 m average point spacing) and UAV–SfM point clouds (0.019–0.051 m average point spacing). Calculations were carried out by differencing UAV–SfM point clouds from the TLS reference point cloud, with negative distances indicating that the TLS surface was above the UAV–SfM surface and positive values signifying that the UAV–SfM surface was above the reference TLS surface.

3.4 Results

3.4.1 Single camera angle and single flight direction

Images collected along a single flight line orientation (NS or EW) generally resulted in inconsistent coverage, especially along the perimeter of the field area, and substantial data gaps (up to 14 × 8 m) within point clouds. Data gaps due to insufficient coverage typically occurred along steep slopes in different locations throughout the field area, dependent on the flight line orientation and camera tilt angle during acquisition. Due to incomplete coverage and shifting data gap locations, single flight line datasets were considered unsuitable for comparison and removed from further analysis. However, datasets that combined NS and EW flight lines into 'cross-hatch' (NSEW) datasets and/or included supplemental oblique images in various patterns (Figure 3.2) resulted in reduced data gaps. Readers should note that data gaps occurring in the same locations of the

remaining analyses were the expected result of vegetation removal from the TLS reference point cloud (Section 2.4).

3.4.2 Single camera angle and cross-hatch flight lines

Image blocks collected with a single camera angle and cross-hatch flight lines produced complete datasets with smaller data gaps for all overlap scenarios (70/70, 90/70, and 90/90). Datasets collected with a single camera angle always resulted in higher standard deviations (lower precision) of M3C2 distance measurements between UAV–SfM and TLS models than combination datasets (Figure 3.3A) and usually had means further from 0 (lower accuracy) than combination datasets (Figure 3.3B). Single-angle datasets with high tilt angles (25–35°) had mean values similar to or smaller than combination datasets (Figure 3.3B). High tilt angles usually resulted in standard deviations lower than nadir-only datasets and higher than combination datasets (Figure 3.3A).

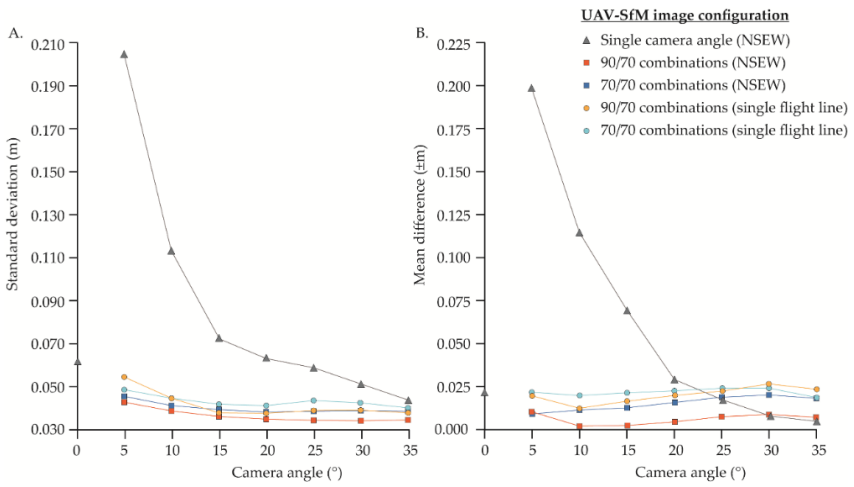

Figure 3.3. Average M3C2-calculated difference between TLS reference dataset and various UAV–SfM image configurations; (A) standard deviation (precision); (B) mean difference (accuracy). M3C2: Multiscale Model to Model Cloud Comparison; NSEW: NS and EW flight lines combined.

Within single-angle datasets (Figure 3.4), overlap did not have a direct relationship with precision (i.e., increasing overlap did not always increase precision). Increasing overlap from 70/70 to 90/70 resulted in better precision for most datasets, but increasing from 90/70 to 90/90 resulted in lower precisions, except for the nadir and 05° datasets (Figure 3.4A). Increasing overlap for single-angle datasets had a direct relationship with mean values (Figure 3.4B); lower overlap (70/70) resulted in smaller mean values, while high overlap (90/70 and 90/90) produced larger mean values for all camera angles. Regardless of camera angle, high-overlap scenarios consistently resulted in higher point counts. Among datasets with similar overlap, increasing camera angle always resulted in lower standard deviations and smaller mean values, with the exception of nadir-only image blocks (Figure 3.4). Nadir-only datasets had lower standard deviations and smaller means than all other single-angle datasets, except for high oblique angles (30–35°), which outperformed all nadir-only datasets regardless of overlap (Figure 3.4). Increasing camera angle typically resulted in decreasing point counts, with nadir-only image blocks containing the most points among similar overlap scenarios.

Although nadir-only datasets generally had higher point counts, higher precision, and mean values closer to 0, the spatial distribution of difference values reveals a systematic pattern of errors (Figure 3.5). This pattern represents UAV–SfM underestimation of height values of high elevation points (near the perimeter of the scene) and overestimation of low elevation points (near the center of the scene) in nadir-only image blocks. All single-angleblique datasets may also contain a systematic error pattern (Figure 3.6). Most evident in lower oblique angles (05–15°), this pattern contains differences in which lows are too low and highs are too high.

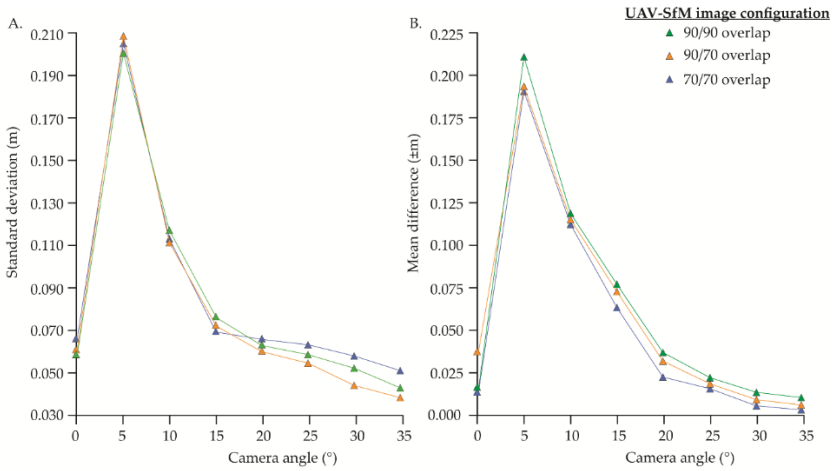

Figure 3.4. M3C2-calculated difference between TLS reference dataset and UAV–SfM image configurations collected with a single camera angle and various image overlap settings (70/70, 90/70, and 90/90) with cross-hatch flight lines (NSEW); (A) standard deviation (precision); (B) mean difference (accuracy).

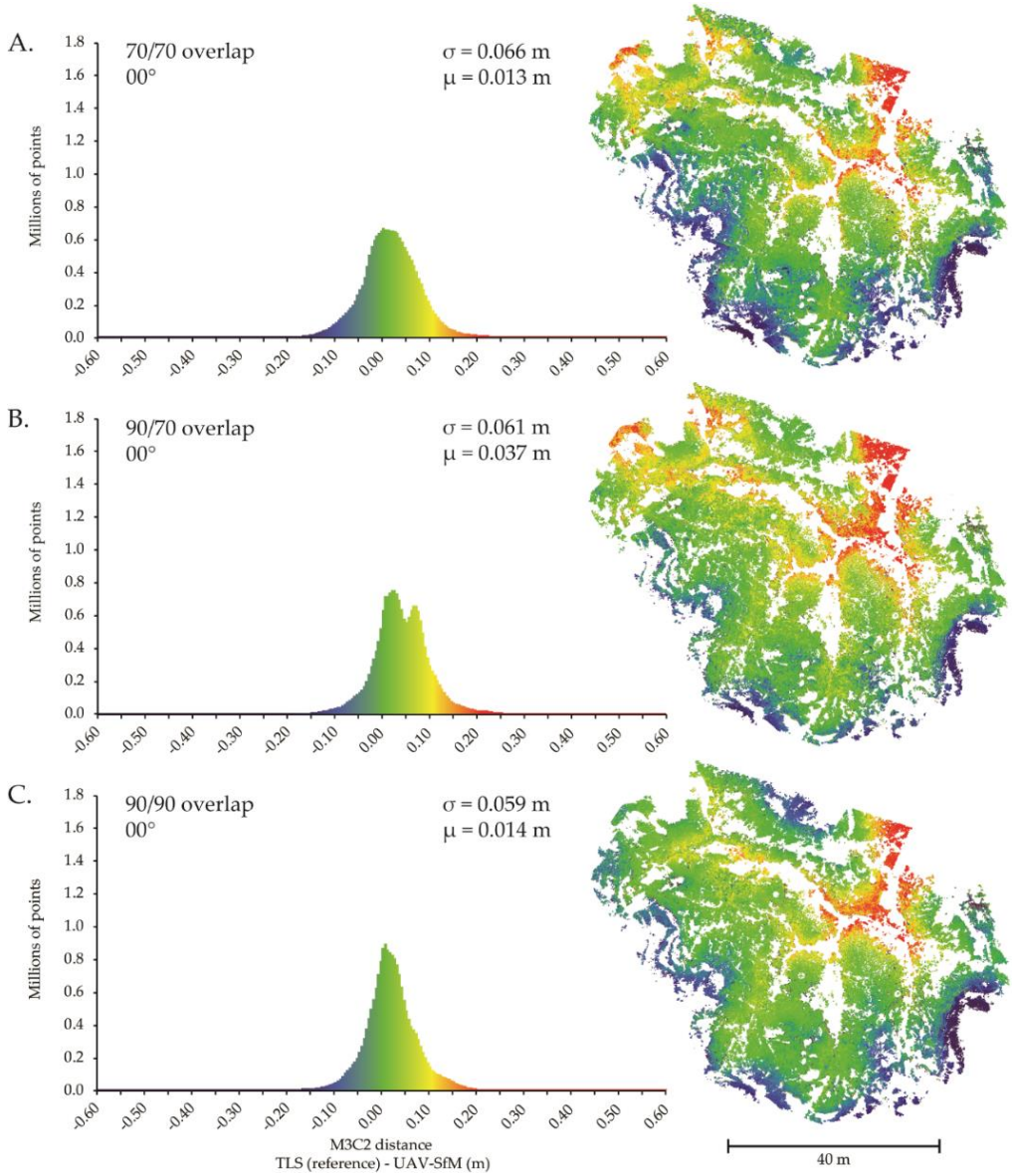

Figure 3.5. M3C2-calculated distance between TLS reference dataset and UAV–SfM data sets collected with nadir camera angles and cross-hatch flight lines (NSEW) with various image overlap settings: (A) 70/70, (B) 90/70, and (C) 90/90. Positive values indicate UAV–SfM surface above TLS reference surface; negative values suggest UAV–SfM surface below. Note the systematic distribution of error with low points (near the center of the field area) higher than the reference dataset and high points (near the perimeter of the field area) lower than the reference dataset. This systematic error is similar to that noted by James and Robson (2014) and is present regardless of overlap.

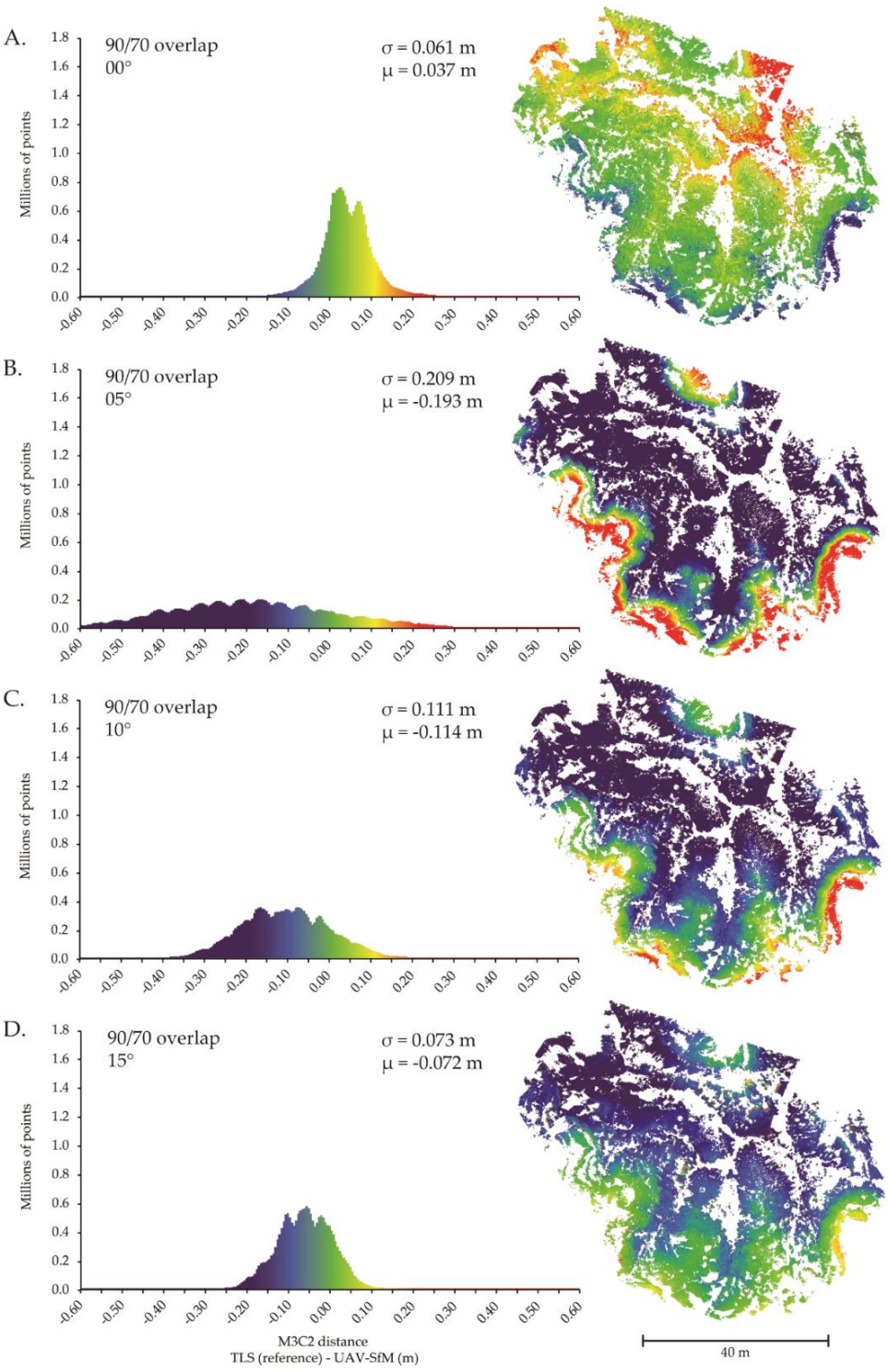
A.
90/70 overlap
00°
σ = 0.061 m
μ = 0.037 m
B.
90/70 overlap
05°
σ = 0.209 m
μ = -0.193 m
C.
90/70 overlap
10°
σ = 0.111 m
μ = -0.114 m
D.
90/70 overlap
15°
σ = 0.073 m
μ = -0.072 m
Millions of points
0.0
0.2
0.4
0.6
0.8
1.0
1.2
1.4
1.6
1.8
-0.60
-0.50
-0.40
-0.30
-0.20
-0.10
0.00
0.10
0.20
0.30
0.40
0.50
0.60
M3C2 distance
TLS (reference) - UAV-SfM (m)
40 m

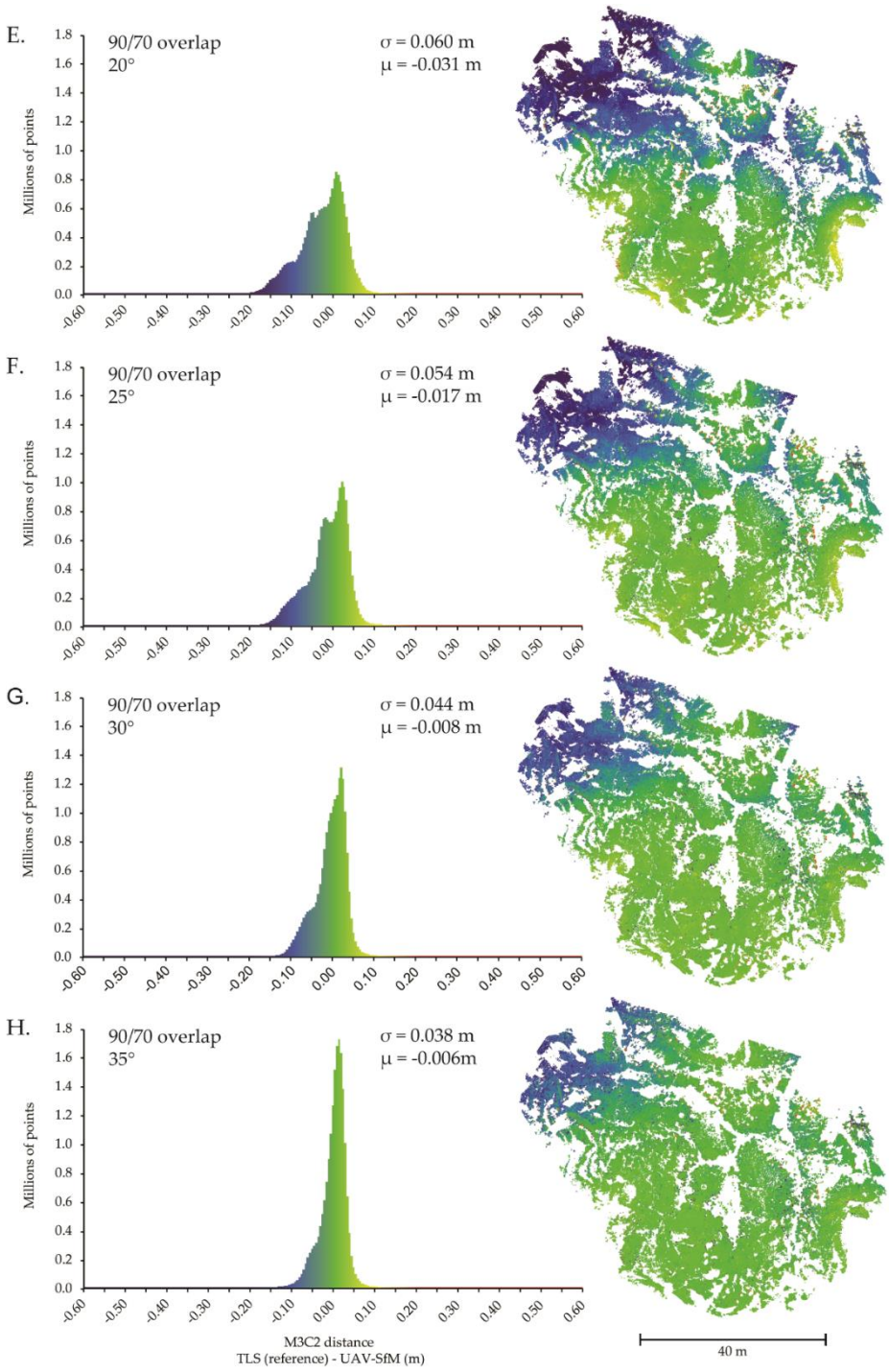

Figure 3.6. M3C2-calculated distance between TLS reference dataset and UAV–SfM image sets collected with 90/70 overlap, cross-hatch flight lines (NSEW), and a single camera angle; (A) 00° (nadir); (B) 05°; (C) 10°; (D) 15°; (E) 20°; (F) 25°; (G) 30°; (H) 35°. Positive values indicate UAV–SfM surface above TLS reference surface; negative values suggest UAV–SfM surface below.

3.4.3 Nadir image block (NSEW) supplemented with oblique images

Inclusion of oblique images into nadir image blocks with cross-hatch (NSEW) flight lines diminished the systematic error present in nadir-only image blocks, regardless of oblique image angle and flight pattern (Figure 3.7). In each oblique combination scenario, precision and accuracy were better than or equal to any nadir-only dataset (Figure 3.3). Datasets incorporating oblique combinations had a maximum difference in precision of 0.027 m and absolute difference in accuracy of ±0.028 m. Among combination datasets, high-overlap scenarios typically had lower standard deviations than lower-overlap scenarios, regardless of oblique flight pattern (Figure 3.8A,B). Combinations that included high angles had smaller standard deviations in both 90/70 and 70/70 overlap scenarios. Combinations with supplemental oblique camera angles between 10–15° had the smallest means, while 25–30° were consistently further from 0 (Figure 3.8C,D). Nadir image blocks supplemented with oblique images always resulted in more points than any single-angle image block with similar overlap. Point increases for combination datasets (relative to nadir-only datasets) were typically greatest for oblique angles of 15° and smallest for angles of 35° (low-overlap scenario) or 5–10° (high-overlap scenario).

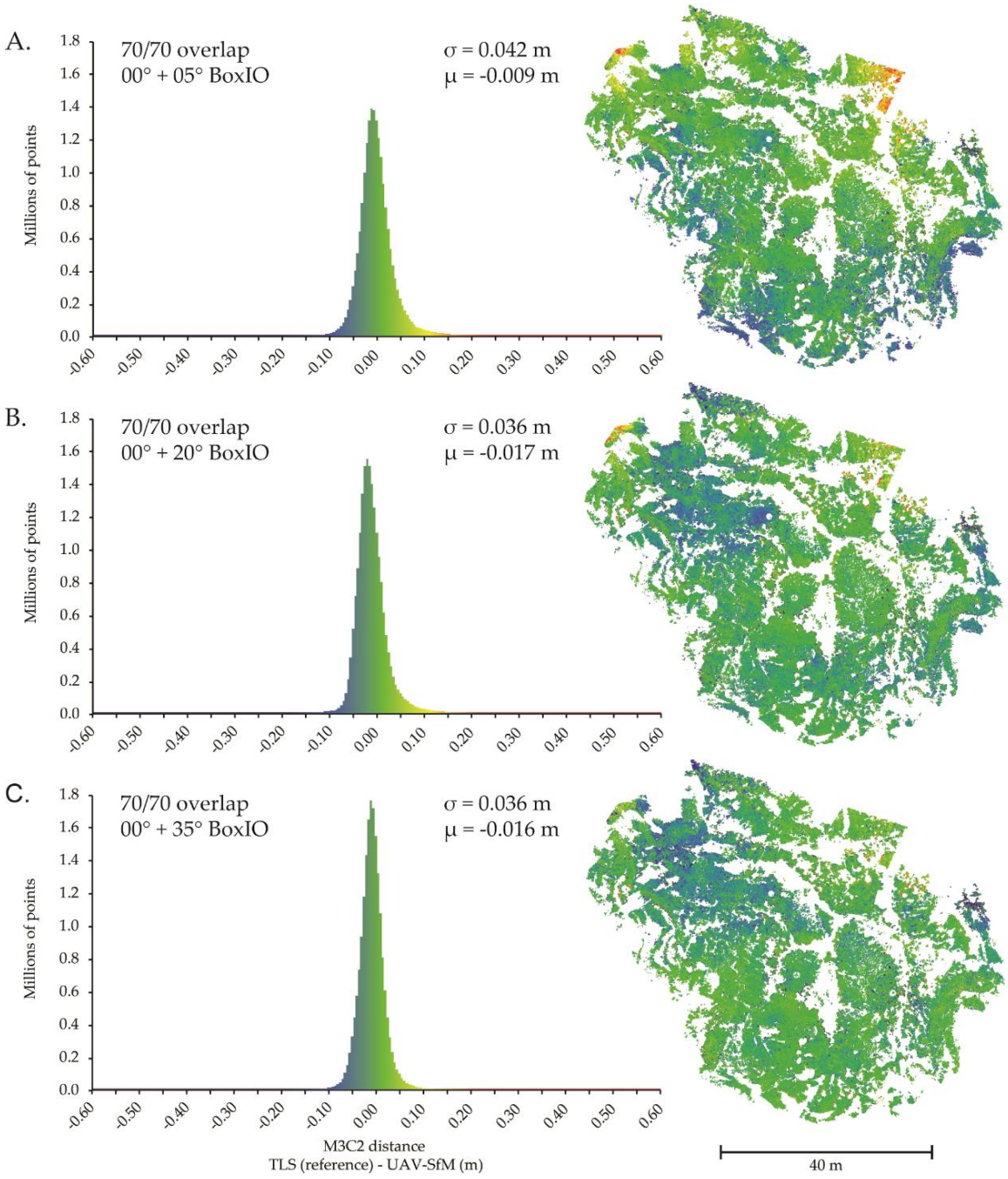
A.
70/70 overlap
00° + 05° BoxIO
σ = 0.042 m
μ = -0.009 m
B.
70/70 overlap
00° + 20° BoxIO
σ = 0.036 m
μ = -0.017 m
C.
70/70 overlap
00° + 35° BoxIO
σ = 0.036 m
μ = -0.016 m
Millions of points
0.0
0.2
0.4
0.6
0.8
1.0
1.2
1.4
1.6
1.8
-0.60
-0.50
-0.40
-0.30
-0.20
-0.10
0.00
0.10
0.20
0.30
0.40
0.50
0.60
M3C2 distance
TLS (reference) - UAV-SfM (m)
40 m

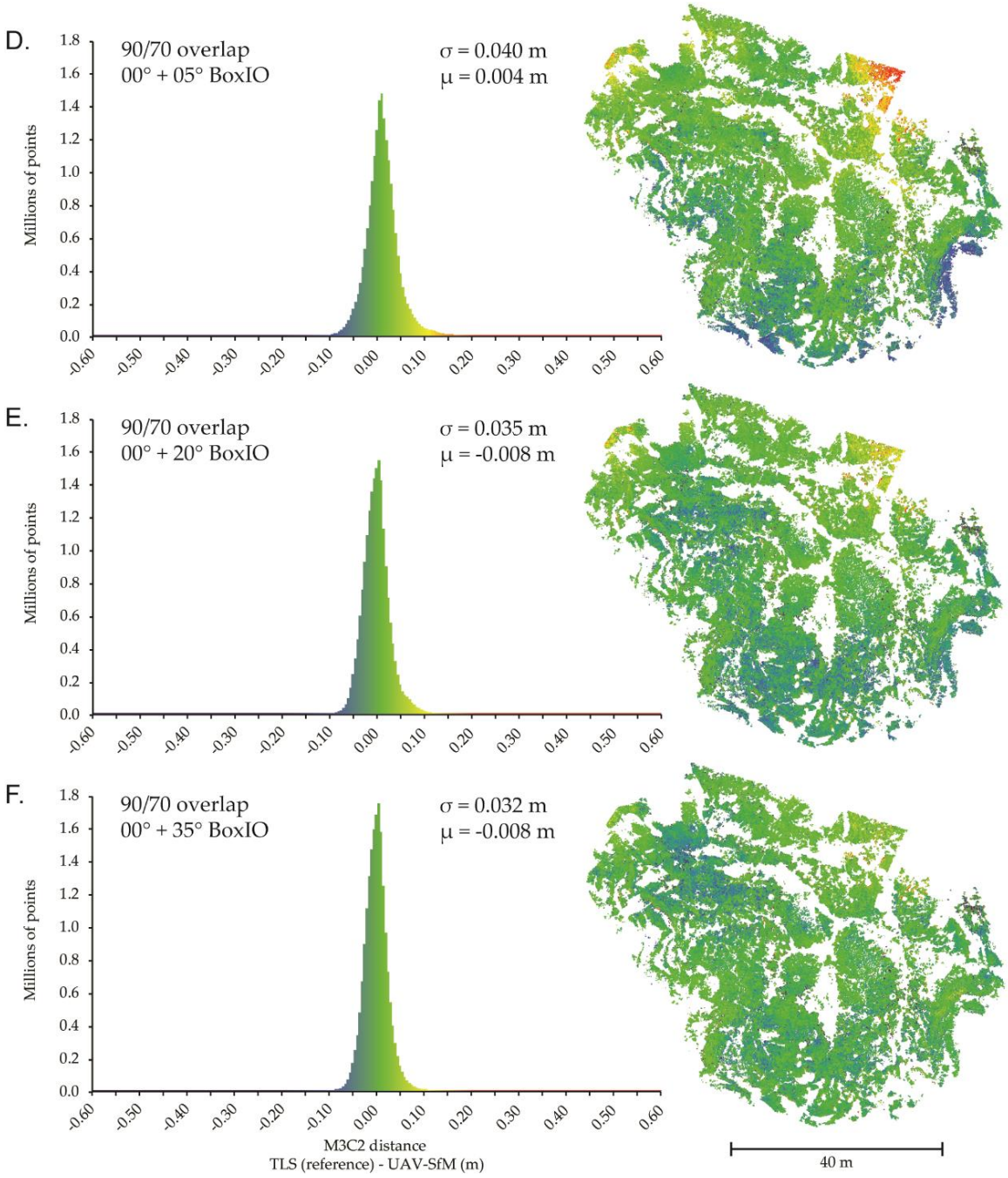

Figure 3.7. M3C2-calculated distance between TLS reference dataset and UAV–SfM combination image sets: (A) 70/70—05° BoxIO; (B) 70/70—20° BoxIO; (C) 70/70—35 ° BoxIO; (D) 90/70—05° BoxIO; (E) 90/70—20° BoxIO; (F) 90/70—35° BoxIO. See Figure 3.2 for description of flight patterns. Positive values indicate UAV–SfM surface above TLS reference surface; negative values suggest UAV–SfM surface below.

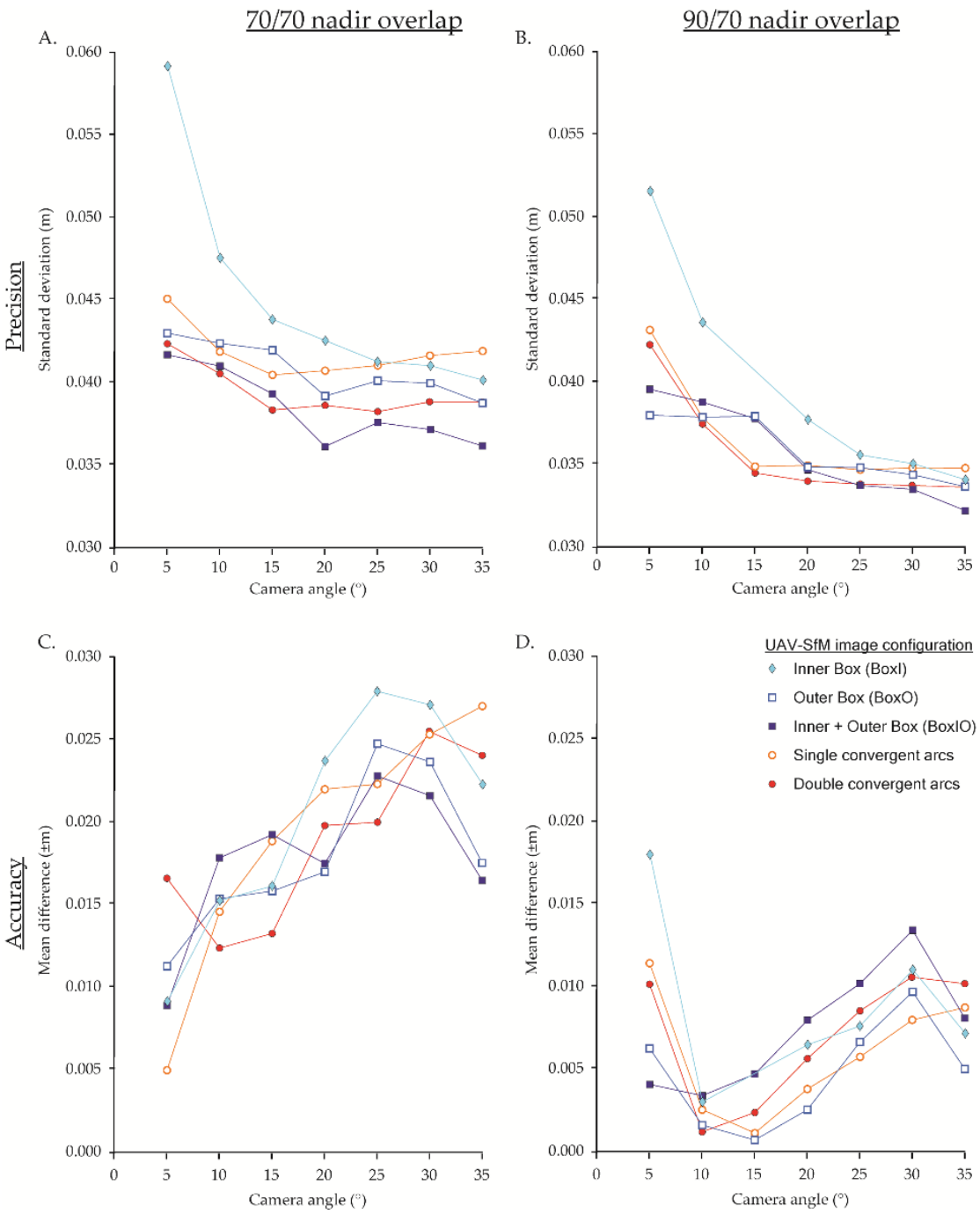

Figure 3.8. M3C2-calculated difference between TLS reference dataset and various UAV–SfM combination datasets with different image configurations: (A) standard deviation, 70/70 overlap combinations; (B) standard deviation, 90/70 overlap combinations; (C) mean difference, 70/70 overlap combinations; (D) mean difference, 90/70 overlap combinations. See Figure 3.2 for description of flight patterns.

3.4.4 Nadir image blocks (single flight line) supplemented with oblique images

Single flight direction (NS or EW) datasets supplemented with oblique images produced complete coverage and reduced data gaps compared to those without oblique images. Single flight direction datasets supplemented with oblique images had lower standard deviations than all nadir-only and most single oblique camera angle datasets (Figure 3.3A). Single flight line combinations generally had slightly lower precision (Figure 3.3A) and lower accuracy (Figure 3.3B) than cross-hatched flight line combinations with similar overlap. For oblique angles 15–35°, high-overlap (90/70) single flight line combinations had similar standard deviations to low-overlap (70/70) cross-hatched flight line combinations.

3.4.5 Combination datasets — flight pattern

Image configuration of supplemental oblique images had some effect on UAV–SfM dataset precision and accuracy (Figure 3.8). The inner box (BoxI) and single convergent arc patterns (Figure 3.2B,D, respectively) generally resulted in the highest standard deviations and means farthest from 0 compared to datasets with similar overlap and camera angle. Outer box (BoxO), inner/outer box (BoxIO), and double convergent arc patterns (Figure 3.2A,C,E) usually resulted in highest precisions; double convergent arcs were more effective for low angles (10–15°), while box patterns were slightly more effective for high angles (25–35°), particularly for the 70/70 overlap scenario (Figure 3.8A). Mean difference values were also affected by different oblique image configurations, although results were less consistent. Oblique flight patterns resulting in small means (closest to 0 m) varied considerably within the 70/70 overlap scenario (Figure 3.8C), while the 90/70 scenario typically had smallest means for single

convergent arcs and BoxO patterns and largest mean values for BoxIO and double convergent arc patterns (Figure 3.8D).

3.5 Discussion

Our results confirm the presence of systematic vertical deformations (i.e., 'dome effect'; James and Robson, 2014) within UAV–SfM datasets processed from parallel-axis (nadir) image blocks and further verify effective data acquisition strategies for mitigating such errors. We build upon recommended image acquisition strategies (e.g., James and Robson, 2014) by evaluating more than 150 scenarios and quantifying differences among various oblique imaging angles. Results indicate that imaging angle has a profound impact on accuracy and precision for data acquisition with a single camera angle (Figure 3.6) in topographically complex scenes. Combination scenarios generally revealed consistent improvements relative to nadir-only image blocks, regardless of oblique imaging angle and pattern. However, differences among oblique imaging patterns and camera angles for combination datasets only revealed subtle differences that do not decisively determine an optimal configuration for UAV–SfM applications in complex topographic landscapes.

Results are based on M3C2 distances, which are calculated in the direction of surface normals of the reference point cloud, rather than strictly vertical distances. Relating results and GCP residuals to the topography of the field site (Figure 3.1B) suggests that vertical error is more prevalent than horizontal. Differences between the TLS reference dataset and UAV–SfM datasets could be attributed to inconsistencies/deformation of reconstructed surface shape (relative accuracy), georeferencing errors (absolute accuracy), or a combination of both. Within this

investigation, TLS data was considered as the reference dataset because of its superior precision and a final georegistration error of 0.013 m. UAV–SfM datasets had resulting precisions more than a magnitude lower than the TLS, but GCP residuals in UAV–SfM datasets were generally comparable. This suggests that deviations between the TLS reference dataset and various UAV–SfM scenarios were primarily a result of differences in surface shape in the dense point clouds. Some datasets, however, exhibited large inconsistencies in both georeferencing and surface shape, most notably 05–10° (Figure 3.6B,C), which had vertical RMSE values up to 0.13 m.

3.5.1 Nadir-only image blocks

Nadir-only image blocks resulted in systematic 'dome' errors that can be attributed to inaccurate estimation of radial lens distortion from self-calibration of the relatively unstable, consumer-grade digital camera used on the UAV (James and Robson, 2014). Although this has been well-documented in the literature, nadir-only image blocks remain widespread UAV–SfM data collection strategies. Applications in the geosciences have often accounted for systematic doming by using well-dispersed and high-precision control points. However, as previously stated (James and Robson, 2014) and documented (James et al., 2017b, Figure 3.6A) and further confirmed by our results (Figure 3.5), use of GCPs does not guarantee that systematic vertical doming errors will be reduced to negligible levels.

Some authors have suggested that increasing overlap or including cross-strips in airborne image blocks can help reduce systematic errors due to higher redundancy (Gerke and Przybilla, 2016; Gerke et al., 2016). Others have noted that increased overlap results in shorter baselines (distance between adjacent photos) and subsequently narrower angles

of ray convergence, ultimately subjecting calculated object space locations to errors, especially in depth/height (Eltner and Schneider, 2015; James et al., 2017b). Our results suggest that increasing overlap may slightly lower the standard deviation in nadir-only scenarios (Figures 3.4 and 3.5), but an increase in the number of images does not linearly increase accuracy (Eltner et al., 2016) and systematic doming errors remained clearly visible, regardless of overlap (Figure 3.5).

3.5.2 Single oblique camera angle image blocks

Collecting image blocks with a single off-nadir camera angle has been recommended as an effective means for reducing systematic deformation (James and Robson, 2014); however, recommendations within the literature are not consistent (Table 3.1). Our results quantify the effects of different imaging angles on point cloud accuracy in high-relief landscapes. Lower oblique image angles between 0–15° (Figure 3.6B–D) clearly reveal a systematic error that also corresponds to lower precisions and means further from 0 m. However, deformation appears as a concave 'bowl' shape rather than a convex dome. Large GCP residuals in these datasets appear to contribute to the large discrepancies with the TLS reference through large mean offsets (Figure 3.6B–D); however, the wide range of values suggests that surface reconstruction is also contributing to errors relative to the reference data.

Based on these results, users should be cautioned against collecting full image sets at very low-oblique angles to the object of interest. Specifically, this may pertain to applications flown with a manual ‘free flight’ mode in which camera angles may be close, but not directly orthogonal to the surface. Additionally, data quality in manual flight modes is inherently reliant on the remote piloting skills of the operator and can

often result in notable data gaps, especially in complex landscapes (Martin et al., 2016). Increasing camera angle further off-nadir appears to mitigate the systematic bowl effect and increase precision and accuracy (Figure 3.6E–H). Precisions achieved with these single camera angle (20–35°) image blocks are similar to the 1:1000 ratio attained by James and Robson (2012), while lower oblique camera angles fail to achieve the ~1:640 ratio realized in Smith and Vericat (2015). It is worth considering that systematic errors may still be occurring outside our assessment area, but this is subject to future research considerations. Good GCP distribution appears specifically necessary for these single camera angle datasets, as the most prevalent errors consistently occur in the N–NW areas (Figure 3.6), outside the constraints of GCPs.

Collection of image blocks with single off-nadir camera angles is not a common practice in UAV or piloted aircraft image collection. These datasets resemble multicam image sets (one nadir and four 45° off-nadir sensors), which are growing in popularity in both conventional and SfM communities for mapping complex 3D scenes, such as cities. Multicams with oblique sensors are not yet widely available for UAVs and research on the capabilities of such imaging geometries is still developing. However, our results suggest that SfM software is capable of processing off-nadir image sets and may produce more optimal results than nadir-only image blocks.

3.5.3 Combination datasets

Our findings further confirm that supplementing parallel-axis (nadir) image blocks with oblique images reduces or eliminates systematic dome errors in UAV–SfM datasets, regardless of overlap, camera angle, and oblique image configuration (Figure 3.7). Combination datasets always resulted in more points produced, lower standard

deviations (higher precision), and had comparable or better mean values relative to nadir-only datasets (Figure 3.3). Nadir-only datasets consistently had precision:viewing distance ratios of ~1:1000, while nadir image blocks supplemented with oblique images produced ratios ~1:1500, regardless of oblique imaging pattern and overlap. Production of more points can be simply explained by a higher number of input images allowing for the calculation of more matching points within the final SfM model. Additionally, oblique images may obtain a better viewing angle of steep slopes that are not easily visible in nadir images, thus producing more potential matching points in both SfM and MVS steps. This is consistent with Vacca et al. (2017), who found tie point matching to be quite successful between nadir and oblique (45°) images.

Increasing camera tilt angle in combination datasets generally improved precision, but also resulted in lower accuracy (Figure 3.8). Lower oblique images (05–10°) have a similar perspective to nadir images and therefore may not provide substantial benefits for self-calibration due to narrow angles of intersection (parallactic angles). In contrast, inclusion of higher oblique camera angles resulted in larger parallactic angles (closer to 90°) known to be beneficial for self-calibration (Wolf et al., 2014; Eltner et al., 2016; Luhmann et al., 2016). Regardless of oblique tilt angle, higher-overlap scenarios typically resulted in higher precision and accuracy (Figure 3.3), which is likely a result of greater redundancy (i.e., more object points observed in more images). This is consistent with other studies (Remondino et al., 2014; Rupnik et al., 2015; Gerke et al., 2016) and the direct relationship between overlap and precision of nadir-only image blocks within this study (Figure 3.4A). In combination scenarios, accuracy may be adversely affected by the proportion of oblique images relative to nadir images used in SfM processing.

Suggestions from the literature indicate that oblique images should constitute ~10% of an image block (Carbonneau and Dietrich, 2017). Our results seem to show agreement with this suggestion, with higher-overlap image blocks (6.7–14.4% oblique images) typically producing better results than the lower-overlap scenarios (up to 33.3% oblique images); however, a more rigorous investigation on the impact of oblique image proportions within a given image block is warranted.

Imaging pattern of oblique images also appears to have an influence on precision and accuracy. Oblique image patterns with more images (e.g., BoxIO and double convergent arcs) consistently produced datasets with the highest precision (Figure 3.8A,B), but lowest accuracy (Figure 3.8C,D), especially in the higher overlap scenario. Higher precision and lowest accuracy may again be related to the proportion of oblique images, but we suspect that image locations also have a strong influence. For example, a 30° oblique image in BoxI may record ~40% of the field area, leaving more than half of the image frame unused in generating tie points, and as a result, tie point matches are concentrated in only a portion of the image frame, which is considered less than ideal for self-calibrating bundle adjustment (Luhmann and Robson, 2006). Conversely, a 30° oblique image in the BoxO pattern captures ~65% of the scene, and consequently, has the potential to produce more tie point matches and have a greater influence on camera calibration.

3.5.4 Cameras and calibration

Low-cost sensors commonly used in UAV applications, such as the one used in this study, are relatively unstable (Nex and Remondino, 2014; Carrivick et al., 2016) and common SfM processing solutions may give a false sense of quality while errors

propagate into the final model (Luhmann et al., 2016; Mosbrucker et al., 2017), as demonstrated in this investigation. Previous studies have thoroughly demonstrated the benefits of oblique images for camera calibration (Luhmann and Robson, 2006; James and Robson, 2014); however, obtaining an optimal image network for both calibration purposes and scene reconstruction is not always straightforward (Remondino and Fraser, 2006). Self-calibration can be performed prior to data acquisition (precalibration) or calculated simultaneously with 3D object space point coordinates ('on-the-job'). Remondino et al. (2011) suggested that a separation of calibration and scene reconstruction is preferable, but this assumes similar conditions between calibration and scene acquisition. In contrast, a direct comparison of pre- and 'on-the-job' self-calibration of UAV image blocks has yielded similar results (Harwin et al., 2015). Within this investigation, 'on-the-job' self-calibration with combination scenarios that included oblique images provided satisfactory results and improved precision relative to single camera angle datasets. Due to practical and logistical concerns, 'on-the-job' self-calibration is likely to remain the most applied method within geoscience research (James and Robson, 2014; Forlani et al., 2018).

Although cameras are continuously being produced in smaller sizes with improved resolution and stability, an accurate camera calibration will always be essential for reliable photogrammetric measurements. Many UAVs have the flexibility to facilitate improved calibration by collecting airborne images with varying orientations (e.g., multirotor platforms with gimbaled cameras, senseFly S.O.D.A. 3D (https://www.sensefly.com/camera/sensefly-s-o-d-a-3d/; accessed 22 January 2019). Therefore, we strongly urge practitioners employing UAV–SfM (and ground-based SfM)

methods to implement data collection strategies that consider the well-established 'rules' of self-calibration (Section 1), specifically items (1–3).

3.5.5 GCPs

Precise and well-distributed GCPs are important for obtaining accurate and reliable UAV–SfM models; GCPs define the absolute orientation and scale within an external coordinate system and provide constraints within the bundle adjustment (James and Robson, 2014; Rupnik et al., 2015; Eltner et al., 2016; James et al., 2017a). Our results show that GCPs are especially important for single camera angle datasets. The zone of weakness occurring in the NW corner of Figure 3.6E–H (peripheral to all GCPs) is a textbook example of the deficiencies that can result outside the surface constrained by GCPs. At a minimum, for accurate results, GCPs should be placed around the perimeter of the field area of interest (Luhmann and Robson, 2006); however, feasibility and accessibility may hinder GCP planning.

As a result, logistical and practical motivations are driving interests in a number of applications (e.g., geologic mapping) to reduce or completely omit the use of GCPs. Incorporation of oblique images should reduce the need for a dense network of precise GCPs (James et al., 2017a), particularly for constraining the bundle adjustment. Harwin et al. (2015) found that with fewer GCPs or lower precision measurements, oblique images were especially effective for improving camera calibration and resulting 3D model accuracy; however, more GCPs should be preferred. Combination datasets in this investigation (Figure 3.7) appear to reduce GCP requirements; in the NW zone of weakness (outside the GCP area), errors were reduced by nearly 50% in combination datasets (most notably in 90/70 overlap) relative to single camera angle datasets.

Although oblique images may reduce the need for GCPs, some control measurements are still recommended to add external constraints to the bundle adjustment along with providing absolute orientation.

Recent advances in UAV onboard orientation sensors (e.g., real-time kinematic global navigation satellite system, RTK-GNSS), provide an attractive solution for direct georeferencing (DG) without the need for GCPs. Although DG UAV–SfM has shown comparable planar (x, y) accuracy to surveys incorporating GCPs, vertical accuracy may still be up to a magnitude poorer (Hugenholtz et al., 2016; Forlani et al., 2018). Through the addition of oblique images, accuracy and precision of DG UAV–SfM could be nearly commensurate with surveys incorporating GCPs (Carbonneau and Dietrich, 2017). However, this topic requires further investigation and we expect that higher-grade inertial measurement units (IMUs) may be required to provide accurate angular camera orientation (yaw, pitch, and roll) within the solution, and that weighting capabilities for angular orientation will also need to be available within processing software.

3.5.6 Software and settings

Readers should be cautioned that oblique images may create complications within certain SfM-MVS processing software. A limitation of this study is the evaluation of a single software package, Pix4Dmapper, an established commercial SfM solution that has consistently demonstrated reliability in processing oblique images (e.g., Ostrowski and Bakuła, 2016; Moe et al., 2017; Vacca et al., 2017). A list of additional software packages that have been successfully used in processing oblique images can be found in Verykokou and Ioannidis (2018). Although many commercial photogrammetric software suites have optimized aerial triangulation of oblique images (Moe et al., 2017), most

retain proprietary details and continuously modify algorithms to improve efficiency and precision. Software packages may offer users limited options for processing that can alter image matching strategies; however, the use of a matching strategy that is inappropriate with the image set can result in failure during processing.

3.6 Conclusions

UAV–SfM workflows have demonstrated the ability to map extensive 2D planes and model isolated 3D objects. Complex scenes with high-relief and intricate morphology, however, require deeper consideration of imaging strategy to maintain detail and accuracy in planar (x, y) and vertical (z) dimensions. Within topographically complex scenes, image sets collected with a single camera angle are unlikely to produce complete datasets and are prone to higher levels of deformation along steep slopes. Parallel-axis image sets (i.e., nadir image blocks) are susceptible to systematic 'dome' deformation, even with the use of survey-grade control points within high-relief scenes. As suggested by several authors, our results confirm that supplementing nadir image blocks with oblique images consistently mitigates these systematic error patterns within complex topography. Results from more than 150 scenarios with various combinations of overlap and imaging angles provide quantitative evidence of increased precision, higher accuracy, and reduced data gaps within combination datasets. Based on our results and the existing literature, we provide the following recommendations for improving UAV–SfM surveys in high-relief terrain. These recommendations should be equally adaptable for SfM data acquisition in alternative scenarios (e.g., vertical façades from UAV or ground-based imaging):

1. Combination datasets (i.e., nadir image block supplemented with off-nadir images) are preferred over image sets collected using a single camera angle.
2. Higher overlap is preferred for combination datasets.
3. Higher camera tilt angles (15–35°) in combination datasets generally increase precision, but may have an adverse effect on accuracy.
4. Single-angle image sets at higher-oblique angles (30–35°) can produce reliable results if combination datasets are not possible. However, single-angle image sets collected at lower angles may be more volatile and can result in large systematic errors. This should prove cautionary for image sets collected at near orthogonal angles using manual 'free flight' modes.

3.7 References

Agüera-Vega, F., Carvajal-Ramírez, F., Martínez-Carricondo, P.J., Sánchez-Hermosilla López, J., Mesas-Carrascosa, F.J., García-Ferrer, A., and Pérez-Porras, F.J., 2018, Reconstruction of extreme topography from UAV structure from motion photogrammetry: Measurement: Journal of the International Measurement Confederation, v. 121, p. 127–138, doi:10.1016/j.measurement.2018.02.062.

Aicardi, I., Chiabrando, F., Grasso, N., Lingua, A.M., Noardo, F., Spanò, A., and Spanó, A., 2016, UAV photogrammetry with oblique images: First analysis on data acquisition and processing: International Archives of the Photogrammetry, Remote Sensing and Spatial Information Sciences - ISPRS Archives, v. 2016-Janua, p. 835–842, doi:10.5194/isprsarchives-XLI-B1-835-2016.

Bash, E.A., Moorman, B.J., and Gunther, A., 2018, Detecting Short-Term Surface Melt on an Arctic Glacier Using UAV Surveys: Remote Sensing, v. 10, p. 1547,

doi:10.3390/rs10101547.

Bemis, S.P., Micklethwaite, S., Turner, D., James, M.R., Akciz, S., Thiele, S.T., Bangash, H.A., T. Thiele, S., and Bangash, H.A., 2014, Ground-based and UAV-Based photogrammetry: A multi-scale, high-resolution mapping tool for structural geology and paleoseismology: Journal of Structural Geology, v. 69, p. 163–178, doi:10.1016/j.jsg.2014.10.007.

Brodu, N., and Lague, D., 2012, 3D terrestrial lidar data classification of complex natural scenes using a multi-scale dimensionality criterion: Applications in geomorphology: ISPRS Journal of Photogrammetry and Remote Sensing, v. 68, p. 121–134, doi:10.1016/j.isprsjprs.2012.01.006.

Brown, D.C., 1971, Close-range camera calibration: Photogrammetric Engineering, v. 37, p. 855–866, doi:10.1.1.14.6358.

Campbell, I.A., 1970, Erosion rates in the steveville badlands, Alberta: Canadian Geographer, v. XIV, p. 202–216, doi:10.1111/j.1541-0064.1970.tb01568.x.

Carbonneau, P.E., and Dietrich, J.T., 2017, Cost-effective non-metric photogrammetry from consumer-grade sUAS: Implications for direct georeferencing of structure from motion photogrammetry: Earth Surface Processes and Landforms, v. 42, p. 473–486, doi:10.1002/esp.4012.

Carrivick, J.L., Smith, M.W., and Quincey, D.J., 2016, Structure from Motion in the Geosciences: Oxford, UK, Wiley-Blackwell.

Carvajal-Ramírez, F., Agüera-Vega, F., and Martínez-Carricondo, P.J., 2016, Effects of image orientation and ground control points distribution on unmanned aerial vehicle photogrammetry projects on a road cut slope: Journal of Applied Remote Sensing, v.

10, p. 034004, doi:10.1117/1.JRS.10.034004.

Cawood, A.J., Bond, C.E., Howell, J.A., Butler, R.W.H., and Totake, Y., 2017, LiDAR, UAV or compass-clinometer? Accuracy, coverage and the effects on structural models: Journal of Structural Geology, v. 98, p. 67–82, doi:10.1016/j.jsg.2017.04.004.

Chesley, J.T., Leier, A.L., White, S., and Torres, R., 2017, Using unmanned aerial vehicles and structure-from-motion photogrammetry to characterize sedimentary outcrops: An example from the Morrison Formation, Utah, USA: Sedimentary Geology, v. 354, p. 1–8, doi:10.1016/j.sedgeo.2017.03.013.

CloudCompare, 2019, Version 2.9. GPL Software. Available online: http://www.cloudcompare.org (accessed15 October 2019):

Colomina, I., and Molina, P., 2014, Unmanned aerial systems for photogrammetry and remote sensing: A review: ISPRS Journal of Photogrammetry and Remote Sensing, v. 92, p. 79–97, doi:10.1016/j.isprsjprs.2014.02.013.

Dandois, J.P., and Ellis, E.C., 2013, High spatial resolution three-dimensional mapping of vegetation spectral dynamics using computer vision: Remote Sensing of Environment, v. 136, p. 259–276, doi:10.1016/j.rse.2013.04.005.

Dandois, J.P., and Ellis, E.C., 2010, Remote sensing of vegetation structure using computer vision: Remote Sensing, v. 2, p. 1157–1176, doi:10.3390/rs2041157.

Dueholm, K.S., and Olsen, T., 1993, Reservoir analog studies using multimodel photogrammetry: a new tool for the petroleum industry: American Association of Petroleum Geologists Bulletin, v. 77, p. 2023–2031, doi:10.1306/BDFF8FBA-1718-11D7-8645000102C1865D.

Durkin, P.R., Hubbard, S.M., Weleschuk, Z., Smith, D.G., Palmer, M., Torres, A., and Holbrook, J., 2015, Spatial and Temporal Evolution of an Ancient Fluvial Meanderbelt (Upper Cretaceous Dinosaur Park Formation , Southeastern Alberta , Canada) With Emphasis on Characterization of Counter Point Bar Deposits, *in* AAPG Search and Discovery, Denver, CO, USA, p. Article 90216.

Eltner, A., Kaiser, A., Castillo, C., Rock, G., Neugirg, F., and Abellán, A., 2016, Image-based surface reconstruction in geomorphometry – merits, limits and developments of a promising tool for geoscientists: Earth Surface Dynamics Discussions, p. 1445–1508, doi:10.5194/esurfd-3-1445-2015.

Eltner, A., and Schneider, D., 2015, Analysis of Different Methods for 3D Reconstruction of Natural Surfaces from Parallel-Axes UAV Images: Photogrammetric Record, v. 30, p. 279–299, doi:10.1111/phor.12115.

Fonstad, M.A., Dietrich, J.T., Courville, B.C., Jensen, J.L.R., and Carbonneau, P.E., 2013, Topographic structure from motion: A new development in photogrammetric measurement: Earth Surface Processes and Landforms, v. 38, p. 421–430, doi:10.1002/esp.3366.

Forlani, G., Dall'Asta, E., Diotri, F., di Cella, U.M., Roncella, R., and Santise, M., 2018, Quality assessment of DSMs produced from UAV flights georeferenced with on-board RTK positioning: Remote Sensing, v. 10, doi:10.3390/rs10020311.

Fraser, C.S., 1997, Digital camera self-calibration: ISPRS Journal of Photogrammetry and Remote Sensing, v. 52, p. 149–159, doi:10.1016/S0924-2716(97)00005-1.

Fritsch, D., and Rothermel, M., 2013, Oblique Image Data Processing - Potential, Experiences and Recommendations: Photogrammetric Week '13, p. 73–88.

Gerke, M., 2009, Dense Matching in High Resolution Oblique Airborne Images: ISPRS - International Archives of the Photogrammetry, Remote Sensing and Spatial Information Sciences, v. XXXVIII, p. 77–82, http://www.isprs.org/proceedings/XXXVIII/3-W4/.

Gerke, M., Nex, F., Remondino, F., Jacobsen, K., Kremer, J., Karel, W., Huf, H., and Ostrowski, W., 2016, Orientation of oblique airborne image sets - Experiences from the ISPRS/Eurosdr benchmark on multi-platform photogrammetry: International Archives of the Photogrammetry, Remote Sensing and Spatial Information Sciences - ISPRS Archives, v. 2016-Janua, p. 185–191, doi:10.5194/isprsarchives-XLI-B1-185-2016.

Gerke, M., and Przybilla, H.-J.H.-J., 2016, Accuracy Analysis of Photogrammetric UAV Image Blocks: Influence of Onboard RTK-GNSS and Cross Flight Patterns: Photogrammetrie - Fernerkundung - Geoinformation, v. 2016, p. 17–30, doi:10.1127/pfg/2016/0284.

Gienko, G.A., and Terry, J.P., 2014, Three-dimensional modeling of coastal boulders using multi-view image measurements: Earth Surface Processes and Landforms, v. 39, p. 853–864, doi:10.1002/esp.3485.

Harwin, S., and Lucieer, A., 2012, Assessing the accuracy of georeferenced point clouds produced via multi-view stereopsis from Unmanned Aerial Vehicle (UAV) imagery: Remote Sensing, v. 4, p. 1573–1599, doi:10.3390/rs4061573.

Harwin, S., Lucieer, A., and Osborn, J., 2015, The Impact of the Calibration Method on the Accuracy of Point Clouds Derived Using Unmanned Aerial Vehicle Multi-View Stereopsis: Remote Sensing, v. 7, p. 11933–11953, doi:10.3390/rs70911933.

Hugenholtz, C.H., Brown, O.W., Walker, J., Barchyn, T.E., Nesbit, P.R., Kucharczyk, M., and Myshak, S., 2016, Spatial Acccuracy of UAV-Derived Orthoimagery and Topography: Comparing Photogrammetric Models Processed with Direct Geo-Referencing and Ground Control Points: Geomatica, v. 70, p. 21–30, doi:10.5623/cig2016-102.

Hugenholtz, C.H., Moorman, B.J., Riddell, K., and Whitehead, K., 2012, Small unmanned aircraft systems for remote sensing and earth science research: Eos, Transactions American Geophysical Union, v. 93, p. 236, doi:10.1117/1.3474649.

James, M.R., and Robson, S., 2014, Mitigating systematic error in topographic models derived from UAV and ground-based image networks: Earth Surface Processes and Landforms, v. 39, p. 1413–1420, doi:10.1002/esp.3609.

James, M.R., and Robson, S., 2012, Straightforward reconstruction of 3D surfaces and topography with a camera: Accuracy and geoscience application: Journal of Geophysical Research: Earth Surface, v. 117, p. 1–17, doi:10.1029/2011JF002289.

James, M.R., Robson, S., D'Oleire-Oltmanns, S., and Niethammer, U., 2017a, Optimising UAV topographic surveys processed with structure-from-motion: Ground control quality, quantity and bundle adjustment: Geomorphology, v. 280, p. 51–66, doi:10.1016/j.geomorph.2016.11.021.

James, M.R., Robson, S., and Smith, M.W., 2017b, 3-D uncertainty-based topographic change detection with structure-from-motion photogrammetry: precision maps for ground control and directly georeferenced surveys: Earth Surface Processes and Landforms, v. 42, p. 1769–1788, doi:10.1002/esp.4125.

Jiang, S., and Jiang, W., 2017, On-board GNSS/IMU assisted feature extraction and

matching for oblique UAV images: Remote Sensing, v. 9, doi:10.3390/rs9080813.

Jiang, S., Jiang, W., Huang, W., and Yang, L., 2017, UAV-based oblique photogrammetry for outdoor data acquisition and offsite visual inspection of transmission line: Remote Sensing, v. 9, doi:10.3390/rs9030278.

Kung, O., Strecha, C., Beyeler, A., Zufferey, J.C., Floreano, D., Fua, P., and Gervaix, F., 2012, The Accuracy of Automatic Photogrammetric Techniques on Ultra-Light Uav Imagery: ISPRS - International Archives of the Photogrammetry, Remote Sensing and Spatial Information Sciences, v. XXXVIII–1, p. 125–130, doi:10.5194/isprsarchives-XXXVIII-1-C22-125-2011.

Lague, D., Brodu, N., and Leroux, J., 2013, Accurate 3D comparison of complex topography with terrestrial laser scanner: Application to the Rangitikei canyon (N-Z): ISPRS Journal of Photogrammetry and Remote Sensing, v. 82, p. 10–26, doi:10.1016/j.isprsjprs.2013.04.009.

Luhmann, T., Fraser, C.S., and Maas, H.G., 2016, Sensor modelling and camera calibration for close-range photogrammetry: ISPRS Journal of Photogrammetry and Remote Sensing, v. 115, p. 37–46, doi:10.1016/j.isprsjprs.2015.10.006.

Luhmann, T., and Robson, S., 2006, Photogram Book 1: Dunbeath, Whittles, 1–510 p., doi:http://doi.org/10.1016/B978-0-08-101285-7.00001-0.

Markelin, L., Honkavaara, E., Näsi, R., Nurminen, K., Hakala, T., Nasi, R., Nurminen, K., and Hakala, T., 2014, Geometric processing workflow for vertical and oblique hyperspectral frame images collected using UAV: International Archives of the Photogrammetry, Remote Sensing and Spatial Information Sciences - ISPRS Archives, v. 40, p. 205–210, doi:10.5194/isprsarchives-XL-3-205-2014.

Martin, R.A., Rojas, I., Franke, K.W., and Hedengren, J.D., 2016, Evolutionary View Planning for Optimized UAV Terrain Modeling in a Simulated Environment: Remote Sensing, v. 8, p. 26, doi:10.3390/rs8010026.

Mikhail, E.M., Bethel, J.S., and McGlone, J.C., 2001, Introduction to modern photogrammetry: New York, USA, John Wiley & Sons, Inc.

Moe, K., Toschi, I., Poli, D., Lago, F., Schreiner, C., Legat, K., and Remondino, F., 2017, Changing the production pipeline – use of oblique aerial cameras for mapping purposes: Official Publication - EuroSDR, v. 2017, p. 44–61, doi:10.5194/isprsarchives-XLI-B4-631-2016.

Moreels, P., and Perona, P., 2007, Evaluation of Feature Detectors and Descriptors based on 3D Objects: International Journal of Computer Vision, v. 73, p. 263–284, doi:10.1007/s11263-006-9967-1.

Mosbrucker, A.R., Major, J.J., Spicer, K.R., and Pitlick, J., 2017, Camera system considerations for geomorphic applications of SfM photogrammetry: Earth Surface Processes and Landforms, v. 42, p. 969–986, doi:10.1002/esp.4066.

Nesbit, P.R., Durkin, P.R., Hugenholtz, C.H., Hubbard, S.M., and Kucharczyk, M., 2018, 3-D stratigraphic mapping using a digital outcrop model derived from UAV images and structure-from-motion photogrammetry: Geosphere, v. 14, p. 1–18, doi:10.1130/GES01688.1.

Nex, F., Gerke, M., Remondino, F., Przybilla, H.-J., Bäumker, M., and Zurhorst, A., 2015, ISPRS benchmark for multi-platform photogrammetry: ISPRS Annals of the Photogrammetry, Remote Sensing and Spatial Information Sciences, v. 2, p. 135–142, doi:10.5194/isprsannals-II-3-W4-135-2015.

Nex, F., and Remondino, F., 2014, UAV for 3D mapping applications: a review: Applied Geomatics, v. 6, p. 1–15, doi:10.1007/s12518-013-0120-x.

Nieminski, N.M., and Graham, S.A., 2017, Modeling Stratigraphic Architecture Using Small Unmanned Aerial Vehicles and Photogrammetry: Examples From the Miocene East Coast Basin, New Zealand: Journal of Sedimentary Research, v. 87, p. 126–132, doi:10.2110/jsr.2017.5.

Niethammer, U., James, M.R., Rothmund, S., Travelletti, J., and Joswig, M., 2012, UAV-based remote sensing of the Super-Sauze landslide: Evaluation: Engineering Geology, v. 128, p. 2–11, doi:10.1016/j.enggeo.2011.03.012.

O'Connor, J., Smith, M.J., and James, M.R., 2017, Cameras and settings for aerial surveys in the geosciences: optimising image data: Progress in Physical Geography, v. 41, p. 325–344, doi:10.1177/0309133317703092.

Ostrowski, W., 2016, Accuracy of measurements in oblique aerial images for urban environment: International Archives of the Photogrammetry, Remote Sensing and Spatial Information Sciences - ISPRS Archives, v. 42, p. 79–85, doi:10.5194/isprs-archives-XLII-2-W2-79-2016.

Ostrowski, W., and Bakuła, K., 2016, Towards efficiency of oblique images orientation: International Archives of the Photogrammetry, Remote Sensing and Spatial Information Sciences - ISPRS Archives, v. 40, p. 91–96, doi:10.5194/isprsarchives-XL-3-W4-91-2016.

Pavlis, T.L., and Mason, K.A., 2017, The New World of 3D Geologic Mapping: GSA Today, v. 27, p. 4–10, doi:10.1130/GSATG313A.1.

Rains, B., Shaw, J., Skoye, R., Sjogren, D., and Kvill, D., 1993, Late Wisconsin

subglacial megaflood paths in Alberta: Geology, v. 21, p. 323–326, doi:10.1130/0091-7613(1993)021<0323:LWSMPI>2.3.CO;2.

Rau, J.Y., Jhan, J.P., and Hsu, Y.C., 2015, Analysis of oblique aerial images for land cover and point cloud classification in an Urban environment: IEEE Transactions on Geoscience and Remote Sensing, v. 53, p. 1304–1319, doi:10.1109/TGRS.2014.2337658.

Remondino, F., Barazzetti, L., Nex, F., Scaioni, M., and Sarazzi, D., 2011, UAV photogrammetry for mapping and 3d modeling–current status and future perspectives: The International Archives of the Photogrammetry, Remote Sensing and Spatial Information Sciences, v. 38–1/C22, p. 25–31, doi:10.5194/isprsarchives-XXXVIII-1-C22-25-2011.

Remondino, F., and Fraser, C.S., 2006, Digital camera calibration methods: Considerations and comparisons: International archives of photogrammetry and remote sensing, v. 36, p. 266–272, http://www.mendeley.com/research/digital-camera-calibration-methods-12/.

Remondino, F., Spera, M.G., Nocerino, E., Menna, F., and Nex, F., 2014, State of the art in high density image matching: The Photogrammetric Record, v. 29, p. 144–166, doi:10.1111/phor.12063.

Rittersbacher, A., Buckley, S.J., Howell, J.A., Hampson, G.J., and Vallet, J., 2014, Helicopter-based laser scanning : a method for quantitative analysis of large-scale sedimentary architecture: Geological Society, London, Special Publications, v. 387, p. 185–202, doi:10.1144/SP387.3.

Rosenberg, A.S., 2009 [Thesis], An evaluation of a UAV guidance system with consumer

grade GPS receivers; Proquest, Umi Dissertation Publishing: Ann Arbor, MI, USA, 175 p.

Rossi, P., Mancini, F., Dubbini, M., Mazzone, F., and Capra, A., 2017, Combining nadir and oblique UAV imagery to reconstruct quarry topography: methodology and feasibility analysis: European Journal of Remote Sensing, v. 50, p. 211–221, doi:10.1080/22797254.2017.1313097.

Rupnik, E., Nex, F., and Remondino, F., 2014, Oblique Multi - Camera Systems - Orientation and Dense Matching Issues: v. XL, p. 12–14, doi:10.5194/isprsarchives-XL-3-W1-107-2014.

Rupnik, E., Nex, F., Toschi, I., and Remondino, F., 2015, Aerial multi-camera systems: Accuracy and block triangulation issues: ISPRS Journal of Photogrammetry and Remote Sensing, v. 101, p. 233–246, doi:10.1016/j.isprsjprs.2014.12.020.

Shufelt, J.A., 1999, Performance Evaluation and Analysis of Monocular Building Extraction From Aerial Imagery: {IEEE} Trans. Pattern Anal. Mach. Intell., v. 21, p. 311–326.

Smith, M.W., Carrivick, J.L., and Quincey, D.J., 2015, Structure from motion photogrammetry in physical geography: Progress in Physical Geography, v. 40, p. 247–275, doi:10.1177/0309133315615805.

Smith, M.W., and Vericat, D., 2015, From experimental plots to experimental landscapes: Topography, erosion and deposition in sub-humid badlands from Structure-from-Motion photogrammetry: Earth Surface Processes and Landforms, v. 40, p. 1656–1671, doi:10.1002/esp.3747.

Snavely, N., Seitz, S.M., and Szeliski, R., 2008, Modeling the world from Internet photo

collections: International Journal of Computer Vision, v. 80, p. 189–210, doi:10.1007/s11263-007-0107-3.

Stumpf, A., Malet, J.P., Allemand, P., Pierrot-Deseilligny, M., and Skupinski, G., 2015, Ground-based multi-view photogrammetry for the monitoring of landslide deformation and erosion: Geomorphology, v. 231, p. 130–145, doi:10.1016/j.geomorph.2014.10.039.

Thoeni, K., Guccione, D.E., Santise, M., Giacomini, A., Roncella, R., and Forlani, G., 2016, The potential of low-cost rpas for multi-view reconstruction of sub-vertical rock faces: International Archives of the Photogrammetry, Remote Sensing and Spatial Information Sciences - ISPRS Archives, v. 41, p. 909–916, doi:10.5194/isprsarchives-XLI-B5-909-2016.

Toth, C., and Jóźków, G., 2016, Remote sensing platforms and sensors: A survey: ISPRS Journal of Photogrammetry and Remote Sensing, v. 115, p. 22–36, doi:10.1016/j.isprsjprs.2015.10.004.

Vacca, G., Dessì, A., and Sacco, A., 2017, The Use of Nadir and Oblique UAV Images for Building Knowledge: ISPRS International Journal of Geo-Information, v. 6, p. 393, doi:10.3390/ijgi6120393.

Verhoeven, G.J.J., Doneus, M., Briese, C., and Vermeulen, F., 2012, Mapping by matching: a computer vision-based approach to fast and accurate georeferencing of archaeological aerial photographs: Journal of Archaeological Science, v. 39, p. 2060–2070, doi:10.1016/j.jas.2012.02.022.

Verykokou, S., and Ioannidis, C., 2016, Automatic Rough Georeferencing of Multiview Oblique and Vertical Aerial Image Datasets of Urban Scenes: Photogrammetric

Record, v. 31, p. 281–303, doi:10.1111/phor.12156.

Verykokou, S., and Ioannidis, C., 2018, Oblique aerial images: a review focusing on georeferencing procedures: International Journal of Remote Sensing, v. 39, p. 3452–3496, doi:10.1080/01431161.2018.1444294.

Vetrivel, A., Gerke, M., Kerle, N., and Vosselman, G., 2015, Identification of damage in buildings based on gaps in 3D point clouds from very high resolution oblique airborne images: ISPRS Journal of Photogrammetry and Remote Sensing, v. 105, p. 61–78, doi:10.1016/j.isprsjprs.2015.03.016.

Vollgger, S.A., and Cruden, A.R., 2016, Mapping folds and fractures in basement and cover rocks using UAV photogrammetry, Cape Liptrap and Cape Paterson, Victoria, Australia: Journal of Structural Geology, v. 85, p. 168–187, doi:10.1016/j.jsg.2016.02.012.

Wackrow, R., and Chandler, J.H., 2008, A convergent image configuration for DEM extraction that minimises the systematic effects caused by an inaccurate lens model: Photogrammetric Record, v. 23, p. 6–18, doi:10.1111/j.1477-9730.2008.00467.x.

Westoby, M.J., Brasington, J., Glasser, N.F., Hambrey, M.J., and Reynolds, J.M., 2012, "Structure-from-Motion" photogrammetry: A low-cost, effective tool for geoscience applications: Geomorphology, v. 179, p. 300–314, doi:10.1016/j.geomorph.2012.08.021.

Whitehead, K., Hugenholtz, C.H., Myshak, S., Brown, O.W., LeClair, A., Tamminga, A.D., Barchyn, T.E., Moorman, B.J., and Eaton, B.C., 2014, Remote sensing of the environment with small unmanned aircraft systems (UASs), part 2: scientific and commercial applications 1: Journal of Unmanned Vehicle Systems, v. 02, p. 86–102,

doi:10.1139/juvs-2014-0007.

Wolf, P.R., Dewitt, B.A., and Wilkinson, B.E., 2014, Elements of Photogrammetry with Application in GIS, Fourth Edition: Maidenhead, McGraw-Hill Education.

Wood, J.M., 1989, Alluvial architecture of the Upper Cretaceous Judith River Formation, Dinosaur Provincial Park, Alberta, Canada: Bulletin of Canadian Petroleum Geology, v. 37, p. 169–181.

Wu, B., Xie, L., Hu, H., Zhu, Q., and Yau, E., 2018, Integration of aerial oblique imagery and terrestrial imagery for optimized 3D modeling in urban areas: ISPRS Journal of Photogrammetry and Remote Sensing, v. 139, p. 119–132, doi:10.1016/j.isprsjprs.2018.03.004.

Xie, L., Hu, H., Wang, J., Zhu, Q., and Chen, M., 2016, An asymmetric re-weighting method for the precision combined bundle adjustment of aerial oblique images: ISPRS Journal of Photogrammetry and Remote Sensing, v. 117, p. 92–107, doi:10.1016/j.isprsjprs.2016.03.017.

Zahm, C., Lambert, J., and Kerans, C., 2016, Use of unmanned aerial vehicles (UAVs) to create digital outcrop models: An example from the Cretaceous Cow Creek Formation, Central Texas.: GCAGS Journal, v. 5, p. 180–188.

Chapter 4

Digital Re-Evaluation of Down-Dip Channel Fill Architecture in Deep-Water Slope Deposits: Multi-Scale Perspectives from UAV-SfM

4.1 Abstract

Deep-water channel systems are important pathways for sediment transport. Studying the morphodynamic processes and long-term evolution of these systems is often challenging due to accessibility limitations and their appreciable extent. Recent advances in seafloor surveying, experiments, and modeling have revealed new insight into seafloor processes; however, understanding how these short-term perspectives influence longer-term evolution of deep-water systems has been limited by the difficulty in linking processes to products in the stratigraphic record. Outcrops present opportunities to characterize detailed internal architecture of deep-water channel fill over a wide range of timescales, but obtaining observations is compounded by challenges in outcrop accessibility and perspective along broad exposures. To demonstrate the potential value of modern remote sensing techniques in supplementing geologic fieldwork, we revisit an extensive dip-oriented outcrop exposure of Cretaceous deep-water channel fill deposits using a 3D digital outcrop model (DOM) generated from uninhabited/unmanned aerial vehicle (UAV) photogrammetry. Results confirm previous field-based documentation of coarse-scale stratigraphic architecture and reveal nuanced internal detail that was not captured from field-based perspectives alone. Subtle internal channel-fill architecture including discontinuous sandstone wedges and the interpreted stratigraphic products of upslope migrating crescentic bedforms, are recognized. This case study demonstrates the

sedimentary detail that can be uncovered by integrating conventional field-based approaches limited by viewable scale, perspective, and/or accessibility, with emerging remote sensing techniques. The UAV photogrammetry DOM approach used here provides valuable supplemental data in the investigation of deep-water channel system deposits and has the potential to overcome inherent challenges in outcrop mapping for numerous geologic applications.

4.2 Introduction

Deep-water slope channel systems are important conduits for transporting sediment from continents to the deep ocean. Their deposits provide important information about the formative sedimentary processes that occur throughout the evolution of a depositional system across a variety of geologic timescales (Mutti and Normark, 1987; Clark and Pickering, 1996; Gardner et al., 2003; Hodgson et al., 2011; Hubbard et al., 2014; Romans et al., 2016; Malkowski et al., 2018). Understanding relationships between depositional processes and associated products in the rock record has been particularly challenging in deep-water settings due to: (1) their appreciable extent (10s - 100s km); (2) a historical lack of meter and sub-meter scale observations from modern systems; and (3) difficulties comparing across the observational scales provided by different methods of investigation (Mutti and Normark, 1987; Normark et al., 1993; Talling et al., 2015). Flume experiments (e.g., Baas et al., 2004; Sumner et al., 2008) and recent repeat imaging and monitoring (e.g., bathymetric surveys) of active deep-sea channels (e.g., Hughes Clarke, 2016; Hage et al., 2018; Paull et al., 2018; Vendettuoli et al., 2019) have offered new insight into seafloor processes; however, these methods have limited spatial and temporal resolution and can only provide a short-term perspective (i.e., days to

years). Therefore, ancient deposits are used as complementary datasets to better understand longer-term system evolution, and have historically served as a basis for depositional models (e.g., Walker, 1978; Posamentier and Kolla, 2003).

Subsurface (e.g., seismic reflection) datasets have been used to distinguish sedimentary units and interpret depositional environments at a regional-scale, but are limited to a coarse resolution (10s of meters vertically) that excludes the ability to deduce the internal heterogeneity of deep-water channel strata in most instances (e.g., Abreu et al., 2003; Mayall et al., 2006; Deptuck et al., 2007). This typically limits interpretation to highly composite stratigraphic architecture (e.g., channel complexes or coarser) and precludes identification of the fine-scale architecture and facies of channel fills, which may reveal valuable insight into formative morphodynamic processes within these systems.

Observations from outcrop belts provide opportunities to characterize internal architectural characteristics and link observations across various spatial and temporal scales (Hodgson et al., 2011; Macauley and Hubbard, 2013; Hubbard et al., 2014; Rittersbacher et al., 2014; Casciano et al., 2019). However, outcrops are often non-continuous, variably accessible, and offer a limited perspective determined by exposure orientation relative to depositional dip. These factors have led to development of models of submarine channel evolution, that are primarily focused on strike-oriented perspectives that resolve channel form-shaped sedimentary bodies, generally > 100s m wide and 10s m thick (Campion et al., 2000; Arnott, 2007; Hubbard et al., 2014), commonly referred to as channel elements (McHargue et al., 2011; Macauley and Hubbard, 2013). The variability of facies and stratigraphic architecture along depositional dip has rarely been

addressed, due to a lack of extensive and continuous dip-oriented exposures (e.g., Plink-Bjorklund et al., 2001).

Compounding issues inherent to down-dip characterization of deep-water channel strata is a paucity in practical approaches for documenting and measuring outcrop features at multiple scales. Coarse-scale observations can often be revealed by 'stepping back' and gaining a distant perspective that permits sketching and/or acquisition of a gigapan or photomosaic of the outcrop (e.g., Arnot et al., 1997; Benhallam et al., 2016). This technique is familiar to most field geologists and only requires a field notebook and/or camera; however, it lacks geospatial data constraints and scaling required for quantitative characterization. Additional practical considerations include the need for an unobstructed viewpoint and the inability to quickly switch among perspectives (e.g., overview, intermediate, and up-close), which may restrict recognition of perceptible characteristics in outcrop.

Recently, a host of geospatial techniques have been applied in constraining stratigraphic architecture in outcrop studies. Differential global positioning systems (dGPS), sometimes aided by a laser rangefinder, have been used to record points along key bedding surfaces (e.g., Durkin et al., 2015; Pemberton et al., 2016), but also require physical access or an unobstructed view of the outcrop. Digital outcrop models (DOMs), also known as virtual outcrops, collected with ground-based or airborne light detection and ranging (LiDAR), have been used to digitally document 3D outcrops (e.g., Bellian et al., 2005; McCaffrey et al., 2005; Buckley et al., 2008, 2010; Hodgetts, 2013; Rittersbacher et al., 2014). However, LiDAR systems can be prohibitively expensive,

practically immobile, and also require several suitable scanning locations (Rittersbacher et al., 2014; Chesley et al., 2017).

Alternatively, modern photogrammetry using structure-from-motion (SfM) software with uninhabited/unmanned aerial vehicle (UAV) images has recently demonstrated potential for geologic mapping applications. Integration of UAV-SfM workflows into sedimentary studies has proven effective for mapping plan-view exposures (e.g., Chesley and Leier, 2018) and demonstrated the ability to recognize localized stratigraphic architecture in vertical to sub-vertical outcrops (Nieminski and Graham, 2017; Pitts et al., 2017; Nesbit et al., 2018). Recent developments in 3D enabled software provide opportunities to map geologic features, integrate multiple datasets, and make advanced interpretations from DOMs (e.g., virtual reality geology studio - Hodgetts et al., 2007, LIME - Buckley et al., 2019). UAV-SfM datasets and 3D software are still in the early stages in providing supplemental evidence for geologists, but have yet to realize their full potential for advancing geologic investigations and understanding.

To demonstrate the additional multi-scale perspectives and quantitative potential provided by a UAV-SfM workflow, we revisit an extensive dip-oriented outcrop of Cretaceous deep-water channel fill deposits in the Magallanes Basin, southern Chile, previously documented with conventional field methods (sedimentary logs, field observations, and dGPS surface mapping; Daniels, 2015, 2019). A well-exposed cliff-face (15-40 m height) reveals 7 km of nearly continuous outcrop roughly parallel to paleoflow, providing excellent opportunities to investigate longitudinal (down-system) variations. This study aims to: (1) document digital methods for performing observation and interpretation of stratigraphic architecture from DOMs; (2) evaluate digital

interpretations relative to conventional field-based approaches; (3) recognize and capture previously overlooked features in sedimentary deposits due to limitations in data acquisition methods; and (4) characterize subtle down-dip architecture internal to channel-form sedimentary bodies and discuss implications for deep-water depositional models.

4.3 Geologic Setting and Study Area

The Magallanes retroarc foreland basin was formed and filled in response to Andean uplift and denudation throughout much of the Late Cretaceous (Wilson, 1991; Fildani and Hessler, 2005; Fosdick et al., 2014). Its fill largely records the evolution of Late Cretaceous deep-water depositional systems, preserved in expansive outcrops throughout Chilean and Argentine Patagonia (Romans et al., 2011; Malkowski et al., 2016; Daniels et al., 2018, 2019). The deep-water depositional history is characterized by three phases of basin infilling, represented by deposits of the Punta Barrosa, Cerro Toro, and Tres Pasos formations (Figure 4.1A; Katz, 1963; Romans et al., 2011). Together with the shallow-marine Dorotea Formation, the Tres Pasos Formation records the terminal phase of marine sedimentation in the basin (Hubbard et al., 2010; Daniels et al., 2018). The Tres Pasos Formation records deposition along a submarine slope that was > 40 km long and characterized by > 1 km of relief (Figure 4.1B; Bauer et al., 2020). Although the Tres Pasos Formation consists predominantly of siltsone deposits, packages of sandstone up to 300 m thick crop out along the studied transect, and are interpreted to represent the products of channelization along the basin-margin slope (Hubbard et al., 2010, 2014; Macauley and Hubbard, 2013; Pemberton et al., 2016). The area of interest for this study is a 15-40 m thick, nearly continuous exposure of the Tres Pasos Formation

revealed along a sub-vertical ridgeline cliff (Figure 4.1C). The strata were deposited on the paleo-slope, at least 30 km from the shelf edge (Daniels et al., 2018; Bauer et al., 2020). Regional paleoflow direction, derived from more than 350 measurements at various points along the transect (Daniels, 2015), indicate that the outcrop is oriented roughly parallel to paleoflow direction from north to south throughout the study area.

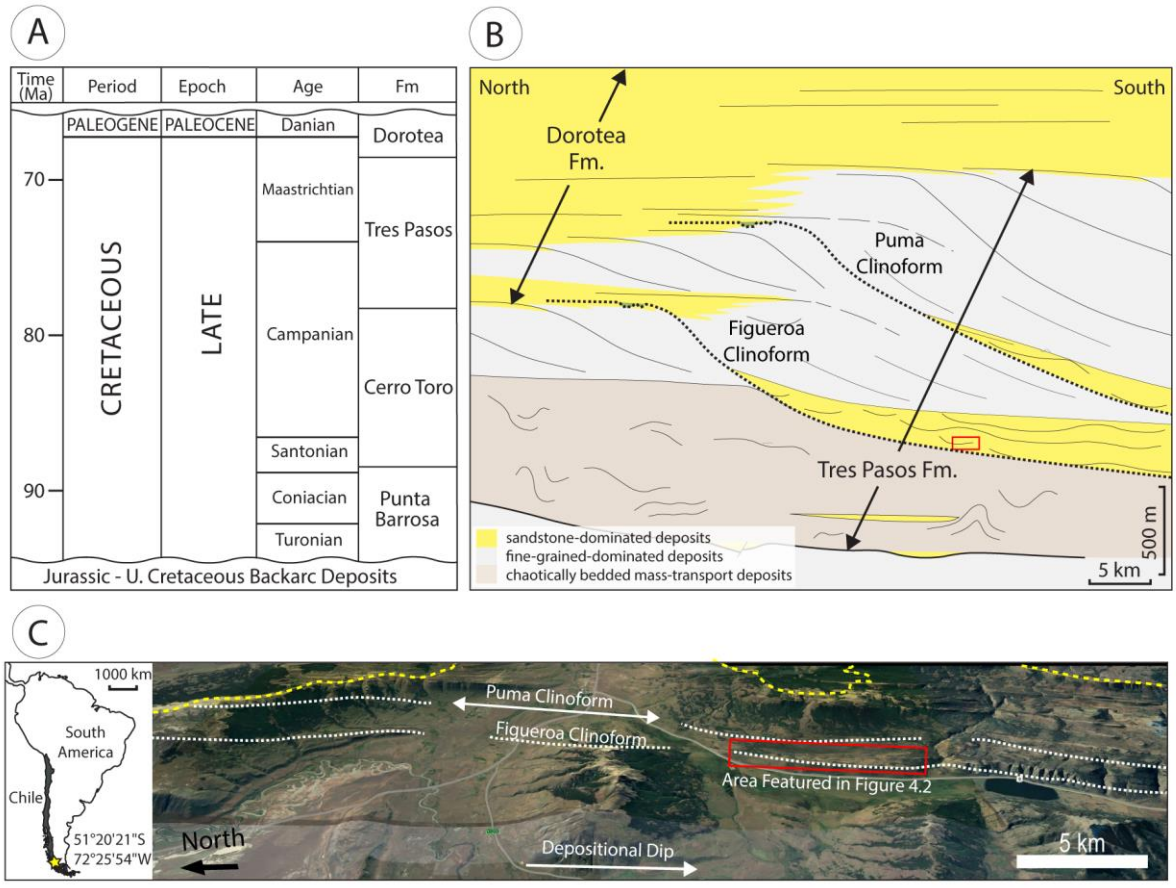

Figure 4.1. Overview of regional lithostratigraphy and field area. A) summary of Late Cretaceous formations associated with the Magallanes-Austral basin.; B) regional dip-oriented stratigraphic cross-section of the Tres Pasos and Dorotea formations showing coarse-scale clinoforms, modified from (Bauer et al., 2020); C) field location relative to A and B. Note: red box in (B-C) indicates area displayed in Figure 4.2.

Recent field-based work in the region (Daniels, 2015) documented twenty distinct channel elements using traditional field data-acquisition techniques and dGPS to constrain stratigraphic architecture (Figure 4.2). The investigation emphasized stratigraphic correlation of slope channel strata, as well as fine-scale sedimentological characterization in measured sections. No notable changes of intra-element channel fill composition or architecture were discerned, but we note that cliff exposures were often inaccessible and idealized perspectives to acquire photomosaics were not available. We postulate that these limitations of the outcrop at Alvarez Ridge may have prevented the recognition of important sedimentary detail from a conventional field-based approach.

4.4 Methods

We use a digital outcrop model (DOM) derived from UAV images to digitally record and interpret stratigraphic architecture at multiple scales and compare with previously reported field-based results (Daniels, 2015). A 2 km, depositional-dip oriented segment of the Daniels (2015) dataset was investigated, featuring six channel elements (delineated by blue boxes in Figure 4.2B). Field measurements from the original study included eight sedimentary logs (125 m cumulative), which recorded bed thickness, grain size, sedimentary structures, paleo-flow indicators (primarily derived from sole marks), and nature of bedding contacts. In the original study, widespread stratigraphic surfaces were mapped by: (i) walking along unit contacts and recording point locations with a dGPS, (ii) projecting dGPS points onto a 2D plane, and (iii) interpreting a down-dip cross-sectional stratigraphic profile from 2D projected points. The digital method adopted in this analysis follows a similar workflow, replacing field-based dGPS points (step (i) above) with digital observations derived using the workflow described below.

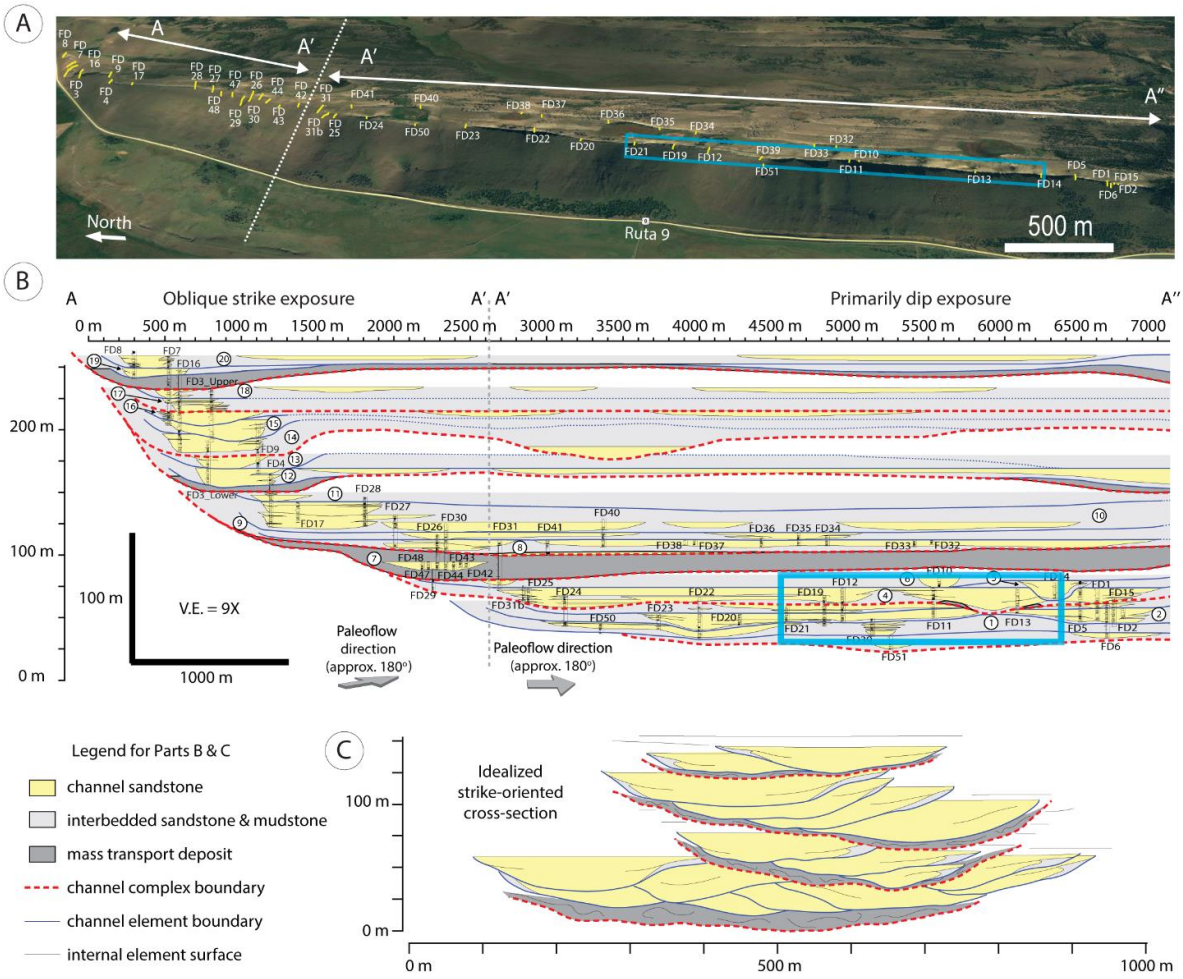

Figure 4.2. A) Oblique perspective of field area from satellite imagery in Google Earth including the locations of measured stratigraphic sections (yellow lines). B) Regional cross-section produced from GPS mapping and measured section field data documented with traditional field methods (Daniels, 2015). C) Stratigraphic hierarchical framework of deep-water channel systems in strike-oriented cross-section, modified from (Covault et al., 2016). Note: blue box in (A-B) specifies location for UAV-SfM analysis in this study (Figure 4.5).

4.4.1 Digital data collection and processing

DOMs were generated from a collection of UAV images processed using structure-from-motion multi-view stereo (SfM-MVS), commonly referred to as SfM photogrammetry. Images were collected with a DJI Phantom 3 Professional quadcopter controlled using the freely available Pix4Dcapture application for iOS. Flights were performed using manual 'free flight' mode, allowing user control of lateral movement, altitude, and camera pitch angle while images trigger automatically with changes in position. Primary flights were performed with the camera plane approximately parallel to the outcrop at a distance of 10-15 m in a grid-like pattern along the near-vertical outcrop exposure. Additional flights were performed with a nadir (downward facing) and oblique camera angle of ~45° along the outcrop ridge in order to: (1) increase coverage of the complex outcrop faces (Nesbit et al., 2018); (2) obtain images of features above the ridgeline to use as ground control points (GCPs); and (3) enhance image network geometry for a higher 3D accuracy in a complex exposure (Nesbit and Hugenholtz, 2019). A total of 50 distinct natural points above, below, and on the outcrop were selected as GCPs and recorded with dGPS to constrain the scale and orientation of the model during SfM processing.

More than 2400 images from all flights were processed together using Pix4Dmapper on a capable workstation (Intel® Core™ i9-7900X CPU @ 3.30 GHz with 64 GB RAM and an NVIDIA GeForce GTX 1080 graphics card). Images were divided into a northern and southern half of the model to decrease processing time and to reduce strain on the hardware later during the digital characterization phase. Processing settings followed those outlined by Nesbit et al. (2019), with two modifications. In the Initial

Processing (Step 1), we use ‘free flight’ matching strategy instead of ‘Aerial grid or corridor.’ Additionally, during point cloud densification and mesh generation (Step 2), we opted to generate a 3D textured mesh to enhance interpretation.

4.4.2 Digital outcrop characterization, projection, and interpretation

Digital observations of stratigraphic surfaces were made directly within Pix4Dmapper (Figure 4.3A-B) following the workflow outlined by Nesbit et al. (2018), because of its capabilities to seamlessly digitize and visualize large 3D point clouds and meshes (Nesbit et al., 2020). Digitized points and lines were created using both the dense point cloud and textured mesh DOMs, with individual observations often confirmed in individual UAV images. Digital observations were then exported as point shapefiles (.shp) and converted into tabular format with identifier (name) and location (x, y, z) attributes. To account for post-depositional tectonic effects on bedding geometry, tabular point data were imported into Petrel (Schlumberger, 2020) and divided into three segments based on slight variations in structural dip of bedding along the outcrop belt (Daniels, 2015). Data from each segment were then projected onto a 2D plane oriented perpendicular to bedding (striking north-south, dipping east) following methods outlined by (Englert et al., 2018), resulting in a down-dip 2D cross-sectional profile with restored dimensions (Figure 4.3C). Data projected in the 2D cross-section were then correlated laterally relying on the digital observations made within Pix4Dmapper to reveal related stratigraphic surfaces. Subsequently, strata were interpreted further by grouping internal beds or bedding packages of similar lithofacies by cross-referencing the 3D model and/or individual UAV images. To remain consistent with the study of Daniels (2015), channel-form bodies were the focus of mapping along the outcrop belt.

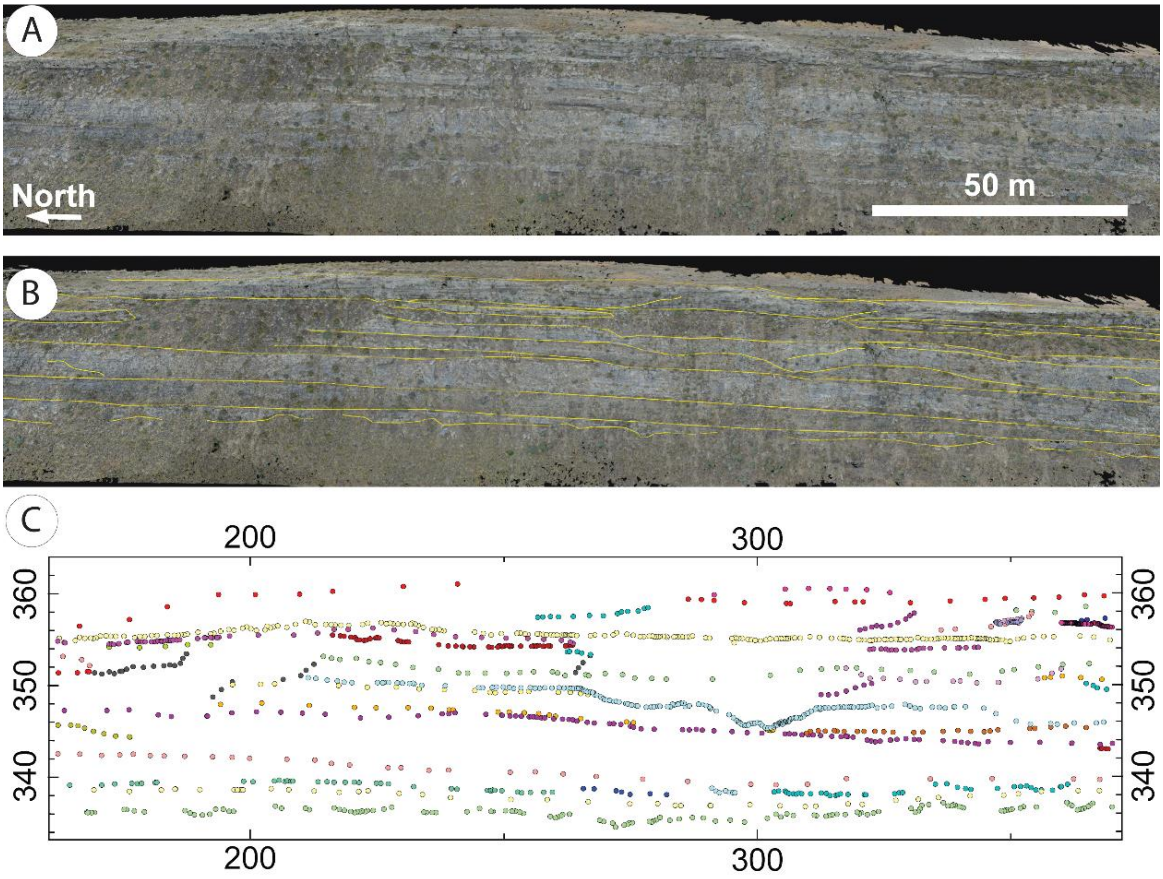

Figure 4.3. Methodology for documenting stratigraphic architecture. A) 3D DOM processed and visualized in Pix4Dmapper; B) Interpret potential surfaces using manual tie points directly within Pix4Dmapper; C) Export points, project from 3D to 2D plane following Englert et al. (2018) and interpret related sedimentary bodies on 2D plane while cross-referencing data in the 3D model resulting in Figure 4.5B.

4.5 Results

4.5.1 Sedimentary Facies

The mapping and stratigraphic architecture focus of this study is grounded in a series of sedimentary facies, including: F1) thick-bedded sandstone and/or conglomerate (with local pebble- to cobble-sized clast accumulations); F2) thick- to thin-bedded sandstone and mudstone; F3) thin-bedded mudstone with sandstone; and F4) chaotically-bedded, poorly sorted mudstone and sandstone. The main characteristics of these facies are summarized in Figure 4.4 and Table 4.1. Facies reveal that subaqueous turbidity currents and other gravity flows were the dominant mode of sediment transfer recorded in the Tres Pasos Formation, including high-density turbidity currents (e.g., F1, Lowe, 1982), low-density turbidity currents (e.g., F2 and F3, Bouma, 1962), and mass-wasting processes, including debris flows and slumping (e.g., F4, Lowe, 1982; Talling et al., 2012). Similar facies have been described and interpreted in numerous studies within and directly adjacent to the study transect (e.g., Macauley and Hubbard, 2013; Daniels, 2015; Pemberton et al., 2016), and as such, an exhaustive description is not repeated here.

4.5.2 Traditional Field-Based Approach

4.5.2.1 Description

Traditional field-based mapping approaches resulted in the identification of two packages of sandstone-dominated strata (F1) separated by a surface that is mappable across the entire outcrop transect (red line, Figure 4.5A). The bounding surface is commonly overlain by recessive units, including thin-bedded turbidites (F2), concordant siltstone (F3), or mass-transport deposits (F4). It is highly undulous in nature, with up to 10 m of relief (red line, Figure 4.6A,B). The sandstone-dominated packages above and

below the widespread bounding surface vary in thickness along the outcrop, from 25-40 m (Figure 4.5A). Each of the sandstone-dominated packages can be subdivided into three sedimentary bodies 5-25 m thick, defined by basal surfaces that have concave upward shape. These surfaces are oriented parallel to sub-parallel to the main bounding surface, and are characterized with clearly defined smooth bases and local changes in relief up to 10 m (blue lines, Figure 4.6B,C). The sedimentary body bases are overlain by mudstone drape (F3) or mudstone rip-up clasts/conglomerate lag (F1) deposits; the bulk of the bodies are composed of thick-bedded sandstone (F1) and, sometimes fine upwards due to increased proportions of mudstone interbeds. Internally, the sedimentary bodies commonly contain less through-going surfaces (< 10^2 m extent) characterized by slightly smooth to undulous (< 4 m relief) geometries (black lines, Figure 4.6B,C). These internal surfaces truncate individual beds and bedsets, and sometimes onlap the bases of sedimentary bodies.

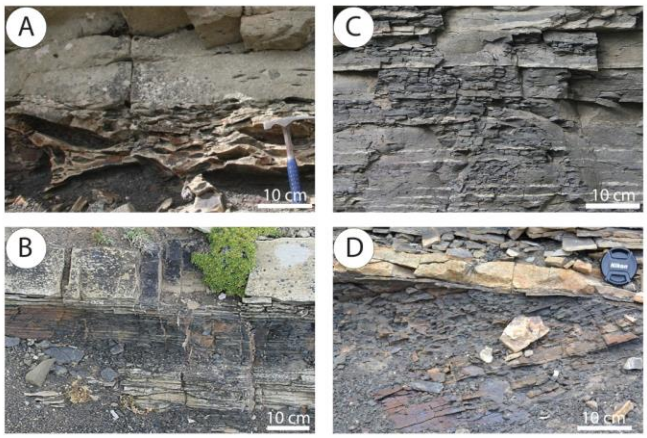

Figure 4.4. Lithofacies associations within the Tres Pasos Formation in the study area described in Table 4.1 adapted from Daniels (2019). A) F1: thick-bedded sandstone and/or conglomerate; B) F2: thick- to thin-bedded sandstone and mudstone; C) F3: thin-bedded mudstone with sandstone; D) F4: chaotically bedded, poorly sorted mudstone and sandstone associated with Mass Transport Deposits (MTD).

Lithofacies	Grain Size	Sedimentary Features	Bed Geometry	Thickness Range	Lower/Upper Contact	Process Interpretations
F1: Thick-bedded sandstone and/or conglomerate	V. coarse grained sandstone at base - fining upwards; conglomerate consist of matrix supported pebble to cobble clasts	Massive amalgamated to non-amalgamated beds	Lenticular with smaller-scale scour and cut and fill features	0.2-2.5 m thick; amalgamated packages <6 m	Sharp base with undulations caused by scours containing extrabasinal or mudstone clast accumulations; gradational top	Erosion and deposition from high-density turbidity currents
F2: Thick- to thin-bedded sandstone and mudstone	Fine-grained sandstone and siltstone	Incomplete Bouma sequences (T_b to T_d); ripple and planar laminations common	Lenticular to tabular	0.02-0.2 m thick; packages <5 m thick	Sharp and commonly flat base	Low-density turbidity currents associated with traction sedimentation; some scouring
F3: Thin-bedded mudstone with sandstone	Siltstone and fine-grained sandstone	Incomplete Bouma sequences (T_c to T_e); some ripple and planar laminations	Tabular to lenticular	0.02-0.2 m thick; packages <2.5 m thick	Typically sharp and sometime undulatory	Low-density turbidity currents; bypass; almost no scouring
F4: Chaotically bedded, poorly sorted mudstone and sandstone	Siltstone with sandstone	Chaotic bedding and poorly sorted	Chaotic	Sandstone <0.2 m thick; siltstone <3.0 m thick with accumulations 0.2-15 m thick	Variable, typically sharp and undulous	Deposition following mass wasting; Mass Transport Deposits (MTD)

Table 4.1. Characteristic facies for the Tres Pasos Formation at Alvarez Ridge.

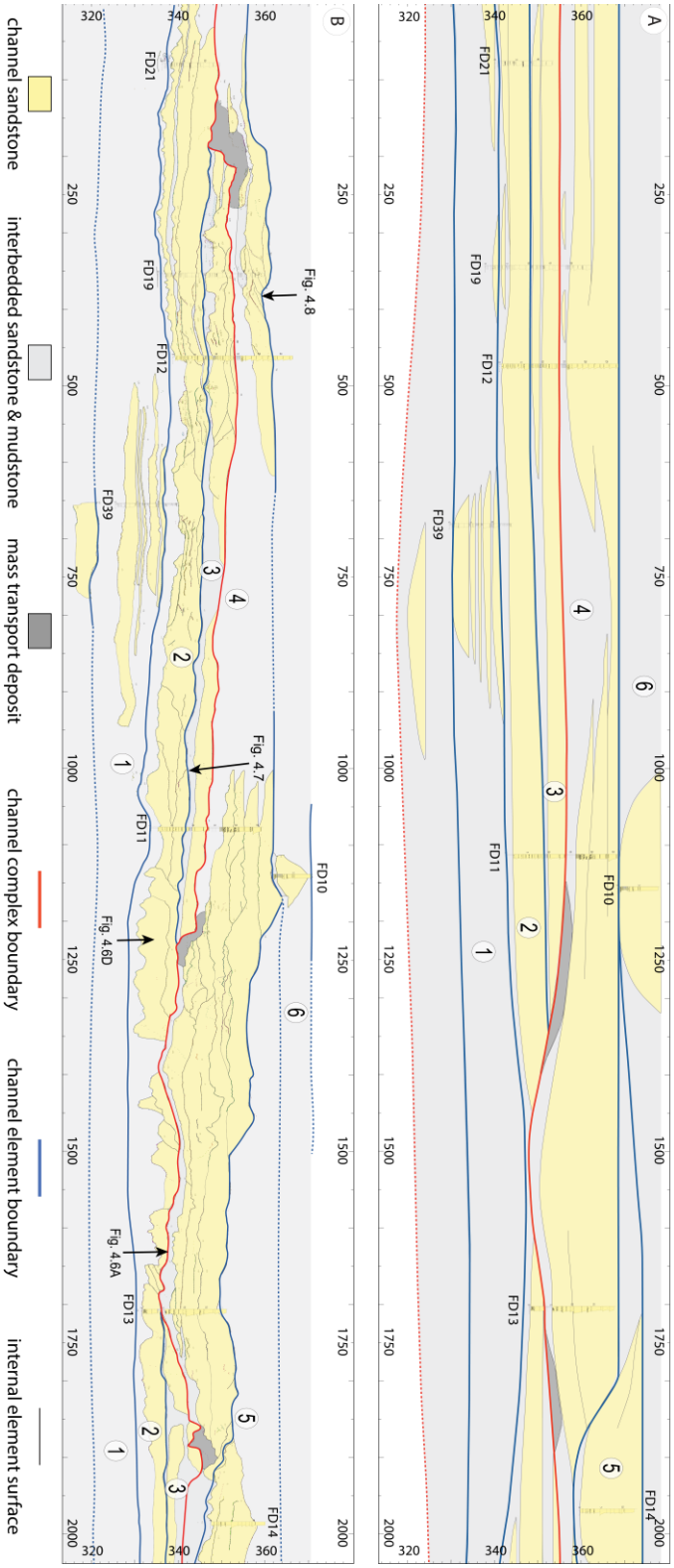

Figure 4.5. Down-dip cross-sectional profile of interpreted stratigraphic architecture. A) Traditional field methods (Daniels, 2015); B) Digital UAV-SfM DOM methods.

4.5.2.2 Interpretation

Identification of a hierarchical arrangement of strata can aid in the interpretation of sedimentary processes that took place during the long-term evolution of slope channel systems (Pickering et al., 1995). Daniels (2015) used regional mapping and context (Figure 4.2B), as well as sedimentological characterization to divide the outcrop into a hierarchical framework for submarine channel strata (Figure 4.2C, Sprague et al., 2002, 2005; McHargue et al., 2011). The most prevalent stratigraphic surface bounds two sandstone-dominated packages, interpreted as channel complexes (Figure 4.5A). Channel complexes generally record the position of a submarine sediment-routing system over significant time and contain two or more stacked elements (McHargue et al., 2011).

Within the study area, each channel complex is characterized by three sedimentary bodies that are 5-25 m thick, which represent channel elements (cf. Mutti and Normark, 1987; McHargue et al., 2011; Hubbard et al., 2014), and are numbered successively from the base of section (Figure 4.5A). Channel elements provide a record of inception through final infill of a single submarine conduit on the seafloor and include evidence for numerous phases of erosion and infill to form composite channelform deposits (Fildani et al., 2013; Covault et al., 2014; Hubbard et al., 2014). In the field area, bases of channel elements record evidence of erosion and sediment bypass (e.g., lag deposits and drapes; Fildani et al., 2013; Stevenson et al., 2015), followed by evidence for infilling from collapsing turbidity currents or channel abandonment (McHargue et al., 2011). Internal surfaces within channel elements were only locally mapped, and interpreted to have been sculpted by multiple phases of cut and fill through scours oriented sub-parallel to the channel element base erosion surface (Hubbard et al., 2014).

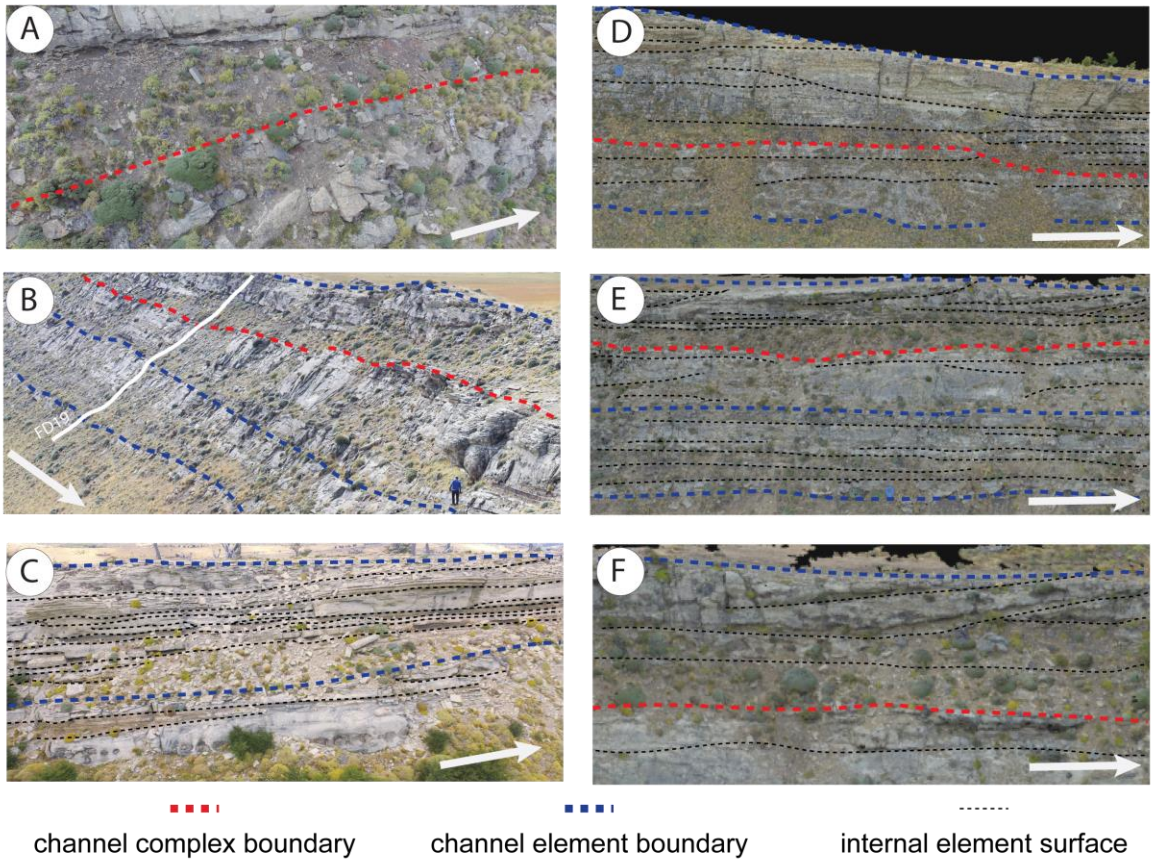

Figure 4.6. Examples of surface characteristics as seen in the field (A-C) and in the digital outcrop model (D-F). Channel complex boundary (A and D, red); channel element boundary (B and E, blue); internal element surfaces (C and F, black). Note: arrows indicate paleoflow direction.

4.5.3 Digital DOM Approach

4.5.3.1 Description

Digital mapping approaches also revealed two sandstone-dominated stratigraphic packages (F1) separated by a distinct interval (1-8 m thick) characterized by recessive units (F2, F3, and F4) that extends throughout the digital model (Figure 4.5B). The base of this recessive interval is highly undulatory with up to 12 m change in local relief, commonly truncating underlying strata (Figure 4.6D). As with the field-based approach, sandstone-dominated packages above and below the bounding surface vary in thickness 20-40 m and are each subdivided into three sedimentary bodies (5-20 m thick) with mappable basal surfaces marked by a sharp change in lithology. The base of these surfaces are typically marked by a 0.4 - 2 m thick recessive mudstone (F3 or F2) overlain by sandstone (F1), which is often highly amalgamated and structureless (Figure 4.6E). The surfaces that define sedimentary body bases are identifiable along the extent of the outcrop (10^2 - 10^3 m) and commonly oriented nearly parallel to the bounding surface that separates the two sandstone-dominated packages (local variations in relief up to 4 m; Figure 4.5B).

Within each sedimentary body, numerous surfaces (10^1 - 10^2 m in length) are recognized throughout the outcrop. These surfaces can be sub-horizontal to highly undulatory, with vertical relief up to 6 meters (Figure 4.6F). In most instances, the surfaces truncate strata within sedimentary bodies, although they onlap surfaces locally (Figure 4.6D). The internal surfaces bound lenticular or wedge-shaped units with asymmetric geometries commonly steeper in the upslope direction. Surfaces can appear discontinuous (e.g., Figure 4.7), or in some instances may bound 0.5 - 3 m thick beds

stacked in a back-setting arrangement, with each dipping towards the upslope direction (Figure 4.8). Since these architectures were unnoticed in the initial outcrop study, they were lithologically calibrated in the field following digital interpretation of the architecture. Facies of these back-setting beds are predominantly ascribed to F1, with abundant mudstone-clasts overlying undulating erosion surfaces (Figure 4.8).

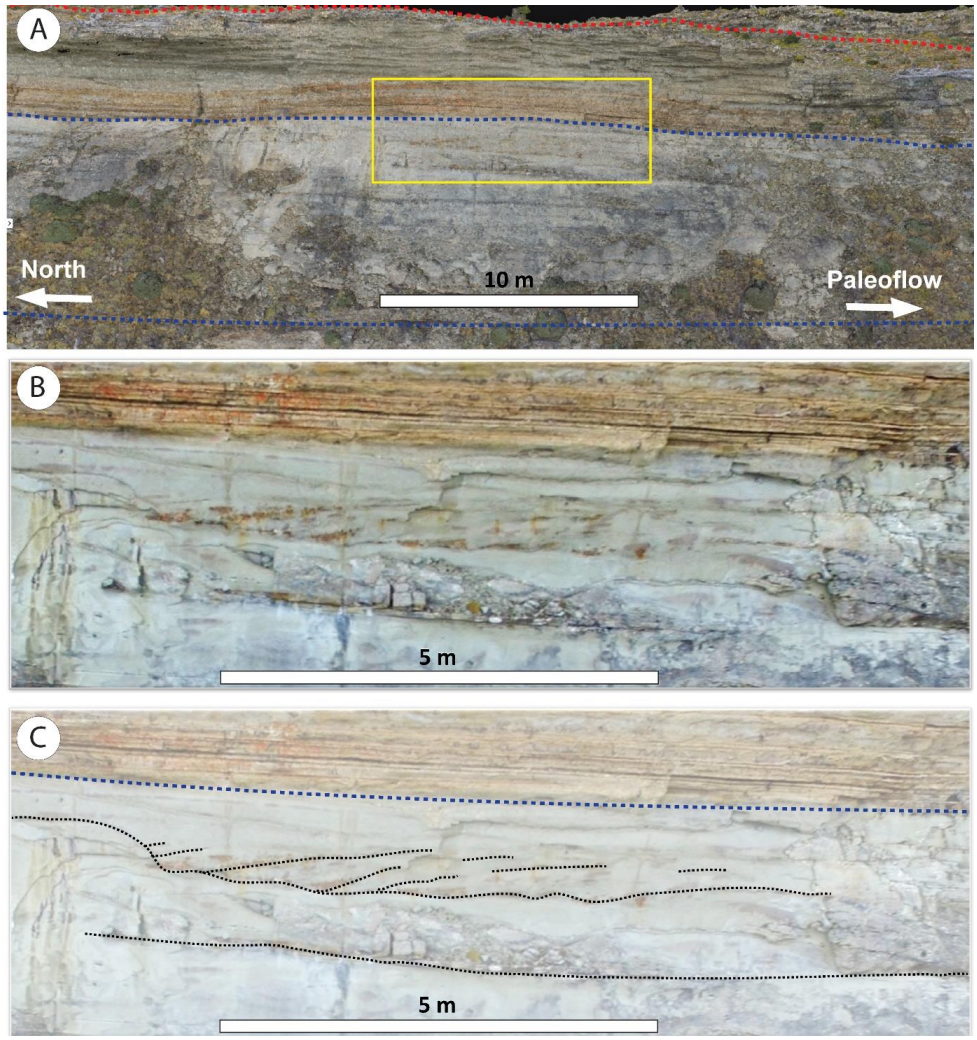

Figure 4.7. Example of discontinuous internal surfaces that become undetectable in amalgamated sandstone. A) Contextual overview (see Figure 4.5B for broader context), yellow box specifies location in (B-C); B) UAV image of inaccessible amalgamated sandstone; C) line drawing of overlying channel element surface (blue) and discontinuous internal element surfaces (black) superimposed on image from part B.

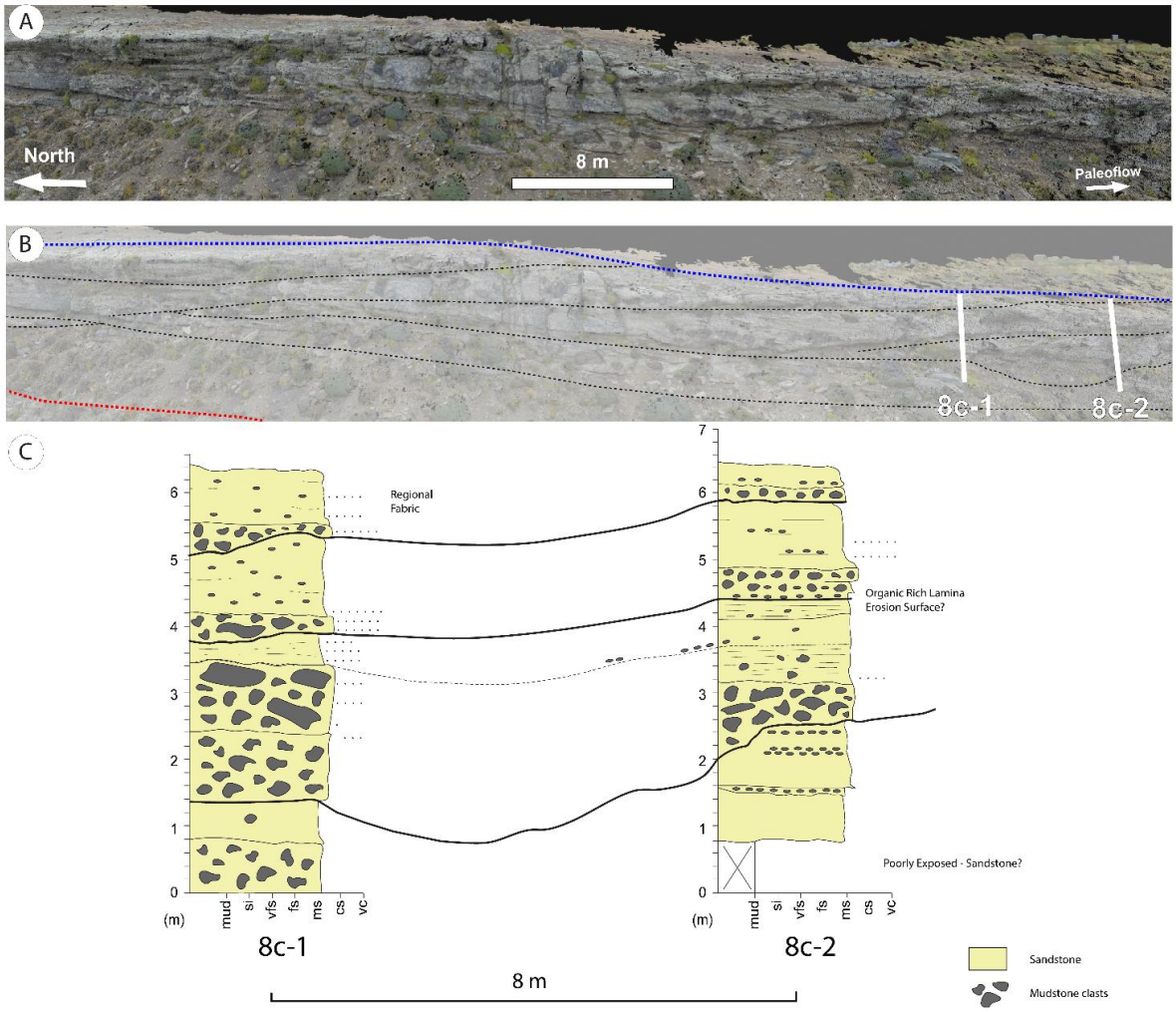

Figure 4.8. Example of internal surfaces revealing nuanced detail of a sequence of low-angle inclined surfaces. A) Oblique view of UAV-SfM DOM; B) line drawing of underlying channel complex boundary (red), overlying channel element boundary (blue), and internal element surfaces (black) superimposed on image in part A. Internal surfaces bound lenticular wedge-shaped bodies with low-angle inclined surfaces that dip in the upslope direction forming a backsetting stacking pattern. These features are similar in scale and geometry to upslope migrating bedforms that were not recognized with conventional field-based approaches. C) Field logs collected following digital DOM analysis to lithologically calibrate digital interpretations of architecture.

4.5.3.2 Interpretation

Interpretations from the digital methods are primarily dependent on the architectural characteristics and surface expression of facies described in Table 4.1. In the model, thick sandstone is distinguished from finer-grained units by outcrop color (i.e., light-colored tan or grey sandstone) and is typically more resistant to weathering than recessive and often vegetated fine-grained lithologies. In some instances, a dark and mottled appearance of the outcrop is associated with mass-transport deposits (F4). As interpreted by traditional outcrop field methods, the base of the prominent recessive interval that separates the two sandstone-dominated packages is interpreted as the bounding surface between two channel complexes and is traceable throughout the study area. Likewise, sedimentary bodies (5-20 m thick) within channel complexes are distinguished by sharp changes in lithology at their base, with a thin recessive layer overlain by sandstone-dominated deposits. These bodies are interpreted as channel elements, and are numbered chronologically in Figure 4.5B.

The internal stratigraphic surfaces which bound sedimentary units within channel elements have various expressions, but generally are indicative of sediment transport and reworking in submarine channels. Similar interpretations have been made for strike-oriented cross-sectional profiles of channel elements (e.g., Hubbard et al., 2014), in which the authors documented a long-lived history of sediment deposition, bypass, and erosion within submarine channels based on variations in facies and the presence of abundant secondary channelform surfaces. Like most previous authors, however, the down-dip expression of erosion surfaces was not explored over greater than 400-500 m. The methods utilized in this study document internal surfaces within largely

amalgamated sandstone facies (F1), revealing lenticular wedges of sediment in the down-channel orientation. Though some of these surfaces terminate or become undetectable after 10s of meters, particularly in amalgamated sandstone (Figure 4.7), some reveal finer-scale geometries and characteristics that were not interpreted from initial field observations. These could be related to bedform or barform deposits in the channels (e.g., Nakajima et al., 2009; Conway et al., 2012) or erosional remnants of previously deposited units (e.g., Heiniö and Davies, 2007; Hage et al., 2018). For example, although the lenticular wedges are largely characterized by apparently structureless sandstone (F1), in a number of instances the DOM reveals a series of inclined surfaces that dip shallowly upslope, forming a backsetting stacking pattern (Figure 4.8). We interpret these internal features to be upslope migrating crescentic bedform deposits, similar in scale and architecture to features recently documented by Hage et al. (2018), West et al. (2019), and Englert et al. (in press).

4.6 Discussion

4.6.1 Comparison of Results from Field and Digital Approaches

Stratigraphic surfaces interpreted in both field and digital methods (Figures 4.5A-B, respectively) produced similar results in broad-scale architecture, but notable differences at finer scales. Both methods identified two channel complexes composed of three distinct channel elements bound by a well-defined, relatively thin interval of recessive material (F2, F3, or F4). In general, digital methods resulted in interpretation of more undulous surfaces, which can be expected with more observation points and less interpolation. The bounding surfaces of channel elements and the channel complex (base of channel element 4) have similar general form between the two methods with two

exceptions: (1) a sharp change in relief (> 5 m) associated with an MTD was recognized at the northern end of the DOM (200 m mark in Figure 4.5B) truncating channel element 3, which was not depicted in interpretations based on conventional methods; and (2) the basal surface of channel element 4 was originally interpreted to truncate to the base of channel element 2 (1500 m mark in Figure 4.5A), whereas the digital interpretations demonstrate remnants of channel element 2 sandstone are preserved (Figure 4.5B).

Differences between interpretations of element-scale channel-form surfaces from conventional (field-based) and digital (UAV-SfM DOM) techniques may be explained by shortcomings in either method. For example, differences may result from the inability to correlate an unexposed contact laterally in the field or the inability to obtain ground data in digital methods. Geometric differences can also be explained by similar challenges; field-based interpretations were commonly based on interpolation between scarcely distributed points, resulting in generally smoother surfaces, while digital observations were often laterally continuous following exposed geometries. In both approaches, interpreted surfaces are strongly influenced by outcrop exposure quality and continuity in addition to stratal geometry. Regardless, differences in overall delineation of channel elements were negligible and produce similar interpretations of channel element stacking patterns.

Internal surfaces within channel elements and the discontinuous bodies they define are less similar between the two methods. DOM observations produced interconnected internal surfaces that were characterized into 75 unique sandstone bodies (Figure 4.5B), while the original interpretations distinguished 24 bodies (Figure 4.5A) in the study area. Fewer discrete bodies can be attributed to inaccessible (e.g., steep cliffs),

apparently structureless, sandstone that could not be directly observed or captured in the field. Conversely, many of the surfaces that define intra-channel element sedimentary units were not confidently characterized using digital methods due to poor contextual exposure or lack of validating field data where surfaces were indistinct with more subtle variations in color or weathering on the DOM (e.g., Figure 4.7).

4.6.2 Implications of New Fine-Scale Digital Observations

Surfaces internal to channel elements identified using digital methods resulted in the recognition of numerous subtle sedimentary geometries that were not documented in conventional field-based techniques. These additional observations reflect formative, near-bed-scale processes (e.g., event scale) that deposited, eroded, and reworked sediments throughout channel evolution. Complementary observations have been noted in most outcrop studies of submarine channel fills, but are challenging to document and have not been characterized extensively down-dip. When combined with outcrop-orientation limitations, a complete 3D perspective is commonly elusive. For example, Hubbard et al. (2014) and Li et al. (2016) represented the poly-phase history of slope channels in dominantly 2D strike-oriented perspectives. The observations made along dip in this study complement their findings, enabling a more complete 3D perspective of internal surface geometry and provides key criteria for the interpretation of formative channel maintenance processes (i.e., erosion, bypass, deposition). In the studied outcrop belt, this locally revealed the prevalence of features attributed to upslope supercritical bedform migration (Figure 4.8), complementing recent studies that have documented similar features in 3D over much shorter dip-oriented outcrop profiles in a variety of

deep-water depositional settings (e.g., Lang et al., 2017; Hage et al., 2018; Ono and Plink-Björklund, 2018; Cornard and Pickering, 2019; Postma et al., 2020).

The prevalence of crescentic-shaped, upslope migrating bedforms on seafloor slopes from prodelta channels to submarine fan lobes is now widely appreciated based on numerous high-resolution seafloor surveys from around the world (Smith et al., 2005; Paull et al., 2011, 2018; Hughes Clarke, 2016; Symons et al., 2016; Hage et al., 2018; Vendettuoli et al., 2019). Although these bedforms are commonly identified on steep slopes in locations with distinct change in flow confinement, there is uncertainty with regard to their prevalence in different segments along submarine sediment-routing systems (e.g., Covault et al., 2017). Nonetheless, such features are perhaps underrepresented in deep-water channel deposits as comparatively fewer examples have been identified in outcrop.

Factors influencing the positive identification of upslope migrating bedform deposits possibly include the low preservation potential for full-relief or near full-relief bedforms, a lack of recognition criteria for their deposits, and a previous under appreciation of their prevalence (Piper and Kontopoulos, 1994; Symons et al., 2016; Hage et al., 2018; Englert et al., in press). Recent work using repeat bathymetry surveys has revealed that depositional geometries resulting from upslope bedform migration are characteristically discontinuous along slope, primarily consisting of the eroded remnants of bedform deposits (Hage et al., 2018; Vendettuoli et al., 2019). Internal channel element surfaces identified from UAV-SfM mapping in this study exhibit similar geometries and we hypothesize that some of these surfaces may derive from bedform migration at the Alvarez Ridge outcrop belt.

4.6.3 Future Considerations for UAV-SfM DOM Mapping

Long-established field-based techniques are essential for characterization of outcrops, but can conceivably be limited by inaccessibility, discontinuity, and obtainable viewpoints. UAV-SfM approaches have recently demonstrated their effectiveness in supplementing field data with additional perspectives allowing for measurement and recognition of intermediate-scale outcrop features (Chesley et al., 2017; Chesley and Leier, 2018; Nesbit et al., 2018; Durkin et al., 2020). In this study, we take this one step further to reveal entire scales of observation that have been previously under documented with use of field-based approaches. Although this study presents a single example, similar cases undoubtedly exist in different depositional settings.

UAV-SfM offers similar advantages to LiDAR methods described more than a decade ago (e.g., Bellian et al., 2005; Buckley et al., 2008; 2010), with added benefits in terms of portability, cost, and practicality for covering large areas. UAV-SfM DOMs are ideal for multi-scale analysis of inaccessible areas allowing users to seamlessly change perspectives, view locations on individual images, and switch between views to 'step back' (or zoom out) and zoom in to the outcrop. Digital datasets can be used to concurrently identify broad-scale stratigraphic architecture and characterize fine-scale features. Though geologic calibration, or ground-truthing, with conventional field-based observations should be carried out whenever possible, we highlight that such best practices are not always feasible.

Although UAV-SfM DOMs can provide spatially constrained perspectives and quantitative constraints, they require careful photogrammetric consideration (i.e., imaging geometry, processing, and georeferencing strategies). In use of SfM, researchers often

emphasize the importance of relative accuracy in lieu of absolute accuracy (and GCPs), but must recognize that both are susceptible to systematic and random errors propagating from unconstrained input data (e.g. poor imaging geometry, lack of control points). In other words, practitioners should be aware that high relative accuracy cannot be assumed in SfM datasets, as geometric errors can propagate with poor consideration of photogrammetric principles. Future research should investigate the effects of imaging, processing, and georeferencing strategies on accuracy of UAV-SfM DOMs in challenging 3D geometries commonly associated with outcrop exposures (e.g., sub-vertical cliffs).

4.7 Conclusions

Outcrops provide opportunities to characterize sedimentological detail within depositional systems across geologic timescales, but outcrop geometry and accessibility may not always allow for complete characterization. Emerging remote sensing techniques, such as UAV-SfM, can supplement field-studies with additional perspectives and reveal nuanced detail that is imperceptible in the field. We present a case study in which UAV-SfM mapping methods reasonably align with previous field-based documentation of coarse-scale stratigraphic architecture in deep-water channel deposits, but also reveal subtle internal details (including the deposits from upslope migrating crescentic bedforms) that were largely overlooked using a conventional field-based approach. These results expose the complexity of channel-filling processes evidenced by numerous wedge-shaped sedimentary bodies internal to channel elements. Our results demonstrate that UAV-SfM workflows can support multi-scale analyses and geological characterizations that have been elusive in some outcrop settings. These supplemental

perspectives can provide new geological insight and enable a key opportunity to link morphodynamic processes with their associated deposits in the rock record. Though this is one case study, we speculate that use of similar strategies could produce comparable outcomes (i.e., reveal new perspectives and subtle geological detail) from challenging outcrop exposures in various depositional environments.

4.8 References

Abreu, V., Sullivan, M., Pirmez, C., and Mohrig, D., 2003, Lateral accretion packages (LAPs): An important reservoir element in deep water sinuous channels: Marine and Petroleum Geology, v. 20, p. 631–648, doi:10.1016/j.marpetgeo.2003.08.003.

Arnot, M.J., Good, T.R., and Lewis, J.J.M., 1997, Photogeological and image-analysis techniques for collection of large-scale outcrop data: Journal of Sedimentary Research, v. 67, p. 984–987, doi:-.

Arnott, R.W.C., 2007, Stratal architecture and origin of lateral accretion deposits (LADs) and conterminuous inner-bank levee deposits in a base-of-slope sinuous channel, lower Isaac Formation (Neoproterozoic), East-Central British Columbia, Canada: Marine and Petroleum Geology, v. 24, p. 515–528, doi:10.1016/j.marpetgeo.2007.01.006.

Baas, J.H., van Kesteren, W., and Postma, G., 2004, Deposits of depletive high-density turbidity currents: A flume analogue of bed geometry, structure and texture: Sedimentology, v. 51, p. 1053–1088, doi:10.1111/j.1365-3091.2004.00660.x.

Bauer, D.B., Hubbard, S.M., Covault, J.A., and Romans, B.W., 2020, Inherited Depositional Topography Control on Shelf-Margin Oversteepening, Readjustment, and Coarse-Grained Sediment Delivery to Deep Water, Magallanes Basin, Chile:

Frontiers in Earth Science, v. 7, doi:10.3389/feart.2019.00358.

Bellian, J.A., Kerans, C., Jennette, D.C., and Jennete, D.C., 2005, Digital outcrop models: applications of terrestrial scanning lidar technology in stratigraphic modeling: Journal of Sedimentary Research, v. 75, p. 166–176, doi:10.2110/jsr.2005.013.

Benhallam, W., Turner, A., Stright, L., and Johnson, C.L., 2016, Spatial Analysis of Channel-Belt Stacking Patterns: Metrics To Discriminate Between Local and Regional Controls On Deposition In the Fluvial John Henry Member of the Straight Cliffs Formation, Southern Utah, U.S.A.: Journal of Sedimentary Research, v. 86, p. 1210–1227, doi:10.2110/jsr.2016.77.

Bouma, A.H., 1962, Sedimentology of Some Flysch Deposits; A Graphic Approach to Facies Interpretation: Amsterdam, Elsevier, 168 p.

Buckley, S.J., Enge, H.D., Carlsson, C., and Howell, J.A., 2010, Terrestrial laser scanning for use in virtual outcrop geology: Photogrammetric Record, v. 25, p. 225–239, doi:10.1111/j.1477-9730.2010.00585.x.

Buckley, S.J., Howell, J.A., Enge, H.D., and Kurz, T.H., 2008, Terrestrial laser scanning in geology: Data acquisition, processing and accuracy considerations: Journal of the Geological Society, v. 165, p. 625–638, doi:10.1144/0016-76492007-100.

Buckley, S.J., Ringdal, K., Naumann, N., Dolva, B., Kurz, T.H., Howell, J.A., and Dewez, T.J.B., 2019, LIME : Software for 3-D visualization , interpretation , and communication of virtual geoscience models: Geosphere, v. 15, p. 1–14, doi:10.1130/GES02002.1/4610849/ges02002.pdf.

Campion, K.M., Sprague, A.R., Mohrig, D., Lovell, R.W., Drzewiecki, P.A., Sullivan, M.D., Ardill, J.A., Jensen, G.N., and Sickafoose, D.K., 2000, Outcrop Expression of

Confined Channel Complexes: Deep-Water Reservoirs of the World: 20th Annual, p. 127–150, doi:10.5724/gcs.00.15.0127.

Casciano, C.I., Patacci, M., Longhitano, S.G., Tropeano, M., McCaffrey, W.D., and Di Celma, C., 2019, Multi-scale analysis of a migrating submarine channel system in a tectonically-confined basin: The Miocene Gorgoglione Flysch Formation, southern Italy: Sedimentology, v. 66, p. 205–240, doi:10.1111/sed.12490.

Chesley, J.T., and Leier, A.L., 2018, Sandstone-body variability in the medial-distal part of an ancient distributive fluvial system, Salt Wash Member of the Morrison Formation, Utah, U.S.A.: Journal of Sedimentary Research, v. 88, p. 568–582.

Chesley, J.T., Leier, A.L., White, S., and Torres, R., 2017, Using unmanned aerial vehicles and structure-from-motion photogrammetry to characterize sedimentary outcrops: An example from the Morrison Formation, Utah, USA: Sedimentary Geology, v. 354, p. 1–8, doi:10.1016/j.sedgeo.2017.03.013.

Clark, J.D., and Pickering, K.T., 1996, Architectural Elements and Growth Patterns of Submarine Channels: Application to Hydrocarbon Exploration: AAPG Bulletin, v. 80, p. 194–221.

Conway, K.W., Barrie, J.V., Picard, K., and Bornhold, B.D., 2012, Submarine channel evolution: Active channels in fjords, British Columbia, Canada: Geo-Marine Letters, v. 32, p. 301–312, doi:10.1007/s00367-012-0280-4.

Cornard, P.H., and Pickering, K.T., 2019, Supercritical-flow Deposits and Their Distribution in a Submarine Channel System, Middle Eocene, Ainsa Basin, Spanish Pyrenees: Journal of Sedimentary Research, v. 89, p. 576–597, doi:10.2110/jsr.2019.34.

Covault, J.A., Kostic, S., Paull, C.K., Ryan, H.F., and Fildani, A., 2014, Submarine channel initiation, filling and maintenance from sea-floor geomorphology and morphodynamic modelling of cyclic steps: Sedimentology, v. 61, p. 1031–1054, doi:10.1111/sed.12084.

Covault, J.A., Kostic, S., Paull, C.K., Sylvester, Z., and Fildani, A., 2017, Cyclic steps and related supercritical bedforms: Building blocks of deep-water depositional systems, western North America: Marine Geology, v. 393, p. 4–20, doi:10.1016/j.margeo.2016.12.009.

Covault, J.A., Sylvester, Z., Hubbard, S.M., Jobe, Z.R., and Sech, R.P., 2016, The Stratigraphic Record of Submarine-Channel Evolution: The Sedimentary Record, v. 14, p. 4–11, doi:10.2110/sedred.2016.3.4.

Daniels, B.G., 2015, Downslope characterization of channel fill and stratigraphic architecture along and ancient basin margin, Tres Pasos Formation, southern Chile: University of Calgary, 153 p.

Daniels, B.G., 2019, Multi-scale stratigraphic and geochronologic investigations of Late Cretaceous sediment-routhing systems, Magallanes Basin, Chile: University of Calgary, 302 p.

Daniels, B.G., Auchter, N.C., Hubbard, S.M., Romans, B.W., Matthews, W.A., and Stright, L., 2018, Timing of deep-water slope evolution constrained by large-n detrital and volcanic ash zircon geochronology, Cretaceous Magallanes Basin, Chile: Bulletin of the Geological Society of America, v. 130, p. 438–454, doi:10.1130/B31757.1.

Daniels, B.G., Hubbard, S.M., Romans, B.W., Malkowski, M.A., Matthews, W.A., Bernhardt, A., Kaempfe, S.A., Jobe, Z.R., Fosdick, J.C., Schwartz, T.M., Fildani, A., and Graham, S.A., 2019, Revised chronostratigraphic framework for the Cretaceous Magallanes-Austral Basin, Última Esperanza Province, Chile: Journal of South American Earth Sciences, v. 94, p. 102209, doi:10.1016/j.jsames.2019.05.025.

Deptuck, M.E., Sylvester, Z., Pirmez, C., and O'Byrne, C., 2007, Migration-aggradation history and 3-D seismic geomorphology of submarine channels in the Pleistocene Benin-major Canyon, western Niger Delta slope: Marine and Petroleum Geology, v. 24, p. 406–433, doi:10.1016/j.marpetgeo.2007.01.005.

Durkin, P.R., Hubbard, S.M., Boyd, R.L., and Leckie, D.A., 2015, Stratigraphic expression of intra-point-bar erosion and rotation: Journal of Sedimentary Research, v. 85, p. 1238–1257, doi:10.2110/jsr.2015.78.

Durkin, P., Hubbard, S.M., Holbrook, J., Weleschuk, Z., Nesbit, P., Hugenholtz, C., Lyons, T., and Smith, D.G., 2020, Recognizing the product of concave-bank sedimentary processes in fluvial meander-belt strata (Accepted): Sedimentology,.

Englert, R.G., Hubbard, S.M., Cartigny, M.J.B., Clare, M.A., Coutts, D., Hage, S., Hughes Clarke, J., Jobe, Z.R., Lintern, G., Stacey, C., and Vendettuoli, D., 2020, Quantifying the 3D stratigraphic expression of upslope-migrating bedforms by integrating seafloor and outcrop observationstle (In Press): Sedimentology,.

Englert, R.G., Hubbard, S.M., Coutts, D.S., and Matthews, W.A., 2018, Tectonically controlled initiation of contemporaneous deep-water channel systems along a Late Cretaceous continental margin, western British Columbia, Canada: Sedimentology,

v. 65, p. 2404–2438, doi:10.1111/sed.12472.

Fildani, A., and Hessler, A.M., 2005, Stratigraphic record across a retroarc basin inversion: Rocas Verdes-Magallanes Basin, Patagonian Andes, Chile: Bulletin of the Geological Society of America, v. 117, p. 1596–1614, doi:10.1130/B25708.1.

Fildani, A., Hubbard, S.M., Covault, J.A., Maier, K.L., Romans, B.W., Traer, M., and Rowland, J.C., 2013, Erosion at inception of deep-sea channels: Marine and Petroleum Geology, v. 41, p. 48–61, doi:10.1016/j.marpetgeo.2012.03.006.

Fosdick, J.C., Graham, S.A., and Hilley, G.E., 2014, Influence of attenuated lithosphere and sediment loading on flexure of the deep-water Magallanes retroarc foreland basin, Southern Andes: Tectonics, v. 33, p. 2505–2525, doi:10.1002/2014TC003684.

Gardner, M.H., Borer, J.M., Melick, J.J., Mavilla, N., Dechesne, M., and Wagerle, R.N., 2003, Stratigraphic process-response model for submarine channels and related features from studies of Permian Brushy Canyon outcrops, West Texas: Marine and Petroleum Geology, v. 20, p. 757–787, doi:10.1016/j.marpetgeo.2003.07.004.

Hage, S., Cartigny, M.J.B., Clare, M.A., Sumner, E.J., Vendettuoli, D., Clarke, J.E.H., Hubbard, S.M., Talling, P.J., Gwyn Lintern, D., Stacey, C.D., Englert, R.G., Vardy, M.E., Hunt, J.E., Yokokawa, M., Parsons, D.R., Hizzett, J.L., Azpiroz-Zabala, M., and Vellinga, A.J., 2018, How to recognize crescentic bedforms formed by supercritical turbidity currents in the geologic record: Insights from active submarine channels: Geology, v. 46, p. 563–566, doi:10.1130/G40095.1.

Heiniö, P., and Davies, R.J., 2007, Knickpoint migration in submarine channels in response to fold growth, western Niger Delta: Marine and Petroleum Geology, v. 24,

p. 434–449, doi:10.1016/j.marpetgeo.2006.09.002.

Hodgetts, D., 2013, Laser scanning and digital outcrop geology in the petroleum industry: A review: Marine and Petroleum Geology, v. 46, p. 335–354, doi:10.1016/j.marpetgeo.2013.02.014.

Hodgetts, D., L. Gawthorpe, R., Wilson, P., and Rarity, F., 2007, Integrating Digital and Traditional Field Techniques Using Virtual Reality Geological Studio (VRGS): 69th EAGE Conference and Exhibition incorporating SPE EUROPEC 2007, p. 11–14, doi:10.3997/2214-4609.201401718.

Hodgson, D.M., Di Celma, C.N., Brunt, R.L., and Flint, S.S., 2011, Submarine slope degradation and aggradation and the stratigraphic evolution of channel-levee systems: Journal of the Geological Society, v. 168, p. 625–628, doi:10.1144/0016-76492010-177.

Hubbard, S.M., Covault, J.A., Fildani, A., and Romans, B.W., 2014, Sediment transfer and deposition in slope channels: Deciphering the record of enigmatic deep-sea processes from outcrop: Bulletin of the Geological Society of America, v. 126, p. 857–871, doi:10.1130/B30996.1.

Hubbard, S.M., Fildani, A., Romans, B.W., Covault, J.A., and McHargue, T.R., 2010, High-Relief Slope Clinoform Development: Insights from Outcrop, Magallanes Basin, Chile: Journal of Sedimentary Research, v. 80, p. 357–375, doi:10.2110/jsr.2010.042.

Hughes Clarke, J.E., 2016, First wide-angle view of channelized turbidity currents links migrating cyclic steps to flow characteristics: Nature Communications, v. 7, doi:10.1038/ncomms11896.

Katz, H.R., 1963, Revision of Cretaceous stratigraphy in Patagonian Cordillera of Ultima Esperanza, Magallanes Province, Chile: AAPG Bulletin, v. 47, p. 506–524.

Lang, J., Brandes, C., and Winsemann, J., 2017, Erosion and deposition by supercritical density flows during channel avulsion and backfilling: Field examples from coarse-grained deepwater channel-levée complexes (Sandino Forearc Basin, southern Central America): Sedimentary Geology, v. 349, p. 79–102, doi:10.1016/j.sedgeo.2017.01.002.

Li, P., Kneller, B.C., Hansen, L., and Kane, I.A., 2016, The classical turbidite outcrop at San Clemente, California revisited: An example of sandy submarine channels with asymmetric facies architecture: Sedimentary Geology, v. 346, p. 1–16, doi:10.1016/j.sedgeo.2016.10.001.

Lowe, D.R., 1982, Sediment Gravity Flows: II Depositional Models with Special Reference to the Deposits of High-Density Turbidity Currents: Journal of Sedimentary Research, v. 52, p. 270–297, doi:10.1306/212F7F31-2B24-11D7-8648000102C1865D.

Macauley, R. V., and Hubbard, S.M., 2013, Slope channel sedimentary processes and stratigraphic stacking, Cretaceous Tres Pasos Formation slope system, Chilean Patagonia: Marine and Petroleum Geology, v. 41, p. 146–162, doi:10.1016/j.marpetgeo.2012.02.004.

Malkowski, M.A., Grove, M., and Graham, S.A., 2016, Unzipping the Patagonian Andes-Long-lived influence of rifting history on foreland basin evolution: Lithosphere, v. 8, p. 23–28, doi:10.1130/L489.1.

Malkowski, M.A., Jobe, Z.R., Sharman, G.R., and Graham, S.A., 2018, Down-slope facies variability within deep-water channel systems: Insights from the Upper Cretaceous Cerro Toro Formation, southern Patagonia: Sedimentology, v. 65, p. 1918–1946, doi:10.1111/sed.12452.

Mayall, M., Jones, E., and Casey, M., 2006, Turbidite channel reservoirs-Key elements in facies prediction and effective development: Marine and Petroleum Geology, v. 23, p. 821–841, doi:10.1016/j.marpetgeo.2006.08.001.

McCaffrey, K.J.W., Jones, R.R., Holdsworth, R.E., Wilson, R.W., Clegg, P., Imber, J., Holliman, N.S., and Trinks, I., 2005, Unlocking the spatial dimension: digital technologies and the future of geoscience fieldwork: Journal of the Geological Society, v. 162, p. 927–938, doi:10.1144/0016-764905-017.

McHargue, T., Pyrcz, M.J., Sullivan, M.D., Clark, J.D., Fildani, A., Romans, B.W., Covault, J.A., Levy, M., Posamentier, H.W., and Drinkwater, N.J., 2011, Architecture of turbidite channel systems on the continental slope: Patterns and predictions: Marine and Petroleum Geology, v. 28, p. 728–743, doi:10.1016/j.marpetgeo.2010.07.008.

Mutti, E., and Normark, W.R., 1987, Comparing examples of modern and ancient turbidite systems: problems and concepts, *in* Marine clastic sedimentology, Springer, Dordrecht, p. 1–38.

Nakajima, T., Peakall, J., McCaffrey, W.D., Paton, D.A., and Thompson, P.J.P., 2009, Outer-Bank Bars: A New Intra-Channel Architectural Element within Sinuous Submarine Slope Channels: Journal of Sedimentary Research, v. 79, p. 872–886, doi:10.2110/jsr.2009.094.

Nesbit, P.R., Boulding, A., Hugenholtz, C., Durkin, P., and Hubbard, S., 2020, Visualization and Sharing of 3D Digital Outcrop Models to Promote Open Science: GSA Today, doi:10.1130/gsatg425a.1.

Nesbit, P.R., Durkin, P.R., Hugenholtz, C.H., Hubbard, S.M., and Kucharczyk, M., 2018, 3-D stratigraphic mapping using a digital outcrop model derived from UAV images and structure-from-motion photogrammetry: Geosphere, v. 14, p. 1–18, doi:10.1130/GES01688.1.

Nesbit, P.R., and Hugenholtz, C.H., 2019, Enhancing UAV-SfM 3D model accuracy in high-relief landscapes by incorporating oblique images: Remote Sensing, v. 11, doi:10.3390/rs11030239.

Nieminski, N.M., and Graham, S.A., 2017, Modeling Stratigraphic Architecture Using Small Unmanned Aerial Vehicles and Photogrammetry: Examples From the Miocene East Coast Basin, New Zealand: Journal of Sedimentary Research, v. 87, p. 126–132, doi:10.2110/jsr.2017.5.

Normark, W.R., Posamentier, H., and Mutti, E., 1993, Turbidite Systems: State of the Art and Future Directions: Reviews of Geophysics, v. 31, p. 91–116.

Ono, K., and Plink-Björklund, P., 2018, Froude supercritical flow bedforms in deepwater slope channels? Field examples in conglomerates, sandstones and fine-grained deposits (P. Talling, Ed.): Sedimentology, v. 65, p. 639–669, doi:10.1111/sed.12396.

Paull, C.K., Caress, D.W., Ussler, W., Lundsten, E., and Meiner-Johnson, M., 2011, High-resolution bathymetry of the axial channels within Monterey and Soquel submarine canyons, offshore central California: Geosphere, v. 7, p. 1077–1101, doi:10.1130/GES00636.1.

Paull, C.K., Talling, P.J., Maier, K.L., Parsons, D., Xu, J., Caress, D.W., Gwiazda, R., Lundsten, E.M., Anderson, K., Barry, J.P., Chaffey, M., O'Reilly, T., Rosenberger, K.J., Gales, J.A., Kieft, B., McGann, M., Simmons, S.M., McCann, M., Sumner, E.J., Clare, M.A., and Cartigny, M.J., 2018, Powerful turbidity currents driven by dense basal layers: Nature Communications, v. 9, p. 1–9, doi:10.1038/s41467-018-06254-6.

Pemberton, E.A.L., Hubbard, S.M., Fildani, A., Romans, B., and Stright, L., 2016, The stratigraphic expression of decreasing confinement along a deep-water sediment routing system: Outcrop example from southern Chile: Geosphere, v. 12, p. 114–134, doi:10.1130/GES01233.1.

Pickering, K.T., Clark J.D., Smith, R.D.A., Hiscott, R.N., Ricci Lucchi, F., and Kenyon, N.H., 1995, Architectural element analysis of turbidite systems, and selected topical problems for sand-prone deep-water systems, *in* Pickering, K.T., Hiscott, R.N., Kenyon, N.H., Ricci Lucchi, F., and Smith, R.D.A. eds., Atlas of Deep Water Environments: Architectural Style in Turbidite Systems, London, Chapman and Hall, p. 1–10.

Piper, D.J.W., and Kontopoulos, N., 1994, Bed Forms in Submarin Channels: Comparison of Ancient Examples From Greece with Studies of Recent Turbidite Systems: Journal of Sedimentary Research1, v. A64, p. 247–252, doi:1073-130X/94/0A64-247.

Pitts, A.D., Casciano, C.I., Patacci, M., Longhitano, S.G., Di Celma, C., and McCaffrey, W.D., 2017, Integrating traditional field methods with emerging digital techniques for enhanced outcrop analysis of deep water channel-fill deposits: Marine and

Petroleum Geology, v. 87, p. 2–13, doi:10.1016/j.marpetgeo.2017.05.001.

Plink-Bjorklund, P., Mellere, D., and Steel, R.J., 2001, Turbidite variability and architecture of sand-prone, deep-water slopes: eocene clinoforms in the central basin, spitsbergen: Journal of Sedimentary Research, v. 71, p. 895–912, doi:10.1306/030501710895.

Posamentier, H.W., and Kolla, V., 2003, Seismic geomorphology and stratigraphy of depositional elements in deep-water settings: Journal of Sedimentary Research, v. 73, p. 367–388.

Postma, G., Lang, J., Hoyal, D.C., Fedele, J.J., Demko, T., Abreu, V., and Pederson, K.H., 2020, Reconstruction of bedform dynamics controlled by supercritical flow in the channel-lobe transition zone of a deep-water delta (Sant Llorenç del Munt, north-east Spain, Eocene): Sedimentology, doi:10.1111/sed.12735.

Rittersbacher, A., Buckley, S.J., Howell, J.A., Hampson, G.J., and Vallet, J., 2014, Helicopter-based laser scanning : a method for quantitative analysis of large-scale sedimentary architecture: Geological Society, London, Special Publications, v. 387, p. 185–202, doi:10.1144/SP387.3.

Romans, B.W., Castelltort, S., Covault, J.A., Fildani, A., and Walsh, J.P., 2016, Environmental signal propagation in sedimentary systems across timescales: Earth-Science Reviews, v. 153, p. 7–29, doi:10.1016/j.earscirev.2015.07.012.

Romans, B.W., Fildani, A., Hubbard, S.M., Covault, J.A., Fosdick, J.C., and Graham, S.A., 2011, Evolution of deep-water stratigraphic architecture, Magallanes Basin, Chile: Marine and Petroleum Geology, v. 28, p. 612–628, doi:10.1016/j.marpetgeo.2010.05.002.

Schlumberger, 2020, Petrel E&P Software Platform: Schlumberger Limited, Houston, Texas, https://www.software.slb.com/products/petrel.

Smith, D.P., Ruiz, G., Kvitek, R., and Iampietro, P.J., 2005, Semiannual patterns of erosion and deposition in upper Monterey Canyon from serial multibeam bathymetry: Bulletin of the Geological Society of America, v. 117, p. 1123–1133, doi:10.1130/B25510.1.

Sprague, A.R., Garfield, T.R., Goulding, F.J., Beaubouef, R.T., Sullivan, M.D., C., R., Campion, K.M., Sickafoose, D.K., Abreu, V., Schellpeper, M.E., Jensen, G.N., Jennette, D.C., Pirmez, C., Dixon, B.T., Ying, D., Ardill, J., Mohrig, D.C., M.L., P., Farrell, M.E., and Mellere, D., 2005, Integrated slope channel depositional models: the key to successful prediction of reservoir presence and quality in offshore West Africa: CIPM, cuarto EExitep, p. 1–13.

Sprague, A.R., Sullivan, M.D., Campion, K.M., Jensen, G.N., Goulding, F.J., Sickafoose, D.K., and Jennette, D.C., 2002, The physical stratigraphy of deep-water strata: a hierarchical approach to the analysis of genetically related elements for improved reservoir prediction, *in* AAPG Annual Meeting Programs with Abstracts, Houston, Texas, p. 10–13.

Stevenson, C.J., Jackson, C.A.-L., Hodgson, D.M., Hubbard, S.M., and Eggenhuisen, J.T., 2015, Deep-water sediment bypass: Journal of Sedimentary Research, v. 85, p. 1058–1081, doi:10.2110/jsr.2015.63.

Sumner, E.J., Amy, L.A., and Talling, P.J., 2008, Deposit Structure and Processes of Sand Deposition from Decelerating Sediment Suspensions: Journal of Sedimentary Research, v. 78, p. 529–547, doi:10.2110/jsr.2008.062.

Symons, W.O., Sumner, E.J., Talling, P.J., Cartigny, M.J.B., and Clare, M.A., 2016, Large-scale sediment waves and scours on the modern seafloor and their implications for the prevalence of supercritical flows: Marine Geology, v. 371, p. 130–148, doi:10.1016/j.margeo.2015.11.009.

Talling, P.J., Allin, J., Armitage, D.A., Arnott, R.W.C., Cartigny, M.J.B., Clare, M.A., Felletti, F., Covault, J.A., Girardclos, S., Hansen, E., Hill, P.R., Hiscott, R.N., Hogg, A.J., Clarke, J.H., Jobe, Z.R., Malgesini, G., Mozzato, A., Naruse, H., Parkinson, S., Peel, F.J., Piper, D.J.W., Pope, E., Postma, G., Rowley, P., Sguazzini, A., Stevenson, C.J., Sumner, E.J., Sylvester, Z., Watts, C., and Xu, J., 2015, Key Future Directions For Research On Turbidity Currents and Their Deposits: Journal of Sedimentary Research, v. 85, p. 153–169, doi:10.2110/jsr.2015.03.

Talling, P.J., Masson, D.G., Sumner, E.J., and Malgesini, G., 2012, Subaqueous sediment density flows: Depositional processes and deposit types: Sedimentology, v. 59, p. 1937–2003, doi:10.1111/j.1365-3091.2012.01353.x.

Vendettuoli, D., Clare, M.A., Hughes Clarke, J.E., Vellinga, A., Hizzet, J., Hage, S., Cartigny, M.J.B., Talling, P.J., Waltham, D., Hubbard, S.M., Stacey, C., and Lintern, D.G., 2019, Daily bathymetric surveys document how stratigraphy is built and its extreme incompleteness in submarine channels: Earth and Planetary Science Letters, v. 515, p. 231–247, doi:10.1016/j.epsl.2019.03.033.

Walker, R.G., 1978, Deep-water sandstone facies and ancient submarine fans: models for exploration for stratigraphic traps: AAPG Bulletin, v. 62, p. 932–966.

West, L.M., Perillo, M.M., Olariu, C., and Steel, R.J., 2019, Multi-event organization of deepwater sediments into bedforms: Long-lived, large-scale antidunes preserved in

deepwater slopes: Geology, v. 47, p. 391–394, doi:10.1130/G45825.1.

Wilson, T.J., 1991, Transition from back-arc to foreland basin development in the southernmost Andes: Stratigraphic record from the Ultima Esperanza District, Chile: Geological Society of America Bulletin, v. 103, p. 98–111.

Chapter 5

Visualization and Sharing of 3D Digital Outcrop Models to Promote Open Science

A version of this chapter was published as:

Nesbit, P.R., Boulding, A.D., Hugenholtz, C.H., Durkin, P.R., and Hubbard, S.M. 2020. Visualization and sharing of 3D Digital Outcrop Models to promote open science. *GSA Today*, 30 (5), p. 4-10. doi:10.1130/GSATG425A.1

5.1 Abstract

High-resolution 3D datasets, such as digital outcrop models (DOMs) are increasingly being used by geoscientists to supplement field observations and enable multiscale and repeatable analysis that was previously difficult, if not impossible, to achieve using conventional methods. Despite an increasing archive of DOMs driven by technological advances, the ability to share and visualize these datasets remains a challenge due to large files and the need for specialized software. Together, these issues limit the open exchange of datasets and interpretations. To promote greater data accessibility for a broad audience, we implement three modern platforms for disseminating models and interpretations within an open science framework: Sketchfab, potree, and Unity. Web-based platforms, such as Sketchfab and potree, render interactive 3D models within standard web browsers with limited functionality, whereas game engines, such as Unity, enable development of fully customizable 3D visualizations compatible with multiple operating systems. We review the capabilities of each platform using a DOM of an extensive outcrop exposure of Late Cretaceous fluvial stratigraphy

generated from UAV images. Each visualization platform provides end-users with digital access and intuitive controls to interact with large DOM datasets, without the need for specialized software and hardware. We demonstrate a range of features and interface customizability that can be created and suggest potential use cases to share interpretations, reinforce student learning, and enhance scientific communication through unique and accessible visualization experiences.

5.2 **Introduction**

High-resolution three-dimensional (3D) digital models are becoming increasingly common datasets in academic and commercial applications. In the geosciences specifically, digital outcrop models (DOMs), or virtual outcrops, can provide geoscientists with photorealistic models that preserve spatial precision, dimensionality, and geometric relationships between geologic features that are inherently three-dimensional and susceptible to distortion and/or loss of information when rendered in 2D (Bellian et al., 2005; McCaffrey et al., 2005; Jones et al., 2009). Digital 3D mapping approaches using DOMs have enabled geoscientists to perform supplemental measurements, correlations, and interpretations that are difficult, or impossible, to obtain with traditional methods (Figure 5.1-2; Pavlis and Mason, 2017; Nesbit et al., 2018).

Until recently, however, collection and use of digital datasets has been limited to specialists, due to hardware and software limitations. A number of methods are now available for collecting and processing 3D models. In particular, structure-from-motion and multi-view stereo (SfM-MVS) photogrammetry software, commonly paired with uninhabited aerial vehicles (UAVs), enables geoscientists to produce photorealistic

DOMs through a highly streamlined UAV-SfM workflow (Chesley et al., 2017; Nieminski and Graham, 2017; Pavlis and Mason, 2017; Nesbit and Hugenholtz, 2019). Related efforts have centered on the development of 3D software solutions with tools for geoscience applications. Custom software packages, such as Virtual Reality Geology Studio (VRGS; Hodgetts et al., 2007) and LIME (Buckley et al., 2019), offer users a lightweight executable with tools and opportunities to analyze and revisit data at multiple scales. Open source programs, such as Blender, can also be used for data exploration and measurement, and some (e.g., CloudCompare; CloudCompare, 2019) integrate geoscience specific tools (e.g., Brodu and Lague, 2012; Dewez et al., 2016; Thiele et al., 2017).

Figure 5.1. Geologic interpretations (line drawing on 2D field photograph), a common conventional method to highlight stratigraphic architecture and distribution of related units. Mudstones are grey to light brown, sandstones are light grey to white. This process is often performed on photos or a photomosaic acquired in the field.

Although acquiring DOMs has become more straightforward and various 3D analysis programs are available, dissemination of DOMs, interpretations, and results has remained a challenge due to software and file size barriers. Specialty 3D programs are often hindered by product licensing and can involve a considerable learning curve to understand controls, file formats, and integrated tools. Furthermore, DOMs can easily exceed multiple gigabytes (GB) in size, which can be taxing on computational resources

for rendering, file storage, and data transfer. With the growing collection of high-resolution DOMs and similar 3D datasets, there is a need for dedicated, intuitive, and accessible 3D visualization platforms.

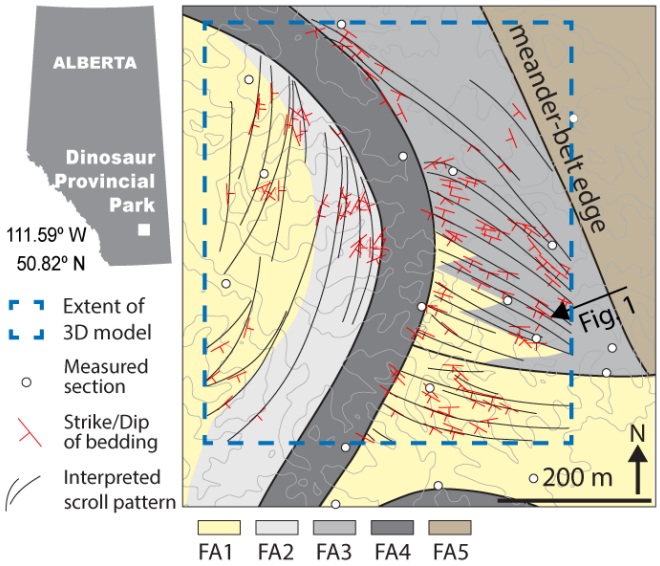

Figure 5.2. Traditional geologic map used to share field measurements, observations, and interpretations in 2D plan-view. This geologic map was constructed from the integration of traditional field work methods (measured sections as well as paleoflow and bedding measurements) with DOM mapping to characterize heterolithic channel-belt deposits exposed at Dinosaur Provincial Park, southeastern Alberta, Canada. Field-based Facies Associations (FA)1: sandy point bar; FA2: heterolithic point bar; FA3 Counter-point bar; FA4: abandoned channel; FA5: mudstone. Bedding surfaces, noted in Figure 5.1 (red), were digitally mapped on the 3D model and yield a more refined and detailed interpretation of accretion surface orientation and stratigraphic architecture. These methods are being widely applied, yet the results are difficult to disseminate and share in 3D.

Given the challenges outlined above, we examined existing visualization solutions that could potentially enable sharing of DOMs and support open science through increased data accessibility. To provide a functional introduction to modern visualization platforms, we illustrate the capabilities and functionality of two web-based interfaces

(Sketchfab and potree) and a cross-platform videogame engine (Unity) using a geologic case study. A DOM was produced through a UAV-SfM workflow for an extensive outcrop (1 km^2) exposed within the badland landscape of Dinosaur Provincial Park (Alberta, Canada). Each visualization platform provides access to the large DOM through an intuitive lightweight interface without the need for high-end hardware, specialized software, or transfer and storage of large files. This prompts an increased ability to share datasets, interpretations, and results with a wider community, expanding opportunities for scientific communication and open science education.

5.3 Related Work

Visualization of digital 3D models has been practical for more than two decades, however early geoscience applications were typically restricted to dedicated geovisualization labs and required specialized software (e.g. Thurmond et al., 2006; Jones et al., 2009; Bilke et al., 2014). Today, visualization of large 3D datasets is no longer limited to sophisticated labs, but rather an average computer can render 3D models efficiently, due in large part to inexpensive hardware, such as dedicated graphics processing units (GPUs). Despite the capabilities of modern computing hardware, bottlenecks remain with a lack of accessible visualization software and need to transfer large files.

Though separate 3D viewers are available to supplement proprietary software (e.g., Trimble RealWorks, FugroViewer), they typically require local storage of large files, learning curves, and have associated licensing restrictions. Alternative applications, such as digital globes (e.g., Google Earth) are a popular method for disseminating spatial and non-spatial data in an interactive, semi-immersive environment, with intuitive

controls (Goodchild et al., 2012). Digital globes have been used to create 'virtual field trips' (McCaffrey et al., 2010; Simpson and DePaor, 2010; DePaor and Whitmeyer, 2011) and present 3D datasets (Blenkinsop, 2012; DePaor, 2016). Although digital globes provide tremendous benefits, displaying DOMs within digital globes requires a significant reduction of detail and results in overlay issues relative to underlying base layers (Tavani et al., 2014).

Web-based dissemination may be one of the most promising and practical means for rapidly streaming 3D digital datasets without transferring raw data (Turner, 2006; von Reumont et al., 2013). Advances of application programming interfaces (APIs), such as WebGL, allow modern internet browsers to access the local GPU to improve rendering of 2D and 3D graphics, without the need for plug-ins or extensions (Boutsi et al., 2019). Though not guaranteed, WebGL enables GPU functionality on various operating systems and devices (Schuetz, 2016). Several proprietary web viewers, such as Sketchfab (https://www.sketchfab.com), use WebGL for sharing 3D models. Proprietary web-based viewers have recently been used by geologic databases (e.g., Safari Database, https://www.safaridb.com: Howell et al., 2014; eRock: Cawood et al., 2019).

Web viewers based on open source code, such as potree (Schuetz, 2016), use WebGL API to efficiently render massive point clouds (>10^9 points) in standard internet browsers. Potree does not require end-users to install software or download large datasets (Schuetz, 2016) and has been adopted by various organizations, including the USGS for sharing and visualizing national topographic LiDAR datasets (USGS, 2019). Similarly, OpenTopography and Pix4Dcloud provide online viewers, similar to potree, allowing subscribers to share point clouds through standard web-browsers.

Alternative methods have incorporated use of game engines to create customized geovisualizations compatible with various operating systems. Unity and Unreal Engine are two popular game development platforms that are well-documented, have vast online programming communities, and are available for free to developers producing revenue below a defined threshold. Recently, game engines have been used in the geosciences for sharing 3D datasets in immersive VR (Bilke et al., 2014), translating ArcGIS data into a 3D environment using Unity (Robinson et al., 2015), and presenting virtual archaeological sites (Martinez-Rubi et al., 2016; Boutsi et al., 2019).

Modern visualization platforms provide opportunities for researchers to extend access of large 3D models, such as DOMs, to a wider audience, but have seldom been used in geoscience applications. Researchers commonly rely on specialist software for analysis and visualization (e.g., CloudCompare, VRGS), but often revert to traditional formats for sharing data (e.g., 2D screen captures or fly-through videos with pre-defined viewpoints). Through the presentation of a large DOM in a complex badland landscape, we examine the advantages and limitations associated with three existing visualization platforms that could potentially enhance 3D data dissemination and promote increased accessibility and educational opportunities.

5.4 Case Study: Fluvial Stratigraphy, Dinosaur Provincial Park

5.4.1 Geological overview

Dinosaur Provincial Park is a UNESCO World Heritage Site in southeastern Alberta, Canada recognized for an abundance of well-preserved dinosaur fossils and characteristic badland topography (Dodson, 1971; Currie and Koppelhus, 2005). This case study presents a 1 km^2 subsection within the northeastern portion of the park

containing extensive 3D exposures of the Late Cretaceous Dinosaur Park Formation (Wood et al., 1988; Eberth and Hamblin, 1993). Contrasting layers of siltstone and fine- to medium-grained sandstone along with the stratigraphic architecture are representative of successive meandering channel belts cutting through adjacent floodplain mudstones (Figure 5.1-2; Smith et al., 2009; Nesbit et al., 2018; Durkin et al., 2020). Most of the park is a natural preserve accessible only through research permits or guided programs. The digital model provides a viewing window into a small section of the park without disrupting the natural wildlife and landscape.

5.4.2 Data collection and DOM processing

Images were collected through eight flights with a sensefly eBee fixed-wing UAV equipped with a Sony WX220 18.2 megapixel camera, resulting in 1760 images. Images were recorded at a pitch angle of 10º off-nadir to increase point visibility along sub-vertical surfaces and increase precision of final models within the high relief topography (Nesbit and Hugenholtz, 2019). Images were processed using Pix4Dmapper v4.3 following a similar workflow described by previous authors (Küng et al., 2012; Nesbit et al., 2018). Following initial processing, the model was divided into four quadrants and processed into a dense point cloud and 3D textured mesh. Mesh outputs were exported as Autodesk Filmbox (.fbx) format, which generally result in smaller file sizes than commonly used 3D polygon (.ply) and wavefront (.obj) formats.

5.4.3 Visualization approaches

DOMs are presented in textured mesh and dense point cloud formats, using three different visualization platforms (Sketchfab, potree, and Unity). Although other platforms are available, these were intentionally selected for their ability to provide end-users with

access to 3D datasets without specialty software or transfer of large datasets and are representative of the current capabilities of modern viewers.

5.4.3.1 Web-based 3D mesh (Sketchfab)

Using a web-based interface, Sketchfab allows authors to intuitively upload models, define rendering options (e.g., lighting, material properties), and provide supplementary annotations (Figure 5.3A). Upload limitations of 200 MB, including all mesh and texture components, prevented rendering of the complete 1 km^2 field area within a single viewer without significant texture distortion. To preserve detail within the field area, we present each quadrant separately. Multiple texture resolutions and VR compatibility are automatically generated during upload to provide end-users with different Level of Detail (LoD) rendering options based on the capabilities of their viewing device. Location specific annotations describing geologic features and concepts to end-users were added to models using the upload interface. Additional datasets could not be integrated within 3D model space.

5.4.3.2 Web-based 3D point cloud (potree)

Viewers using potree code can render raw point clouds and integrate multiple datasets into a single viewer with customizable options. The dense point cloud for the 1 km^2 field area is approximately 25.5 GB and contains more than 805 million points (Figure 5.3B). Point cloud datasets can be compressed (from .las to .laz format) to reduce file size and converted into potree file and folder structure for efficient tile-based rendering using the potree converter (Schuetz, 2016) with a final size of 3.5 GB. By default, the potree code includes an interactive overview map that displays the viewer's location and view direction, various navigation options and settings, and several

measurement tools allowing end-users to record simple measurements, including distances, areas, volumes, and topographic cross-sections. Following conversion, the files and folder structure can be added to a web host and dispersed through a standard web domain. Information on getting started can be found on the potree GitHub page or homepage (http://www.potree.org). An example is presented in Figure 5.3B using the Pix4Dcloud viewer, which implements the potree library.

5.4.3.3 Videogame engine (Unity)

Videogame engines allow the production of unique end-user experiences through customized data visualization and presentation (Figure 5.4). Unity provides a platform to design and develop videogames and is well-documented through user manuals, community forums, and online tutorials (e.g., https://unity.com/learn/get-started). The program interface contains simple 'drag and drop' functions for creation of simple scenes, but also allows fully customizable objects and interaction through scripting. Unity supports various formats, including point clouds, meshes, and 2.5D digital elevation models (DEMs). However, point cloud rendering through Unity can be challenging (Fraiss, 2017) and DEM interpolations are susceptible to distortion along slopes (Bellian et al., 2005; Pavlis and Mason, 2017). Therefore, we used 3D meshes (.fbx files) and associated textures (.jpg), which made up much of the final videogame file size (~1 GB). Navigation within the scene was programmed through a first-person movement script, in which the camera is controlled by directional keys on the keyboard and orientation based on the mouse. Camera movement was restricted within the scene boundaries by enabling the 'mesh collider' option within the mesh options panel. Various components were added to the scene, such as the sky background, surrounding topography, and interactive

features. Sky textures were adapted from the Unity Asset Store (assetstore.unity.com). Surrounding topography was added by creating a Terrain object within Unity, defining height values by importing a 10 m DEM (AltaLIS, 2017), textured with 10 m true-color satellite image (Copernicus, 2018). Interactive features were added to a dropdown menu within the user interface (UI) and included several 'points of interest' that automatically transport end-users to areas with educational information within the scene. The UI menu allows users to navigate between integrated datasets and associated information panels within the scene and can be exited at anytime to return to free fly mode.

5.5 Discussion

Sharing of large 3D datasets without specialist software is possible through modern viewers, however, a host of challenges remain with current solutions before the full potential can be realized. Data acquisition technologies continue to offer higher resolutions and larger file sizes. Contrastingly, visualization platforms commonly limit file sizes, forcing a compromise between field area extent and detail. As demand increases for sharing larger 3D datasets, more advanced multi-resolution rendering solutions, such as LoD in Sketchfab and LIME or tiled approaches similar to potree, will be essential. Options for end-users to select display quality based on capabilities of their machine provides additional avenues to smoothly render large datasets; for example, the Unity UI offers *Quality* and *Screen Resolution* settings upon startup and potree code provides adjustable options for *Point Budget* and *Quality*.

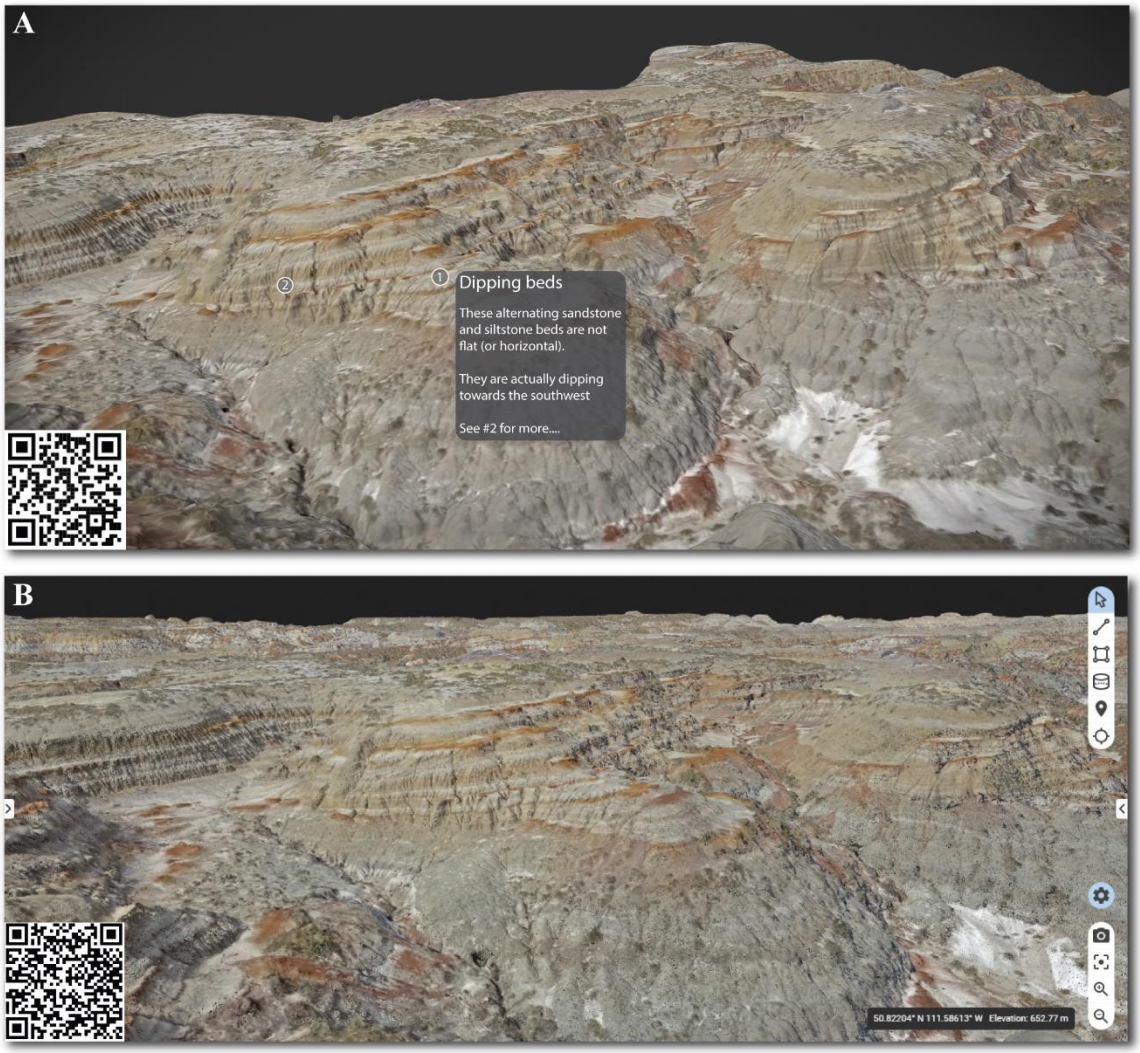

Figure 5.3. Digital outcrop models (DOMs) of the heterolithic channel-belt deposits in Figure 5.1, presented in two different viewers. A) Sketchfab viewer contains 3D textured mesh DOM, but is limited by resolution and only supports text annotations to provide supplemental information; note the limited field area loaded to preserve detail in texture and topography – additional interactive models of the field area can be found on the web at https://sketchfab.com/paulnesbit or by following the QR code. Additional proprietary web viewers include Euclidean Vault (https://www.euclideon.com/vaultinfo/), and voxxlr (https://www.voxxlr.com/). B) Visualization of the 3D dense point cloud DOM of the entire 1 km^2 field area (>805 million points) in a standard web browser using potree code applied in customized web viewer from Pix4D. QR code provides digital access to the fully interactive viewer also available at http://tiny.cc/Pix4DpotreeViewer.

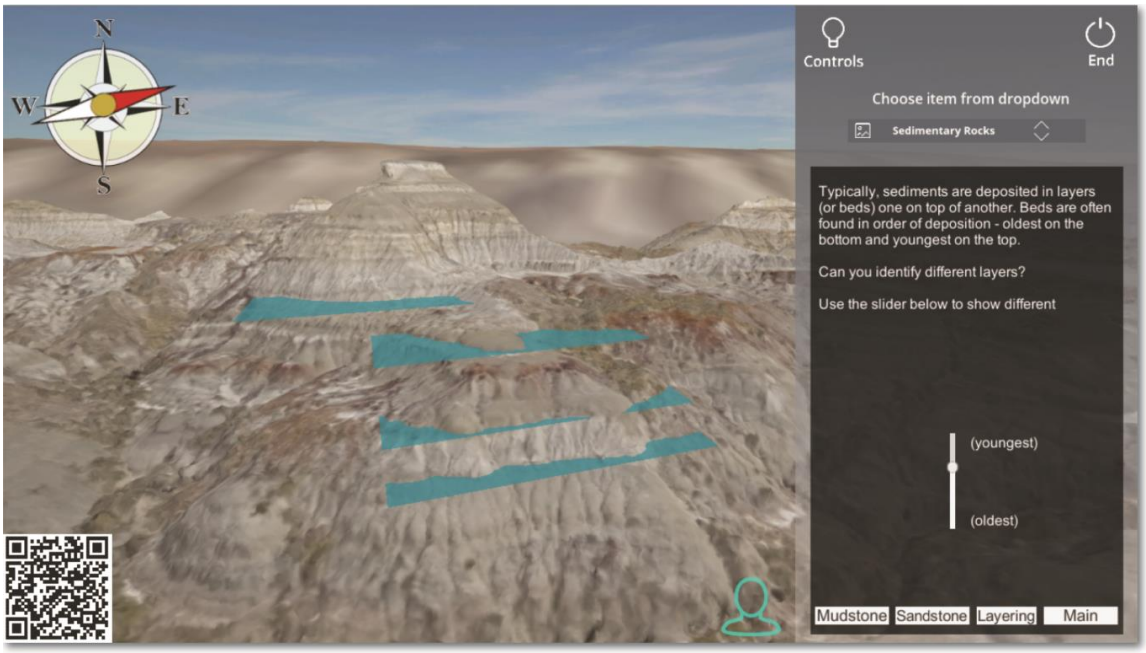

Figure 5.4. Videogame viewer (executable application) of the entire 1 km^2 field area rendered as a textured mesh and created with Unity. Note the dynamic orientation arrow in the upper left corner of the game, the options menu to the right of the screen and interpretations of geologic surfaces turned ‘on’. Drop-down menu in the side panel provides end-users with options to navigate to pre-defined 'points of interest' throughout the field area, simulating virtual field trip stops. Note the resolution difference between the foreground UAV model and the peripheral topography and landscape, created with a DEM draped with a 10 m satellite image. End-users can also select 'Free Fly' mode in order to navigate throughout the field site on their own. Full interactive viewer available in Supplementary File 5.1 and 5.2 (Appendix C; also accessible from the QR code).

Capabilities of 3D viewers can be expanded through incorporation of basic interpretation tools, the ability to integrate multiple datasets, and customizable interfaces. There are various levels of customizability in modern platforms. Sketchfab, for example, currently permits addition of text and web-linked photo annotations, but does not support integration of additional 3D objects, shapefiles, or drawings. Open source platforms (e.g.,

potree and Unity) contain support to integrate meshes, shapefiles, and custom objects within a scene (Figure 5.4) but require additional coding to convert and render data properly. The default potree code supports basic measurement tools (see Figure 5.3B), but further customization within potree or Unity requires significant upfront programming efforts.

Compatibility and design considerations may also emerge as issues for visualization platforms. Although potree code is currently compatible with standard web browsers, future updates to browsers may impede performance. Similarly, users who rely on third party applications are subject to decisions made by suppliers. On the other hand, formats supported by Unity (e.g., Windows [.exe], Apple [.app], mobile device [iOS, Android], Sony PlayStation 4, Microsoft Xbox, and WebGL) have been standard for their respective platforms and are likely to maintain functionality through updates, as backwards compatibility is often built into new versions.

Cartographic principles will become increasingly important as 3D visualizations are used to disseminate spatial data layers with 3D DOMs. This technique has the potential to extend models beyond simple visuals into scientific visualizations designed to aid the understanding of data, provide new perspectives, and provoke individual knowledge construction (MacEachren and Kraak, 1997). Delivering data in this way, requires consideration of cartographic design as it relates to the purpose of a model, intended audience, and how to best present data. For example, use of these platforms as geospatial data viewers still requires basic map components (e.g., scale, orientation, legend, metadata, etc.), which are not currently available in some 3D viewers, but are essential for extending these 3D models to spatially meaningful 3D geovisualizations.

5.6 Conclusions and Recommended Use

Tools for collecting high-resolution 3D datasets have recently become commonplace in both commercial and academic fields; however, sharing 3D datasets typically requires end-users to have specialty software, high-end processing computers, and/or locally store large files. Through the presentation of a large UAV-SfM derived DOM, we introduce three representative visualization platforms that harness potential to advance 3D data dissemination and promote open science communication to end-users without the need for specialized software and hardware.

Web-based viewers, such as Sketchfab and potree, provide practical options for sharing datasets with end-users without cumbersome transfer and storage of large files. Web-based viewers typically provide an easy solution to share 3D visualizations without the need for programming, though customizability and file sizes are limited. The default potree code has extended capabilities, such as measurement tools, display options, and the ability to integrate multiple file types within a single viewer. Open-source code allows capable programmers to customize the potree viewer and could potentially be used as a raw data viewer or educational supplement. A web-domain and web storage are required to host potree visualizations, which may limit uptake for educational purposes, but it remains promising for sharing raw datasets with collaborators or commercial partners.

Game engines require more significant coding knowledge for customized visualizations and measurement tools and may therefore be less practical as a raw data viewer. However, videogames create opportunities to broaden scientific communication and education, beyond conventional 2D maps and photo-based line drawings (e.g., Figure

5.1-2) by contextualizing 3D information within a 3D, immersive, and realistic environment (Figure 5.4). Videogame visualization could be used for engaging museum displays, presentation of course material, or virtual field trips, in which 'participants' can follow guided prompts or explore the scene freely in self-navigation mode.

Although virtual platforms provide exciting potential for enhanced student learning and improved scientific communication to the broader public, their efficacy as a learning tool necessitates future research. Regardless, emerging visualization platforms provide access to 3D datasets, without the need for advanced software and hardware. Though often limited by logistical constraints, we encourage authors to share high-resolution DOM datasets whenever possible. Methods of 3D data dissemination and visualization are still in their infancy behind the relatively recent rise in 3D mapping applications and acquisition techniques; as the latter continue to grow, we expect the former to develop in new and unique ways to facilitate open science initiatives through communication and democratization of photorealistic 3D models.

5.7 References

AltaLIS, 2017, Alberta 20K Digital Elevation Model (DEM):

Bellian, J.A., Kerans, C., Jennette, D.C., and Jennete, D.C., 2005, Digital outcrop models: applications of terrestrial scanning lidar technology in stratigraphic modeling: Journal of Sedimentary Research, v. 75, p. 166–176, doi:10.2110/jsr.2005.013.

Bilke, L., Fischer, T., Helbig, C., Krawczyk, C., Nagel, T., Naumov, D., Paulick, S., Rink, K., Sachse, A., Schelenz, S., Walther, M., Watanabe, N., Zehner, B., Ziesch, J., and Kolditz, O., 2014, TESSIN VISLab—laboratory for scientific visualization: Environmental Earth Sciences, v.72, p.3881–3899, doi:10.1007/s12665-014-3785-5.

Blenkinsop, T.G., 2012, Visualizing structural geology: From Excel to Google Earth: Computers and Geosciences, v. 45, p. 52–56, doi:10.1016/j.cageo.2012.03.007.

Boutsi, A., Ioannidis, C., and Soile, S., 2019, Interactive online visualization of complex 3D geometries: The International Archives of the Photogrammetry, Remote Sensing and Spatial Information Sciences, v. XLII-2/W9, p. 6–8.

Brodu, N., and Lague, D., 2012, 3D terrestrial lidar data classification of complex natural scenes using a multi-scale dimensionality criterion: Applications in geomorphology: ISPRS Journal of Photogrammetry and Remote Sensing, v. 68, p. 121–134, doi:10.1016/j.isprsjprs.2012.01.006.

Buckley, S.J., Ringdal, K., Naumann, N., Dolva, B., Kurz, T.H., Howell, J.A., and Dewez, T.J.B., 2019, LIME : Software for 3-D visualization , interpretation , and communication of virtual geoscience models: Geosphere, v. 15, p. 1–14, doi:10.1130/GES02002.1/4610849/ges02002.pdf.

Cawood, A.J., and Bond, C.E., 2019, eRock: An Open-Access Repository of Virtual Outcrops for Geoscience Education: GSA Today,.

Chesley, J.T., Leier, A.L., White, S., and Torres, R., 2017, Using unmanned aerial vehicles and structure-from-motion photogrammetry to characterize sedimentary outcrops: An example from the Morrison Formation, Utah, USA: Sedimentary Geology, v. 354, p. 1–8, doi:10.1016/j.sedgeo.2017.03.013.

CloudCompare, 2019, Version 2.9. GPL Software. Available online: http://www.cloudcompare.org (accessed15 October 2019):

Copernicus, 2018, Sentinal data. Retrieved from USGS, Earth Explorer 15 August 2019, processed by ESA:

Currie, P.J., and Koppelhus, E.B., 2005, Dinosaur Provincial Park: A Spectacular Ancient Ecosystem Revealed (P. J. Currie & E. B. Koppelhus, Eds.): Indiana University Press.

DePaor, D.G., 2016, Virtual Rocks: GSA Today, p. 4–11, doi:10.1130/GSATG257A.1.1.

DePaor, D.G., and Whitmeyer, S.J., 2011, Geological and geophysical modeling on virtual globes using KML, COLLADA, and Javascript: Computers and Geosciences, v. 37, p. 100–110, doi:10.1016/j.cageo.2010.05.003.

Dewez, T.J.B., Girardeau-Montaut, D., Allanic, C., and Rohmer, J., 2016, Facets : A cloudcompare plugin to extract geological planes from unstructured 3d point clouds: International Archives of the Photogrammetry, Remote Sensing and Spatial Information Sciences - ISPRS Archives, v. 41, p. 799–804, doi:10.5194/isprsarchives-XLI-B5-799-2016.

Dodson, P., 1971, Sedimentology and taphonomy of the Oldman Formation (Campanian), Dinosaur Provincial Park, Alberta (Canada): Palaeogeography, Palaeoclimatology, Palaeoecology, v. 10, p. 21–74.

Durkin, P.R., Hubbard, S.M., Holbrook, J.M., Weleschuk, Z., Nesbit, P.R., Hugenholtz, C.H., Lyons, T., and Smith, D.G., 2019, [in press] Counter-point-bar deposit recognition: the product of concave-bank sedimentary processes in fluvial meander belts: Sedimentology,.

Eberth, D.A., and Hamblin, A.P., 1993, Tectonic, stratigraphic, and sedimentologic significance of a regional discontinuity in the upper Judith River Group (Belly River wedge) of southern Alberta, Saskatchewan, and northern Montana: Canadian Journal of Earth Sciences, v. 30, p. 174–200, doi:10.1139/e93-016.

Fraiss, S.M., 2017, Rendering Large Point Clouds in Unity: , p. 38.

Goodchild, M.F., Guo, H., Annoni, A., Bian, L., de Bie, K., Campbell, F., Craglia, M., Ehlers, M., van Genderen, J., Jackson, D., Lewis, A.J., Pesaresi, M., Remetey-Fulopp, G., Simpson, R., Skidmore, A., Wang, C., and Woodgate, P., 2012, Next-generation Digital Earth: Proceedings of the National Academy of Sciences, v. 109, p. 11088–11094, doi:10.1073/pnas.1202383109.

Hodgetts, D., L. Gawthorpe, R., Wilson, P., and Rarity, F., 2007, Integrating Digital and Traditional Field Techniques Using Virtual Reality Geological Studio (VRGS): 69th EAGE Conference and Exhibition incorporating SPE EUROPEC 2007, p. 11–14, doi:10.3997/2214-4609.201401718.

Howell, J.A., Martinius, A.W., and Good, T.R., 2014, The application of outcrop analogues in geological modelling : a review , present status and future outlook The application of outcrop analogues in geological modelling : a review , present status and future outlook: Geological Society, London, Special Publications, p. 1–25, doi:10.1144/SP387.12.

Jones, R.R., McCaffrey, K.J.W., Clegg, P., Wilson, R.W., Holliman, N.S., Holdsworth, R.E., Imber, J., and Waggott, S., 2009, Integration of regional to outcrop digital data: 3D visualisation of multi-scale geological models: Computers and Geosciences, v. 35, p. 4–18, doi:10.1016/j.cageo.2007.09.007.

Küng, O., Strecha, C., Fua, P., Gurdan, D., Achtelik, M., Doth, K.-M., and Stumpf, J., 2012, Simplified Building Models Extraction From Ultra-Light Uav Imagery: ISPRS - International Archives of the Photogrammetry, Remote Sensing and Spatial Information Sciences, v. XXXVIII-1/, p. 217–222, doi:10.5194/isprsarchives-

XXXVIII-1-C22-217-2011.

MacEachren, A.M., and Kraak, M.J., 1997, Exploratory Cartographic Visualization : Advancing the Agenda: Computers & Geosciences, v. 23, p. 335–343.

Martinez-Rubi, O., de Kleijn, M., Verhoeven, S., Drost, N., Attema, J., van Meersbergen, M., van Nieuwpoort, R., de Hond, R., Dias, E., and Svetachov, P., 2016, Using modular 3D digital earth applications based on point clouds for the study of complex sites: International Journal of Digital Earth, v. 9, p. 1135–1152, doi:10.1080/17538947.2016.1205673.

McCaffrey, K.J.W., Hodgetts, D., Howell, J.A., Hunt, D., Imber, J., Jones, R.R., Tomasso, M., Thurmond, J., and Viseur, S., 2010, Virtual fieldtrips for petroleum geoscientists: Geological Society, London, Petroleum Geology Conference series, v. 7, p. 19–26, doi:10.1144/0070019.

McCaffrey, K.J.W., Jones, R.R., Holdsworth, R.E., Wilson, R.W., Clegg, P., Imber, J., Holliman, N.S., and Trinks, I., 2005, Unlocking the spatial dimension: digital technologies and the future of geoscience fieldwork: Journal of the Geological Society, v. 162, p. 927–938, doi:10.1144/0016-764905-017.

Nesbit, P.R., Durkin, P.R., Hugenholtz, C.H., Hubbard, S.M., and Kucharczyk, M., 2018, 3-D stratigraphic mapping using a digital outcrop model derived from UAV images and structure-from-motion photogrammetry: Geosphere, v. 14, p. 1–18, doi:10.1130/GES01688.1.

Nesbit, P.R., and Hugenholtz, C.H., 2019, Enhancing UAV-SfM 3D model accuracy in high-relief landscapes by incorporating oblique images: Remote Sensing, v. 11, doi:10.3390/rs11030239.

Nieminski, N.M., and Graham, S.A., 2017, Modeling Stratigraphic Architecture Using Small Unmanned Aerial Vehicles and Photogrammetry: Examples From the Miocene East Coast Basin, New Zealand: Journal of Sedimentary Research, v. 87, p. 126–132, doi:10.2110/jsr.2017.5.

Pavlis, T.L., and Mason, K.A., 2017, The New World of 3D Geologic Mapping: GSA Today, v. 27, p. 4–10, doi:10.1130/GSATG313A.1.

von Reumont, F., Arsanjani, J.J., and Riedl, A., 2013, Visualization of geologic geospatial datasets through X3D in the frame of WebGIS: International Journal of Digital Earth, v. 6, p. 483–503, doi:10.1080/17538947.2011.627471.

Robinson, A., Gordon, C.E., Houghton, J., Lloyd, G.E., and Morgan, D.J., 2015, ArcGIS to Unity: a design pipeline for creation of 3D terrain in serious egames for geology One: Geology Today, v. 31, p. 237–240.

Schuetz, M., 2016 [Thesis], Potree: Rendering Large Point Clouds in Web Browsers: Vienna University of Technology, 84 p.

Simpson, C., and DePaor, D.G., 2010, Restoring maps and memoirs to four-dimensional space using virtual globe technology: a case study from the Scottish Highlands: Geological Society, London, Special Publications, v. 335, p. 429–441, doi:10.1144/sp335.20.

Smith, D.G., Hubbard, S.M., Leckie, D.A., and Fustic, M., 2009, Counter point bar deposits: Lithofacies and reservoir significance in the meandering modern peace river and ancient McMurray formation, Alberta, Canada: Sedimentology, v. 56, p. 1655–1669, doi:10.1111/j.1365-3091.2009.01050.x.

Tavani, S., Granado, P., Corradetti, A., Girundo, M., Iannace, A., Arbués, P., Muñoz,

J.A., Mazzoli, S., Munoz, J.A., and Mazzoli, S., 2014, Building a virtual outcrop, extracting geological information from it, and sharing the results in Google Earth via OpenPlot and Photoscan: An example from the Khaviz Anticline (Iran): Computers and Geosciences, v. 63, p. 44–53, doi:10.1016/j.cageo.2013.10.013.

Thiele, S.T., Grose, L., Samsu, A., Micklethwaite, S., Vollgger, S.A., and Cruden, A.R., 2017, Rapid, semi-automatic fracture and contact mapping for point clouds, images and geophysical data: Solid Earth, v. 8, p. 1241–1253, doi:10.5194/se-2017-83.

Thurmond, J.B., Løseth, T.M., Rivenæs, J.C., Martinsen, O.J., and Aiken, C.L.V., 2006, Using Outcrop Data in the 21st Century – New methods and applications , with example from the Ainsa Turbidite System ,: Deep-Water Outcrops of the World Atlas, p. CD-ROM, doi:10.1306/12401010St563281.

Turner, A.K., 2006, Challenges and trends for geological modelling and visualisation: Bulletin of Engineering Geology and the Environment, v. 65, p. 109–127, doi:10.1007/s10064-005-0015-0.

USGS, 2019, 3D Elevation Program (3DEP):, https://www.usgs.gov/news/usgs-3dep-lidar-point-cloud-now-available-amazon-public-dataset (accessed October 2019).

Wood, J.M., Thomas, R.G., and Visser, J., 1988, Fluvial processes and vertebrate taphonomy: the upper Cretaceous Judith River formation, South-Central Dinosaur Provincial Park, Alberta, Canada: Palaeogeography, Palaeoclimatology, Palaeoecology, v. 66, p. 127–143, doi:10.1016/0031-0182(88)90085-5.

Chapter 6

Thesis Summary and Concluding Remarks

6.1 Detailed Summary of Research Findings and Contributions

Recent advances in high-resolution remote sensing tehniques have resulted in widespread use within a broad range of academic and commercial applications. Light detection and ranging (LiDAR) and modern structure-from-motion (SfM) photogrammetry can be employed from ground-based or close-range airborne platforms, such as uninhabited aerial vehicles (UAVs), to produce datasets at unprecedented detail (Hugenholtz et al., 2012; Colomina and Molina, 2014; Whitehead et al., 2014; Carrivick et al., 2016; Toth and Jóźków, 2016). However, geologic outcrops commonly present unique challenges (e.g., inaccessible, 3D exposures) that require special consideration, including (i) data collection and processing approaches, (ii) digital mapping and interpretation workflows, and (iii) dissemination strategies. Results from each study in this dissertation address these inherent challenges and, as a whole, contribute to better constraining digital geologic mapping workflows using small UAVs and SfM photogrammetry.

In **Chapter 2**, a UAV-SfM workflow was established for data collection, processing, and analysis of geologic features exposed within a highly dissected, three-dimensional, badland landscape. To address the challenging 3D exposures typical of outcrops, this investigation proposed use of 'intermediate' datasets generated during the UAV-SfM processing workflow, such as the dense point cloud and textured mesh, as 3D digital outcrop models (DOMs). This study reveals that DOMs can preserve details along steep slopes that are distorted or completely omitted in typical 2D outputs (i.e.,

orthomosaic images). This investigation builds upon recent stratigraphic mapping applications using UAV-SfM for relatively flat and featureless outcrops (e.g., Chesley et al., 2017) by documenting data collection, processing, and analysis methods for exposures in complex topographic settings. Results demonstrated that digital observations from DOMs can yield comparable results to field-based observations in the measurement of macro-scale features (e.g., primary bounding surfaces) and fine-scale detail (e.g., individual beds and bedsets). This work contributes to the current literature by establishing a straightforward workflow and technique for data collection, processing, and interpretation of 3D digital datasets. Additionally, results provide a baseline understanding of digital sedimentary observations from UAV-SfM DOMs compared with conventional methods and indicates future directions in the ability to identify and measure laterally extensive geologic features.

Chapter 3 documented the impacts of image collection strategy on accuracy, precision, and detail for UAV-SfM derived 3D datasets in high-relief landscapes. More than 150 applied data collection scenarios were considered with variation to imaging angle, image overlap, and flight pattern. A comprehensive review of photogrammetric literature relative to incorporation of oblique imaging angles processed with SfM-based photogrammetric algorithms revealed that, though incorporation of oblique images can be beneficial (e.g., Luhmann and Robson, 2006; Wackrow and Chandler, 2008; Bemis et al., 2014; James and Robson, 2014; Eltner and Schneider, 2015; Harwin et al., 2015; Carbonneau and Dietrich, 2017; James et al., 2017; Agüera-Vega et al., 2018), there was no prior consensus of appropriate imaging angle and a paucity of application within high-relief terrain. Results from this investigation provide some clarity and guidance for

incorporating oblique image angles. Previous studies have documented the presence of a systematic 'doming' error in UAV-SfM image blocks collected with a nadir-facing camera, typical of most surveys (James and Robson, 2014; James et al., 2017). Findings from this analysis provide evidence that similar issues are present in image blocks collected with any single camera angle (nadir or off-nadir) and persist despite the incorporation of ground control points (GCPs). Additionally, outcomes from the applied scenarios confirm that supplementing nadir image blocks with oblique images consistently improves precision and accuracy of 3D datasets by minimizing systematic errors. Results suggest that disparities among imaging angle and pattern are subtle, but higher oblique imaging angles (20 - 35°) typically resulted in higher precisions than nadir-only image blocks. Conclusions and recommendations from this investigation provide guidance for minimizing systematic errors, increasing precision and accuracy, and maintaining detail along slopes through practical flight plans that can be implemented in typical geologic applications, along with other high-relief settings.

Chapter 4 built on results presented in Chapters 2-3 and applied an extended UAV-SfM workflow to characterize stratigraphic architecture at multiple scales, revealing details that were previously not recognized from field-based perspectives. A UAV-SfM derived DOM was used to revisit and re-interpret stratigraphic architecture in an extensive, nearly continuous, sub-vertical outcrop exposure previously documented using conventional field-methods by Daniels (2015, 2019). Interpretations of stratigraphic architecture exhibited similarities between field- and digital- methods for large scale features, similar to Chapter 2. However, outcomes from this case study also demonstrate the subtle sedimentary detail that may be overlooked, due to viewable scale,

perspective, and/or accessibility, when solely using conventional field-based approaches. Digital methods resulted in the recognition of nuanced features that could not be discerned while on the outcrop in the field. Digital measurements indicate that these features resemble upslope crescentic bedform deposits that have seldom been recognized in ancient deposits, despite recent acknowledgement of their prevalence in analogous modern settings (Symons et al., 2016; Hage et al., 2018; Englert et al., in press). Conclusions suggest that UAV-SfM techniques could be widely applied to other geologic mapping scenarios to provide a perspective and scale of analysis that were previously difficult, or impossible, to achieve and could result in new interpretations that may help in linking ancient deposits with modern morphodynamic processes.

Digital outcrop models and interpretations generated in Chapters 2-3 were used in assessing strategies for visualization and sharing of 3D datasets in **Chapter 5**. Although technological advances have increased the ability to collect and analyze high-resolution 3D DOMs, there has been a bottleneck in the ability to share these datasets, as they generally require specialty software, advanced hardware, and transfer of large files. This research reviews available techniques for the visualization and sharing of 3D DOMs and scientific information with a broad (i.e., non-specialist) audience. Through a case study within Dinosaur Provincial Park (Alberta, Canada), contributions from this chapter included a functional introduction to three modern visualization platforms along with developed examples demonstrating the functionalities of each platform. Limitations and benefits of each platform reveal the need for advancement in visualization strategies, user interfaces, and basic measurement and interpretation tools to extend the utility of available platforms. Conclusions provide suggested use cases suitable to the unique

capabilities of each platform, such as the potential of potree as a raw data viewer for collaborations among colleagues or videogame engines potential for providing customizable and impactful educational material using common computing platforms. Outcomes from this research offer an initial look at modern methods to disseminate and visualize 3D datasets through unique approaches that can facilitate and promote open science.

6.2 Limitations and Implications for Future Work

Geospatial technologies are adding a new component to geologic mapping and analysis - the ability to constrain interpretations and supplement field methods with high-resolution digital datasets that offer new, multi-scale perspectives and facilitate quantitative measurements (Whitmeyer et al., 2010; House et al., 2013; Pavlis and Mason, 2017). Altogether, outcomes from this dissertation contribute necessary initial steps in establishing and evaluating novel workflows and insight into challenges associated with use of UAV-SfM for mapping outcrop exposures in complex 3D scenes. Although sedimentary environments and features are the focus of this research, I believe outcomes are applicable to various 3D outcrop mapping scenarios (e.g., structural, metamorphic) and provide insight that is applicable within the broader geosciences.

Strategies documented in Chapters 2-4 demonstrate the ability to obtain details along steep slopes in complex topographic settings using a UAV-SfM workflow that can produce observations commensurate with field-based approaches. Though examples presented within this work are applied to sedimentary deposits and features, outcomes of this research provide a baseline approach to data collection and analysis in other geoscience applications. However, it should be noted that results were reliant on camera

resolution, flight distance from the target, and outcrop characteristics. Following the sampling theorem in remote sensing, clearly resolvable features should be at least twice the cell size of images (Woodcock and Strahler, 1987). UAV images can easily achieve and exceed centimeter detail, however, this is not the only factor affecting resolvable detail. Outcrop characteristics, such as exposure geometry and weathered surface expression control visibility from remote platforms, such as UAVs. For example, outcrop exposure in Chapter 4 were roughly aligned with paleoflow, which permitted the recognition of backsetting beds; similarly, surface coloration in Chapter 2 controlled the identification of different facies and accretion surfaces. Detection of sub-bedding detail (e.g., laminations, grain size) has not been achieved in the literature and is likely to remain elusive as weathered surfaces often conceal this sedimentary detail and require ground-based investigation. Although digital techniques resulted in commensurable interpretations within this dissertation, fieldwork will remain essential for understanding fundamental characteristics within outcrop.

UAV-SfM techniques, however, present opportunities to supplement field-based observations with DOMs to provide new perspectives and quantitative potential in recognizing and measuring subtle patterns that may not be recognizable in the field (e.g., Chapter 4). Though this case study presented a few examples, I believe that many similar scenarios exist in which a UAV-SfM approach can reveal new information from outcrops with restricted accessibility or limited perspectives. Outcrops are often partially, or entirely, inaccessible to reach on foot; also, it may not be feasible to 'step back' and obtain an overview perspective of an outcrop. DOMs generated from UAV-SfM

workflows make it possible to view outcrops from multiple perspectives and quickly change scales by zooming in or out to aid observation and interpretation.

Though the primary aims of this dissertation were on establishing and evaluating methods for mapping geologic features in challenging landscapes, it is worth considering the added, or needed, value of resulting datasets. UAV-SfM can produce centimeter-level detail, previously only practical from ground-based methods, with the added ability to obtain this detail over large spatial extents ($> 10^4$ m^2). This may not be required for all problems and could generate excessive detail, but I see this previously inaccessible information as providing opportunities to build new knowledge and/or validate current geologic understanding. UAV-SfM techniques could be particularly effective for physically inaccessible locations or for laterally extensive features that were previously difficult, or impossible, to document and measure using conventional methods. New quantitative datasets could provide opportunities for more complete characterization that may enhance, or even change, understanding of long-term processes (e.g., linkages between physical morphodynamic processes and deposits in the rock record). This work is an initial step that provides foundational insight that can be applied to unique geologic problems, or revisit old ones. The true value of data garnered from these nascent approaches is yet to be fully appreciated and will be determined as geoscientists implement these strategies in unique applications.

Much of the geoscience literature using UAVs has focused on tailoring workflows (e.g., Bemis et al., 2014), developing new tools for analysis (e.g., Buckley et al., 2019), assessing accuracy (e.g., Cawood et al., 2017), use in new applications (e.g., Chesley et al., 2017; Nieminski and Graham, 2017). The ability to share 3D datasets outside of

specialist audiences (i.e., colleagues) has remained a challenge that is not readily considered in the literature. Visualization of 3D datasets and interpretations within a 3D, immersive, and realistic environment can help users contextualize information and build cognitive understanding beyond standard 2D figures (MacEachren and Kraak, 1997). Although Chapter 5 documented novel visualization strategies and provided a functional introduction to three modern visualization platforms, further technical developments will change the capabilities for scientific communication in the geosciences and beyond.

Technological advancements will provide new capabilities within these visualization systems, noteably: (i) rendering strategies (e.g., controls for display quality, point budget) that increase user accessibility, (ii) ability to integrate additional layers (e.g., shapefiles, additional models), measurement tools, and educational information. As new capabilities and features emerge, researchers will find innovative ways of applying these relatively new visualization methods for sharing 3D information. For example, online repositories, such as SafariDB (Howell et al., 2014) and related https://V3Geo.com, can serve as digital teaching resources when fieldwork is not possible or in-person classes are suddenly shifted to virtual instruction. Videogame visualizations can be further customized to create engaging, realistic, and interactive virtual field experiences that allow users to follow pre-set prompts of information or explore, make measurements, and build interpretations of thier own. Integration of these 3D datasets into classroom settings is in its infancy and their efficacy as learning tools necessitates future research. Regardless, visualization strategies for 3D datasets will continue to develop in new and unique applications alongside 3D mapping techniques and together present exciting opportunities for education, research, and scientific communication.

6.3 Final Remarks

Conventional geologic mapping techniques are well-established for obtaining primary observations from outcrop exposures and have remained a largely unchanged foundational component for more than two centuries. However, observations using such approaches may be incomplete, due to practical and/or logistical constraints (e.g., inaccessibility, outcrop extent, available perspectives) afforded by intricate outcrop exposures in high-relief terrain. UAVs paired with modern SfM photogrammetry present an opportunity to confront these challenging outcrop scenarios by providing high-resolution, photorealistic, scaled, oriented, and georeferenced 3D DOMs. This dissertation addressed several aspects of adopting UAV-SfM workflows to generate 3D DOMs for mapping complex, highly three-dimensional scenes commonly associated with outcrop exposures.

Although results prove promising for mapping, analysis, and sharing of 3D digital methods, UAV-SfM generated DOMs are not considered a replacement for conventional field-mapping methods. Instead, these modern technologies can be used to enhance common field tools with supplemental perspectives, measurements, and observations that are difficult, or impossible, to obtain from conventional fieldwork alone. This additional information could potentially add valuable insight and contribute to more complete outcrop characterization and ultimately inform and/or confirm existing geologic understanding (e.g., reservoir and morphodynamic models). Contributions from this dissertation provide foundational insight into the limitations and potential of UAV-SfM approaches that will guide future applications and create opportunities for expanded geologic characterization and understanding in myriad geologic settings.

6.4 References

Agüera-Vega, F., Carvajal-Ramírez, F., Martínez-Carricondo, P.J., Sánchez-Hermosilla López, J., Mesas-Carrascosa, F.J., García-Ferrer, A., and Pérez-Porras, F.J., 2018, Reconstruction of extreme topography from UAV structure from motion photogrammetry: Measurement: Journal of the International Measurement Confederation, v. 121, p. 127–138, doi:10.1016/j.measurement.2018.02.062.

Bemis, S.P., Micklethwaite, S., Turner, D., James, M.R., Akciz, S., Thiele, S.T., Bangash, H.A., T. Thiele, S., and Bangash, H.A., 2014, Ground-based and UAV-Based photogrammetry: A multi-scale, high-resolution mapping tool for structural geology and paleoseismology: Journal of Structural Geology, v. 69, p. 163–178, doi:10.1016/j.jsg.2014.10.007.

Buckley, S.J., Ringdal, K., Naumann, N., Dolva, B., Kurz, T.H., Howell, J.A., and Dewez, T.J.B., 2019, LIME : Software for 3-D visualization , interpretation , and communication of virtual geoscience models: Geosphere, v. 15, p. 1–14, doi:10.1130/GES02002.1/4610849/ges02002.pdf.

Carbonneau, P.E., and Dietrich, J.T., 2017, Cost-effective non-metric photogrammetry from consumer-grade sUAS: Implications for direct georeferencing of structure from motion photogrammetry: Earth Surface Processes and Landforms, v. 42, p. 473–486, doi:10.1002/esp.4012.

Carrivick, J.L., Smith, M.W., and Quincey, D.J., 2016, Structure from Motion in the Geosciences: Oxford, UK, Wiley-Blackwell.

Cawood, A.J., Bond, C.E., Howell, J.A., Butler, R.W.H., and Totake, Y., 2017, LiDAR, UAV or compass-clinometer? Accuracy, coverage and the effects on structural

models: Journal of Structural Geology, v. 98, p. 67–82, doi:10.1016/j.jsg.2017.04.004.

Chesley, J.T., Leier, A.L., White, S., and Torres, R., 2017, Using unmanned aerial vehicles and structure-from-motion photogrammetry to characterize sedimentary outcrops: An example from the Morrison Formation, Utah, USA: Sedimentary Geology, v. 354, p. 1–8, doi:10.1016/j.sedgeo.2017.03.013.

Colomina, I., and Molina, P., 2014, Unmanned aerial systems for photogrammetry and remote sensing: A review: ISPRS Journal of Photogrammetry and Remote Sensing, v. 92, p. 79–97, doi:10.1016/j.isprsjprs.2014.02.013.

Daniels, B.G., 2015, Downslope characterization of channel fill and stratigraphic architecture along and ancient basin margin, Tres Pasos Formation, southern Chile: University of Calgary, 153 p.

Daniels, B.G., 2019, Multi-scale stratigraphic and geochronologic investigations of Late Cretaceous sediment-routhing systems, Magallanes Basin, Chile: University of Calgary, 302 p.

Eltner, A., and Schneider, D., 2015, Analysis of Different Methods for 3D Reconstruction of Natural Surfaces from Parallel-Axes UAV Images: Photogrammetric Record, v. 30, p. 279–299, doi:10.1111/phor.12115.

Englert, R.G., Hubbard, S.M., Cartigny, M.J.B., Clare, M.A., Coutts, D., Hage, S., Hughes Clarke, J., Jobe, Z.R., Lintern, G., Stacey, C., and Vendettuoli, D., 2020, Quantifying the 3D stratigraphic expression of upslope-migrating bedforms by integrating seafloor and outcrop observationstle (In Press): Sedimentology,.

Hage, S., Cartigny, M.J.B., Clare, M.A., Sumner, E.J., Vendettuoli, D., Clarke, J.E.H., Hubbard, S.M., Talling, P.J., Gwyn Lintern, D., Stacey, C.D., Englert, R.G., Vardy, M.E., Hunt, J.E., Yokokawa, M., Parsons, D.R., Hizzett, J.L., Azpiroz-Zabala, M., and Vellinga, A.J., 2018, How to recognize crescentic bedforms formed by supercritical turbidity currents in the geologic record: Insights from active submarine channels: Geology, v. 46, p. 563–566, doi:10.1130/G40095.1.

Harwin, S., Lucieer, A., and Osborn, J., 2015, The Impact of the Calibration Method on the Accuracy of Point Clouds Derived Using Unmanned Aerial Vehicle Multi-View Stereopsis: Remote Sensing, v. 7, p. 11933–11953, doi:10.3390/rs70911933.

House, P.K., Clark, R., and Kopera, J., 2013, Overcoming the momentum of anachronism : American geologic mapping in a twenty-first-century world: Geological Society of America Special Papers, v. 2502, p. 103–125, doi:10.1130/2013.2502(05).

Howell, J.A., Martinius, A.W., and Good, T.R., 2014, The application of outcrop analogues in geological modelling: a review, present status and future outlook: Geological Society, London, Special Publications, v. 387, p. 1–25, doi:10.1144/SP387.12.

Hugenholtz, C.H., Moorman, B.J., Riddell, K., and Whitehead, K., 2012, Small unmanned aircraft systems for remote sensing and earth science research: Eos, Transactions American Geophysical Union, v. 93, p. 236, doi:10.1117/1.3474649.

James, M.R., and Robson, S., 2014, Mitigating systematic error in topographic models derived from UAV and ground-based image networks: Earth Surface Processes and Landforms, v. 39, p. 1413–1420, doi:10.1002/esp.3609.

James, M.R., Robson, S., and Smith, M.W., 2017, 3-D uncertainty-based topographic change detection with structure-from-motion photogrammetry: precision maps for ground control and directly georeferenced surveys: Earth Surface Processes and Landforms, v. 42, p. 1769–1788, doi:10.1002/esp.4125.

Luhmann, T., and Robson, S., 2006, Photogram Book 4, *in* p. 475–510.

MacEachren, A.M., and Kraak, M.J., 1997, Exploratory Cartographic Visualization : Advancing the Agenda: Computers & Geosciences, v. 23, p. 335–343.

Nieminski, N.M., and Graham, S.A., 2017, Modeling Stratigraphic Architecture Using Small Unmanned Aerial Vehicles and Photogrammetry: Examples From the Miocene East Coast Basin, New Zealand: Journal of Sedimentary Research, v. 87, p. 126–132, doi:10.2110/jsr.2017.5.

Pavlis, T.L., and Mason, K.A., 2017, The New World of 3D Geologic Mapping: GSA Today, v. 27, p. 4–10, doi:10.1130/GSATG313A.1.

Symons, W.O., Sumner, E.J., Talling, P.J., Cartigny, M.J.B., and Clare, M.A., 2016, Large-scale sediment waves and scours on the modern seafloor and their implications for the prevalence of supercritical flows: Marine Geology, v. 371, p. 130–148, doi:10.1016/j.margeo.2015.11.009.

Toth, C., and Jóźków, G., 2016, Remote sensing platforms and sensors: A survey: ISPRS Journal of Photogrammetry and Remote Sensing, v. 115, p. 22–36, doi:10.1016/j.isprsjprs.2015.10.004.

Wackrow, R., and Chandler, J.H., 2008, A convergent image configuration for DEM extraction that minimises the systematic effects caused by an inaccurate lens model: Photogrammetric Record, v. 23, p. 6–18, doi:10.1111/j.1477-9730.2008.00467.x.

Whitehead, K., Hugenholtz, C.H., Myshak, S., Brown, O.W., LeClair, A., Tamminga, A.D., Barchyn, T.E., Moorman, B.J., and Eaton, B.C., 2014, Remote sensing of the environment with small unmanned aircraft systems (UASs), part 2: scientific and commercial applications 1: Journal of Unmanned Vehicle Systems, v. 02, p. 86–102, doi:10.1139/juvs-2014-0007.

Whitmeyer, S.J., Nicoletti, J., and De Paor, D.G., 2010, The digital revolution in geologic mapping: GSA Today, v. 20, p. 4–10, doi:10.1130/GSATG70A.1.

Woodcock, C.E., and Strahler, A.H., 1987, The Factor of Scale in Remote-Sensing: Remote Sensing of Environment, v. 21, p. 311–332, doi:10.1016/0034-4257(87)90015-0.

Appendix A
Additional Peer-Reviewed Contributions

In addition to the three peer-reviewed contributions and fourth manuscript (in preparation for publication) encompassing the main chapters of this doctoral thesis, I also co-authored three peer-reviewed articles during the course of this degree, referenced below:

Durkin, P.R., Hubbard, S.M., Holbrook, J., Weleschuk, Z., **Nesbit, P.**, Hugenholtz, C., Lyons, T., and Smith, D.G. 2020. Recognizing the product of concave-bank sedimentary processes in fluvial meander belt strata. *Sedimentology* (in press). doi: 10.1111/sed.12743.

Hugenholtz, C., Brown, O., Walker, J., Barchyn, T., **Nesbit, P.**, Kucharczyk, M. and Myshak, S., 2016. Spatial accuracy of UAV-derived orthoimagery and topography: Comparing photogrammetric models processed with direct geo-referencing and ground control points. *Geomatica, 70(1)*, pp.21-30. doi: 10.5623/cig2016-102.

Nesbit, P.R., Barchyn, T.E., Hugenholtz, C.H., Cripps, S. and Kucharczyk, M., 2017. Reported UAV incidents in Canada: analysis and potential solutions. *Journal of unmanned vehicle systems, 5(2)*, pp.51-61. doi: 10.1139/juvs-2016-0033.

Appendix B

Copyright Permissions

The information below provides the Copyright policy of the Geological Society of America (GSA), which applies to the content of Chapter 2 (Nesbit et al., 2018 – *Geosphere*) and Chapter 5 (Nesbit et al., 2020 – *GSA Today*):

Author Guidelines

Copyright Information

- "Fair Use" Permission
- Permission Granting and Payment
- License Fees
- Additional Information for Authors
- Open Access Content

GSA obtains copyright ownership from authors of all articles and books. (See "Open Access Content" below, for exceptions.) Works prepared by U.S. government employees in the course of their work are in the public domain, however, and are not copyrighted. It is the responsibility of those requesting permission(s) to determine if an article meets this test and is in the public domain.

Special "Fair Use" permission

If you want to use a single figure, a brief paragraph, or a single table from a GSA publication, GSA considers this to be fair usage, and you need no formal permission and no fees are assessed unless you or your publisher require a formal permission letter. In that case, you should print a copy of this document and present it to your publisher.

An author has the right to use his or her article or a portion of the article in a thesis or dissertation without requesting permission from GSA, provided the bibliographic citation and the GSA copyright credit line are given on the appropriate pages.

Check the permission statement in each publication

Each publication includes a statement of copyright policy for that publication that permits and describes limited usages. These statements are found on the front or back of the title page or the table-of-contents page in the masthead statement. In most cases, these statements grant to individual scientists the right to reproduce a limited number of copies for purposes that further education and/or science, including classroom use. If your usage falls within the statement appearing in the publication in which you are interested, you need no further permission from that usage.

Other usages are also allowed by these statements, with instructions to remit a minimum fee to the Copyright Clearance Center (CCC), along with the ISSN or ISBN number of the publication. Within the U.S., the CCC collects and remits payments to GSA. Other organizations throughout the world are authorized by GSA to collect and remit payments for copyright usage in various countries. If your usage falls within the scope of these usages, please follow our instructions or observe the lawful practice within your country if you are outside the U.S. Please **do not write for permission**.

See also GSA's Open Access Policy.

Open Access Content

In January 2018, *Lithosphere* and *Geosphere* became gold open access journals, and all papers published from January 2018 on are published under either the Creative Commons license CC-BY-NC or CC-BY (https://creativecommons.org/). Papers published before January 2018 are freely accessible online, but copyright may apply. If you want to use material from *Geosphere* or *Lithosphere*, or from any open access papers in *Geology*, *GSA Bulletin*, or GSA books, check the paper for its copyright or Creative Commons status.

- CC-BY-NC: Allows anyone to copy, redistribute, remix, transform, and build upon the contribution, in any format or medium, as long as the contribution and authors are credited, a link to the license is provided, any changes made from the original are indicated, and no suggestion is made by others that the authors endorse the use. The material may not be used for commercial purposes (generally defined as primarily intended for or directed toward commercial advantage or monetary compensation).
- CC-BY: Allows anyone to copy, redistribute, remix, transform, and build upon the contribution, in any format or medium, for any purpose including commercial purpose, as long as the contribution and authors are credited, a link to the license is provided, any changes made from the original are indicated, and no suggestion is made by others that the authors endorse the use.

See the full legal codes of the Creative Commons licenses at https://creativecommons.org/.

All permission requests should be addressed to:
Copyright Permissions
Geological Society of America
P.O. Box 9140
Boulder, CO 80301-9140
fax: 303-357-1070
e-mail: editing@geosociety.org

The information below provides the Copyright policy of the MDPI, which applies to the content of Chapter 3 (Nesbit and Hugenholtz – *Remote Sensing*):

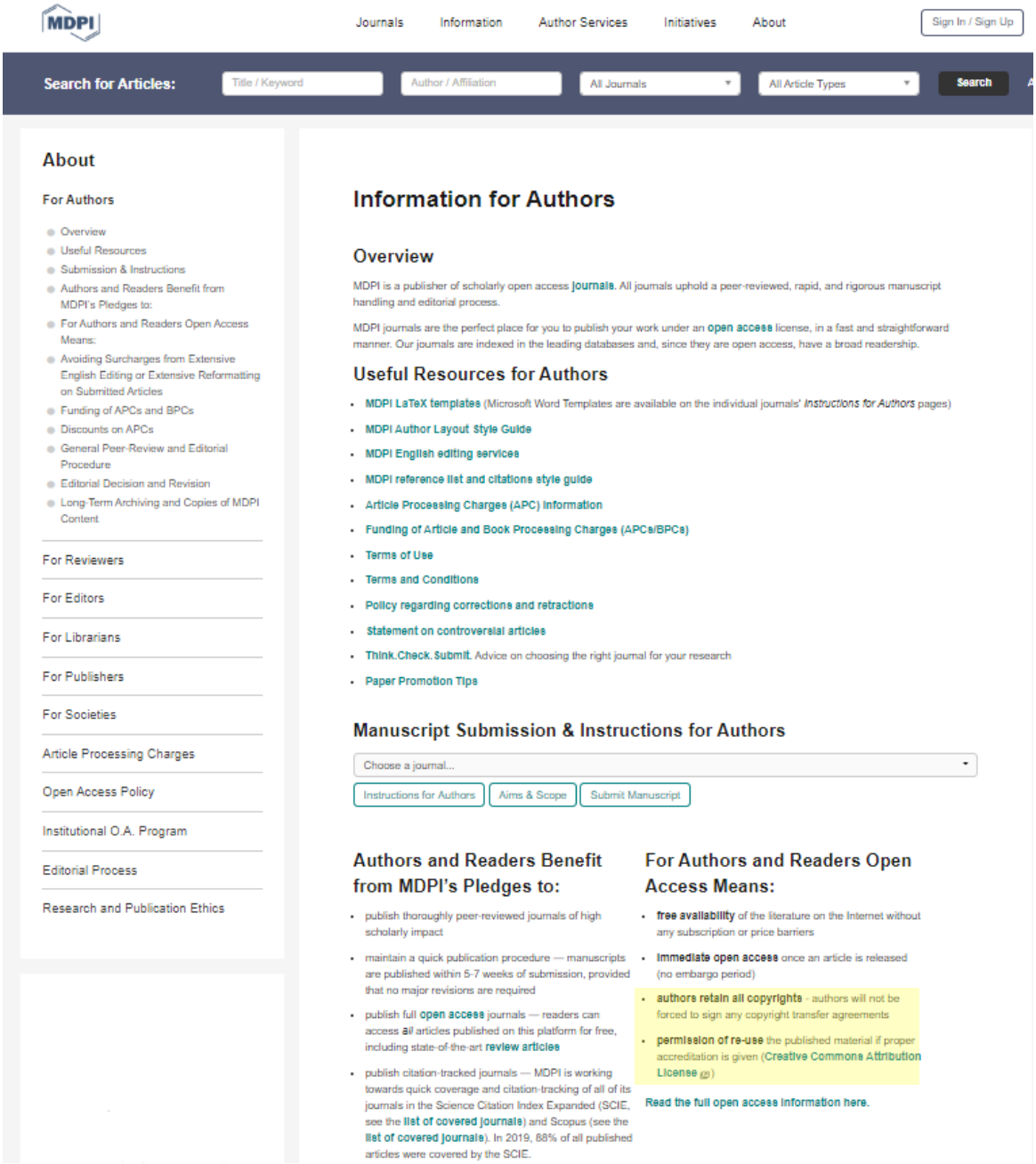

Included below are written confirmations from each of my co-authors agreeing to use specific published materials within this dissertation for Chapters 2, 3, and 5:

RE: Written Permission for use of Co-Authored Materials

Chris Hugenholtz < >
Mon 7/13/2020 4:42 PM
To: Paul Nesbit < >
I confirm – Chris H.

From: Paul Nesbit
Sent: July 13, 2020 4:39 PM
To: Chris Hugenholtz
Subject: Written Permission for use of Co-Authored Materials

Hi Chris,

Will you please confirm that you agree that each of the following co-authored and published manuscripts can be included within my dissertation:

- Nesbit, P.R., Durkin, P.R., Hugenholtz, C.H., Hubbard, S.M., and Kucharczyk, M. 2018. 3-D stratigraphic mapping using a digital outcrop model derived from UAV images and structure-from-motion photogrammetry. *Geosphere*, 14 (6), p. 2469-2486. doi:10.1130/GES01688.1
- Nesbit, P.R. and Hugenholtz, C.H. 2019. Enhancing UAV-SfM 3D model accuracy in high-relief landscapes by incorporating oblique images. *Remote Sensing*, 11 (239), p. 2469-2486. doi:10.3390/rs11030239.
- Nesbit, P.R., Boulding, A.D., Hugenholtz, C.H., Durkin, P.R., and Hubbard, S.M. 2020. Visualization and sharing of 3D Digital Outcrop Models to promote open science. *GSA Today*, 30 (5), p. 4-10. doi:10.1130/GSATG425A.1

Thank you!

Paul R. Nesbit

Re: Written Permission for use of Co-Authored Materials

Stephen Michial Hubbard < >
Mon 7/13/2020 6:05 PM
To: Paul Nesbit < >
Yes- confirmed.

Steve

On Jul 13, 2020, at 4:42 PM, Paul Nesbit < > wrote:

Hi Steve,

Will you please confirm that you agree that each of the following co-authored and published manuscripts can be included within my dissertation:

- Nesbit, P.R., Durkin, P.R., Hugenholtz, C.H., Hubbard, S.M., and Kucharczyk, M. 2018. 3-D stratigraphic mapping using a digital outcrop model derived from UAV images and structure-from-motion photogrammetry. *Geosphere*, 14 (6), p. 2469-2486. doi:10.1130/GES01688.1

- Nesbit, P.R., Boulding, A.D., Hugenholtz, C.H., Durkin, P.R., and Hubbard, S.M. 2020. Visualization and sharing of 3D Digital Outcrop Models to promote open science. *GSA Today*, 30 (5), p. 4-10. doi:10.1130/GSATG425A.1

Thank you!

Paul R. Nesbit

Re: Written Permission for use of Co-Authored Materials

Paul Durkin < >
Mon 7/13/2020 4:43 PM
To: Paul Nesbit < >
[△EXTERNAL]

Confirmed.

Paul

Paul Durkin
Assistant Professor
Geological Sciences
University of Manitoba
Ph: 204-474-7826

On Jul 13, 2020, at 17:42, Paul Nesbit < > wrote:

Caution: This message was sent from outside the University of Manitoba.

Hi Paul,

Will you please confirm that you agree that each of the following co-authored and published manuscripts can be included within my dissertation:

- Nesbit, P.R., Durkin, P.R., Hugenholtz, C.H., Hubbard, S.M., and Kucharczyk, M. 2018. 3-D stratigraphic mapping using a digital outcrop model derived from UAV images and structure-from-motion photogrammetry. *Geosphere*, 14 (6), p. 2469-2486. doi:10.1130/GES01688.1
- Nesbit, P.R., Boulding, A.D., Hugenholtz, C.H., Durkin, P.R., and Hubbard, S.M. 2020. Visualization and sharing of 3D Digital Outcrop Models to promote open science. *GSA Today*, 30 (5), p. 4-10. doi:10.1130/GSATG425A.1

Thank you!

Paul R. Nesbit

RE: Written Permission for use of Co-Authored Materials

Maja Kucharczyk <
Mon 7/13/2020 4:44 PM
To: Paul Nesbit <
Hi Paul,

I confirm.

Thank you,
Maja Kucharczyk

From: Paul Nesbit <
Sent: Monday, July 13, 2020 4:43 PM
To: Maja Kucharczyk <
Subject: Written Permission for use of Co-Authored Materials

Hi Maja,

Will you please confirm that you agree that the following co-authored and published manuscript can be included within my dissertation:

- Nesbit, P.R., Durkin, P.R., Hugenholtz, C.H., Hubbard, S.M., and Kucharczyk, M. 2018. 3-D stratigraphic mapping using a digital outcrop model derived from UAV images and structure-from-motion photogrammetry. *Geosphere*, 14 (6), p. 2469-2486. doi:10.1130/GES01688.1

Thank you!

Paul R. Nesbit

Re: Written Permission for use of Co-Authored Materials

Adam David Boulding < >
Mon 7/13/2020 4:58 PM
To: Paul Nesbit < >

Yes.

Sincerely,

Adam Boulding

From: Paul Nesbit <
Sent: Monday, July 13, 2020 4:43:10 PM
To: Adam David Boulding < >
Subject: Written Permission for use of Co-Authored Materials

Hi Adam,

Will you please confirm that you agree that the following co-authored and published manuscript can be included within my dissertation:

- Nesbit, P.R., Boulding, A.D., Hugenholtz, C.H., Durkin, P.R., and Hubbard, S.M. 2020. Visualization and sharing of 3D Digital Outcrop Models to promote open science. *GSA Today*, 30 (5), p. 4-10. doi:10.1130/GSATG425A.1

Thank you!

Paul R. Nesbit

Appendix C

Supplemental Files and Resources

Supplemental Files referenced in **Chapter 2** and can all be accessed in the Geological Society of America (GSA) data share repository (https://doi.org/10.1130/GES01688.S1):

- Supplemental File 2.1. Animated fly through of the dense point cloud 3D DOM (part 1 of 2)
- Supplemental File 2.2. Animated fly through of the dense point cloud 3D DOM (part 2 of 2)
- Supplemental File 2.3. Point bar accretion surfaces interpreted from the dense point cloud UAV-SfM DOM, see Figure 2.10. Note this model contains 1.2 of an original 5.2 million points for this subsection (low resolution).
- Supplemental File 2.4. Point bar accretion surfaces interpreted from the dense point cloud UAV-SfM DOM, see Figure 2.10. Note this model contains 3.7 of an original 5.2 million points for this subsection (high resolution).
- Supplemental File 2.5. Counter point bar accretion surfaces interpreted from the dense point cloud UAV-SfM DOM, see Figure 2.11. Note this model contains 1.2 of an original 8.5 million points for this subsection (low resolution).
- Supplemental File 2.6. Counter point bar accretion surfaces interpreted from the dense point cloud UAV-SfM DOM, see Figure 2.11. Note this model contains 3.8 of an original 8.5 million points for this subsection (low resolution).

Supplemental Files referenced in **Chapter 5** and can all be accessed in the Geological Society of America (GSA) data repository (https://www.geosociety.org/datarepository/2020):

- Supplemental File 5.1 - Interactive videogame visualization presenting a 'virtual field trip' introducing basic geology concepts using a UAV-SfM textured mesh model within Dinosaur Provincial Park (Alberta, Canada). Standalone application (.exe file) for machines running Windows (no software required). Note the README.txt file after Unzipping prior to running.
- Supplemental File 5.2 - Interactive videogame visualization presenting a 'virtual field trip' introducing basic geology concepts using a UAV-SfM textured mesh model within Dinosaur Provincial Park (Alberta, Canada). Standalone application (.app file) for machines running macOS (no software required). Note the README.txt file after Unzipping prior to running.